Hydrodynamics and energy conversion in nanofluidic systems : a molecular perspective

Cecilia Herrero Guillen

N° d'ordre NNT: 2021LYSE1199

THÈSE DE DOCTORAT DE L'UNIVERSITÉ DE LYON
opérée au sein de
l'Université Claude Bernard Lyon 1

École Doctorale ED52
Physique et Astrophysique de Lyon

Spécialité de doctorat :
Discipline : Physique

Soutenue publiquement le 14/10/2021, par:
Cecilia HERRERO

Hydrodynamics and Energy Conversion in Nanofluidic Systems: A Molecular Perspective

---

Devant le jury composé de:

Daan FRENKEL, Professeur Émerite, Cambridge University	Président
Guillaume GALLIERO, Professeur des Universités, UPPA	Rapporteur
Céline LEONARD, Professeure des Universités, Université Paris-Est	Rapporteure
Catherine BARENTIN, Professeure des Universités, Université Lyon 1	Examinatrice
Aziz GHOUFI, Maître des Conférences, Université de Rennes 1	Examinateur
Virginie MARRY, Professeure des Universités, Sorbonne Université	Examinatrice
Samy MERABIA, Directeur de Recherche, Université Lyon 1	Invité
Laurent JOLY, Professeur des Universités, Université Lyon 1	Directeur de thèse

A mi padre, que me enseñó a contar

To my father, who taught me to count

The work in this thesis is based on the following publications:

1. C. Herrero, T. Omori, Y. Yamaguchi and L. Joly. "Shear force measurement of the hydrodynamic wall position in molecular dynamics". *The Journal of Chemical Physics* (Communication) **151**, 041103 (2019)

2. C. Herrero, G. Tocci, S. Merabia and L. Joly. "Fast increase of nanofluidic slip in supercooled water: the key role of dynamics". *Nanoscale* **12**, 20396-20403 (2020)

3. C. Herrero and L. Joly. "Poisson-Boltzmann formulary". arXiv:2105.00720 (2021)

4. H. Oga, T. Omori, C. Herrero, S. Merabia, L. Joly and Y. Yamaguchi. "Theoretical framework for the atomistic modeling of frequency-dependent liquid-solid friction". *Physical Review Research*, **3**, L032019 (2021)

5. C. Herrero, M. de San Feliciano, S. Merabia and L. Joly. "Fast and versatile thermo-osmotic flows with a pinch of salt." *Nanoscale* (Communication) (2022)

6. C. Herrero, M. Pauletti, G. Tocci, M. Iannuzzi and L. Joly. "Connection between water's dynamical and structural properties: insights from *ab initio* simulations". arXiv:2112.05525, *under review* (2022)

7. C. Herrero, L. Joly and S. Merabia. "Ultra-high liquid-solid thermal resistance using nanostructured gold surfaces coated with graphene". *submitted* (2022)

Contents

Acknowledgements

It is necessary to acknowledge, and thank, all the people without whose advice, support, and comments, all the work presented in this manuscript would have been for sure worse or even inexistent.

First of all I would like to thank all the members of my jury for accepting to be part of it, and for taking their time to read and think about the work, sometimes dense, presented here. Thank you to Guillaume Galiero and Céline Leonard, who wrote extensive and detailed reports on this work, and who posed interesting questions and highlighted some possible weaknesses, which allowed me to prepare my defense and improve the present manuscript. Also thank you to Catherine Barentin, Aziz Ghoufi and Virginie Marie, and special thanks to Daan Frenkel, who could take an airplane from the United Kingdom to assist in person to the defense, an effort that I particularly appreciate given these strange times of pandemic. It was a great honor to have you here and a great pleasure to discuss with you.

It is unavoidable to mention here my thesis director, Laurent Joly, without whose help and advice this work would have not been possible. I feel extremely lucky and grateful about finding a thesis advisor like Laurent, and many are the things I have learnt from him during these last three years. Scientifically, Laurent's deep physical understandings and intuitions have allowed me to benchmark all the projects presented here. During my thesis with him, I felt my opinions (even the most mistaken ones) where always listened, considered, and discussed. It is indeed in the scientific discussions with him, where I feel I have grown up more scientifically speaking. But far more is what cannot be appreciated from the bare words of the papers: the coffee breaks, the nice restaurants in Japan, the politeness and kindness (even with the meanest referee in the submission process), the sense of responsibility and the passion for his job and research... I hope to have managed to absorb and make mine any (at least one) of these things. Thank you for being always available and for your unconditional support and advice.

I also want to thank here all the people who directly collaborated in this thesis. Special thanks to Samy Merabia, invited member of my jury due to his strong influence all along my PhD. Samy's expertise, specifically on thermal transport, was critical for different projects. In addition, his door was always open for me to annoy him at any moment, it did not matter how strange or unexpected it was my concern; he always gladly tackled it and explained it. Thank you to Yasutaka Yamaguchi and Takeshi Omori, who welcomed me in Osaka two times during my thesis studies. I felt extremely well treated when I was there and even by distance we managed to advance in some projects that are cited in the present manuscript. Thank you to Gabriele Tocci, who has given me valuable feedback on several projects in this thesis work and whom, together with Marcella Iannuzzi, patiently solved my doubts and introduced me in the quantum (or almost quantum) world of *ab initio* molecular dynamics. I also mention here the PhD students from both groups, Haruki Oga, and Michela Pauletti, with whom I had the opportunity to learn some beautiful mathematical

idea departing from the Langevin equation, and the (far more subtle and difficult than expected) machine learning world. Also thank you to Michael de San Feliciano, whose internships with Laurent, Samy, and myself, provided fruitful insights and perspectives on thermo-osmosis.

Aside of these collaborators, I also had the opportunity to scientifically interact with different people along my thesis: Christophe Ybert, Anne-Laure Biance, Yanbo Xie... With special mention to the two post-docs I met during my PhD: Li Fu and Simon Gelin, who always addressed my questions and concerns (avoiding me to overwhelm Laurent with too many silly questions), and who have helped me a lot, both at the beginning and the end of my PhD. I am deeply grateful for your kindness and advice.

It may seem far in time but I also want to thank my advisors during my master in Spain: Francisco Alarcón and Chantal Valeriani. Their kindness and passion for their work made my interest on computer simulations grew and lent me to this thesis. I cannot help to think what I would be doing now if they had not appeared on my path.

This PhD would have been different without the life in the lab, thank you to my team, MMCI, who allowed me to present my work several times and practice for different presentations during the group meetings, and whose members always have interesting comments to improve my work. I also thank my colleagues and specially the friends in the lab (and outside, with a special mention here to my very nice flat mates, Mai and Thu, who would always smile even if they had understood nothing when I would talk about my work). I will not mention their names here because then I would take the risk to forget somebody, but all the lunch times, after work beers, restaurants, hikes, and long office discussions (obligatory mention here to Bastien, my longest-in-time office mate, who decided to choose my office in his first day of work despite my selfish will of placing my stuff in his desk) have been part of this experience and it is something I will never forget.

Muchas gracias a mi familia. En especial a mi madre, cuyo cariño y apoyo constante ha sido fundamental, y a María, que me han apoyado y animado desde la distancia con este trabajo. También mencionar aquí a mis tías y tíos. Me siento muy contenta de teneros a todos de mi lado y por sentirme siempre querida por todos vosotros, ya sea desde Madrid, San Mateo, Almería, Murcia o Guatemala. Gracias a mi padre, que me llamó todas las semanas durante dos años y me enseñó, hace mucho tiempo los números, pero también la honestidad y el dar lo mejor de uno mismo. Todo este trabajo no habría sido posible sin ninguna de estas tres cosas, y por eso esta tesis va dedicada a ti.

Finally thank you to Dolachay, who supported me along this process, in the best and in the worst moments, and without whom the writing of this thesis would have been a harder work. Thank you for always being there and for significantly lowering the level of difficulty. It made my days lighter to know I could always count on you, either to tell me everything was going to be ok, or to bring me smuggled Spanish food.

Abstract

"Tout ce qui va arriver, peut et doit être prévu."
Les Shadox, *french animated TV series* 1968–1974.

Nanofluidics, the study of fluid transport at nanometer scales, appears as a promising field to tackle some great challenges faced by our society, such as the development of alternative sustainable energies. Nanofluidic devices could contribute in energy conversion by e.g. the use of membranes with nanoscale porosity, which allow to obtain electricity from the different salt concentrations between fresh and sea water at the estuaries, or to harvest waste heat by e.g. generating osmotic flows or electric currents from temperature gradients via thermo-osmosis or thermoelectricity. As the size decreases, surfaces have an increasingly important role, and it is critical at the nanoscale to understand the molecular mechanisms occurring at liquid-solid interfaces. One important property is the failure of the hydrodynamic no-slip boundary condition. Instead, a velocity jump occurs at the interface, defining the slip velocity, which is related to the liquid-solid friction coefficient. In this manuscript we start from the slip boundary condition, and characterize the position where the boundary applies from a molecular point of view, using classical molecular dynamics simulations. Afterwards, we study the temperature dependence of the liquid-solid friction coefficient, and compare it to its bulk transport analogous, the shear viscosity of the fluid. With special focus on supercooled water, we reveal the molecular mechanisms controlling friction by decomposing the interfacial transport coefficient into a static and a dynamic contribution, and we assess the effect of supercooling on the large slippage we observe at the lower temperatures. Aside of hydrodynamic transport, we also study interfacial thermal transport by determining the most suitable surface structure, for a system constituted in water on nanopatterned gold coated with a graphene sheet, in order to increase the interface resistance. We also perform first principle simulations, which explicitly solve the electronic structure, to explore the bulk water shear viscosity and diffusion coefficient temperature evolution. Motivated by a connection between dynamics and structure, we assess the validity of the excess entropy scaling relations, which relate the bulk transport coefficients with integrals of the pair radial distribution functions. Finally, we also study thermo-osmosis flows, by proposing an analytical model that accounts for specific interactions between solvent and ions with the wall. Within this model, we study the parameters that control the thermo-osmotic response of the system, predicting large responses for systems with large slippage, and a change of the osmotic flow direction with the salt concentration, which could explain experiments where the flow direction cannot be predicted by the classical theory.

Résumé

"Pourquoi faire simple quand on peut faire compliqué..."
Les Shadox, *french animated TV series* 1968–1974.

La nanofluidique, l'étude du transport des fluides à l'échelle nanométrique, apparaît comme un domaine prometteur pour relever certains grands défis auxquels notre société est confrontée, comme le développement d'énergies alternatives durables. Les dispositifs nanofluidiques pourraient contribuer à la conversion d'énergie, par exemple en utilisant des membranes à porosité nanométrique, qui permettent d'obtenir de l'électricité à partir des différentes concentrations en sel entre l'eau douce et l'eau de mer dans les estuaires, ou de récolter la chaleur perdue, par exemple en générant des écoulements osmotiques ou des courants électriques à partir de gradients de température par thermo-osmose ou thermoélectricité. À mesure que la taille diminue, les surfaces jouent un rôle de plus en plus important, et il est essentiel, à l'échelle nanométrique, de comprendre les mécanismes moléculaires qui se produisent aux interfaces liquide-solide. Une propriété importante est l'échec de la condition hydrodynamique de non glissement. Au lieu de cela, un saut de vitesse se produit à l'interface, définissant la vitesse de glissement, qui est liée au coefficient de frottement liquide-solide. Dans ce manuscrit, nous partons de la condition limite de glissement, et nous caractérisons la position où la limite s'applique d'un point de vue moléculaire, en utilisant des simulations classiques de dynamique moléculaire. Ensuite, nous étudions la dépendance en température du coefficient de frottement liquide-solide, et nous le comparons à son analogue en volume, la viscosité de cisaillement du fluide. En nous concentrant sur l'eau surfondue, nous révélons les mécanismes moléculaires qui contrôlent le frottement en décomposant le coefficient de transport interfacial en une contribution statique et une contribution dynamique, et nous expliquons l'effet important de la surfusion sur le glissement que nous observons aux basses températures. En dehors du transport hydrodynamique, nous étudions également le transport thermique interfacial en déterminant la structure de surface la plus appropriée, pour un système constitué d'eau sur de l'or nanotexturé recouvert d'une feuille de graphène, afin d'augmenter la résistance de l'interface. Nous effectuons également des simulations ab initio, qui résolvent explicitement la structure électronique, pour explorer l'évolution en température de la viscosité de cisaillement et du coefficient de diffusion de l'eau. Motivés par un lien entre la dynamique et la structure, nous évaluons la validité des lois d'échelle de l'excès d'entropie, qui relient les coefficients de transport en volume à des intégrales de fonctions de distribution radiale. Enfin, nous étudions également les écoulements thermo-osmotiques, en proposant un modèle analytique qui rend compte des interactions spécifiques du solvant et des ions avec la paroi. Dans ce modèle, nous étudions les paramètres qui contrôlent la réponse thermo-osmotique du système, et nous prédisons des réponses importantes pour les systèmes avec un grand glissement, ainsi qu'un changement de la direction de l'écoulement osmotique avec la concentration en sel, ce qui pourrait expliquer les expériences où la direction de

l'écoulement ne peut pas être prédite par la théorie classique.

List of Symbols

In order to help the eventual reader, we present here the notation of some important quantities used along this thesis manuscript.

General quantities

- inverse thermal energy $\beta = 1/(k_{\mathrm{B}}T)$, with k_{B} the Boltzmann constant and T the temperature
- absolute ionic charge $q = Ze$, with e the elementary charge and Z the ion valence
- number of degrees of freedom N_{f}
- temperature T
- total pressure P
- mass density $\rho = m/V$, with m the particle's mass and V the volume
- number density $n = N/V$, with N the number of particles and V the volume
- electronic density n_{e}
- contact angle θ

Characteristic lengths

- effective molecular diameter σ[1]
- Bjerrum length ℓ_{B}
- Debye length λ_{D}
- Gouy-Chapman length ℓ_{GC}
- slip length b (see hydrodynamic transport)
- Kapitza length ℓ_{K} (see thermal transport)

Hydrodynamic transport

- slip velocity v_{slip}
- shear viscosity in bulk η
- interface (liquid-solid) friction coefficient λ
- slip length $b = \eta/\lambda$
- hydrodynamic wall position z_{s}
- shift between the hydrodynamic and the physical wall position Δ
- shear stress at the wall τ^1, τ_{w}
- diffusion coefficient D
- hydrodynamic radius R_{h}

Thermal transport

- bulk thermal conductivity λ_{th}
- interface thermal conductance G
- interface thermal resistance $R = 1/G$
- Kapitza length $\ell_{\text{K}} = \lambda_{\text{th}}/G$

Dynamic times

- Maxwellian relaxation time t_{Maxwell}
- Green-Kubo relaxation time τ_{GK}, related to the decay of the traceless components of the pressure tensor autocorrelation
- total structural relaxation time τ_ρ, related to the decay of the density autocorrelation, and decomposed as a weighted sum of a short time decay τ_β and a long time decay τ_α such as $\tau_\rho = (1 - A)\tau_\beta + A\tau_\alpha$

Poisson-Boltzmann Framework

- electric field E
- electrostatic potential V
- reduced potential $\phi = \beta q V$
- their value at the wall V_{s} and ϕ_{s}
- ion densities $n_\pm$
- charge density ρ_{e}

- solvent dielectric permittivity ε[1]
- salt concentration $n_0 = n_+ = n_-$ in the bulk/reservoirs
- surface charge density Σ

[1] In Chapter 2 $\{\varepsilon, \sigma, \tau\}$ correspond to reduced Lennard-Jones units referring, respectively, to liquid-liquid interaction energy, distance, and system's characteristic time $\tau = \sigma\sqrt{m/\varepsilon}$

Chapter 1

Introduction

"The validity of the no-slip boundary condition at a fluid-solid interface was debated for some years during the last century, there being some doubt about whether molecular interactions at such an interface lead to momentum transfer of the same nature as that at a surface in the interior of a fluid; ***but the absence of slip at a rigid wall is now amply confirmed by direct observations*** *and by the correctness of its many consequences under normal conditions."*

George K. Batchelor, *An Introduction to Fluid Dynamics* 1967

Contents

1.1 Nanofluidics, a land of opportunities

Nanofluidics, consisting in the study of fluids that are confined at the nanometer scale, has emerged as a new and interesting field in the past few decades due to novel behavior associated to this length scale. Indeed, nanofluidics lies in the validity limit of continuum approaches, and a discrete description of the molecular mechanisms become critical to understand some of the physical and chemical processes taking place. With that regard, thanks to the great increase of computational power over time, molecular dynamics simulations have appeared as a fundamental tool to explore fluid transport at small length scales, generating a great scientific interest and contributing to the development of nanofluidics. From an experimental perspective, the great technological progress in the recent years can also be associated to the evolution of nanofluidics: advances in observation and measurement techniques have made possible to control what happens at the nanoscale, and to accurately determine the small physical quantities associated.

The recent and generalized interest in nanofluidics cannot be exclusively associated to the technological development, moving towards smaller devices, but also to the expectation

that new properties related to interfacial processes will emerge. The expected new fluid behavior can be associated to the broad spectrum of characteristic lengths existing at the nanoscale arising, for example, from electrostatics, fluid dynamics, or related to the size of the fluid molecule. The competition and coupling between different mechanisms associated to these lengths give rise to novel phenomena and may imply complex fluid behavior that cannot be observed in larger systems. Therefore, a better understanding of the molecular mechanisms taking place at the nanoscale can allow us to profit from them. Also, nanofluidic systems are ubiquitous in nature, and govern a large variety of biological processes, as those related to the transport of biomolecules across cell walls [1, 2, 3, 4].

Our body is constituted by a fine and efficient machinery and a better understanding of it can allow us to reproduce and exploit it in our benefit. A paradigmatic example is the salt filtration by the kidney, which takes place thanks to a subtle combination of geometry and osmotic processes [5]. The osmotic exchange at the functional units of the kidney, the nephrons, is due to the combination of aquaporins, the proteins that regulate water flow in the human body, and salt pumps, that allow the absorption of the salts by our body. With a water loss on the order of 1% [5, 6], kidney filtration is an extremely efficient mechanism both in terms of separation and energy, and the reproduction of its machinery via nanofluidic artificial devices could have potential applications in portable dialysis devices or in water pretreatment for desalination.

Indeed, the development of alternative solutions to the classical methods for seawater desalination based on evaporation (very energetically costly) is key to face the water crisis related to the lack of fresh water, typically in isolated or underdeveloped regions. With that regard, nanofluidic devices could present cheap and portable alternatives, by filtrating sea water employing membranes with nanoscale porosity. The main idea of these state-of-the-art devices is to separate two regions with different salt concentration (such as sea and fresh water) by a semipermeable membrane, and then use pressure driven processes to overcome the natural osmotic pressure, creating a water flux from the high to the low salt concentration region: this operation is known as reverse osmosis. Although the power consumption of technologies based on reverse osmosis has experienced a striking decrease over time (from ~ 15 kWh/m^3 in 1970 to ~ 2 kWh/m^3 in 2008), it is still higher than the so-called thermodynamic limit on the order of ~ 1.06 kWh/m^3, defined as the theoretical minimum energy required to desalinate 35 g/L at 50% of recovery [7]. Alternatively, different technologies are still being proposed taking advantage of interfacial phenomena, as for instance thermo-osmosis, based on thermally pumping water across nanotube membranes and with predicted flow rates on the order of 7.77 L/h from temperature differences of only 15 K [8].

Aside of water desalination, the need and development of renewable sources of energy is indubitably one of the greatest challenges faced by our society. World energy consumption is significantly increasing every year, and yet a large percentage is based on burning fossil fuels, increasing the world emissions of carbon dioxide and contributing to global warming [9]. In contrast, sustainable, abundant and inexpensive sources of energy appear as a critical alternative to tackle the problem, and nanofluidic systems could contribute significantly in that field. We will see how nanofluidic systems can help us to harvest energy and how can we take advantage of the novel interfacial phenomena occurring at the nanoscale. But, first, let's have an overview of the different components at play in hydrodynamics, interfaces, and energy conversion.

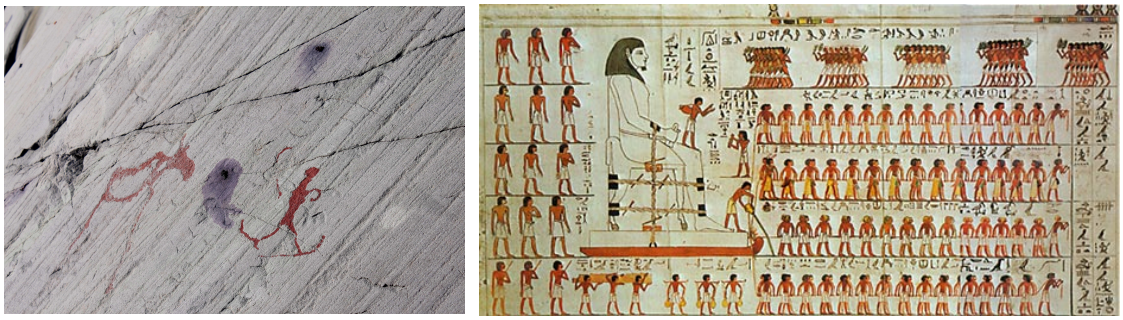

(a) (b)

Figure 1.1: (a) Stone age rock drawing of Alta, Norway, dated between 4300 and 500 BC. The image represents a man on skis with a bow pursuing an elk. [Photo: Ralph Frenken 2012]. (b) Depiction from the tomb of Djehutilohept at el-Bersheh, Egypt, dated around 1800 BC. The wall painting represents several workers moving a colossal statue, and one of them (in the middle) pouring some liquid in front of the sledge. [Taken from [11]].

1.2 Tribology and hydrodynamics: a historical review

In nanofluidics, as confinement increases, the surfaces play an increasingly important role, and it becomes critical to study the different phenomena taking place at the interface. One of the interfacial quantities we will be interested in studying and controlling is the friction between the liquid and the solid surface.

Tribology, from the Greek words *tribos* meaning "rubbing" and *logos* meaning "reason", encompasses the sciences and technologies of interacting surfaces in relative motion. Among the multiple interests of tribology, we can highlight the study of friction. Historically, one of the objectives of technology development in humankind has been to reduce the friction force, via *e.g.* lubrication, with the motivation of facilitating the daily activities such as construction or agriculture. The first hints of use of human imagination in order to reduce friction can be found already in the middle stone age (Mesolithic period, 11000-5500 years ago), where we can find represented in rock drawings the transportation of materials by sledges, wheeled vehicles, bearings, or the use of skis for hunting (Fig. 1.1a) [10]. We can also find early examples of lubrication, for example, in an Egyptian painting from the tomb of Djehutilohept at el-Bersheh (1800 BC, Fig. 1.1b), where we can observe the image of a man pouring lubricant (probably water) in front of a sledge to transport a big statue [11].

However, we have to wait until the Renaissance to account for the first scientific developments in the study of friction. Leonardo da Vinci (1452-1519) was the first author to leave written proof of his systematic studies of friction on horizontal and inclined planes [12]. Nevertheless, he left his studies unpublished, and we have to wait 200 years to find the first publications on the classical laws of dry friction by Guillaume Amontons, in 1699, who stated that the friction force is directly proportional to the applied load, and independent of the apparent area of contact [13]. The next important advance on solid-solid friction was made in 1750 by Leonard Euler, who was the first one to distinguish between two different types of dry friction: static friction, when an object is placed on a surface, and kinetic (or dynamic) friction, related to the movement of an object on a surface [14]. Finally, it is also important to highlight the work of Charles A. Coulomb as well on dry friction, who defined friction mathematical formulas based on his own experiments, extending Amontons work, and who also studied friction on fluids, introducing the concepts of external friction,

between laminae of different bodies, and internal friction, between laminae of one body [15].

In parallel to the works on dry friction, who were mostly focused on engineering applications, another field was being developed at the same time, related to the movement of fluids. On this topic, which was considered a different subject at that time, there are the well known works of Isaac Newton on viscous flows [16], where he defined the *defectu lubricitatis* or what nowadays we know as viscosity, which can be understood as the internal friction of fluids. Along with the industrial revolution, several advances were made by Leonard Euler, Daniel Bernouilli and Jean-Léonard M. Poiseuille, stating the basics of fluid dynamics [17]. An important advance in hydrodynamics was made by the end of the 18th century by Claude Navier, who included the viscous terms in Newton's laws for flowing fluids, and by George G. Stokes, who defined the basics of viscous flow [18]. It was the combination of the work of these two scientists, who developed their studies separately, which gave rise to the Navier-Stokes equations, that allow us to describe from air flows in the atmosphere of our planet to ocean currents, and basically any phenomena involving fluids.

Although the systematic study of confined flows and liquid-solid friction did not reach popularity until the second half of the 20th century, it was Claude Navier, in his "*Mémoire sur les lois du mouvement des fluides*" from 1823, who first thought in linking the concepts of internal and external friction for confined fluids [19]. Working in the need of a well defined boundary for what we know nowadays as the Navier-Stokes equations, Navier considered, together with the viscosity of the liquid ε, what he called *la résistance provenant du glissement* (the resistance coming from slip, E) at the liquid-solid interface. He concluded that both liquid-liquid and liquid-solid friction were related at the interface, stating the relation, in his original notation:

$$Ev + \varepsilon \frac{\mathrm{d}v}{\mathrm{d}x} = 0,$$

where v is the fluid velocity and x the normal to the wall. It is common nowadays, and so we will do in the present manuscript, to generalize Navier's boundary condition for moving walls (defining v_{slip} as the velocity jump at the interface), and to re-express the boundary equation in terms of the slip length as:

$$v_{\mathrm{slip}} = b \left. \frac{\mathrm{d}v}{\mathrm{d}z} \right|_{\mathrm{wall}}, \tag{1.1}$$

with z the normal to the wall, and $b = \varepsilon/E$. In the following we will use the standard notation η and λ to refer to the shear viscosity and the liquid-solid friction coefficient, so $b = \eta/\lambda$.

1.3 Slip length measures, state of the art

Although Navier's boundary condition (BC) was stated at the beginning of the 19th century, a common assertion in textbooks on hydrodynamics was to consider the no-slip BC, *i.e.* a vanishing fluid profile when in contact to the wall due to the absence of slip [20]. It was in the 1970's that the slip BC gained relevance due to the huge slip predicted by P. G. de Gennes for complex fluids, particularly for entangled polymer melts [21]. De Gennes stated that, supposing the monomer friction λ_1 of a similar order of magnitude than the friction of a simple fluid, an entangled polymer melt would present a large slip

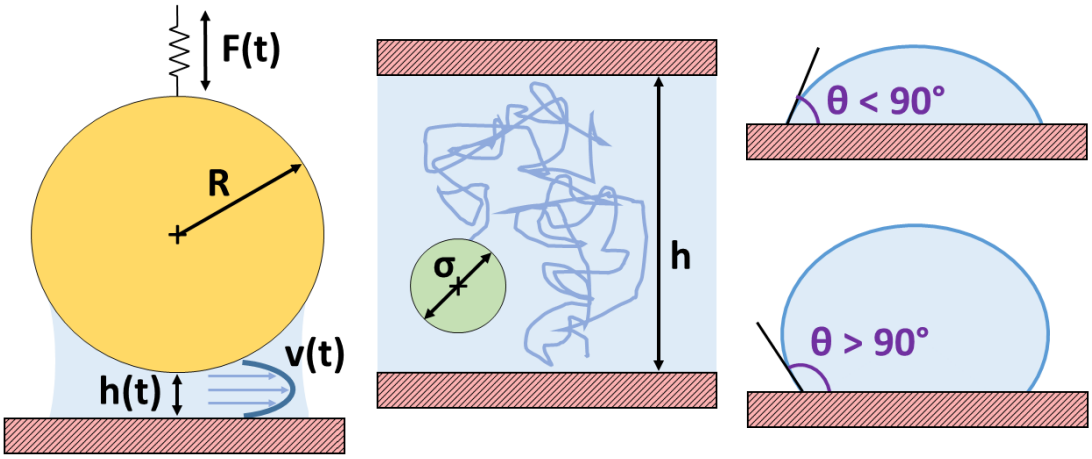

(a) Dissipation: SFA (b) Fluctuations: diffusion (c) Wetting

Figure 1.2: (a) Schematics of the surface force apparatus (SFA) used to experimentally determine slippage from the force acting on a plane in response to small oscillations of a sphere of radius R. Note that the sketch is not to scale, with the sphere radius on the order $R \sim$ mm and the height on the order $h \sim$ nm so $R \gg h$. (b) Scheme of the confined diffusion experiment, used to determine slippage from the thermal fluctuations of a colloid of diameter σ. (c) Sketch of wetting properties, defined from the contact angle θ of a sessile liquid droplet at the surface. When $\theta < 90°$ the surface is considered hydrophilic or wetting. When $\theta > 90°$ the surface is considered hydrophobic or non-wetting.

b_N at the surface, as compared to the monomer slip b_1, due to the large polymer viscosity η_N; following the simple decomposition:

$$b_N = \frac{\eta_N}{\lambda_1} = \frac{\eta_N}{\eta_1}\frac{\eta_1}{\lambda_1} = \frac{\eta_N}{\eta_1} b_1 \gg b_1.$$

De Gennes predictions have been broadly confirmed experimentally, measuring slip lengths on the order of ~ 10 μm for polymer melts [22, 23].

Although the large slippage exhibited by complex fluids was confirmed, the question about the presence of slip remained in the case of simple liquids and, specifically, water, where the slip would be expected to be comparable to a molecule size [24] and therefore significantly more difficult to determine experimentally. It was at the beginning of the 21st century that great advances were made in experimentally determining slippage for simple fluids. Due to the broad literature on different experimental techniques to characterize liquid slippage on a great variety of interfaces [25], we will briefly mention two of them as an illustration, not only on the great creativity needed to characterize phenomena at small length scales, but also as an exemplification of the power of the fluctuation-dissipation relation in statistical physics.

The first example of experiment to measure slippage for water is by using a surface force apparatus (SFA), consisting in a sphere of radius R on the order of mm attached to a spring, allowing the sphere to oscillate, generating a time dependent force $F(t)$ as a response. The sphere is located at a distance $h(t)$ from the solid surface for which we want to characterize the liquid-solid friction coefficient, and a flow $v(t)$ is generated in the liquid (*e.g.* water in [26]) enclosed between the sphere and the surface (see Fig. 1.2a). The idea, following Ref. 26, is to measure the dissipation which has to be modified by slippage. The presence of friction at the interface increases the force F, and by measuring the force

versus the velocity profile the authors deduce b following the relation:

$$F \approx \eta \frac{R^2}{h+b} v.$$

Note that this is an approximate expression and that a more complex, but exact one, is used in practice.

The second example, followed in Ref. 27, is based on confined diffusion of particles suspended in the liquid (water) enclosed in between the surfaces for which we want to characterize slippage. In this paper, the authors looked at fluctuations of small colloids in confinement (see Fig. 1.2b). While they move, the colloids will interact with the surface and the idea is to extract information on b from the colloid motion: the fluctuations will be modified by slippage. In this case, b should modify the diffusion coefficient D as compared to the bulk diffusion coefficient D_{bulk} in the form:

$$D - D_{\text{bulk}} \approx -\frac{\sigma}{h+b},$$

where h is the slit height and σ the colloid diameter. This expression is again an approximation intended to give the correct order of magnitude, and in practice the authors used a full numerical solution.

The results of both experiments, SFA [26] and confined diffusion [27], are in agreement, determining a slippage $b < 1$ nm for a hydrophilic surface (pyrex) and $b \sim 20$ nm for a hydrophobic surface (pyrex coated with a hydrophobic self-assembled monolayer, OTS). A typical way to characterize the wetting properties of a surface is from the contact angle θ formed between the surface and the tangent of a liquid droplet suspended on it. As sketched in Fig. 1.2c, when $\theta < 90°$ we will refer to a hydrophilic (wetting) surface, and when $\theta > 90°$ to a hydrophobic (non-wetting) one. Several efforts have been done experimentally to state the relation between slippage and the wetting properties of the solid surface. A selection of experiments, including SFA (Cottin et al. [26]) and confined diffusion (Joly et al. [27]), can be found in Fig. 1.3a. In this figure we see that the low wettability reduces water-solid friction, implying a larger slippage. Such tendency has also been confirmed via molecular dynamics (MD) simulations (Fig. 1.3b), where a scaling of $b \propto (1 + \cos\theta)^{-2}$ has been determined [28]. Although Figures 1.3a and 1.3b show a global tendency followed by both experiments and simulations, we can note a quantitative disagreement between the experimental results and the MD simulations, on the order of one order of magnitude (*e.g.* for $\theta \sim 80°$, $b \sim 10$ nm in experiments and $b \sim 1$ nm in simulations), whose origin remains unclear nowadays.

Once the existence of slippage for simple fluids as water had been assessed experimentally, intriguing results were provided related to novel 2D materials, specifically those based on carbon. For instance, recent experiments observed fast water transport on graphene, and particularly in carbon nanotubes (CNTs) [30, 31], whose origin is not yet fully understood. One example of the implications of this fast water transport is in terms of hydrodynamic permeability, which has been found to be between one and four orders of magnitude larger for CNTs than for other well performing biological water transporters such as aquaporins [30, 32, 33, 31, 34], with important applications in water treatment technologies.

In terms of slippage, one of the first reports for water in CNTs [30] experimentally determined slip lengths on the order of ~ 1 μm, which is four orders of magnitude larger than the originally expected values, on the order of the molecular diameter. Although the origin, or even the existence, of such a massive slippage is still strongly debated [35], other experiments have also recently determined large values of slippage for water-CNTs

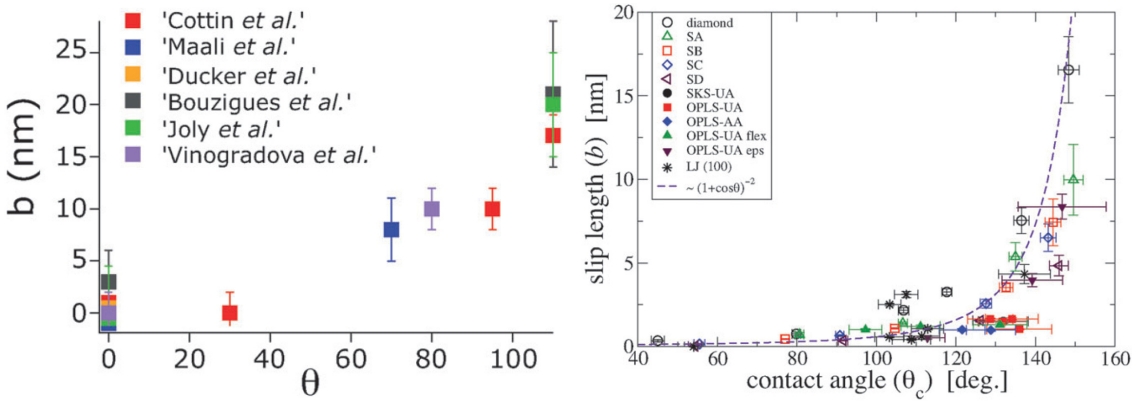

(a) Experiments (b) Simulations

Figure 1.3: Slip length versus contact angle for water on different smooth surfaces obtained from (a) experiments and (b) molecular dynamics simulations. A qualitative agreement, with $b \propto (1 + \cos\theta)^{-2}$, is observed, although a quantitative disagreement is appreciated with smaller values of slippage reported from simulations as compared to experiments for a given contact angle [Taken from [29]].

[32, 33, 36], with *e.g.* a measured slip $b \sim 300$ nm for CNTs of radius ~ 15 nm as reported in Ref. 31, with their results reproduced in Fig. 1.4a. Although there are some disagreements in terms of orders of magnitude between different experiments, all the results consistently observe an effect of the radius of the CNT on the slip length, with larger slippage for the most confined systems [37]. On the theory side, the evidence of curvature dependent friction has been already assessed via MD simulations with, in analogy to experiments, larger b related to smaller CNT radius [38, 39, 40], as seen in Fig. 1.4b. Nevertheless, we can observe in Fig. 1.4 that experiments and simulations show again a qualitative but not quantitative agreement, with a slip length on the order of ~ 200 nm for CNT radius of ~ 1 nm obtained from MD simulations, in contrast with the experimental results, which obtained a slippage of such order of magnitude for much larger CNT radius, on the order of ~ 17 nm. This quantitative disagreement between simulations and experiments is reminiscent of the slippage results on bare surfaces with different wetting properties (Fig. 1.3).

Therefore, there is still further work needed in order to understand the special properties of the water-graphene interface. One specificity discussed in the literature [41, 42] is the 2D smooth crystallographic structure of graphene. With that regard, it can be interesting to compare the results obtained for graphene with the ones of another 2D structure, boron nitride (BN). Motivated by this perspective, MD simulations have been performed for CNTs and BNNTs, assessing slippage differences between both systems for tube radius on the order of 1 nm [43]. However, such results are not in agreement with experimental results, which extrapolate to comparable slip lengths for BNNT and CNT at large radius, $R \sim 100$ nm, and significant slippage differences were observed for radius of ~ 35 nm (Fig. 1.4a). This disagreement again between simulation and experiments hinted in this case to the intrinsic inability of classical MD, based on Newton's equations of motion and using empirical interaction potentials, to capture the electronic characteristics of the system. Indeed, although both carbon and BN present the same crystallography and wetting properties (with contact angles of 86° and 87° respectively [44]), both surfaces differ in their electronic structure, with carbon being a semi-metal and BN a strongly isolating ionic crystal. This motivated the study of friction via first-principle or *ab initio*

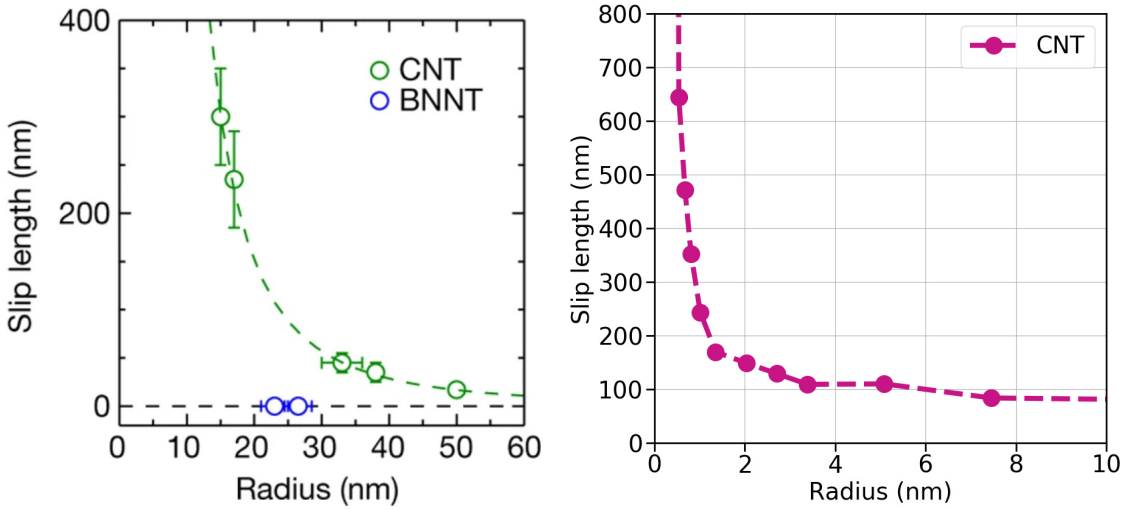

(a) Experiments (b) Simulations

Figure 1.4: Slip versus radius for water in carbon (CNT) and boron-nitride (BNNT) nanotubes, determined from (a) experiments [Taken from [31]] and (b) molecular dynamics simulations [Data taken from [40]]. A qualitative agreement is observed, with an exponential decrease of slippage with the nanotube size; although a quantitative disagreement is appreciated with great slippage values reported from simulations for significantly smaller nanotube radius as compared to experiments.

simulations, based on the Schrödinger equation, in order to solve the electronic structure problem. In Ref. 45, the authors determined the liquid-solid friction coefficient of water on planar graphene and BN sheets via *ab initio* MD simulations, reporting three times larger friction for water-graphene than for water-BN, highlighting the importance not only of the wetting properties on slippage but also of the electronic properties of the material. Notwithstanding, a difference of a factor of three in slippage is not enough to explain the exponential increase of slip with the radius observed in CNT experiments. Further and exciting venues are still on their way of being explored, pointing towards the development of a quantum theory of friction which accounts for the quantum fluctuations that cannot be captured by standard *ab initio* simulations [46].

1.4 Other interfacial phenomena: characteristic lengths

Aside of the slip length, which can be understood as the depth inside the solid where the linear extrapolation of the fluid velocity profile vanishes (see Fig. 1.5), a broad variety of characteristic lengths exist in the nanoscale, which can be related to different interfacial phenomena. We will highlight here the characteristic lengths that we further study in the present manuscript, although additional descriptions and details can be found in . 29, 47.

The Bjerrum length Most of the interesting applications related to energy conversion and desalination employing nanodevices are related to solutions of salts dissolved in water, with a bulk number density n_s. An important length scale related to electrostatics is the Bjerrum length ℓ_B, which is defined as the distance at which the thermal energy $k_B T$ (with k_B the Boltzmann constant and T the temperature) is comparable to the electrostatic

energy. Therefore,

$$\ell_{\mathrm{B}} = \frac{q^2}{4\pi\varepsilon k_{\mathrm{B}} T}, \tag{1.2}$$

where ε is the solvent dielectric permittivity and $q = Ze$ the absolute ionic charge, with e the elementary charge and Z the ion valence. The order of magnitude of the Bjerrum length plays a critical role for electrolyte solutions. When ℓ_{B} is comparable to or smaller than the interatomic distance, it implies that the thermal energy can overcome the electrostatic bonds, so that a molecule on the surface can be dissociated to release ions. This is the reason of why non-polar liquids (such as hydrocarbon oils or toluene), due to their strong electrostatic interactions, cannot present ion transport (ℓ_{B} for these fluids is much larger than the interatomic distance), in contrast to polar liquids. For example, in the case of a monovalent salt dissolved in water, $\ell_{\mathrm{B}} \sim 0.7$ nm at room temperature, making this polar fluid extremely suitable for nanofluidic applications.

The Debye length Another relevant characteristic length related to electrostatics is the Debye length λ_{D}, defined as

$$\lambda_{\mathrm{D}} = \frac{1}{\sqrt{8\pi\ell_{\mathrm{B}} n_{\mathrm{s}}}}. \tag{1.3}$$

The Debye length is related to the extension of the electric double layer or electrostatic diffusive layer (EDL): when ions are dissolved in a fluid, *e.g.* water, and enclosed in between charged walls with a surface charge density Σ, the ions reorganize to create a compensating charge within a distance λ_{D} from the wall (see Fig. 1.5). It is interesting to note that although a channel with charged walls is needed to form an EDL, its extension over λ_{D} is independent of Σ. Indeed from Eq. (1.3) we see that, at a given temperature, λ_{D} only depends on the bulk concentration of the ionic species. For a monovalent salt in water at room temperature $\lambda_{\mathrm{D}} \sim 0.3 \text{ nm}/\sqrt{n_{\mathrm{s}}(\mathrm{mol/L})}$. In experiments, typically $n_{\mathrm{s}} \in [10^{-4}, 1]$ M, related to Debye lengths $\lambda_{\mathrm{D}} \sim [30, 0.3]$ nm.

The Gouy-Chapman length In contrast to the Debye length, we can also find the so-called Gouy-Chapman length ℓ_{GC}, related to the surface charge density as:

$$\ell_{\mathrm{GC}} = \frac{q}{2\pi\ell_{\mathrm{B}}|\Sigma|}. \tag{1.4}$$

The Gouy-Chapman length defines the distance from the wall at which the electrostatic interaction of a single ion with the charged surface is on the order of the thermal energy. Typical Σ limits in experiments are between 1 and 300 mC/m^2, with associated $\ell_{\mathrm{GC}} \in [40, 0.2]$ nm.

The Kapitza length Aside of the characteristic lengths related to hydrodynamics and electrostatics, other interfacial phenomena arise from different transport processes as, for example, thermal transport. In analogy with hydrodynamic transport (discussed in detail in the coming chapters), a temperature jump ΔT occurs at the interface in the transport of heat across a channel, defining a characteristic length, the Kapitza length ℓ_{K}, from the boundary condition:

$$\Delta T = \ell_{\mathrm{K}} \left.\frac{\mathrm{d}T}{\mathrm{d}z}\right|_{\mathrm{wall}}, \tag{1.5}$$

with z the direction normal to the wall and $\ell_{\mathrm{K}} = \lambda_{\mathrm{th}}/G$, where G is the interface thermal conductance and λ_{th} the bulk thermal conductivity of the fluid. Despite of the similarity

in the BC expressions for hydrodynamic and thermal transport, the coupling between both processes is still subject of debate [48]. In analogy to slip, ℓ_K can typically reach on the order of $\sim 10\sigma$, with σ the molecular size [49].

Coupled phenomena: an illustrative example We mentioned that a rich range of novel behaviors can occur due to the competition at the nanoscale between different characteristic lengths related to different interface phenomena. Here we briefly describe an example of coupled effect for the canonical case of electro-osmosis, although the same reasoning can be extended to any other type of linear response, as thermo-osmosis, thermoelectricity, diffusio-osmosis, etc.

Let's start by considering a semi-infinite channel consisting in an aqueous electrolyte and a charged wall, see Fig. 1.5. We already discussed for this system type that the presence of the charged surface produces a compensating charge in the EDL, which extends over a characteristic distance from the wall given by the Debye length λ_D. By applying an electric field E along the interface, the charge density in the channel creates a driving force generating what we call an electro-osmotic flow. The electro-osmotic flow is characteristically a constant flow far from the wall at a velocity v_{EO}, and a shear flow within the EDL. The viscous shear stress τ is simply given by $\eta v_{EO}/\lambda_D$. In contrast, the stress related to the driving force per unit area is given by the number of ions in the EDL times the electrostatic force qE. Then, because of charge neutrality, the number of ions in the EDL times the charge q has to be opposite to the surface charge density Σ, and by force balance between both stresses at the interface we obtain $\eta v_{EO}/\lambda_D \sim -\Sigma E$. Finally, taking into account that the normal electric field at the surface is given by Σ/ε, with this electric field $\sim V_s/\lambda_D$ where V_s is the potential at the surface, we can then substitute Σ in the previous expression, obtaining the so-called Smoluchowski formula [29]:

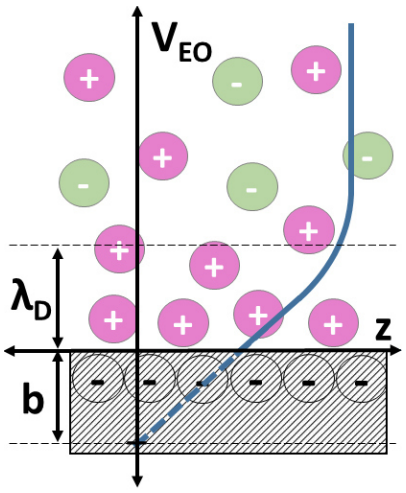

Figure 1.5: Schematics of the electro-osmotic velocity flow for a dissolved electrolyte on a slipping surface. Both characteristic lengths, Debye λ_D and hydrodynamic slip b, affect the induced flow profile.

$$v_{EO} = -\frac{\varepsilon V_s}{\eta} E. \tag{1.6}$$

This formula can be easily found in textbooks and indicates that, surprisingly, the electro-osmotic flow velocity is independent of the Debye length. But, what happens if we also account for slippage? By doing so, the previous reasoning still holds, and we just have to modify the viscous stress that is now given by $\eta v_{EO}/(\lambda_D + b)$, as it is straightforward from the velocity profile represented in Fig. 1.5. By following then the exact same procedure than for the no-slip case, we finally obtain that the electro-osmotic velocity scales as

$$v_{EO} = -\frac{\varepsilon V_s}{\eta} E\left(1 + \frac{b}{\lambda_D}\right), \tag{1.7}$$

meaning that slippage can significantly amplify the system response. To exemplify this, let's make some numbers. A reasonable down limit for the Debye length can be set at 0.3 nm, and typical slip length values vary between a few and hundreds of nanometers. This means that slippage can generate between 10 and 1000 times larger flow rates as compared to the no-slip situation.

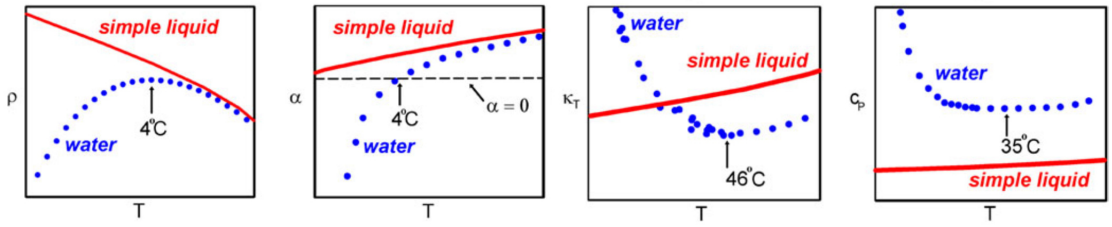

Figure 1.6: Thermodynamic properties of water, namely density ρ, thermal expansion coefficient α, isothermal compressibility κ_T, and isobaric capacity c_P, as a function of temperature and compared to the ones of simple liquids. [Taken from [57]].

1.5 Water is important: not such a simple fluid

In the study of hydrodynamics in nanofluidic systems with the objective of energy conversion, water appears as the most extended choice due to its ubiquitous nature and special properties. For instance, we already discussed its polar nature, which becomes a critical characteristic for salt dissociation at room temperature.

Newtonian fluids, also called simple fluids, are defined as those with purely viscous nature, *i.e.* the shear rate is directly proportional to the shear stress, where the proportionality constant is the shear viscosity of the fluid. It is common, and reasonable, to find in most textbooks [20, 50] the presentation of most or all metallic liquids and van der Waals liquids, including water, as the archetypal example of Newtonian fluids. Nevertheless, bulk water viscoelastic properties have been already assessed both via MD simulations and experimentally [51, 52, 53], and recent work on liquid-solid friction frequency dependence has also been able to determine the viscoelastic properties of the interface transport coefficient [54, 55]. Still, it is fair to indicate that such viscoelastic behavior is related to time scales on the order of few femtoseconds at room temperature, and water viscoelastic nature may only be an important concern when working at very low temperatures [56].

Aside of its viscoelastic behavior (one could argue that any fluid presents viscoelastic properties at short enough time scales), water presents itself as a special and interesting fluid due to a set of intriguing properties. Indeed, when lowering the temperature, water thermodynamic properties deviate from the expected behavior for simple liquids (Fig. 1.6). To mention a few, water presents a density maximum at 4°C, and it expands instead of contracting when cooling down, allowing ice (less dense) to float on liquid water, which is an important condition for the existence of life on earth [58]. Moreover, cold water is also easier to compress than warmer water. And to top it all, when frozen, its molecules can organize themselves in a number of different crystalline states (thirteen known polymorphs) among which nine of them are stable ices and four metastable [59, 60].

An important characteristic of water, that seems to be key to understand its characteristic behavior, is its ability to remain liquid to temperatures below its freezing point, at 0°C, also known as supercooled state. Indeed we observe a significant deviation of water thermodynamic properties shown in Fig. 1.6 from the typical simple liquids when cooling down water, and some of these properties even seem to diverge when T approaches to -45°C (228 K) [57]. It is difficult to find an explanation to water's anomalous behavior and the proposed understandings are still subject of scientific debate. One of these explanations, proposed almost 30 years ago, is the idea that for supercooled water, water can present itself in two different phases, one of them more dense and structured than the other one. In other words, that there could exist two different types of water and each of them would be a different liquid, creating a second critical point (aside of the well know

liquid-vapor transition) in the phase diagram of water, which should be located between 232 and 160 K [61]. Assessing whether the second critical point exists or not is not an easy task, and several technical difficulties are encountered to experimentally avoid water from freezing at such low temperatures, giving this temperature range the name of "no-man's land". Therefore, MD simulations remain a fundamental tool to explore supercooled water behavior, and indeed some computer simulations have shown promising results indicating the existence of such phase transition [62].

The two phases of supercooled water occur because the hydrogen bond structure of the water molecules can induce two different ways of joining, or packing. Thus, in the lower-density liquid, four water molecules cluster around a fifth central molecule defining a hydrogen-bonded tetrahedron shape. In the higher density liquid, however, a sixth molecule comes into play, which has the effect of increasing the density [63, 64]. Aside of this theoretical (up to now) second phase transition, hydrogen bond network also plays a role in determining different condensed phases in the water phase diagram, as for example allowing to distinguish between different solid phases or solid-liquid transitions due to the disruption of the hydrogen bond network due to thermal fluctuations [65]. Therefore, water molecular interactions are due to a fine balance between van der Waals and hydrogen bond interactions [66], and *ab initio* MD can be an interesting tool to study the electronic structure of water, with applications *e.g.* in ice nucleation on surfaces, and to better understand its anomalous bulk behavior [67].

Also, we have seen that aqueous electrolytes are a fundamental component in the development of energy conversion technologies, and that water polar nature plays an important role on ion transport. Although empirical force fields have been developed to describe ionic solutions in water [68], non-polarizable models seem to dramatically fail in reproducing some important experimental results such as the dependence of water's diffusion coefficient on the salt concentration [69], pointing at the need to account for polarizability to describe aqueous solutions. Nonetheless, developing a good polarizable force field is a difficult task, and it is still strongly dependent on the fine tuning of the different modelled parameters, thus not the best tool to explore novel behavior. *Ab initio* MD appears as a good alternative to classical MD in simulating ionic transport and providing a reliable atomistic description.

Although present in every day life, water still unravels a broad spectrum of anomalous behavior and unanswered questions that remain to be understood. Computer simulations are a fundamental tool to overcome the technical difficulties to experimentally study water under extreme temperature and pressure conditions, to understand its rich phase diagram and to disclose and explore novel bulk and interface phenomena, with important applications to surmount some great challenges faced by our society such as the development of sustainable alternative energies.

1.6 Nanofluidics and energy conversion

Previously, we presented reverse osmosis as an important yet inefficient mechanism to tackle the water crisis. Indeed, most of the energy consumption in reverse osmosis processes come from the large pressure values needed to overcome the natural osmotic pressure (on the order of 30 bars for sea water [70]), imposing a great constrain in the efficiency of reverse osmosis mechanisms for water desalination. This energetic cost for desalination can be calculated from the entropy change associated to mixing salty and fresh water, related to a Gibbs free energy change $\Delta G \approx 1$ kWh/m^3, benchmarking the thermodynamic limit at which reverse osmosis becomes a profitable process [7].

Nonetheless, one could think in the inverse point of view, and the energy cost to desalinate water is the same amount of energy one could extract from mixing fresh and sea water. Although this energy density is not as great as the one related to other sources of energy (*e.g.* 4 or 5 orders of magnitude smaller than fossil fuels), the abundance of fresh and salty water and the large water fluxes change the picture. To illustrate this, let's consider the longest and mightiest river in the world: the Amazon River, with a flux $Q \simeq 209000$ m^3/s. We can compute the power associated to this flux when flowing into the Atlantic, simply given by the product $Q \cdot \Delta G$, obtaining a power loss on the order of 1 TW, equivalent to the power of 1000 nuclear reactors [71]. Even if we were able to harvest just 1% of this energy, we would still manage very profitable numbers.

The extraction of the energy of mixing water with different salinity concentrations, as from the estuaries, transforming salinity gradients into electricity, receives the name of "blue energy". The enormous potential of blue energy presents a very appealing renewable and non-intermittent energy reservoir, but the main scientific question is: how can we harvest it? Currently there are two main technologies to harvest blue energy: pressure retarded osmosis (PRO) and reverse electro-dyalisis (RED). PRO technologies start from the idea of using the net water flux generated by placing a semipermeable membrane between two reservoirs with different salt concentration. Then, the driven osmotic flow due to the salinity gradient results into a mechanical force, which can be used to run a turbine. The simplicity of the idea under PRO motivated to test it for large scale energy production. However, it was concluded that the energy production is not sufficient to be commercially interesting [72, 71]. While PRO stands on water fluxes, in opposition, RED technologies are based on the ionic fluxes generated by placing a semipermeable membrane that only allows one of the ionic species to pass, whether anions or cations, generating a current (or voltage) under a concentration gradient between two reservoirs. After, the ionic current is transformed into an electronic current by redox conversion at electrodes [73].

The conversion efficiency of RED technologies, on the order of a few watt per square meter of membrane, points at RED to have more large-scale availability than its PRO counterpart. Still, both RED and PRO technologies are quite inefficient and present a number of disadvantages that need to be tackled. For instance, in the case of PRO, in order to avoid the ions to pass, one needs semipermeable membranes with very small pores, which hinders the water flux and also may cause membrane fouling issues. In the case of RED, an important challenge for its commercialization is the high cost of existing cation/anion selective membranes to separate ions, together with small voltage/electric currents obtained due to large energy losses in the ionic to electronic current conversion, or polarization effects [74].

One can then infer that the big bottleneck encountered in the development of PRO and RED technologies is mostly due to different problems related to the use of membranes. The question now is, can we go beyond? can we find new materials, different than the commercial membranes? Again, nanofluidic phenomena presents itself as a viable solution. By taking advantage of the subtle interface mechanisms that gain relevance at the nanoscale, different innovative solutions to the problem, which avoid the use of semipermeable membranes, have been already proposed. One of the most promising venues is based on diffusio-osmosis, consisting in osmotic flow generation under salt gradient in fully permeable nanochannels. This behavior, directly confirmed by experiments in nanochannels [75], has been obtained together with promising results related to the great electric current measured for BNNT [76]. In this experiment, the authors describe the fabrication and use of ultra-thin membranes pierced by BNNT that connect two reservoirs with different

salt concentration. The results for BNNT are in quantitative and qualitative agreement with the prediction, and large electric currents are related to large surface charges. Furthermore, power densities between $100 - 1000$ W/m^2 were reported, which are in great contrast with the ~ 8W/m^2 reported for the most profitable PRO and RED based devices [77, 78], making the use of nanomaterials industrially relevant and a real alternative. Aside of the mentioned results for BNNT, further recent findings report powers on the order of 1 MW/m^2 for MoS_2 nanopores [79], and promising results and efforts are currently focused in the development of these technologies using carbon nanomaterials, with huge potential for blue energy purposes [80]. Still, their efficiency for large systems, critical for their comercial viability, is a subject of debate, due to *e.g.* power density hindering related to concentration polarization [81, 82].

As an alternative to diffusio-osmosis, similar and less explored options can be based on osmotic current generation by other interfacial mechanisms taking place at the nanoscale, such as thermo-osmosis (thermally driven flows) or electro-osmosis (electrically driven flows). For instance for thermo-osmosis, it has been recently demonstrated that by driving a thermo-osmotic vapour flux across a nanoporous membrane from a hot to a cold reservoir, heat energy can be converted into mechanical work used to move a turbine, with power densities of ~ 3 W/m^2 [83]. Also, recent simulation work on CNT membranes predicts large values of flow velocities [84]. Although the numbers on thermo-osmosis may seem small as compared to diffusio-osmosis, they are still significant and as good as those reported for other blue energy technologies. Moreover, they open the way to another critical challenge: waste heat harvesting. In this line, nanofluidic systems have also shown promising results in electricity production from waste heat through thermoelectricity [85]. The great power of interfacially driven transport allows us to use nanofluidic systems in new and creative ways. Also further perspectives can be put in the use of coupled interfacial phenomena, which may boost the responses by orders of magnitude, as we showed for electro-osmosis in Eq. (1.7).

Overall, nanomaterials and hydrodynamics present as a powerful and promising combination, thanks to the great potential applications to harvest energy, not only from the different salinity concentration between sea and fresh water, but also from waste heat. However, further challenges still remain, and a better understanding of the different mechanisms is yet needed to make them economically profitable and for their applicability in large scale systems. The complex processes occurring at the nanoscale and the subtle balance between different phenomena make nanofluidics a puzzling field, but also a fascinating venue with many opportunities to go beyond.

1.7 Objectives and organization of the thesis

The main objective of this thesis is the search of innovative nanofluidic systems, guided by an accurate understanding of the different molecular mechanisms at play. With special focus on interfacial phenomena, and in particular on interfacial hydrodynamic transport, we will employ both classical and *ab initio* MD simulations to explore the physical processes occurring when a fluid is confined at the nanoscale. We will also develop and extend classical analytical models to account for novel phenomena, such as liquid-solid slip or nanoscale osmotic flows, that have been assessed in the recent years. The final goal will be to apply all the different understandings to optimize energy conversion and waste heat harvesting, showing that the competition between different characteristic length scales and interface mechanisms can imply novel and promising behaviors such as large flow velocities generated by temperature gradients.

The present manuscript is organized as follows. We will start in Chapter 2 by exploring hydrodynamic interfacial transport, specifically Navier's BC. With that regard, although the position where the BC applies is well defined from a continuum perspective, we will wonder where such BC should be applied from a molecular point of view, where we know that the liquid first absorption layer is located at around one molecular diameter from the solid surface, and we will look for a simple analytical description to determine the position of the boundary. Once the BC location is characterized, we will proceed to measure via classical MD simulations the temperature dependence of bulk (viscosity) and interface (liquid-solid friction) transport coefficients, and study how they compare by computing the temperature evolution of their ratio, the slip length. In order to determine the different system properties that play a role on friction and slip temperature evolution, we will consider two different surfaces, a generic hydrophobic wall and graphene, and two different liquids, methanol and water, studying for the latter fluid the effect of supercooling on transport properties.

In Chapter 3, we will look further into understanding the intriguing liquid-solid friction and slip length temperature evolution for supercooled water, trying to reveal the molecular mechanisms at play. With that regard, we will decompose the friction coefficient differentiating between static and dynamic contributions, and we will assess which one dominates in determining the temperature evolution. Following friction decomposition, we will proceed in the same way for the shear viscosity, in order to determine whether the dynamic or the static viscosity-friction ratios are the ones that determine the large slip lengths values we report at low temperatures, on the order of a few hundreds of nanometers for water on graphene. In this chapter, we will also study with classical MD interfacial thermal transport and, with the final objective of minimizing the interface liquid-solid resistance, we will propose the use of innovative structures consisting in supported graphene on nanopatterned gold, with important applications on delaying the temperature at which the boiling crisis occurs.

Following the interesting temperature evolution results of the previous chapter, in Chapter 4 we will proceed to study the effect of temperature on bulk transport coefficients of water, namely shear viscosity and diffusion coefficient, via *ab initio* MD. We will use density functional theory (DFT), which relies on a functional to describe electronic exchange and correlations. We will try to assess which functional better captures the experimental behavior, which is benchmarked by classical MD simulations. We will also explore the validity of the Stokes-Einstein relation for the different functionals considered. Finally, motivated by determining the connection between structure and dynamics, we will explore the validity of the excess entropy scaling relations, that relate the two body entropy excess (consisting of an integral of a function of the pair radial distribution) and the diffusion coefficient.

Finally, in Chapter 5, we will study thermo-osmotic flows in aqueous electrolytes, and propose an analytical model as an extension of the classical theory, which only accounts for the electrostatic ionic interactions. In contrast, we will suggest a theory that also considers the solvent-solid interactions and the depletion of the ions from the wall. After the model is introduced, we will combine classical MD simulations and analytical formulas to compare the different contributions to the thermo-osmotic response coefficient. We will also study how the competition between surface charge, salt concentration and slip, controls the thermo-osmotic response of the system and how a choice of the most suitable parameters can translate into large thermo-osmotic responses. We will also see that our analytical framework predicts a reversal in the flow direction, observed experimentally, which cannot be understood within the classical theory, and that our proposed description can be

employed to study other physical phenomena such as thermoelectricity or thermophoresis.

Allowing myself to cite the beginning of the well known textbook "States of Matter" by D. L. Goodstein [86]: *"Ludwig Boltzmann, who spent much of his life studying statistical mechanics, died in 1906, by his own hand. Paul Ehrenfest, carrying on the work, died similarly in 1933. Now it is our turn to study statistical mechanics. Perhaps it will be wise to approach the subject cautiously."*

Chapter 2

Determining Hydrodynamical Interfacial Transport via Molecular Dynamics Simulations

> *"If any theoretical significance could be attached to it* [discrepancy between the measured and calculated values of the radius] *other than errors of measurement, it would be* ***that there is slip of the liquid at the walls of the capillary. There is no occasion for admitting this hypothesis****, however, since the discrepancy is no greater than might reasonably be expected from tests in and measurements of such small capillaries as here employed."*
>
> R. Bulkley, *Viscous flow and surface films* 1931

Contents

2.1 Introduction

Fluid transport properties at micro and nanometer scales have awaken a general research interest in the past few decades [29, 87] and they have been extensively studied in literature via experiments and numerical work. For instance, the validity of bulk hydrodynamic equations have been corroborated up to confinements of a few nanometers [88, 89, 90]. It has also been shown that the shear viscosity in bulk remains constant and can be efficiently determined for these systems, promoting the efforts in understanding the molecular mechanisms which control this transport coefficient [91, 92]. In addition, working at this length scales may have some critical consequences so its exploration and understanding are crucial in the development of nanofluidic devices. Such is the case of the fluid atom's self-diffusion coefficient, which strongly deviates from its Stokes-Einstein prediction for very confined systems [93, 94], or for which finite size effects have been observed in determining it from molecular dynamics simulations [95]. As confinement increases, interfacial properties will have an increasingly important role in the fluid flow behavior in the channel. For example, it is well known that for confined fluids the fluid particles tend to order close to the wall, forming layers resulting in inhomogeneities in the fluid's density profile. Understanding the local structure and dynamics of such density variations have been of special interest [96, 97] due to its possible impact in some transport properties such as the local viscosity [98].

For a confined system, the walls impose boundary conditions (BCs) to the flow of liquids. The commonly used no-slip boundary condition, which supposes that the fluid velocity vanishes when in contact to the wall, fails to describe flows in nanofluidic systems [29], and needs to be replaced by a more general partial slip BC [99]. This BC can be expressed in terms of stress, as initially done by Navier [19]. Let's consider a Newtonian fluid confined between two parallel smooth walls normal to z. Far from the walls, the viscous shear stress in the liquid is $\eta\,\dot{\gamma}$, with η being the shear viscosity and $\dot{\gamma} = \partial_z v$ being the shear rate. At the interface, the fluid *slips*, implying a non-vanishing velocity profile. This jump of parallel velocity at the interface is defined as the slip velocity v_{slip}, and it is proportional to the shear stress at the wall τ_{w}, which corresponds to the force exerted from the liquid to the solid per unit area. Such proportion can be expressed as $\tau_{\text{w}} = \lambda v_{\text{slip}}$, defining the (fluid) friction coefficient λ. Supposing homogeneous viscosity in the whole slab, the shear stress at the interface is, as well, $\tau_{\text{w}} = \eta\,\partial_z\, v\big|_{z=z_{\text{s}}}$, where z_{s} is the shear plane position, where the boundary condition applies. Both bulk and interface constitutive equations can be combined as a kinematic relation on the velocity field at the interface, also known as the Navier BC or the partial slip BC:

$$v_{\text{slip}} = b\,\frac{\partial v}{\partial z}\bigg|_{z=z_{\text{s}}}, \tag{2.1}$$

where the slip length b is uniquely related to the friction coefficient λ for a fluid with a given viscosity: $b = \eta/\lambda$. This phenomenon has been observed for simple and complex fluids at the nanoscale [100, 101].

Among all fluids, the study of water has always been of special concern for scientist from a broad variety of research fields [102, 103, 104]. Its interest not only lies on its ubiquitousness and its deep link with the existence of life, but also on its rich phase diagram with, for example, different types of ices [105, 106], or on the wide range of properties derived from the hydrogen bond formation, such as the lower density of the solid phase when compared to the liquid one. Several anomalous thermodynamic properties have been reported for water related, for example, to its isothermal compressibility or the density maximum present at 4°C [57, 61]. These anomalies are enhanced when water is driven to

its supercooled regime (*i.e.* the range of temperatures below the freezing point where water keeps its liquid state), becoming critical to study the temperature and pressure dependence of different transport properties [107, 108] and to develop models which aim to explain its anomalous behavior such as "Speedy's stability limit conjecture" [109] or the two states model [63, 64, 110].

For confined water, several work has been done studying the suitability of different water models to reproduce experimental measurements [111] as well as the impact of wall properties such as wettability [112], roughness [113] and surface topology [114]. Several efforts have been done in order to understand the molecular mechanisms that control friction (and slip) experimentally [115, 116, 117], via classical [118, 119] and *ab initio* [45] molecular dynamics (MD), and analytically [120], with special interest on the discussion of the interfacial transport property relation with the autocorrelation of the force exerted by the liquid on the wall [121]. Further discussion has been carried in the literature on how to measure λ from equilibrium simulations (EMD) [122, 123, 124, 125, 126].

Apart from this interesting debate, several questions remains open with regard to friction coefficient. Although water viscosity's viscoelastic behavior is well known, the connection between both bulk and interfacial transport coefficients in Eq. (2.1) opens the possibility of friction's viscoelastic nature [54]. On the other hand, hydrodynamic transport equations remain mathematically equivalent to the ones corresponding to the thermal transport coefficients, establishing an analogy between the hydrodynamic and the thermal boundary condition [48] and introducing the possibility of a link between both transports via, for instance, wall's wetting properties [127, 128]. On the other hand, the temperature evolution of liquid-solid friction also remains unclear nowadays. Several questions can be explored on this regard, such as if friction temperature evolution will be mostly affected by the surface or the liquid type, if friction will follow the same temperature evolution laws than viscosity or if the differences in temperature evolution will have a dramatic impact on the ratio between η and λ: the slip length.

In this framework and state-of-the-art, MD simulations remain a fundamental tool to explore and bring insights on the hydrodynamic transport characterization at the nanometric scales. The aim of this chapter is to introduce different computational and theoretical tools employed to study and describe the hydrodynamic bulk and interfacial transport. After a brief introduction on MD simulations highlighting the main concepts widely employed throughout this manuscript, together with critical concepts as wetting, hydrodynamic flows and water modelization, the main question this chapter tries to answer arises: how to characterize hydrodynamic transport at the interface? Two different sections adress the question from two critical perspectives: *where* and *how*. The first one relates to the exact location of the interface from a molecular perspective, *i.e.* where to apply the hydrodynamic boundary condition defined by Eq. (2.1). Once the boundary is well determined it remains the second point, referred to how do different parameters, such as the fluid and/or the wall type affect the interfacial transport when compared to the bulk one by varying the temperature, with special interest in the temperature regime corresponding to supercooled water.

2.2 Methods

Regardless of its form, the partial slip BC (Eq. (2.1)) defines two independent parameters: the slip length b (or equivalently the friction coefficient λ) and the hydrodynamic wall position (HWP) [122, 129, 130, 131, 132, 118, 43, 133, 134], and it has been used to explore the molecular mechanisms of liquid-solid slip [135, 136, 137, 138, 40, 139, 140, 141,

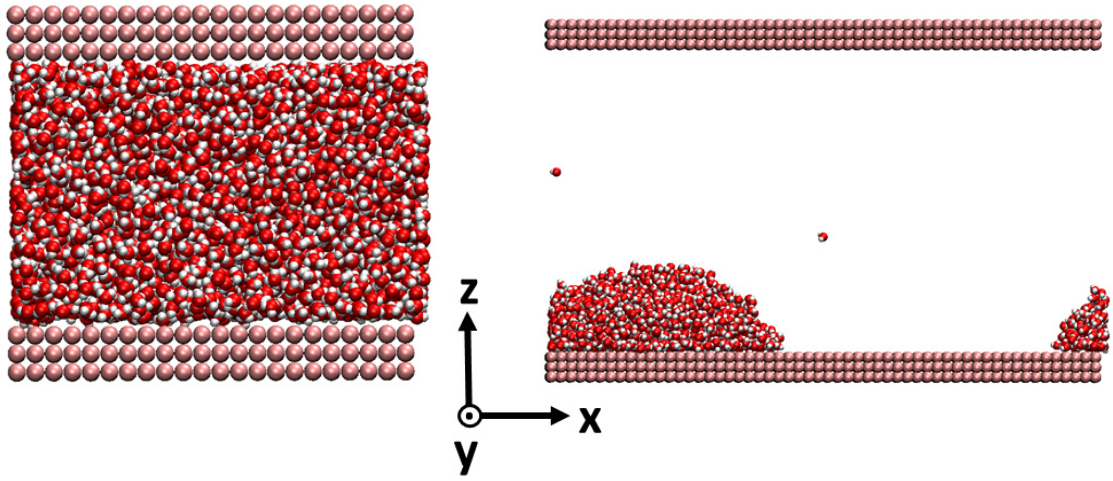

(a) (b)

Figure 2.1: Two characteristic MD simulations examples. Both systems consist in a liquid (water) enclosed between two generic solid walls.(a) System corresponding to a generic transport coefficients measurements configuration, with a bulk region in the middle of the channel and an interfacial region close to the walls. (b) Water droplet simulation, employed to measure the contact angle controlled by the liquid-solid interaction.

45, 142, 143]. A liquid confined between parallel flat walls, with periodic BCs in the lateral directions, is commonly used (two typical system snapshots of MD simulations with this configuration can be found in Fig. 2.1). The liquid-solid interactions at the interface will control the wetting properties of the system, which can be related to the contact angle of a liquid droplet on the solid surface. Once such properties have been determined, we can study how they affect the interfacial transport properties, which can be determined by measuring the system's response to a given perturbation: the generation of a hydrodynamic flow.

2.2.1 Molecular dynamics simulations

Molecular dynamics (MD) simulation is a computational technique that allows us to describe the microscopic scale of a classical many-body problem, by generating a statistical ensemble of configurations for a system of N particles. Classical MD simulations consider the nuclear motion of particles a classical object, *i.e.* it obeys the classical mechanics laws. Quantum effects should be critically accounted only when considering light atoms or molecules (He, H_2), for processes that can be difficult to describe with empirical force-fields (such as electronic polarization effects or chemical reactivity), or when the frequency of the vibrational motion of the atom is greater than the thermal fluctuations, $h\nu > k_{\mathrm{B}}T$. In these cases one can perform the so-called *ab initio* MD; further discussion and details can be found in Chapter 4.

During my thesis, in order to measure physical quantities and to test theoretical predictions, we performed MD simulations of a liquid confined between two parallel walls (Fig. 2.1a) using the LAMMPS package [144]. The aim of this section is to briefly introduce the basic concepts of classical MD, highlighting the ones employed to measure the different transport coefficients. On the whole, the coming discussion on this broad subject is necessarily incomplete, and further detail can be found in [145, 146].

When thinking of MD simulations in an applied context, we can understand them as

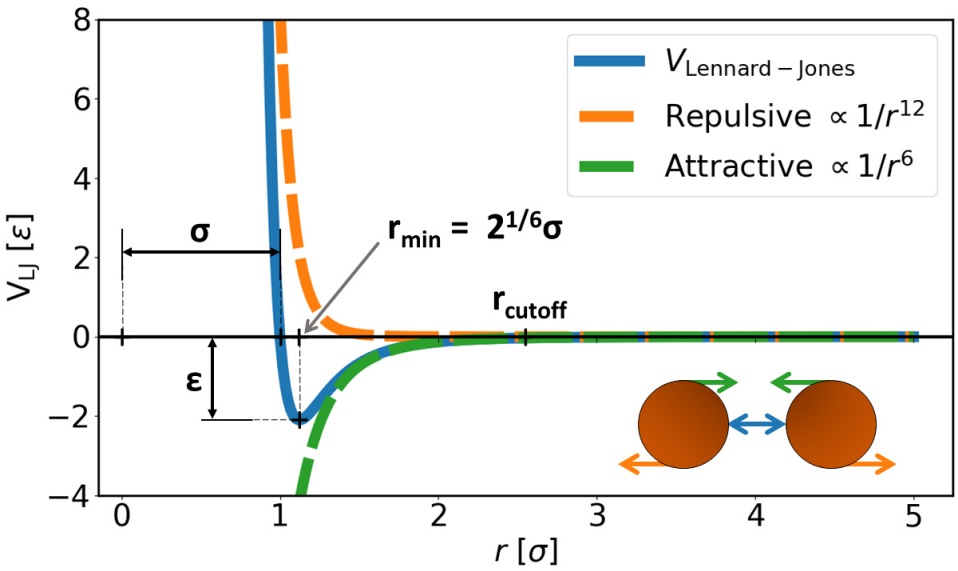

Figure 2.2: Lennard-Jones interaction potential as a function of the interparticle distance r. In discontinuous lines, the repulsive and attractive contributions to V_{LJ}. σ corresponds to the characteristic molecular diameter and ε to its interaction energy. The minimum of the potential is located at r_{min} and the potential will be truncated at r_{cutoff}; typically $r_{\text{cutoff}} \sim 2.5\,\sigma$.

a computational experiment, *i.e.* as a two step process where first we prepare the sample (set the initial conditions, select a model system for N particles, and solve Newton's equations until reaching the steady state), and second we measure the quantity of interest (a physical observable which has to be expressed as a function of the N particles positions and momenta). Starting from this idea, we can describe the different steps to go through when performing a MD simulation.

a. Initial Conditions

The first step in classical MD is to initialize the problem. In the case of a solid, the particles positions should be chosen in agreement with the structure we are willing to simulate. For a slit channel, periodic boundary conditions are typically imposed in the directions parallel to the walls. When working with fluids, a common choice of the initial conditions is to place the atoms evenly spread along the simulation box (in order to avoid overlapping problems) and to assign the atom's velocities according to the Maxwell-Boltzmann distribution. The equipartition theorem allows us to relate, in thermal equilibrium, the kinetic energy per degree of freedom with the temperature T. Because the kinetic energy fluctuates, it is common to use the concept of instantaneous temperature at a time t:

$$T(t) = \frac{1}{k_{\text{B}} N_{\text{f}}} \sum_{i=1}^{N} m_i v_i^2(t), \tag{2.2}$$

where v_i is the velocity of a given particle, m_i is its mass, k_{B} is the Boltzmann constant and N_{f} the degrees of freedom in the kinetic energy. The initial setting of the temperature is not particularly critical as it will change during equilibration, and it can also be controlled by imposing our desired temperature T_0, by for example scaling the particles velocities a factor $(T_0/T(t))^{1/2}$. Therefore, we can obtain the system kinetic energy from the atomic

velocities, whereas the system potential energy can be obtained from the atomic positions. It is at this point when we have to choose what type of interaction potential will better characterize the particle's interactions. The most popular model to describe the generic Van der Waals non-bonded interactions between atoms is the Lennard-Jones (LJ) model. The interaction LJ potential is a pair potential, which neglects the N-body interactions with $N > 0$. The interactions between a pair of particles $\{i, j\}$ are modelled following the expression:

$$V_{ij}(r) = 4\,\varepsilon_{ij}\left[\left(\frac{\sigma_{ij}}{r}\right)^{12} - \left(\frac{\sigma_{ij}}{r}\right)^{6}\right], \tag{2.3}$$

with $r = \|\mathbf{r}_i - \mathbf{r}_j\|$ being the interparticle distance, ε_{ij} and σ_{ij} being the interaction energy and size. In this expression, the term $1/r^6$ is related to the Van der Waals attraction while the term $1/r^{12}$ is related to the repulsion between electron clouds (Fig. 2.2). The LJ potential also introduces a system of reduced units related to the characteristic scale of the system: ε for energy, σ for length, and m for mass. All the other physical quantities can be expressed in terms of these reduced units, such as the reduced time $t^* = t/\tau$ with $\tau = \sigma\sqrt{m/\varepsilon}$, or the reduced temperature $T^* = k_{\mathrm{B}}T/\varepsilon$.

Typically the LJ potentials are parametrized to only provide the interaction energy and size corresponding to a self-interaction (ε_{ii} and σ_{ii}); and the interaction parameters between two different non-bonded atoms are given by a set of equations known as mixing rules. The most common ones are the Lorentz-Berthelot rules, proposed by H. A. Lorentz for the interparticle equilibrium distance and by D. Berthelot for the interaction energy [147]:

$$\sigma_{ij} = \frac{\sigma_{ii} + \sigma_{jj}}{2}\,; \qquad \varepsilon_{ij} = \sqrt{\varepsilon_{ii}\varepsilon_{jj}}. \tag{2.4}$$

The Lorentz-Berthelot rules, also called arithmetic mixing rules, are a frequent choice for the cross-interactions between atoms of type i and j. Nevertheless, different mixing rules can be applied to our system, such as the geometric mixing rules:

$$\sigma_{ij} = \sqrt{\sigma_{ii}\sigma_{jj}}\,; \qquad \varepsilon_{ij} = \sqrt{\varepsilon_{ii}\varepsilon_{jj}}. \tag{2.5}$$

In addition to the atomic interactions, the ionic interactions are typically modeled via a Coulomb potential:

$$V_{ij}(r) = \frac{q_i q_j}{4\pi\varepsilon_0 r}, \tag{2.6}$$

where $q_{\{i,j\}}$ is the charge of the ions, and ε_0 the vacuum dielectric permittivity. The values given to ε_{ij}, σ_{ij} (or analogously the mixing rules choice) and $q_{\{i,j\}}$ will vary depending on the particle kind we want to simulate, and our choice should consider the characteristics of the system we want to study and its force-field modelization.

A typical force field simulates the intermolecular interactions through the described electrostatic (Coulomb, Eq. (2.6)) and van der Waals (LJ, Eq. (2.3)) terms, but intramolecular interactions can also be introduced by adding different terms in the total potential related to the bond stretching (typically modelled with a harmonic potential for *e.g.* water, or by a Morse potential [148]), the bond angle interactions (related to the angle deviation between two bonds, it is often modelled with a simple angle harmonic potential) or the bond rotational or torsional interactions (often neglected for inorganic materials). The introduction of these intramolecular interactions are not needed for the simplest types of fluids (as LJ fluids), although they can be critical to reproduce the behavior of some fundamental molecules as water.

b. Force Calculation

Once the particles interactions have been stated through the interaction potential, the total force on a particle i at a time t, $\mathbf{f}_i$, is calculated as the vector sum of the pair-forces $\mathbf{f}_{ij}(t)$ on i due to every particle j on within its range of interaction, $\mathbf{f}_i(t) = \sum_j \mathbf{f}_{ij}(t)$. Such pair-forces can be derived from the pair potential energy (interactions between particles and external potential), so:

$$\mathbf{f}_{ij}(t) = -\nabla V_{ij}(r). \tag{2.7}$$

Because we are working under classical mechanics framework, the force acting on a given particle i of mass m_i will also obey Newton's second law of motion:

$$\mathbf{f}_i(t) = m_i \frac{\mathrm{d}^2 \mathbf{r}_i(t)}{\mathrm{d}t^2}. \tag{2.8}$$

Force calculation is typically the most time consuming part of the computation. This is because, by only considering pair interactions, for a system of N particles we must evaluate $N(N-1)/2$ pair distances, and therefore the computation time needed for the force evaluation will scale as N^2. Furthermore, it is common to introduce periodic boundary conditions, which make the system effectively infinite and the explicit computation of all pair forces impossible. Nowadays it exists a set of efficient techniques that speed up the computation of the long and short range forces such as the computing time scales as N. One example is the introduction of a cutoff radius in the Lennard-Jones interactions. In Fig. 2.2 we can see that the Lennard-Jones potential V_{LJ} tends to zero for high values of the interatomic distance. Thus, we can suppose neglectful all the V_{LJ} interactions for pair distances greater than a certain cutoff radius r_{cutoff}, imposing $V_{\mathrm{LJ}}(r > r_{\mathrm{cutoff}}) = 0$. The choice of r_{cutoff} value can be a delicate issue: if we choose a very small value the force calculation will be faster but we may be neglecting some critical interparticle interactions, while very high r_{cutoff} may imply the computation of force interactions almost negligible and very long computation times. Generally, a common choice of r_{cutoff} is $\sim 2.5\,\sigma$, although when testing the system parameters it is advisable to check that equivalent results are obtained for different r_{cutoff} choices.

Nevertheless, truncating the potential by introducing r_{cutoff} can be a delicate issue. Depending on the system configuration and the nature of the interparticle interactions, the contributions from distant interactions cannot be neglected in some cases. Such contributions are denominated long-range forces; defined as the ones that do not vanish faster than r^{-d}, with d the number of dimensions. Typical examples of long-range interactions are the charge-charge ions interactions, which decay as r^{-1}, or the dipole-dipole molecular interactions, which decay as r^{-3}. Indeed, because of the very slow decay of the first example, *i.e.* the very long-range nature of the Coulombic interactions, the Coulombic interactions require explicit summing over the periodic images of the box. However it would be too costly to perform direct sum, and more efficient methods should be employed. A possible solution are the so-called lattice methods [146], consisting in including more than the nearest or minimum image of a charge in calculating its energy. Some of the most extended methods to compute the Coulombic long-range interactions are the Ewald sum method [149], which computes the interaction of the ion with all its periodic images (see Appendix A for further detail), and its optimizations, such as the particle-particle/particle mesh (PPPM) method [150, 151].

c. Equations of Motion

After we have computed the forces acting on all the particles, the next step is to integrate Newton's equations of motion. Several algorithms have been implemented and can be

found in the literature, but here we would like to introduce one of the most common ones, the Verlet algorithm [152], which combines simplicity and good performance. The general idea is to use finite difference methods, which consist in breaking down the integration into many small steps, each separated in time by a fixed timestep δt during which the force is assumed to be constant, so δt has to be small enough. We start from the Taylor expansion of the coordinate of a particle, obtained taking into account Eq. (2.8):

$$r_i(t+\delta t) = r_i(t) + v_i(t)\delta t + \frac{f_i(t)}{m}\frac{\delta t^2}{2} + \frac{\mathrm{d}^3 r_i}{\mathrm{d}t^3}\frac{\delta t^3}{3!} + \mathcal{O}(\delta t^4). \tag{2.9}$$

Analogously,

$$r_i(t-\delta t) = r_i(t) - v_i(t)\delta t + \frac{f_i(t)}{m}\frac{\delta t^2}{2} - \frac{\mathrm{d}^3 r_i}{\mathrm{d}t^3}\frac{\delta t^3}{3!} + \mathcal{O}(\delta t^4). \tag{2.10}$$

Combining the Taylor expansions of Eq. (2.9) and Eq. (2.10), we finally obtain:

$$r_i(t+\delta t) \approx 2r_i(t) - r_i(t-\delta t) + \frac{f_i(t)}{m}\delta t^2. \tag{2.11}$$

After all the particles positions have been updated, the force on every particle is again evaluated to determine the subsequent particle positions and velocities at $t + 2\delta t$, and so on. Because the velocities are not necessary for generating the particles trajectories, they do not explicitly appear in the Verlet algorithm. To obtain the new velocities, we can calculate the position difference at two different times:

$$v_i(t) = \frac{r_i(t+\delta t) - r_i(t-\delta t)}{2\delta t} + \mathcal{O}(\delta t^2). \tag{2.12}$$

Explicit velocities are implemented in the velocity Verlet algorithm (used in LAMMPS [144]), by also computing velocity at the same timestep than position with a Taylor expansion:

$$v_i(t+\delta t) = v_i(t) + \frac{f_i(t) + f_i(t+\delta t)}{2m}\delta t + \mathcal{O}(\delta t^2). \tag{2.13}$$

d. Statistical Ensemble

Once we have solved the equations of motion, and depending on our simulation characteristics, we will be interested in controlling different physical quantities, such as pressure P, temperature T, number of particles N, volume V, energy E, etc. Depending on the parameters we want to control we will work under a given statistical ensemble. The most common ensembles in MD simulations are the (N, V, E) microcanonical ensemble, (N, V, T) canonical ensemble and (N, P, T) isothermal-isobaric ensemble. Because we are solving Newton's second law Eq. (2.8) for an isolated system, the exchange of energy or particles with the outside is not allowed. As a consequence, without external controls, MD should generate a microcanonical ensemble. However, numerical errors can produce fluctuations on the forces and the energy, and possible drifts.

As it is common in experiments, we can be interested in controlling temperature and pressure in MD simulations. To do so, one of the standard approaches is to reformulate the Lagrangian equations of motion of the system [153]. Let's focus first on how to control the temperature.

Controlling the temperature In MD simulations, the final objective in controlling the temperature is to develop an algorithm that mimics a real thermostat in terms of statistical physics, *i.e.* an algorithm that adds or takes away energy to keep the target temperature T_0 constant. The simplest possible way to control the temperature is through the velocity rescaling algorithm [154, 155], which adjusts the velocities of the atoms with a suitable factor $\lambda(t)$ in order to set the instantaneous temperature of the system exactly equal to T_0 at every timestep:

$$T_0 = \frac{1}{k_{\mathrm{B}} N_{\mathrm{f}}} \sum_{i=1}^{N} m_i \left(\lambda(t)\, v_i(t)\right)^2 = \lambda(t)^2\, T(t), \tag{2.14}$$

so

$$T_0 - T(t) = \left(\lambda(t)^2 - 1\right) T(t); \tag{2.15}$$

which allows us to determine $\lambda(t) = \sqrt{T_0/T(t)}$. Although simple, velocity rescaling algorithm is not the best method for controlling the temperature, since it is unknown how rescaling affects the properties of the system. For instance, it suppresses any possible natural temperature fluctuations in the system, an it may cause significant perturbations of the atom trajectories and of the overall system dynamics. Nevertheless, although it is not the best method, it can be useful to employ it in starting runs when, due to our system configuration, we would be interested in transferring big amounts of heat at each timestep. After this starting run, other thermostat should be employed to ensure the good dynamics of the system.

A variation of the velocity rescaling algorithm is the Berendsen thermostat [156], which couples the system to an external heat bath that is fixed at the desired temperature T_0. As a consequence, the system temperature will be maintained as its energy continuously fluctuates due to the interaction of the system with the heat bath. The main idea of the algorithm is therefore to rescale the velocities in order to achieve a mean kinetic energy consistent with the target temperature T_0, such that:

$$\frac{\mathrm{d}T}{\mathrm{d}t} = \frac{1}{\tau} \left(T_0 - T(t)\right); \tag{2.16}$$

thus, from the temperature change between two successive timesteps, we obtain:

$$\lambda(t) = \sqrt{1 + \frac{\delta t}{\tau} \left(\frac{T_0}{T(t)} - 1\right)}, \tag{2.17}$$

with τ being the relaxation time, which determines how tightly the bath and the system are coupled. The algorithm will be equivalent to velocity rescaling when $\tau = \delta t$. When $\tau \to \infty$ the Berendsen algorithm will be inactive and the system run will be in the microcanonical ensemble. The advantage of Berendsen thermostat when compared to velocity rescaling is that, in Berendsen algorithm, the temperature of the systyem will exponentially relax towards T_0, and thermal fluctuations are allowed. Although broadly used and generally accepted due to its good description of some dynamical quantities in large systems, the Berendsen thermostat should be employed with care because it does not reproduce the velocity distribution of the canonical ensemble. Analogously to the velocity rescaling algorithm, it can be used in a starting run to relax the system.

If we want to mimic a canonical ensemble, one of the best thermostats nowadays for (N, V, T) simulations is the Nosé-Hoover thermostat [157]. As for the Berendsen thermostat, the scheme is based in embedding our system in a thermal bath at the desired

temperature T_0. The main idea of the algorithm, introduced by Nosé [158], is to consider the reservoir as an integral part of the system. We can do so by introducing an artificial coordinate. Denoting $\{\mathbf{r}_i, \mathbf{p}_i\}$ the particles positions and momenta of our original system inside the thermal bath, we will introduce the extra pair of conjugate variables $\{s, p_s\}$ related to the reservoir with an associated mass $Q > 0$. This new variable s introduces a rescaled time (also called virtual time) $\mathrm{d}t$, which relates to the real time $\mathrm{d}t'$ by the expression:

$$\mathrm{d}t = s\,\mathrm{d}t'. \tag{2.18}$$

Denoting $\dot{\square}$ as time derivative, the new Lagrangian will be obtained by introducing the additional coordinate in the Lagrangian of a classical N-body system:

$$\mathcal{L}_{\text{Nosé}} = \sum_{i=1}^{N} \frac{m_i}{2} s^2 \dot{\mathbf{r}}_i^2 - U\left(\mathbf{r}^N\right) + \frac{Q}{2}\dot{s}^2 - g k_{\mathrm{B}} T_0 \ln(s), \tag{2.19}$$

where the first two terms correspond to the kinetic and potential energy of the real system, and the last two terms correspond to the kinetic and potential energy of the reservoir. It can be shown [145, 159] that, for a system with N_{f} degrees of freedom, Eq. (2.19) will produce canonical ensemble for $g = N_{\mathrm{f}} + 1$ in virtual time sampling (corresponding to the Nosé formalism) and for $g = N_{\mathrm{f}}$ in real time sampling (corresponding to the Nosé-Hoover formalism, discussed in the following). From the total Hamiltonian derived from Eq. (2.19) we can derive the so-called Nosé equations of motion:

$$\begin{aligned} \dot{\mathbf{r}}_i &= \frac{\mathbf{p}_i}{m_i s^2}, & \dot{\mathbf{p}}_i &= \mathbf{f}_i; \\ \dot{s}_i &= \frac{p_s}{Q}, & \dot{p}_s &= \sum_{i=1}^{N} \frac{\mathbf{p}_i^2}{m_i s^3} - \frac{g k_{\mathrm{B}} T_0}{s}. \end{aligned} \tag{2.20}$$

From a practical point of view, the main problem of the Nosé Eqs. (2.20) is that they are expressed in terms of the virtual time, which is related to the real time by uneven time intervals depending on the value of s, Eq. (2.18). With that regard, Nosé and Hoover reformulated the equations of motion in terms of real system variables [160, 159]. Defining $\zeta = \dot{s}'/s'$, the Lagrangian equations of motion Eqs. (2.20) can be rewritten as:

$$\begin{aligned} \dot{\mathbf{r}}_i' &= \frac{\mathbf{p}_i'}{m_i}, & \dot{\mathbf{p}}_i' &= \mathbf{f}_i' - \zeta \mathbf{p}_i'; \\ & & \dot{\zeta} &= \sum_{i=1}^{N} \frac{\mathbf{p}_i'^2}{Q m_i} - \frac{g k_{\mathrm{B}} T_0}{Q}. \end{aligned} \tag{2.21}$$

We can understand the introduced variable $\zeta \propto p_s'$ as a thermodynamic friction coefficient, whose time derivative can be re-expressed as:

$$\dot{\zeta} = -\frac{1}{\tau^2}\left(\frac{g}{N_{\mathrm{f}}}\frac{T_0}{T(t)} - 1\right); \tag{2.22}$$

where

$$\tau^2 = \frac{Q}{N_{\mathrm{f}} k_{\mathrm{B}} T_0}, \tag{2.23}$$

is the effective relaxation or damping time. We can observe from Eq. (2.22) that the friction coefficient ζ will control the kinetic energy associated to T to make its time average equal to T_0. The coupling strength τ will control the energy flow between the reservoir and the

real system, thence influencing the temperature fluctuations. When $\tau \to \infty$, *i.e.* $Q \to \infty$, the real system and the reservoir will be perfectly coupled and the system will be in the microcanonical ensemble. We will always work in the canonical ensemble as far as we choose a finite value of the mass Q. Nevertheless, when $\tau \gg 1$ the energy flow will be slow, and too large simulation times will be needed in order to reach the canonical distribution. On the contrary, if τ is small, the energy will oscillate unphysically, causing equilibration problems. A good test to ensure the proper choice of the damping time τ can be to run the same simulation for different coupling strengths; if we obtain equivalent results it means that our τ choice is good and that the system has reached the desired canonical ensemble.

Controlling the pressure When we are working in the canonical (N, V, T) ensemble, we can obtain our system pressure P from Clausius virial theorem. The virial W is defined as the expected value of the sum of the products of the particles coordinates and the forces acting on them:

$$W = -\frac{1}{d}\sum_{i=1}^{N} \mathbf{r}_i \cdot \mathbf{f}_i, \tag{2.24}$$

where d is the dimensionality of the system. For an ideal gas, only the interaction forces that appear are due to the interactions between the gas and the container, and the virial theorem states for this case that the average virial $\langle W \rangle$ equals to $Nk_{\mathrm{B}}T$. Nevertheless, for a real fluid, the pairwise interaction forces between particles will also affect the virial, and thus the pressure. The total virial of the system will thence present a contribution from the ideal gas and another one from the interaction forces:

$$\langle W \rangle = PV - \frac{1}{d}\left\langle \sum_{i<j} \mathbf{r}_{ij} \cdot \mathbf{f}_{ij} \right\rangle = Nk_{\mathrm{B}}T. \tag{2.25}$$

Therefore, the pressure of a classical N-body system is determined as:

$$P = nk_{\mathrm{B}}T + \frac{1}{dV}\left\langle \sum_{i<j} \mathbf{r}_{ij} \cdot \mathbf{f}_{ij} \right\rangle, \tag{2.26}$$

where $n = N/V$ is the number density of the system. This result is derived at constant (N, V, T); still, it is rather common in a laboratory experience to perform the experiment at constant pressure. To do so, we have to employ an algorithm that mimics a real barostat in the sense of statistical physics. Several algorithms have been developed with that regard, such as the Andersen barostat [161] (which controls the pressure by using a fictional piston) or the Parrinello-Rahman barostat [162] (which allows a variable simulation cell shape, typically employed for solid simulations to observe, for example, the solid to solid transition). All these algorithms consider the volume V a dynamical quantity, *i.e.* they work in the (N, P, T) ensemble. However, we may wonder how should we proceed if we want to control the pressure for a constant energy simulation or if we want to apply the barostat to a confined liquid. There are different approaches to solve this issue, but one of the simplest is what we will call the piston equilibration method.

Let's consider a fluid enclosed between two parallel walls constituted by a given crystalline structure. The main idea of the method consists in applying a normal force F_{piston} on one of the walls proportional to the target pressure P_0, $F_{\mathrm{piston}} = P_0\, S$ with S being the wall area. Therefore, the pressure will be set by using one of the walls as a piston during a preliminary run. If this preliminary run is long enough, the piston wall will oscillate around the equilibrium position. We can then measure the average position and fix the

piston wall at it. The system will thus be equilibrated at the target pressure, and thence we can measure the observables of interest for our problem during a posterior production run in the desired constant volume ensemble.

e. Calculate the physical quantities

After going through the different steps to *set our sample* and discussing some of the subtleties related to the different choices, once we are confident about our system conditions (*i.e.* about our MD program), our goal is to *measure* interesting properties of the system. Such properties will be physical observables, which have to be expressed as an average of some function of the coordinates and momenta of the particles in the system. The measure process in physics, specially for dynamical quantities, is based on the ergodic hypothesis: when all the accessible microstates are equiprobable over long enough periods of time, and hence the ensemble average is equivalent to the temporal average. Therefore, any physical quantity of interest should be measured taking into account whether or not the system reached the equilibrium or the steady state. Some examples of observable properties of interest can be thermodynamical quantities, such as temperature T (Eq. (2.2)) or pressure P (Eq. (2.26)); structural quantities, such as the radial pair distribution function $g(r)$; or dynamical quantities, such as the particles mean squared displacement.

We will define equilibrium MD (EMD) simulations when the modelled system satisfies the equilibrium conditions. The coupling of our system to an external one (such a piston or a reservoir), do not necessarily induce thermodynamic fluxes, and the equilibrium conditions can be maintained. Nevertheless, sometimes we might be interested in applying a large perturbation to the system to study its response. Then, the system modelled will not satisfy the equilibrium conditions and we will sample a non-equilibrium ensemble, defining non-equilibrium MD (NEMD) simulations. The dynamical tools that have been introduced to solve EMD (like velocity rescaling or Nosé-Hoover thermostating) lead to the same form of the non-equilibrium equations of motion with an extra term related to the perturbation induced in the system. But, what can be the advantages of NEMD methods? EMD methods are based on linear response theory and time correlations, typically rather noisy. NEMD simulations allow us a higher degree of control of the system, which can improve the efficiency in the transport coefficients calculation. Also, in our picture of MD simulations as computational experiments, NEMD simulations are closer to laboratory experiences, where transport properties such as viscosity η or thermal conductivity λ_{th} are measured inducing a flow (of momentum, energy, etc) in the system. With that regard, NEMD may feel a more natural way to measure transport coefficients, which relate to the way the system responds to a large perturbation.

NEMD also present some important disadvantages when compared to EMD, and their suitability to measure physical observables is still an ongoing debate [163, 164, 165]. For instance, NEMD simulations typically need longer simulation times than their EMD counterpart. This is because the strength of the applied perturbation in NEMD has to be large enough to be able to distinguish it from the statistical noise of the system, implying longer simulation times than those of EMD to reach the steady state. Nevertheless, if we apply a very large perturbation, the system will be out of the linear response regime, and the transport coefficients will no longer be physical constants. Furthermore, whilst for EMD we can work within the microcanonical ensemble, for NEMD it is unavoidable the use of a thermostat. Due to the applied perturbation to the system, such thermostat will be pumping great quantities of heat in order to ensure the imposed temperature T_0, increasing the risk of a nonphysical system behavior. Still, used with care, NEMD simulations can be a powerful tool to calculate some physical quantities, and good agreement can be found when

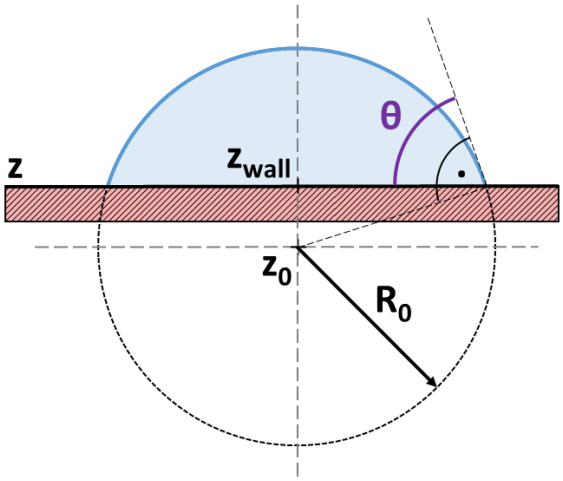

Figure 2.3: Schematics of contact angle θ simulation for a wall located at z_{wall}, where the sessile water drop (in blue) shape is approximated by a sphere centered at z_0 and having a radius R.

computing some transport coefficients, such as viscosity, from EMD and NEMD methods.

2.2.2 Wetting and contact angle

The ability of a liquid to maintain contact with a solid surface is defined as wetting. The wetting properties are directly related to the interaction energy ε_{LS} between liquid (L) and solid (S) atoms, and they can be expressed in terms of the contact angle θ of a liquid droplet on a solid surface. For a given liquid, wetting allows us to characterize the solid surface (see Fig. 2.3). For example, in the case of water, we can distinguish between hydrophobic (small wetting or large contact angle) and hydrophilic (large wetting or small contact angle) surfaces. Wetting properties directly affect the disposition of the liquid particles in the absorption layers: for a very wetting surface, a larger number of liquid particles will be present at the interface, implying a more picked interfacial density profile, while the opposite effect occurs for a non-wetting surface. Therefore, the effect of wetting can have a critical impact on the interfacial transport properties, and its good characterization can allow us to enlighten the molecular mechanisms that control them.

To characterize the wetting in MD simulations, we can measure the contact angle corresponding to a given value of the liquid-solid interaction energy ε_{LS}. With this regard, we should simulate a liquid droplet on a solid surface big enough to avoid interactions of the liquid particles with the periodic images, as we can see in Fig. 2.1b. Supposing that the immobile droplet shape can be fitted by a sphere centered at z_0 and radius R (Fig. 2.3), the radius of the droplet section can be expressed as a function of the section's distance to the wall z as $r(z) = \sqrt{R^2 - (z - z_0)^2}$, and the contact angle θ is determined from the expression:

$$\theta = \arccos\left(\frac{z_{\text{s}} - z_0}{R}\right), \tag{2.27}$$

where z_{s} denotes the effective wall position. We can obtain the value of $r(z)$ from the simulations by fitting the apparent density profile ρ_{app} along the direction z normal to the wall with a spherical shape:

$$\rho_{\text{app}}(z) = \frac{(\rho_{\text{liq}} - \rho_{\text{vap}})\ \pi\, r(z)^2}{L_x L_y} + \rho_{\text{vap}}, \tag{2.28}$$

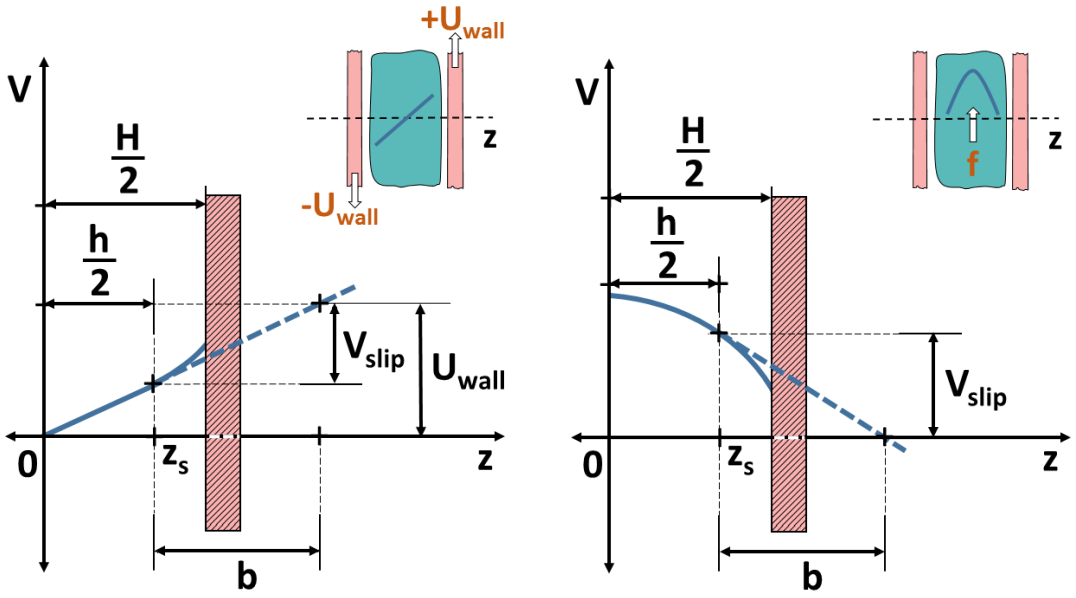

(a) Couette flow (b) Poiseuille flow

Figure 2.4: (a) Velocity profile schematics of a Couette flow generated by applying a shear velocity $\pm U_{\text{wall}}$ to the walls. (b) Velocity profile schematics of a Poiseuille flow generated by applying a constant force density f to the fluid. In both figures, the dashed line represents the ideal velocity profile, obtained from fitting $v(z)$ in the bulk region, while the continuous line represents the real velocity profile, which may deviate from the ideal one at interface due to the density inhomogeneties close to the wall. v_{slip} corresponds to the velocity jump at the interface, and b is the slip length. The position where the boundary condition is applied is at z_{s}.

where $\rho_{\text{liq, vap}}$ corresponds to the real liquid and vapor densities and L_x, L_y denote the wall lateral dimensions. Because the densities are obtained for a given temperature and pressure, both parameters can affect the contact angle values obtained.

2.2.3 Hydrodynamic flows

In the study of the dynamical properties of a confined fluid, we can measure the hydrodynamic transport coefficients from equilibrium (EMD) or non-equilibrium (NEMD) molecular dynamics simulations. The employment of equilibrium formulas with this regard, based on time autocorrelations, is a delicate issue, which will be discussed in detail in Chapter 3. Another path is the employment of NEMD simulations by generating a hydrodynamic flow. Considering a Newtonian, incompressible fluid of density ρ and shear viscosity η, its flow is described by the Navier-Stokes equations [18]:

$$\begin{cases} \rho \frac{\partial \mathbf{v}}{\partial t} + \rho \left(\mathbf{v} \cdot \boldsymbol{\nabla} \right) \mathbf{v} &= -\boldsymbol{\nabla} P + \eta \nabla^2 \mathbf{v} + \mathbf{f}_{\text{ext}}, \\ \boldsymbol{\nabla} \cdot \mathbf{v} &= 0; \end{cases} \tag{2.29}$$

where $\mathbf{v}(t, \mathbf{r})$ is the fluid velocity, P the system's pressure and $\mathbf{f}_{\text{ext}}$ corresponds to an applied external force per unit volume. We can define the Reynolds number Re, in order to compare the spacial derivatives of the velocity in Eq. (2.29). By defining L the typical length scale over which the flow varies, and U the typical velocity, the Reynolds number

is defined as:

$$\frac{(\mathbf{v}\cdot\boldsymbol{\nabla})\mathbf{v}}{\eta\nabla^2\mathbf{v}} \sim \frac{\rho UL}{\eta} = \frac{UL}{\nu} \equiv \mathrm{Re}, \tag{2.30}$$

with $\nu = \eta/\rho$ being the kinematic viscosity. Micro and nanofluidic systems will have $\mathrm{Re} \ll 1$. By also considering steady-state flows where $\frac{\partial \mathbf{v}}{\partial t} = 0$, Eq. (2.29) is simplified to the Stokes equation:

$$\eta\nabla^2\mathbf{v} - \boldsymbol{\nabla}P + \mathbf{f}_{\mathrm{ext}} = \mathbf{0}, \tag{2.31}$$

with the condition of incompressibility:

$$\boldsymbol{\nabla}\cdot\mathbf{v} = 0. \tag{2.32}$$

By considering an ideal Newtonian fluid enclosed between two infinitely long parallel plates separated a distance H, the main steady flows induced are a Couette and a Poiseuille flow.

a. Couette flow

We can produce a Couette flow by applying a constant shear velocity U_{wall} to the walls in opposite x directions for each wall (Fig. 2.4a). By doing so, we will generate a linear velocity profile far from the wall:

$$v_x(z) = \dot{\gamma}(z - z_{\mathrm{s}}) + (U_{\mathrm{wall}} - v_{\mathrm{slip}}), \tag{2.33}$$

where z_{s} is the shear wall position (*i.e.* the effective position where the Navier B.C. applies, Eq. (2.1)), and v_{slip} is the slip velocity, related to the velocity jump at the interface, and defined as $v_{\mathrm{slip}} = U_{\mathrm{wall}} - v_x(z = z_{\mathrm{s}})$. We can see that the related interfacial jump, quantified by the slip length b, can be then determined from the relation $b = v_{\mathrm{slip}}/\dot{\gamma}$.

When working with a NEMD simulation of a Couette flow, we can check if our viscosity and friction measures are in the linear response regime (LRR) by measuring them for different values of the wall velocity U_{wall}, expecting to have equivalent results for different shear velocities. Although it is recommended to always verify that our measures are in the LRR, a good way to estimate an order of magnitude for a shear velocity which will lie in the LRR is to impose U_{wall} to be $\sim 10\%$ smaller than the thermal velocity. From the equipartition theorem we can approximate the thermal velocity as

$$\langle v_x \rangle \sim \sqrt{\frac{k_{\mathrm{B}}T}{m}}. \tag{2.34}$$

For example, for water at 360 K, $\langle v_x \rangle \sim 4 \times 10^{-3}$ Å/fs, and therefore $U_{\mathrm{wall}} \sim 1 \times 10^{-4}$ Å/fs.

Another estimation we should do before running our Couette simulation is to estimate the time it will take to the system to reach the steady state, $t_{\mathrm{st-st}}$. The dynamics of our system will be determined by the dynamic Stoke's equation:

$$\rho\frac{\partial v_x}{\partial t} - \eta\nabla^2 v_x = 0, \tag{2.35}$$

obtained from Eq. (2.29). We can see that this expression corresponds to a diffusive equation with diffusion coefficient $D \propto \eta/\rho = \nu$. Therefore, the kinematic viscosity ν will be related to the characteristic system length L and time t, as $\nu = L^2/t$. From the system relaxation, then $t_{\mathrm{st-st}}$ can be expected to be $t_{\mathrm{st-st}} = (H/2)^2/\nu$, with H the system physical height. For example, considering a system of $H \sim 50$ Å constituted by water molecules at 360 K, $t_{\mathrm{st-st}} \sim 2 \times 10^5$ fs.

b. Poiseuille flow

In contrast to a Couette flow, in a Poiseuille flow both walls are at rest and the flow is generated by applying a constant force density f (typically a pressure gradient, $f = (-\boldsymbol{\nabla} P)$) in the direction x parallel to the wall. In this case, the Stokes Eq. (2.31) simplifies to

$$-\eta \frac{\mathrm{d}^2 v_x}{\mathrm{d}z^2} = f, \tag{2.36}$$

where z is the direction normal to the walls. Considering our system centered at $z = 0$ (Fig. 2.4b), without loss of generality, we can define the hydrodynamic wall distance h as the separation between the two positions where the BC applies, $\{\pm z_\mathrm{s}\}$. Then, in the middle of the channel, the symmetry of the system implies that $\frac{\mathrm{d}v_x}{\mathrm{d}z}\big|_{z=0} = 0$ and, at the bottom wall the partial slip BC, Eq. (2.1) writes as $v(-h/2) = b\, \frac{\mathrm{d}v_x}{\mathrm{d}z}\big|_{z=-h/2}$. We can solve Eq. (2.31) by taking both BC conditions into account, obtaining that the shape for the velocity profile is given by the expression:

$$v_x(z) = \frac{f}{2\eta}\left(\frac{h^2}{4} + bh - z^2\right). \tag{2.37}$$

Analogous to the Couette flow NEMD situation, it important to verify that all the measures performed for a Poiseuille flow simulation belong to the LRR by checking that different values of the applied force density f do not affect the transport coefficient measures. The system relaxation time can be obtained by considering that the motion of the fluid center of mass will be described by the Langevin equation:

$$M\frac{\mathrm{d}v_x}{\mathrm{d}t} = -\lambda S v_x(t) + f, \tag{2.38}$$

with λ being the friction coefficient and S the wall surface. This expression implies that the system will relax within a time proportional to $1/\lambda$, so surfaces with small λ will infer large simulation times. Because the relaxation time is controlled by the friction coefficient, which we typically cannot know *a priori* in our simulations, it can be difficult to estimate beforehand an order of magnitude for f and $t_{\mathrm{st-st}}$ in a Poiseuille flow simulation.

2.2.4 How to simulate water?

The LJ potential introduced in Section 2.2.1, Eq. (2.3), works well when describing the attractive and repulsive interactions between spherically symmetric and neutrally charged molecules as, for example, liquid Argon. However, some modifications have to be implemented for other types of molecules with more complex geometries or inter- and intramolecular interactions. Such is the case of water, the ubiquitous liquid.

The water molecule has a tetrahedron structure centered on the oxygen, with the two hydrogen atoms close to the two corners. The other two corners of such tetrahedron will be the lone pair oxygen electrons. Because the repulsion between the lone pair electrons is greater than the one between the hydrogen atoms, the HOH angle θ_{HOH} is not 109.5° but 104.5°. This charge anisotropy does not only produce the bending of the tetrahedral equilibrium structure but also induces an electrical dipole moment in the molecule. Thus, the water molecule does not follow the two general suppositions of the standard LJ potential formulation: it is not spherically symmetric and it presents effective partial charge and, as a consequence, different modifications have to be introduced to simulate water molecules. With that regard, two different approaches can be followed: first, to introduce a new interaction potential that accounts for the different water special properties such

	q_O	q_H	ε_{OO}	σ_{OO}	d_{OH}	θ_{HOH}	d_{OM}
SPC/E	-0.8476	+0.4238	0.1553	3.166	1.0	109.47°	-
TIP4P/2005	-1.1128	+0.5564	0.1852	3.1589	0.9572	104.52°	0.1546

Table 2.1: Potential parameters for the SPC/E and TIP4P/2005 water models. The charges of oxygen q_O and hydrogen q_H are in elementary charge units, the interaction energy ε_{OO} and distance σ_{OO} between oxygen atoms are in kcal/mol and Å respectively, the bond length between oxygen and hydrogen d_{OH} and between oxygen and center of mass d_{OM} are in Å and the HOH angle θ_{HOH} is in degrees.

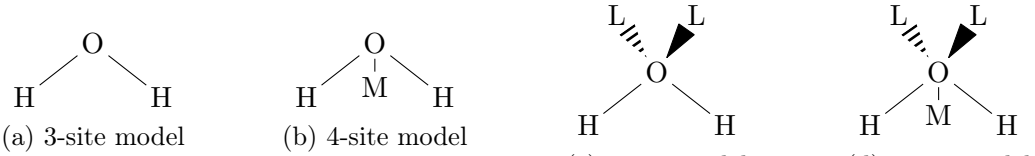

(a) 3-site model (b) 4-site model (c) 5-site model (d) 6-site model

Figure 2.5: Multipoint models for water where O corresponds to the oxygen atom location, H to the hydrogen atoms location, M to the dummy atom location and L to the lone pair electrons location.

as polarizability; or second, to maintain the LJ intermolecular interactions introducing different virtual sites in the water molecule: the multipoint models for water. This second approach is the most extended one, and it can be based from two-point [166] up to a six-point model parametrization, based on the oxygen atom location (O), a dummy atom (negatively charged) location (M), the hydrogen atoms locations (H) treated as positive charges, and the oxygen's lone pair electrons (L) treated as the negative point charges in the 5-site and 6-site water models (Fig. 2.5).

Although a large bibliography can be found on the different water models [167, 146], 3-site models examples are the SPC (simple point charge) and SPC/E (extended SPC) models, introduced by Berendsen et al. [168, 169], or the TIP3P (transferable intermolecular potential three point model) [170]. As 4-site model example we can find TIP4P [170], which can be reparametrized depending on the simulation objective: TIP4P-Ew to use with Ewald sumation methods [171], TIP4P/Ice [60] for solid water ice simulations, and its general reparametrization TIP4P/2005 [172], which reproduces the entire phase diagram of condensed water. Another 5-site and 6-site model extensions can be done with the TIP5P and TIP6P water models [173, 174].

In the present manuscript, MD simulations were performed for SPC/E and TIP4P/2005 models. In both cases the total intermolecular interaction potential between two water molecules is computed as a sum of the Lennard-Jones interactions between oxygen atoms and the Coulomb potentials, Eqs. (2.3),(2.6) with parameters found in Table 2.1 and masses $m_O = 15.9994\,\mathrm{g}$ and $m_H = 1.008\,\mathrm{g}$ for oxygen and hydrogen respectively. All the models described here are rigid water models, *i.e.* the bond lengths and angles as well as the electron clouds are not affected by any external perturbation. In practice, in a MD simulation, constrain algorithms as SHAKE [175, 176], can be used to maintain the two O-H bonds and the H-O-H angle rigid. SPC and TIP4P/2005 can be reparametrized to take into account the intramolecular degrees of freedom in their flexible versions, SPC/Fw and TIP4P/2005f [177, 178].

2.3 Hydrodynamic wall position

Flows in nanofluidic systems are strongly affected by liquid-solid slip, which is quantified by the slip length b and by the hydrodynamic wall position (HWP) z_s where the slip BC applies, Eq. (2.1). Considering a fluid enclosed between two parallel planar walls separated a distance H, we can define Δ as the reported shift between the wall surface and the HWP, defining the hydrodynamic height $h = H - 2\Delta$ (Fig. 2.6a). From a continuous perspective, the Navier BC Eq. (2.1) should be applied at the fluid-solid interface, and physical and hydrodynamic heights match ($H \equiv h$). Nevertheless, the position of such interface becomes a subtle issue at the molecular scale: should we consider the interface at the solid surface atoms? At the first fluid layer close to the wall? Somewhere in between? In practice, most studies assume a given position for the HWP, ranging typically from the physical wall position ($\Delta = 0\,\sigma$, with σ being the molecular diameter) up to the position of the liquid first absorption layer ($\Delta = 1\,\sigma$) [99, 125, 119, 121, 140, 89, 179, 180], or at the Gibbs dividing plane [132, 181, 182, 183], which leaves the simpler task to determine only one parameter: slip length or friction coefficient.

However, can we measure z_s? Only few studies can be found with that regard, which propose to measure the hydrodynamic position of the wall from mode analysis of hydrodynamic fluctuations [184] or from expressions based on Green-Kubo formulas, such as the one derived by Bocquet and Barrat [122]:

$$z_\mathrm{s} = \frac{\int_0^\infty \mathrm{d}s \left\langle F_x(s)\sigma_{xz}^{(\mathrm{f})}(0)\right\rangle_\mathrm{eq}}{\int_0^\infty \mathrm{d}s \left\langle F_x(s)F_x(0)\right\rangle_\mathrm{eq}}, \tag{2.39}$$

with F_x the friction force exerted by the wall on the fluid, $\sigma_{xz}^{(\mathrm{f})}$ the off diagonal term of the stress tensor inside the fluid, and $\langle\cdot\rangle_\mathrm{eq}$ denoting canonical average. Nevertheless, the applicability of these methods in finite-size MD simulations is delicate [123, 124, 126, 184].

Alternatively, we can employ MD simulations to measure both b and z_s. For instance, to avoid the impossibility of solving two unkowns, h and b, from one equation, we can obtain a set of independent equations by simulating two types of flow in the same system, typically a Couette and a Poiseuille flow (combining Eq. (2.33) with $v_\mathrm{slip} = b\,\dot\gamma$ and Eq. (2.37)); or by simulating a Poiseuille flow for two different system heights, see Ref. 146 and references therein. However, these measurements are usually delicate, and the measured b and z_s are very sensitive to the fits in the flow profile, which are affected by thermal fluctuations. Overall, few studies have attempted to measure the hydrodynamic position of the wall. For generic Lennard-Jones (LJ) fluids and walls of different wettabilities and corrugation, the reported shift Δ between the wall surface and the HWP varied between ~ 1.1 and $2.5\,\sigma$ [122, 129, 130, 184].

In this section, we will detail the results presented in Ref. 185, and we will see that viscosity η, slip length b and hydrodynamic wall position z_s can be accurately determined from a single MD simulation of a Poiseuille flow, after identifying a relation between the HWP and the wall shear stress configuration. We will also show that the common practice of applying a gravity-like force per particle to generate a Poiseuille flow in MD simulations imposes by construction that the HWP identifies with the Gibbs dividing plane of the liquid-vaccuum density profile. Simulations of a generic LJ liquid confined between parallel frozen walls show that the HWP for a pressure-driven flow is also close to the Gibbs dividing plane (measured at equilibrium), which therefore provides an inexpensive estimate of the HWP, going beyond the common practice of assuming a given position for the hydrodynamic wall. For instance, we will see that the HWP depends on the wettability of the surface, an effect usually neglected in MD studies of liquid-solid slip.

2.3.1 Theory

Let's start by showing the relation between interfacial shear stress and HWP in a Poiseuille flow. To that aim, it is important to emphasize that the partial slip BC Eq. (2.1) effectively takes into account all the phenomena occurring at the molecular vicinity of the interface and provides a BC for the flow far from the interface where the liquid is described by its bulk properties. As a consequence, in the partial slip BC, the velocity and the shear rate at the interface need to be obtained from the extrapolated bulk velocity field (*i.e.* using the bulk liquid viscosity η), regardless of the true velocity field at the interface, where the viscosity may locally change [98, 186]. This is the rule we will follow in the derivation below.

Let's consider a Poiseuille flow induced by a constant force density f in a liquid confined between two parallel walls located at a vertical position $z = \pm H/2$; (see Figs. 2.4b and 2.6a). The force density can be due to a pressure gradient, $f = (-\nabla P)$, or to a gravity-like field g, $f = \rho\, g$, with ρ being the bulk liquid density. The walls impose a partial slip BC (with a slip length b) applying at a distance Δ from the physical walls, defining the hydrodynamic height $h = H - 2\Delta$ (Fig. 2.6a). The velocity profile will be then given by Eq. (2.37). The key point of our derivation is to take into account that, for this flow, the shear stress applied by the liquid to the wall, $\tau_{\rm w} \equiv \sigma_{xz}^{(\rm f)}$ is:

$$\tau_{\rm w} = \eta \left.\frac{\partial v}{\partial z}\right|_{z=-h/2} = \frac{fh}{2}. \tag{2.40}$$

As a consequence, for a given force density f, the hydrodynamic height can be then measured via the interfacial shear stress,

$$h = \frac{2\tau_{\rm w}}{f}. \tag{2.41}$$

Using this relation, we can now discuss a common approach used in MD simulations to impose a Poiseuille flow, hereafter referred to as "gravity-like flow", where one applies a force per particle, $f_i = f/n_{\rm bulk}$ (with $n_{\rm bulk}$ being the number density) to liquid particles. In this case, the total force applied to the liquid will be $F = Nf_i = Nf/n_{\rm bulk}$, with N being the number of liquid particles. Thus, by definition, the total shear stress between the liquid and each of the two confining walls will be:

$$\tau_{\rm w} = \frac{F}{2S} = \frac{Nf}{2Sn_{\rm bulk}}, \tag{2.42}$$

where S is the wall area. By matching the expressions Eq. (2.40) and Eq. (2.42), it results that

$$n_{\rm bulk} = \frac{N}{h\,S}, \quad \text{or} \quad h = \frac{N}{n_{\rm bulk}S}. \tag{2.43}$$

Introducing the number density profile $n(z)$, Eq. (2.43) can be rewritten as

$$\int_0^{h/2} [n_{\rm bulk} - n(z)]{\rm d}z = \int_{h/2}^{\infty} n(z){\rm d}z, \tag{2.44}$$

namely the HWP identifies with the Gibbs dividing plane (GDP) corresponding to a partitioning of space between a region filled with a homogeneous liquid and another one without any liquid (see Fig. 2.7b). Therefore, the choice made in previous work [132, 181, 182, 183] to fix the HWP at the GDP can be justified based on hydrodynamic arguments. Additionally, because parallel flows do not affect significantly density profiles perpendicular to the walls [187], Eq. (2.43) indicates that the HWP for a gravity-like flow can in fact be measured from the GDP in equilibrium simulations as we will do in the following.

2.3.2 Methods

To test the theoretical predictions presented above, we performed MD simulations of a liquid confined between two parallel walls (Figs. 2.6b and 2.6c) using the LAMMPS package [144]. Liquid-liquid and liquid-solid interactions were modeled with a Lennard-Jones (LJ) potential, Eq. (2.3), $V_{ij}(r;\varepsilon_{ij},\sigma_{ij})$, with r being the interparticle distance, ε_{ij} and σ_{ij} being the interaction energy and size, where i and j can be L for liquid particles and S for solid ones. In the following we will use reduced units based on the particle mass m, and liquid-liquid interaction energy $\varepsilon = \varepsilon_{\mathrm{LL}}$ and size $\sigma = \sigma_{\mathrm{LL}}$. In particular, the unit of time is $\tau = \sigma\sqrt{m/\varepsilon}$. The liquid-solid interaction energy $\varepsilon_{\mathrm{LS}}$ was varied between 0.3 and $0.6\,\varepsilon$, while keeping $\sigma_{\mathrm{LS}} = \sigma$. The potential was truncated at $2.5\,\sigma$. For the walls, we used three atomic layers of a frozen face centered cubic crystal exhibiting a (001) face to the liquid, with an interparticle distance corresponding to mechanical equilibrium, $d = 2^{1/6}\,\sigma$. We used periodic BCs along the lateral x and y directions, and all the measurements were taken in a region with a lateral size $L \equiv L_x = L_y \approx 19\,\sigma$ with 5206 liquid particles and 1728 solid ones. The temperature was set to $T = 0.83\,\varepsilon/k_{\mathrm{B}}$ by applying a Nosé-Hoover thermostat to liquid particles, only along the y and z degrees of freedom perpendicular to the flow, with a damping time of $0.5\,\tau$. Equivalent results were obtained for different damping times and using a Berendsen thermostat. The pressure was set to $0.094\,\varepsilon/\sigma^3$ by using the top wall as a piston during an equilibration stage and fixing it at its equilibrium position during production. The resulting physical height H of the system, defined as the distance between the first inmost layers of the walls, varied between 21 and $22\,\sigma$ for different $\varepsilon_{\mathrm{LS}}$ values. The equations of motion were integrated using the velocity Verlet algorithm, with a timestep of $0.005\,\tau$.

From a MD point of view, the pressure-driven and the gravity-driven flows are not generated in the same way. Whether a real pressure driven flow implies that the force density $f = -\nabla P$ is homogeneously applied in the channel, a gravity-driven flow consists in applying a force per atom f_i to all the atoms in the fluid slab, with f_i being inhomogenous due to the inhomogeneties of the fluid density close to the wall. Therefore, although both pressure-driven and gravity-driven flows are Poiseuille-like in the bulk, they will differ in the molecular vicinity of the wall, and it can be interesting to study if the forcing at the interface can significantly affect the HWP value.

Three different sets of simulations were employed in order to measure the HWP or, equivalently, the Δ parameter: fluid-piston simulations (Δ_{FP}), equilibrium MD (Δ_{GDP}) and gravity-like flow measurements (Δ_{g}). To generate a pressure-driven flow, we used a fluid piston [187, 188, 189] (see Fig 2.6c): we increased the box size along the x direction, from $L_x \approx 19\,\sigma$ to $L_x \approx 43\,\sigma$ (using 11713 liquid particles and 3888 solid ones), we applied along the x direction a force per particle f_i^{piston} to liquid particles in a thin slab of length $l_x^{\mathrm{piston}} \approx 8\,\sigma$ (the fluid piston region), and we measured the wall shear stress τ_{w} and the bulk pressure gradient $f = (-\nabla P)$ in a measurement region of length $l_x^{\mathrm{measure}} \approx 19\,\sigma$ far from the fluid piston. We did not observe any significant difference in the results for a bigger region between the fluid piston and the measurements region. We computed the hydrodynamic height h using Eq. (2.41). Therefore, the corresponding hydrodynamic shift $\Delta = (H - h)/2$ is obtained, for the fluid piston simulations, from the expression:

$$\Delta_{\mathrm{FP}} = \frac{H}{2} - \frac{\tau_{\mathrm{w}}}{f}. \tag{2.45}$$

From the fit of the Poiseuille flow profile in the bulk region with Eq. (2.37), we could also extract the viscosity η and the slip length b, see Section 2.2.3b.

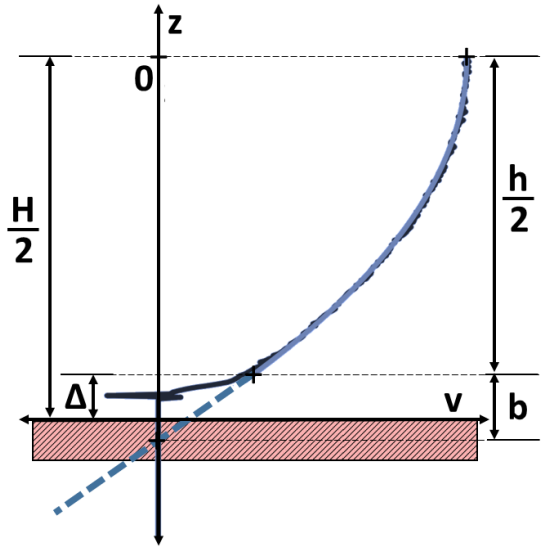

(a)

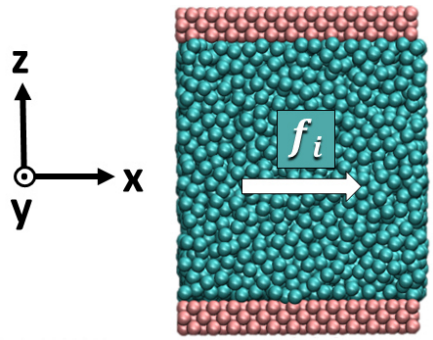

(b)

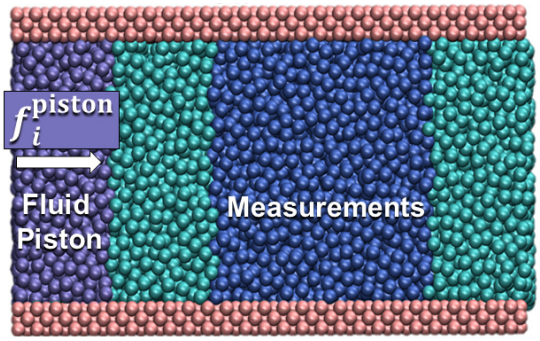

(c)

Figure 2.6: (a) Fluid velocity profile of a Poiseuille flow (black line) for the pressure-driven simulations and its parabolic bulk fit (dark blue line). H represents the physical system height and h the hydrodynamic height where the BC, Eq. (2.1), applies. Δ indicates the distance between the hydrodynamic and physical walls. The slip length b is determined from the slope of the extrapolates bulk velocity field at the hydrodynamic wall position (dashed dark blue line). (b) Simulated system made of a LJ fluid confined between two LJ rigid crystal walls. Periodic BCs were imposed in the x and y directions. A gravity-driven flow was generated by applying a force per particle f_i to all the atoms in the slab. (c) Considered system for the fluid piston simulations: a force per particle f_i^{piston} is applied to liquid particles along the x direction in a thin slab of length $l_x^{\text{piston}} \approx 8\,\sigma$. The measurements of the induced Poiseuille flow were taken in a region far from the fluid piston with the same lateral size as the original system shown in (a).

The HWP can also be directly measured from a gravity-like flow measurement, obtained by applying a force per particle f_i in the whole fluid slab (Fig 2.6b). In this case the HWP was determined from Eq. (2.41) by taking into account that $f = f_i\, n_{\rm bulk}$. Therefore,

$$\Delta_{\rm g} = \frac{H}{2} - \frac{\tau_{\rm w}}{f_i\, n_{\rm bulk}}. \tag{2.46}$$

Finally, we also computed Δ from the density profiles of equilibrium simulations following the Gibbs dividing plane (GDP) description in Eq. (2.43):

$$\Delta_{\rm GDP} = \frac{H}{2} - \frac{N}{2 n_{\rm bulk} S}. \tag{2.47}$$

Note that, first, we also measured the position of the GDP from the fluid piston and gravity-like MD density profiles, obtaining identical results to the equilibrium ones (with slightly higher standard deviation due to larger thermal noise present in NEMD). Second, it is important to highlight that, by construction, we should obtain $\Delta_{\rm g} = \Delta_{\rm GDP}$, although $\Delta_{\rm g}$ does not necessarily have to equal to $\Delta_{\rm FP}$ because, although both flows identify at bulk, some discrepancies can occur at the interface arising from the constant f_i assumption in the measures slab for the fluid piston simulations.

Finally, to compare the fluid-piston results with another more common approach, we performed independent Couette flow simulations on the system illustrated in Fig. 2.6b (shearing the walls instead of applying a force per particle f_i), with lateral size $L \equiv L_x = L_y \approx 19\sigma$ and 5206 liquid particles. We used the hydrodynamic height h measured in the fluid piston simulations; we measured the viscosity as the ratio between the wall shear stress and the bulk shear rate, and the slip length from a fit of the bulk velocity profile. In all the simulations, the equilibration stage lasted 2×10^5 timesteps, and the production lasted 10^7 timesteps.

Although f was directly measured from simulations as the pressure difference between two points in the measurements region (where we expect to have a nice linear pressure profile) per length, $f = \Delta P / l_x^{\rm measure}$, we applied a $f_i^{\rm piston}$ such as f is of the same order of magnitude than f from previous work which lied in the linear response regime. The relation between f and the applied $f_i^{\rm piston}$ can be established from $\Delta P = F/S_{\rm p}$, with F the total force applied in the volume of the piston region proportional to $f_i^{\rm piston}$, and $S_{\rm p}$ the surface perpendicular to F. We finally obtain that $f = f_i^{\rm piston} n_{\rm bulk} l_x^{\rm piston} / l_x^{\rm measure}$.

For fluid-piston MD, gravity-like MD and Couette flows, we simulated a number of different forcing (pressure gradient, $f \in [2.7, 4.7] \times 10^{-3}\, \varepsilon/\sigma^4$, force per atom $f_i \in [1.0, 7.0] \times 10^{-3}\, \varepsilon/\sigma$, or shear velocity, $U \in [0.1, 0.5]\, \sigma/\tau$). Five independent simulations were run for each value of the force density. All the results shown in the present section ($\Delta_{\rm FP}$, $\Delta_{\rm g}$, $\Delta_{\rm GDP}$, b and η) were obtained for a given $\varepsilon_{\rm LS}$ by averaging the results which belonged to the linear response regime, *i.e.* the forcing range in which the measured quantity remained constant. Correspondingly, the maximum shear rates produced were 0.033, 0.035 and $0.048\, \tau^{-1}$ for the fluid piston, the gravity-like and the Couette simulations respectively. These shear rates are below the shear thinning regime of the LJ fluid, around $0.07\, \tau^{-1}$, see *e.g.* Ref. 190. The given error bars correspond to the statistical error within 95 % of confidence level.

2.3.3 Results and discussion

Figure 2.7a presents the measured shifts between the wall surface and the HWP, $\Delta_{\rm FP}$ from fluid piston simulations using Eq. (2.45), $\Delta_{\rm g}$ from gravity-like simulations using

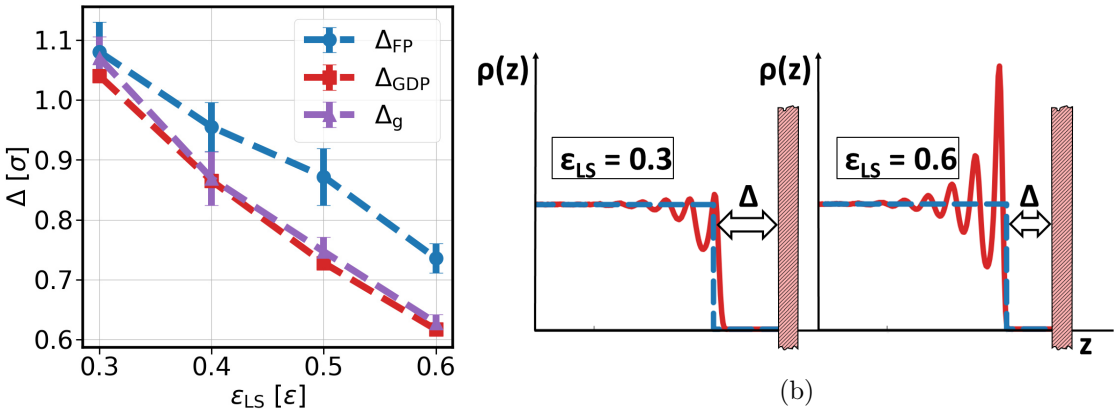

(a) (b)

Figure 2.7: (a) Measured shifts between the wall surface and the HWP, for different interaction strengths ε_{LS} between liquid and solid particles. Blue circles: Δ_{FP} from fluid piston simulations using Eq. (2.45); Red squares: Δ_{GDP} from equilibrium simulations using Eq. (2.47), *i.e.* using the position of the GDP; Purple triangles: Δ_g from gravity-like simulations using Eq. (2.46). As expected from the theoretical derivation, Δ_{GDP} and Δ_g are equivalent. Δ_{FP} and Δ_{GDP} are similar (although they differ slightly at high ε_{LS}); in particular, all of them decrease for a higher wall wettability. (b) Gibbs dividing plane (GDP) representation (dashed blue line) of the liquid interfacial density profile (full red line) for two different ε_{LS}. The GDP is closer to the physical wall for a larger ε_{LS} because of the stronger adsorption.

Eq. (2.46), and Δ_{GDP} from equilibrium simulations using Eq. (2.47), *i.e.* using the position of the GDP. Note that, even though Δ_{GDP} was measured from equilibrium simulations, we will still refer to it as the gravity-like flow hydrodynamic shift, because Eq. (2.43) was derived analytically for a gravity-driven flow. Indeed, as we can see in Fig. 2.7a, both equilibrium and gravity-like measures of the HWP are equivalent, although obtained through different methods and simulations. In this case, the smaller error bars of Δ_{GDP} are due to the smaller thermal fluctuations present in EMD, showing the equilibrium measure of the density profile more suitable than the one from a real gravity-like flow simulation. In Fig. 2.7a, we can also see that Δ_{GDP} is comparable to Δ_{FP}, although they slightly differ for large ε_{LS}.

In general, the hydrodynamic shifts for a pressure-driven and for a gravity-like flow do not have to be identical: indeed, while the pressure gradient and the gravity-like force identify in the bulk, they will generally differ in the molecular vicinity of the interface where the fluid becomes heterogeneous. In particular, the gravity-like force distribution will follow that of the density, and can result in a different effective BC for the bulk flow. In Fig. 2.7a we can also see that, for both flows, the distance between the wall surface and the HWP decreases with the wall wettability controlled by the ε_{LS} parameter (a higher ε_{LS} corresponds to a more wettable system). We can understand this result in terms of the GDP (Fig. 2.7b): for a more wettable system the peaks of the density profile close to the wall are more pronounced so the area of an effective liquid with constant density region is bigger, hence a larger value of h and a smaller value of Δ_{GDP}. We also varied ε_{LL}, and found that its impact was much smaller than that of ε_{LS}. This can be rationalized based on the GDP. Indeed, changing ε_{LL} should (at the first order) rescale the whole liquid density profile, so that the GDP should not change.

	Fluid piston		Couette	
$\varepsilon_{\mathrm{LS}}$	η	b	η	b
0.3	1.422 ± 0.015	6.80 ± 0.10	1.409 ± 0.024	6.64 ± 0.25
0.4	1.421 ± 0.006	3.26 ± 0.02	1.414 ± 0.007	3.27 ± 0.09
0.5	1.428 ± 0.007	1.66 ± 0.08	1.412 ± 0.011	1.61 ± 0.08
0.6	1.417 ± 0.013	0.71 ± 0.08	1.410 ± 0.011	0.64 ± 0.07

Table 2.2: Shear viscosity η (in $\varepsilon\tau/\sigma^3$) and slip length b (in σ) at $T = 0.83\varepsilon/k_B$ and $p = 0.094\varepsilon/\sigma^3$, for different system wettabilities controlled by $\varepsilon_{\mathrm{LS}}$ (in ε): comparison between fluid piston and Couette flow measurements.

The results we obtained here for the HWP are significantly different from the ones obtained by other studies [122, 129, 130, 184] (with Δ between ~ 1.1 and $2.5\,\sigma$) and from the sometimes used assumption [125, 119] that $\Delta = 0\,\sigma$. For the less wettable walls the common assumption [89, 140, 179, 99, 180] that $\Delta \sim 1\,\sigma$ agrees with our results. However, for higher $\varepsilon_{\mathrm{LS}}$ values this assumption is generally not valid, specially in systems with significantly small slip lengths like the one discussed in this section.

From the pressure-driven flow, in addition to the determination of the HWP, we can also measure the system transport coefficients. Table 2.2 reports the η and b results for a set of $\varepsilon_{\mathrm{LS}}$ parameters. Because the shear viscosity is a property of the bulk liquid and in all simulations the temperature and pressure are set constant, there is no effect of the wall wettability on η, and its value is comparable to the one obtained from Couette simulations. As rationalized in previous work [28], the slip length decreases with $\varepsilon_{\mathrm{LS}}$: for a less wettable system the fluid friction coefficient is smaller which implies a higher value of $b = \eta/\lambda$. If we compare these results with those obtained from Couette simulations, we can see that by means of the pressure-driven flow method we obtained equivalent b and η measurements with the same order of magnitude in the error precision.

2.3.4 Conclusions

We have shown that the position where the hydrodynamic BC imposed by walls Eq. (2.1), should be applied can be efficiently determined by measuring the wall shear stress in MD simulations of a Poiseuille flow. As a consequence, we have shown that for gravity-driven flows, the HWP is only controlled by the static density profile of the fluid close to the wall, and identifies with the GDP, which can be measured from equilibrium simulations. Accordingly, the HWP could be estimated from previous work where the equilibrium structure of liquid-solid interfaces was modeled [96]. This was verified from the equivalent HWP results obtained from gravity-driven MD (applying a constant force per particle to the liquid slab) and equilibrium MD. We then simulated a LJ fluid confined between two parallel frozen walls, and measured the HWP by using a fluid piston to generate a pressure-driven flow. The pressure-driven flow hydrodynamic wall was comparable (although not identical) to the GDP. We investigated the effect of wetting by varying the liquid-solid interaction energy. We found that the hydrodynamic BC applies in the liquid, at a distance Δ from the wall surface varying from $\sim 1\sigma$ (with σ the atomic diameter) on non-wetting walls to a fraction of σ on wetting walls. The decrease of Δ for increasing wetting can be rationalized in terms of GDP, which is shifted toward the solid when the adsorption of the fluid increases on more wetting surfaces. The measured values of Δ are generally lower than previous measures, which ranged between 1.1 and 2.5σ, but they correspond approximately to the standard assumption made in MD studies of liquid-solid

slip that $\Delta \sim 1\sigma$. Finally we have shown that, in addition to the HWP, the Poiseuille flow simulation also provides an accurate estimate of the slip length and fluid viscosity, by comparing the measured values with those obtained from independent Couette flow simulations.

Overall, we have presented a simple, fast and accurate method to fully characterize the transport properties of a confined fluid, by measuring the viscosity, slip length, and HWP in a single Poiseuille flow simulation. Note that this method is not limited to the simple slab geometry considered here. For instance, it can easily be extended to cylindrical channels, where the wall shear stress is: $\tau_{\mathrm{w}} = fr/2$, with f the pressure gradient and r the hydrodynamic radius of the pore. The method could also apply to mixtures (for a gravity-like flow, one can show that Eqs. (2.43) and (2.44) apply when replacing the number of liquid particles and the number density by the total mass of the liquid and the mass density, respectively) and to thermalized walls. An analogous approach could also be applied to characterize the effective wall position for interfacial heat transfer. Our simulation results also suggest that the GDP provides a reasonable approximation of the hydrodynamic wall, and can be used as an inexpensive estimate going beyond the common 'one molecular diameter' approximation. In particular the GDP captures the decrease of the distance between the hydrodynamic and physical wall for increasing wettability. We hope these results will help improve the characterization of the hydrodynamic BC by MD simulations in systems of interest for nanofluidic applications.

2.4 Interfacial transport coefficient: determining slippage

We have presented nanofluidics as an emerging field offering innovative solutions for energy harvesting and desalination. The efficiency of these applications depends strongly on the liquid-solid slip b, arising from a favorable ratio between viscosity η and interfacial friction λ in Eq. (2.1). Because reducing friction is key to improve the performance of nanofluidic systems, an intensive experimental effort has been undertaken during the recent years to characterize the ultra-low liquid-solid friction of new 2D materials and their derivative [31, 191, 34, 192]. Further work has been performed to study the impact on friction of different wall features such as wettability [137, 112], roughness [113], crystallographic orientation [114], electronic structure [45, 193, 194], or electrostatic interactions [195].

Among all fluids, the study of water has always been of special concern for scientists from a broad variety of research fields [196, 197, 198]. Its interest not only lies on its ubiquitous nature but also on its many thermodynamic and dynamic anomalies like, among others, the non-monotonous temperature dependence of its isothermal compressibility and density [57, 61]. These anomalies are enhanced when water is driven to its supercooled regime (*i.e.* the range of temperatures below the freezing point where water keeps its liquid state), making this regime ideal to test and refine our current understanding of water. In particular, the temperature dependence of the bulk transport properties of supercooled water has been explored both numerically and experimentally over the last decade [107, 108]. Confined water has also been explored from an experimental and theoretical point of view, with an special interest in the novel 2D materials such as graphene, where the properties of the confined liquid have been already studied at a given thermodynamic conditions for planar walls as well as for carbon nanotubes [40, 199, 200, 201, 111, 202, 203].

In particular, the temperature evolution of supercooled water under confinement has also been the subject of intensive experimental research [204, 205, 206, 207, 208, 209]. Broadband dielectric spectroscopy, nuclear magnetic resonance, as well as neutron scat-

tering experiments have successfully probed water confined in pores with sub-nm radii at temperatures as low as about 130 K, in order to connect the dynamical behavior of supercooled confined water to that of bulk water in the so-called no-man's land (150 K to 230 K) [208]. At temperatures above the no-man's land, marked differences have been found in the time relaxation of supercooled water under confinement compared to bulk water, suggesting that the interfacial water dynamics, and thus water friction, may play an important role. However, the temperature evolution of water friction in the liquid and supercooled regime remains unclear nowadays. Besides achieving a better understanding of interfacial and nanoconfined water dynamics and phase behavior under supercooling, such a knowledge would be instrumental e.g. for the development of innovative nanofluidic systems working in the supercooled regime, and would provide fundamental insight on recent experimental work on anti-icing surfaces [210, 211, 212].

In that context, we reported a study [56] in which the temperature dependence of water viscosity and wall slip are examined in detail. In the following, we will detail the extensive molecular dynamics (MD) simulations we performed to this aim of a slab of water confined between graphene and generic Lennard-Jones (LJ) surfaces. In order to assess the role of supercooling, we compare water, which is in its supercooled state for the lower temperatures, and methanol, which remains liquid for the whole range of temperatures considered in our study. We find that whilst the liquid-solid friction coefficient and the viscosity follow the same fundamental laws and are almost proportional to each other in the liquid state, their behavior strikingly differ for water in the supercooled regime. As a result, the slip length (defined as the ratio between the viscosity and the friction coefficient) increases fast for water as soon as it goes below its melting point; on graphene, we report a twofold enhancement at ~ 240 K, and up to a fivefold enhancement at 225 K, reaching ~ 230 nm. Although the presence of impurities may enhance ice nucleation in supercooled water, a number of experimental works have consistently shown that it is possible to cool down water to the range of temperatures explored in our study and even below [107, 204, 206, 205, 207, 208, 209, 211].

2.4.1 Methods

Before presenting the results for the transport coefficients temperature evolution, it is important to detail the choice we made for the different MD simulations parameters as well as to briefly introduce the laws employed for the fit of such temperature evolution.

a. Simulation details

All the simulations were carried out with the LAMMPS package [144]. The confined system consisted in a fluid (water or methanol) between two parallel walls (Fig. 2.8), with periodic boundary conditions applied in the directions parallel to the walls. For water simulations, 4096 water molecules were modeled with the TIP4P/2005 force field [172]. We considered two different types of walls. First, we modeled wall atoms which interact via a Lennard-Jones potential, Eq. (2.3). The interaction parameters between LJ walls and water molecules were set from Ref. 213 for hydrophobic walls, corresponding, for TIP4P/2005 at 300 K, to a contact angle $\theta \sim 134°$ (computed through the sessile droplet method described in Subsection 2.2.2). Analogous to the MD simulations in the HWP section, the structure of the walls consisted in a frozen face centered cubic crystal constituted by three atomic layers exhibiting a (001) face to the fluid, with a lattice parameter $a = 5.356$ Å (Fig. 2.8). Second, we also simulated graphene walls with cross-interaction parameters taken from Ref. 40, characterized by a contact angle $\theta \sim 80°$ for TIP4P/2005 water at 300 K. For methanol

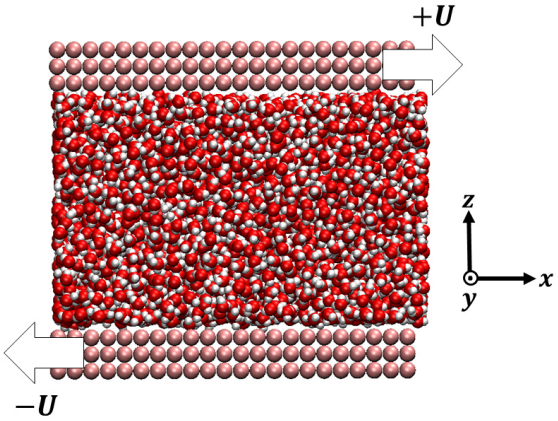

Figure 2.8: Modelled system constituted by a confined fluid between two planar solid walls. The snapshot corresponds to TIP4P/2005 water enclosed by LJ walls. The arrows indicate the shear velocity U directions by which the system is driven out of the equilibrium for the shear flow measurements.

(MeOH) simulations, 4056 molecules were modeled with the interaction parameters given by Refs. 214, 215. For LJ walls and graphene we considered the same interactions between atoms than the ones for water, and the cross-interactions MeOH-wall were determined via the Lorentz-Berthelot mixing rules Eq. (2.4). The surfaces were then characterized for MeOH at 300 K by contact angles $\theta \sim 100°$ and $\theta \sim 0°$ for LJ and graphene walls respectively. The walls dimensions were $L_x = L_y = 58.92$ Å for the LJ wall, and $\{L_x, L_y\} = \{56.57, 58.92\}$ Å for graphene. The pressure was set to 1 atm by using the top wall as a piston during a preliminary run. The vertical height was then obtained by fixing the top wall at its equilibrium position for the given pressure and it corresponded to $H \sim 40$ Å for water and $H \sim 90$ Å for MeOH. The temperature T was varied between 225 K and 360 K by applying a Nosé-Hoover thermostat to the liquid particles (only along the directions perpendicular to the flow for non-equilibrium simulations). Equivalent results were obtained for different damping times, and with a Berendsen thermostat.

To measure the hydrodynamic transport coefficients we performed non-equilibrium molecular dynamics (NEMD) simulations applying a constant shear velocity U_{wall} to the walls in opposite x directions for each wall, producing a Couette (linear) velocity profile far from the wall (see Fig. 2.4a). The viscosity was measured from the ratio between the shear stress and the bulk shear rate, $\eta = \tau_{\text{w}}/\partial_z v_x$, where v_x corresponds to the velocity profile in the bulk region in the direction of the flow. The friction coefficient λ was measured from the ratio between the shear stress τ_{w} and the velocity jump at the interface, $v_{\text{slip}} = U_{\text{wall}} - v_x(h/2)$, where v_x is the fitted bulk velocity profile in the direction of the flow evaluated at the effective wall position z_{s}. As explained in Section 2.3, this effective wall position can be rationalized in terms of a Gibbs dividing plane which defines an effective BC at $h/2$ at a distance Δ from the physical wall position. Δ was determined from equilibrium simulations using Eq. (2.47) by extending this formula for a molecular liquid with

$$h = \frac{M}{\rho_{\text{bulk}} S}, \tag{2.48}$$

where now M is the total liquid mass and ρ_{bulk} its bulk mass density.

Viscosity and friction have been measured during a production time of 4 ns for 3 different shear velocities for each temperature, $U \in [1, 70]$ m/s, in order to verify that our measurements were performed in the linear response regime. For a given shear velocity,

3 independent simulations were run and we measured the shear stress at the top and the bottom walls for each of them. Overall, 18 independent measurements were taken for a given T and the error bars correspond to the statistical error within 95% of confidence level.

b. VTF, SA, Bässler laws: Theory details

Before introducing and discussing the results obtained for the transport coefficients temperature evolution, let's first briefly introduce the common theoretical modelling developed in the literature for bulk properties [107, 216, 108]. Viscosity temperature dependence is well described for liquids with strong intra-molecular bonds by an Arrhenius law that writes, denoting the transport coefficient as X:

$$X = X_0 \cdot \exp\left(\frac{A}{T}\right), \tag{2.49}$$

with activation energy $A > 0$. Nevertheless, fragile liquids, such as water, are characterized by a faster increase. Several models are proposed in the literature [217]. The most accepted ones are the Vogel-Tammann-Fulcher (VTF) law [218, 219, 220], the Speedy-Angell (SA) law [221], and the Bässler law [222], respectively:

$$X = X_0 \cdot \exp\left(\frac{A}{T - T_\mathrm{f}}\right), \tag{2.50a}$$

$$X = X_0 \cdot \left(\frac{T}{T_\mathrm{f}} - 1\right)^{-\gamma}, \tag{2.50b}$$

$$X = X_0 \cdot \exp\left[\left(\frac{T}{T_\mathrm{f}}\right)^2\right]. \tag{2.50c}$$

All these laws introduce a singularity at a finite temperature $T_\mathrm{f} > 0$ so their applicability is restricted to temperatures away from this singularity. Specifically for water, while the above laws provide a good effective description of the temperature evolution of dynamical quantities down to deep supercooling, they fail to describe the extreme supercooled region, where a dynamical cross-over between a fragile and a strong behavior appears, which can be captured by the two-state models of water [63]. Accordingly, T_f does not provide a good indication of the true glass temperature transition of water.

2.4.2 Bulk transport: viscosity temperature dependence

For water in particular, the temperature dependence of the viscosity deviates from Arrhenius behavior of Eq. (2.49) [57]. We tested the three common alternative laws introduced above, VTF (Eq. (2.50a)), SA (Eq. (2.50b)) and Bässler (Eq. (2.50c)). We first computed the shear viscosity η from NEMD with LJ walls to test the applicability of different temperature dependence laws to our simulation results, as done by previous experimental [107, 223] and numerical works [216, 108]. For TIP4P/2005 we find good agreement between our data and the experimental ones [107, 223], as well as previous MD simulations with the TIP4P/2005 and TIP4P/2005f water models [215, 224, 216], as shown in Fig. 2.9a. The fit results are reported in Table 2.3.

Due to the good agreement of VTF and SA fits with our numerical data (Figs. 2.9a and 2.10), we performed χ^2 and R^2 tests to determine which one describes better the results.

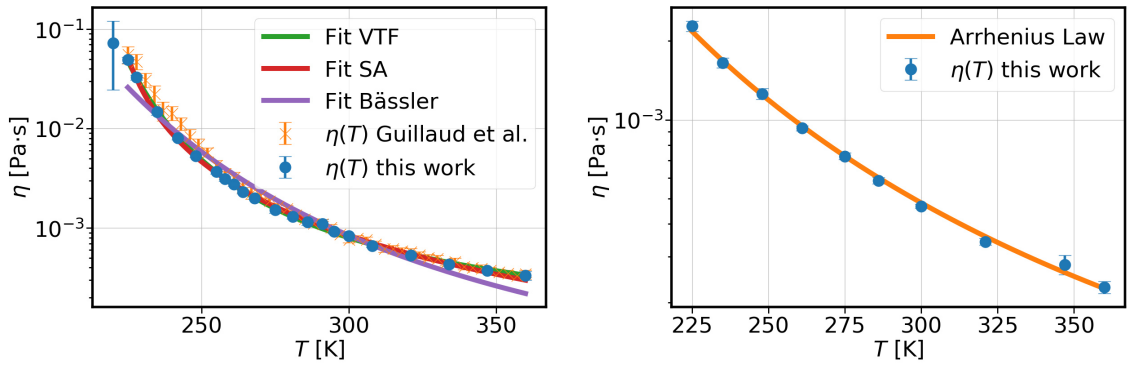

(a) TIP4P/2005 water (b) MeOH

Figure 2.9: Shear viscosity η NEMD measurements temperature evolution for: (a) TIP4P/2005 water; our data set is in good agreement with previous work performed for the TIP4P/2005f force field [216], which is itself in agreement with experiments [107]. Three different fits, VTF, SA and Bässler were performed. (b) MeOH; an Arrhenius fit was performed to our data set in order to describe viscosity temperature dependence.

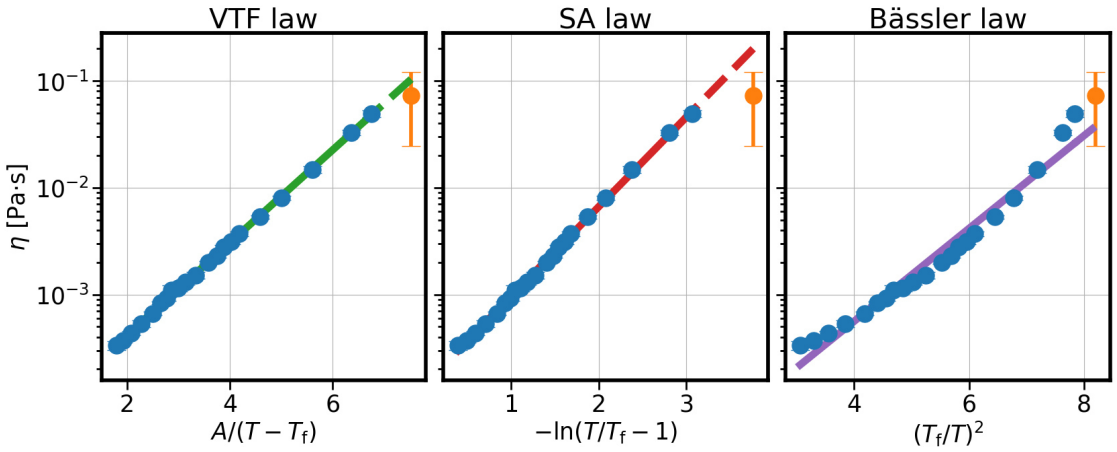

Figure 2.10: Different fits comparison for water shear viscosity. One can observe that our results are globally well described by VTF and SA laws but not by Bässler law. In orange the measure corresponding to $T = 220\,\mathrm{K}$, not taken into account for the fit due to its bigger error. Nevertheless when extending the fit results to lower temperatures this point is well described by VTF law but not by SA law, indicating the better suitability of VTF law for our data, in agreement with the results of the χ^2 and R^2 tests performed.

	TIP4P/2005 - VTF		
	T_f (K)	A (K)	X_0
η	176.26 ± 1.35	329.10 ± 11.43	$5.60 \cdot 10^{-5} \pm 3.72 \cdot 10^{-6}$
λ_{LJ}	165.94 ± 2.68	357.20 ± 20.99	$1.59 \cdot 10^{4} \pm 1.70 \cdot 10^{3}$
$\lambda_{\mathrm{graphene}}$	153.80 ± 4.16	349.32 ± 27.33	$1.60 \cdot 10^{3} \pm 1.93 \cdot 10^{2}$
	MeOH - Arrhenius		
		A (K)	X_0
η		1357.35 ± 22.25	$5.22 \cdot 10^{-6} \pm 4.20 \cdot 10^{-7}$
λ_{LJ}		1056.72 ± 35.63	$8.11 \cdot 10^{3} \pm 1.05 \cdot 10^{3}$
$\lambda_{\mathrm{graphene}}$		899.31 ± 36.71	$3.43 \cdot 10^{2} \pm 4.56 \cdot 10^{2}$

Table 2.3: Fit parameters of VTF Eq. (2.50a) and Arrhenius Eq. (2.49) laws for TIP4P/2005 water and MeOH respectively. We appreciate the similarity of the temperature T_f and the activation energy A between the different transport coefficients, η and λ, and between the two different wall types, LJ walls and graphene. X_0 units are [Pa s] for viscosity and [Pa s/m] for friction.

We obtained $\{\chi^2, \mathrm{R}^2\} = \{8.47 \cdot 10^{-5}, 0.9994\}$ for VTF and $\{\chi^2, \mathrm{R}^2\} = \{3.87 \cdot 10^{-4}, 0.9956\}$ for SA therefore concluding a better agreement with VTF.

For MeOH simulations viscosity's temperature dependence is weaker than for water. The results are in good agreement with previous work [215] and they are well described by an Arrhenius law (Table 2.3).

2.4.3 Interfacial transport: friction temperature dependence

For a given fluid, when varying the wall type we already see a difference in the absolute value of λ being more than one order of magnitude bigger for LJ walls than for graphene (Figs. 2.11,2.12). This effect has already been appreciated and discussed in previous work [40, 45] and it is due to graphene extreme smoothness, which makes the liquid-solid friction extremely small ($\lambda \sim 1.7 \cdot 10^4$ Pa·s/m for water at 300K).

Additionally, in Fig. 2.13a we can see that the temperature dependence changes with the fluid, but for a given fluid, it depends weakly on the wall type. Interestingly, in Table 2.3 we can see that the temperature dependence of of η and λ can be fitted by the same laws (VTF for TIP4P/2005 and Arrhenius for MeOH, corresponding to continuous lines in Fig, 2.13a. However, although very similar, the fit parameters for viscosity and friction are different beyond the error bars.

2.4.4 Slippage: bulk and interface competition

We can go further in exploring the relation between η and λ by plotting the slip length b given by the ratio between both transport coefficients, see Eq. (2.1). In Fig. 2.13b one can see that for a wide range of high temperatures, where the systems are in the stable liquid state, η and λ vary together with T, so their ratio (or equivalently the slip length) is roughly constant. Specifically, for MeOH (which remains a simple liquid for the whole range of simulated temperatures, including those slightly higher than its boiling point at around 338 K), b increases slowly and regularly when T decreases; this indicates a slightly weaker temperature dependence of friction as compared to viscosity. In contrast, for water, b starts to increase very fast when the temperature decreases below the melting point, indicating a much weaker temperature dependence of friction as compared to viscosity, only in the

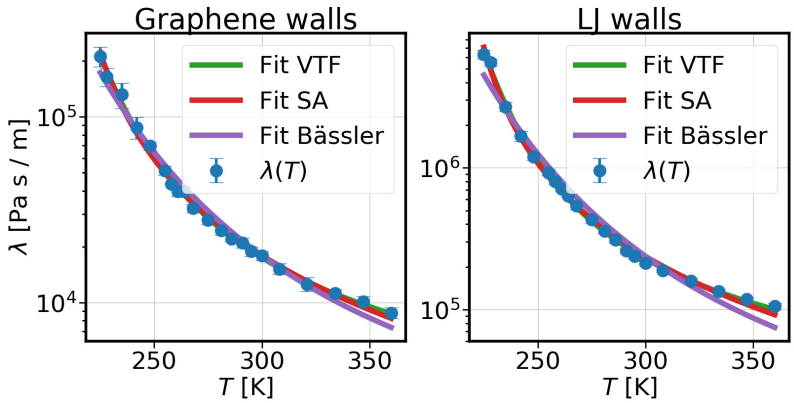

Figure 2.11: Liquid-solid friction coefficient results for TIP4P/2005 water from NEMD simulations for graphene and LJ walls respectively. Although the temperature evolution is similar for both walls, we can appreciate a one order of magnitude difference at a given temperature between the different walls. Three different fits, VTF, SA and Bässler were performed.

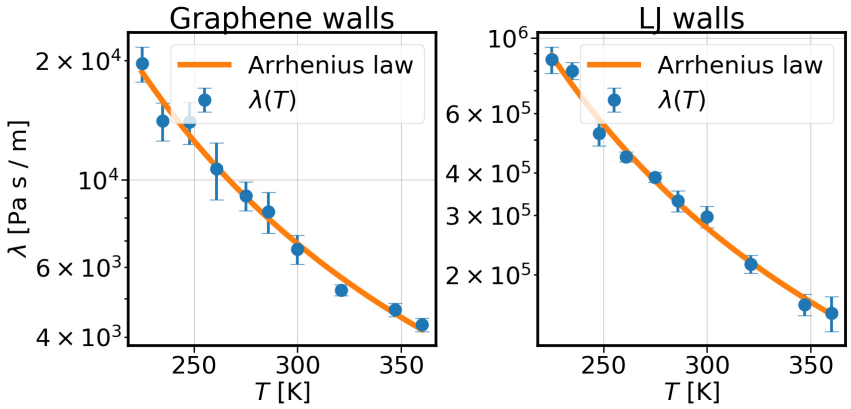

Figure 2.12: Liquid-solid friction coefficient results for MeOH for graphene and LJ walls respectively. Although the temperature evolution is similar for both walls, we can appreciate a much lower friction coefficient for graphene. An Arrhenius fit was performed.

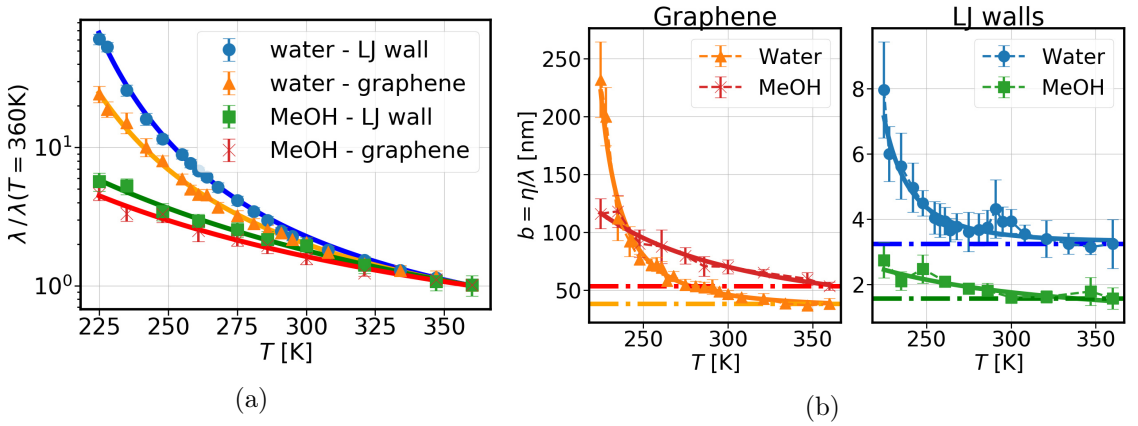

Figure 2.13: (a) Friction's temperature dependence results normalized by the value at 360 K for each fluid and wall, in order to highlight the similar temperature evolution for a given liquid regardless of the wall type. Continuous lines are the respective VTF (for water) and Arrhenius (for MeOH) fits. (b) Temperature dependence of the slip length, $b = \eta/\lambda$. Dash-dotted lines are guide-to-the-eye for a constant b value. One can see a small temperature variation for the highest temperatures (indicating that η and λ evolve in similar ways), while the slip length increases significantly when decreasing the temperature for the lowest Ts, in the supercooled regime. In both subfigures, blue dots correspond to water with LJ walls, orange triangles to water with graphene walls, green squares to MeOH with LJ walls and red crosses to MeOH with graphene walls.

supercooled regime. When comparing these results with those for liquid MeOH one can conclude that this large slip increase is mostly related to the supercooling of water.

The biggest temperature effect on b is observed for water and graphene walls, where it grows by a factor of 5 from the highest to the lowest simulated temperature (225 K), reaching a maximum value of ~ 230 nm. Although experiments of interfacial slip in supercooled water have not yet appeared, we envision that experimental verification of our results may be within reach of capillary flow measurements of water confined between graphene/silica nanochannels [192], considering that nuclear magnetic resonance and neutron scattering experiments of water confined in graphite oxide and silica nanopores have explored water dynamics down to 130 K and 220 K, respectively [205, 207, 204]. Additionally, recent microscopy studies have investigated the dynamical behavior of supercooled water down to 230 K using polyesterene spheres suspended in water [107] and have studied the anti-icing behavior of water droplets sliding on of nanopatterned surfaces around 258 K [211]. As we have seen in our simulations, at temperatures between 225 and 270 K, water slippage is largely affected by the wall type, a result consistent with the experimental observation that the water time relaxation in nanopores is strongly dependent on the nature of the solid surface. Instead, experiments in no-man's land report a universal dynamical behaviour in confined water [208]. Thus, future measurements of water slippage in different nanopores at lower temperatures than those explored here might elucidate whether or not slippage depends on the wall type below 225 K. Enhanced water slippage under supercooling may also have a direct implication for the development of icephobic surfaces, as it may favour droplet condensation and ice removal from surfaces.

2.4.5 Conclusions

In this section we investigated the temperature evolution of bulk and interfacial hydrodynamic transport coefficients for water and MeOH confined between LJ walls and graphene. For a given liquid, the temperature evolution of viscosity and friction were described by the same laws, although with different parameters. The temperature evolution of interfacial friction was weakly affected by the wall type, but changed significantly with the liquid type. We then compared the temperature evolution of viscosity η and friction coefficient λ by considering their ratio, defined as the slip length $b = \eta/\lambda$. We observed, from higher to lower T, that both transport coefficients evolved similarly in the high temperature region where the liquid is stable, but that for water, viscosity increased faster than friction in the supercooled regime, implying a fast growing slip length. The largest temperature effect on b was observed for water and graphene walls, where it grew by a factor of 5 from the highest to the lowest simulated temperature (225 K), reaching a maximum value of ~ 230 nm.

2.5 Summary and conclusions

In this chapter we have introduced classical molecular dynamics simulations as a fundamental and powerful tool to describe the microscopic scale of a classical many-body system, by modelling the atoms and molecules physical interactions with empirical force fields. With a broad range of applications in multiple areas of knowledge such as biochemistry, biophysics or material science, we presented them as a tool to characterize fluid transport properties under confinement. They allow us to characterize the wetting properties of the fluid-wall interactions, as well as the flow generation for a broad range of fluids, from the model Lennard-Jones fluid, where the particles interact by a generic Lennard-Jones potential, to everyday life fluids such as methanol or water.

With the objective of better understand and characterize the partial slip BC, which predicts a fluid velocity jump at the interface with respect to the wall, we first studied how to determine that interface position from a molecular point of view: the hydrodynamic wall position. With that regard we compared the results from two different types of flows: on the one hand, we generated a pressure-driven flow by applying a force per atom in a thin slab far from the measures region (what we called the fluid piston method) where we determined the force density (analogous to a negative pressure gradient which generates the parabolic velocity profile); on the other hand, we generated a gravity-like flow by applying a constant force per atom to all the atoms in the whole fluid slab. We saw that, although both flows identify in the bulk, the subtle differences between the flows at the interface (due to the fluid heterogeneties close to the wall) can generate different effective interface positions. We also saw that, in the case of gravity-driven flows, the hydrodynamic wall position identifies with the Gibbs dividing plane, partitioning a region full of homogeneous fluid and a vacuum region. Because such Gibbs dividing plane is only related to the fluid density profile which, as a static fluid property, can be determined from equilibrium simulations, computationally less expensive than the non-equilibrium ones. We also studied how the wetting properties affect the effective shear plane position by varying the interaction energy between fluid and wall particles. We saw that the effective interface is shifted towards the wall for the more wetting surfaces (higher fluid-solid interaction energy). This result can be understood in terms of the Gibs dividing plane, which will also be shifted towards the solid when the fluid absorption increases on the more wetting surfaces.

Once the position where the partial slip boundary condition has been determined, we wondered how do different fluids and walls affect the liquid-solid friction coefficient, and how does its temperature dependence differ with respect to the viscosity, its bulk transport analogous. We also wondered about the effects of supercooling the fluid on the transport properties by comparing two different fluids in the same range of temperatures: methanol, which remains liquid for the whole range of temperatures considered in the study, and water, in its supercooled state for the lower temperatures. After first assessing the validity of our simulations and measures by comparing the viscosity temperature dependence with previous simulations and experimental results performed in the same range of temperatures and finding good agreement between the different data, we proceed to study friction temperature evolution.

For a given fluid, we saw that viscosity and friction temperature dependence were described by the same laws. We also saw that the friction coefficient was weakly affected by the wall type in terms of temperature evolution, although its absolute value at a given temperature could differ up to a factor of 10 between Lennard-Jones walls and graphene, due to the atomic smoothness of the last surface. We also saw that the fluid type could significantly change the friction temperature evolution, which was described by a modified Arrhenius law for water (which introduces a temperature singularity) or a standard Arrhenius law in the case of methanol. Finally we also saw that, for a given fluid, bulk and interface differences can be quantified in terms of the slip length, defined as the ratio between viscosity and friction. Both for methanol and water, we observed an increase of the slip when lowering the temperature, with a faster growth in the case of water when entering in its supercooled regime, implying a faster increase of the viscosity that the friction when lowering the temperature. Of particular interest is the case of water on graphene, where the slip length is multiplied by up to a factor of five and reaches $\sim 230\,\mathrm{nm}$ at the lowest simulated temperature of $225\,\mathrm{K}$. Experiments on nanopores can reach much lower temperatures [225] and could reveal even more drastic changes. The predicted fast increase in water slip can also be detected at supercoolings reached experimentally in bulk water [107], as well as in droplets flowing on anti-icing surfaces [226], paving the way to explore new behaviors in supercooled nanofluidic systems.

Chapter 3

Understanding Interfacial Transport

> *"**La lettre E représente une constante dont la valeur sera donnée par l'expérience, d'après la nature de la paroi et du fluide**, et qui peut être regardée comme la mesure de leur action réciproque. [...] Il est essentiel de remarquer d'ailleurs, qu'en admettant l'exactitude des expériences connues sur le mouvement uniforme de l'eau dans les canaux découverts et les tuyaux servant à la conduite des eaux, il résulte de la nouvelle théorie exposée dans ce Mémoire, que la supposition d'un mouvement linéaire n'est point propre à représenter complètement les phénomènes de ce mouvement, à l'exception des cas où le diamètre des tuyaux est très petit."*
>
> Claude Navier, *Mémoire sur les lois du mouvement des fluides* 1823

Contents

3.1 Introduction

We have seen in the previous chapter that, as the channel size decreases, interfacial properties have an increasingly important role. We discussed that an interfacial characteristic of special concern at the nanoscale is the existence of a velocity jump v_{slip} ("slippage") at the liquid-solid interface [25, 227, 99]. We also discussed that the simplest approach to describe slip, initially proposed by Navier [19], is through the Navier or partial slip

boundary condition:

$$v_{\text{slip}} = b \left. \frac{\partial v}{\partial z} \right|_{z=z_s}, \tag{3.1}$$

defining, at the effective wall position z_s [185], the slip length $b = \eta/\lambda$ with η the shear viscosity and λ the liquid-solid friction coefficient.

On the modeling side, several efforts have been pursued in order to understand the molecular mechanisms that control friction, with special interest on the relation between the friction coefficient and the time autocorrelation of the force exerted by the liquid on the wall, *i.e.* its Green-Kubo relation [122, 123, 125, 126, 228, 120, 229, 230]. Yet a large number of questions with regard to the interface properties, such as its viscoelastic or purely viscous nature [101, 54, 231] or the possible link with its interfacial thermal transport counterpart via wall's wetting properties [48, 127, 128], remain open nowadays, limiting the perspectives for a rational search of optimal interfaces. And, thus, these are the questions we would like to tackle in the present chapter: first, how can we understand the molecular mechanisms that control viscosity and friction, and how can we explain the unexpected increase of slip on the supercooled water regime presented in the previous chapter. Second, how can we control the thermal transport properties at the interface. The general goal is to obtain a better understanding of both hydrodynamic transport (of momentum) and thermal transport (of heat) processes which, although driven by different physical processes, present similar characteristics as a velocity or temperature jump at the interface, which can be boosted to design novel surfaces and materials with interesting applications in anti-icing coatings or controlling vapor explosions in nuclear power plants.

But let's first introduce the main physical concepts, starting with hydrodynamic transport, that will allow us to improve our understanding of the molecular mechanisms taking place at the interface.

3.2 Interfacial hydrodynamic transport

We finished the previous chapter by reporting a strong increase of slip for water when entering in its supercooled regime, up to a factor of ~ 2 for Lennard-Jones (LJ) walls and of ~ 5 for graphene walls. Can we rationalize such fast increase in terms of physical quantities? And the different enhancement values observed for the two wall types? In the present section, starting from the Green-Kubo expressions for viscosity and friction, we explain the anomalous slip behavior in the supercooled regime by a decoupling between viscosity and bulk density relaxation dynamics, and we rationalize the wall-type dependence of the enhancement in terms of interfacial density relaxation dynamics. While providing fundamental insights on the molecular mechanisms of hydrodynamic transport in both interfacial and bulk water in the supercooled regime, we will see that our study [56] is relevant to the design of anti-icing surfaces and could help explain the subtle phase and dynamical behaviors of supercooled confined water, paving the way to explore new behaviors in supercooled nanofluidic systems.

3.2.1 Green-Kubo expressions

Transport coefficients can be determined from equilibrium molecular dynamics simulations via fluctuation-dissipation relations, by considering that the disturbance in a system created by a weak external perturbation decays in the same way as a spontaneous fluctuation in equilibrium. Such relations are the Green-Kubo (GK) formulas, and they are

based on linear response theory, which establishes the link between time correlation functions at equilibrium and the response to weak perturbations. Different GK relations have been derived for several transport coefficients, such as electrical and thermal conductivity, polarization, diffusion, etc [145, 232, 146]. In the case of shear viscosity, its GK relation writes:

$$\eta = \frac{V}{k_{\mathrm{B}}T}\int_0^\infty \langle p_{ij}(t)p_{ij}(0)\rangle \,\mathrm{d}t, \tag{3.2}$$

with V the volume, k_{B} the Boltzmann constant, T the temperature and p_{ij} the independent traceless components of the pressure tensor: p_{xy}, p_{xz}, p_{yz}, $(p_{xx}-p_{yy})/2$ and $(p_{yy}-p_{zz})/2$ [233]. The general methodology to measure the transport coefficient from GK expressions is to plot the running integral as a function of time and to measure the plateau value for long times. In Fig. 3.1a we observe the typical shape of the GK running integral, and how the time it takes to reach the plateau (*i.e.* the GK relaxation time τ_{GK}) can increase significantly when lowering the temperature. The validity of the results can be assessed by comparing the GK measures with shear-flow measurements. In Fig. 3.1b we can see that equivalent results were obtained in the case of water from non-equilibrium (shear flow) and equilibrium (GK) methods, with small discrepancies for the lowest temperatures. In terms of relaxation times, we can define τ_{GK} by decomposing Eq. (3.2) as $\eta = (V/k_{\mathrm{B}}T)\left\langle p_{ij}^2(0)\right\rangle \tau_{\mathrm{GK}}$, with

$$\tau_{\mathrm{GK}} = \frac{\int_0^\infty \langle p_{ij}(t)p_{ij}(0)\rangle \,\mathrm{d}t}{\left\langle p_{ij}^2(0)\right\rangle}. \tag{3.3}$$

Maxwell model for viscosity states that $\eta = G_\infty t_{\mathrm{Maxwell}}$, where we can identify

$$G_\infty = \frac{V}{k_{\mathrm{B}}T}\left\langle p_{ij}^2(0)\right\rangle, \tag{3.4}$$

with G_∞ the infinity frequency shear modulus and $t_{\mathrm{Maxwell}} \equiv \tau_{\mathrm{GK}}$ the Maxwellian relaxation time. Under this description, G_∞ identifies with bulk's static part and it is typically considered to be constant with temperature, so the temperature evolution is simply described by the assumption $\eta \propto \tau_{\mathrm{GK}}$ [234]. It is common to find in the literature [235, 204, 206, 236] an identification of τ_{GK} with the structural relaxation time τ_α, obtained from the fitting of the self-intermediate scattering function by an exponential or stretched-exponential decay. In particular, this assumption is often used to study, for supercooled liquids (typically water), the validity of the Stokes-Einstein relation between viscosity η and diffusion D:

$$D = \frac{k_{\mathrm{B}}T}{6\pi\eta R_{\mathrm{h}}}, \tag{3.5}$$

with R_{h} the hydrodynamic radius; *i.e.* the validity of the approximation $\eta \propto \tau_\alpha$ or, analogously, $D \propto T/\tau_\alpha$ [204, 206]. As in contrast to the Maxwell model, other authors considered the so-called Gaussian approach [234, 236], consisting in considering the Gaussian solution to the diffusion equation so $D = 1/(q^2\tau_\alpha)$, *i.e.* $D \propto 1/\tau_\alpha$ and, by applying the Stokes-Einstein relation, $\eta \propto T\tau_\alpha$ [237, 235, 238]. Nevertheless, the identification of τ_α with τ_{GK} is a delicate issue, first because both relaxation times present different temperature evolution and second because the assumption of G_∞ to be temperature independent fails for low T [234]. Therefore, an alternative description of η in terms of relaxation times and T dependence should be proposed.

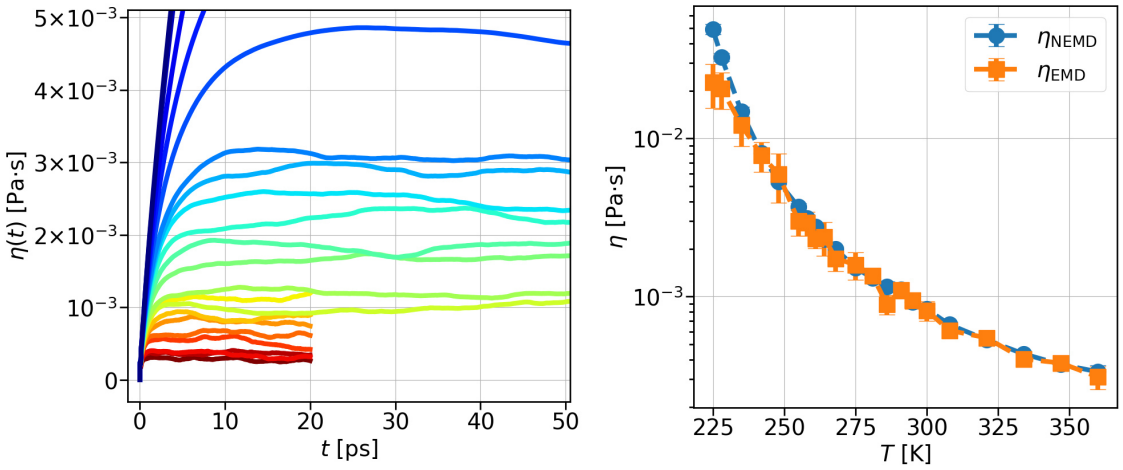

(a) (b)

Figure 3.1: (a) GK running integrals of viscosity, averaged over the independent components of the traceless stress tensor, for different temperatures (warmer colors correspond to higher temepratures). (b) Shear viscosity measures comparison obtained from non-equilibrium methods (NEMD, shear flow) and equilibrium (EMD, Green-Kubo) for different temperatures (from 225 K to 360 K).

As in the case of viscosity, the liquid-solid friction coefficient λ can also be related to the autocorrelation of the equilibrium force at the interface through a GK formula [122, 124]:

$$\lambda = \frac{1}{S_{\text{wall}} k_{\text{B}} T} \int_0^\infty \langle F(t) F(0) \rangle \, \mathrm{d}t, \tag{3.6}$$

where S_{wall} is the surface area, k_{B} the Boltzmann constant, T the temperature and F the force applied by the fluid on the wall. In Ref. 137, Bocquet and Barrat proposed a decomposition of the friction coefficient in different static and dynamical quantities:

$$\lambda \simeq \frac{S\left(q_{\parallel}\right)}{2D\left(q_{\parallel}\right) k_{\text{B}} T} \int_0^\infty \rho(z) V_{\text{FS}}^2(z) \, \mathrm{d}z, \tag{3.7}$$

where $S\left(q_{\parallel}\right)$ is the 2D structure factor in the contact layer, evaluated at the shortest wave vector of the solid surface $q_{\parallel}$, $\rho(z)$ is the fluid number density, V_{FS} the amplitude of the first mode of the Fourier decomposition of the fluid-solid potential energy, and $D\left(q_{\parallel}\right)$ is the collective diffusion coefficient. $D\left(q_{\parallel}\right)$ can be expressed as $D\left(q_{\parallel}\right) = 1/\left(q_{\parallel}^2 \tau_\rho\right)$ where τ_ρ is the relaxation time of the intermediate scattering function $F\left(q_{\parallel}, t\right)$:

$$\tau_\rho = \int_0^\infty F(q,t) \, \mathrm{d}t = \int_0^\infty \frac{\left\langle \rho_{q_{\parallel}}(t) \rho_{-q_{\parallel}}(0) \right\rangle}{\left\langle \rho_{q_{\parallel}}(0) \rho_{-q_{\parallel}}(0) \right\rangle} \mathrm{d}t. \tag{3.8}$$

We can then rewrite Eq. (3.7) in terms of τ_ρ and the force corrugation $f_{q_{\parallel}}(z) = q_{\parallel} V_{\text{FS}}(z)$ as a product of static ("STAT") and dynamical ("DYN") terms of the form:

$$\lambda \equiv \lambda_{\text{STAT}} \cdot \lambda_{\text{DYN}}, \tag{3.9}$$

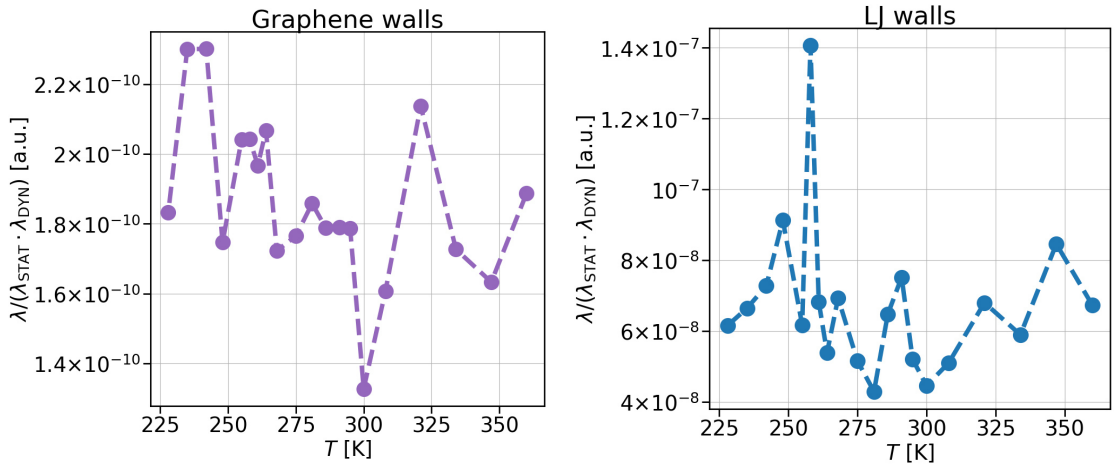

(a) Graphene walls

(b) LJ walls

Figure 3.2: Ratio between the friction coefficient λ measured from non-equilibrium simulations and the theoretical decomposition in static λ_{STAT} and dynamic λ_{DYN} contributions from Eq. (3.9). We can observe that the ratio remains constant with temperature, implying a correct qualitative description of λ temperature dependence by Eq. (3.9).

with

$$\begin{aligned} \lambda_{\mathrm{STAT}} &\approx S(q_{\parallel}) \int_0^{\infty} \rho(z) f_{q_{\parallel}}^2(z)\, \mathrm{d}z, \\ \lambda_{\mathrm{DYN}} &\approx \frac{\tau_\rho}{2k_{\mathrm{B}}T}. \end{aligned} \tag{3.10}$$

Note that we included the $1/(k_{\mathrm{B}}T)$ term of the GK integral in the dynamical part; we will come back to that choice later. It is interesting to note that in Bocquet and Barrat's paper, for a Lennard-Jones (LJ) fluid, only one single decay time for the density autocorrelation is considered, *i.e.* $\tau_\rho \equiv \tau_\alpha$, while in the case of water we will see that it is of great importance for a full description to consider the total decay time, obtained as the weighted sum of the two different decay times of $F(q,t)$ [195].

We can test the validity of Eq. (3.9) by plotting the ratio $\lambda/(\lambda_{\mathrm{STAT}}\cdot\lambda_{\mathrm{DYN}})$ for the water-friction results presented in Chapter 2. In Fig. 3.2 we can observe that for graphene and LJ walls this ratio remains constant with temperature, verifying the suitability of Eq. (3.9) as a qualitative decomposition of friction static and dynamic contributions temperature evolution. Note that in Fig. 3.2 we can see that Eq. (3.9) failed to reproduce λ quantitatively. This is reminiscent of similar quantitative discrepancies reported in previous work using analogous approximations of the full GK expression of λ [40, 193].

3.2.2 Friction static and dynamic contributions

In the previous Chapter 2, we presented a quantitative study about the friction and slip temperature dependence for water and methanol confined between graphene and LJ walls. From this study, two main questions remain to be understood. First, what is the main physical parameter that controls the temperature evolution of the friction coefficient? Second, why bulk and interface have similar temperature dependence at high temperatures and why they do not at the lower ones? In this section we will focus on water to address these questions and to explore, in particular, the effect of supercooling.

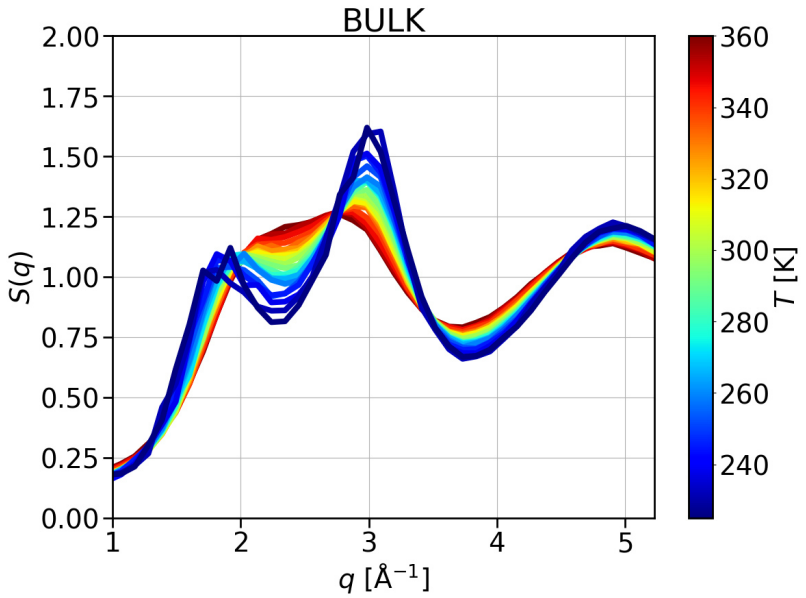

Figure 3.3: Temperature evolution of the static structure factor of bulk water. One can observe a small temperature dependence of the maximum of $S(q)$ located at $q \sim 3\,\text{Å}^{-1}$ as well as the separation of a secondary peak at a lower wave vector q when lowering the temperature.

In order to better understand the molecular mechanisms that control friction temperature dependence, let's start from λ decomposition Eq. (3.9), and study the temperature evolution of the different static and dynamic quantities at the contact layer and how do they compare to the bulk ones. The contact layer was defined as the interfacial liquid region between the wall and the first non-zero minimum of the liquid's density profile, $z_{\text{c.l.}}$.

a. Static terms

Let's start studying the static terms in Eq. (3.9). With regard to the temperature dependence of the static structure factor $S(q)$, in Fig. 3.3 we can observe for bulk the separation of a secondary peak from the absolute maximum for low wave vectors q when the temperature is lowered, in agreement with previous work [239]. We also see a small dependence on temperature of the maximum of $S(q)$, located around $3\,\text{Å}^{-1}$. Analogously, with regard to the interface, we can also see in Fig. 3.4 a small temperature dependence of the maximum of $S(q)$, located in a similar wave vector for both interfaces and close to the bulk value. Nevertheless, for the interface, it is not the $S(q)$ value corresponding to the maximum which should be taken into account to study friction temperature dependence, but the one corresponding to the wall lattice vector $q_{\parallel}$, with $q_{\parallel} = 2\pi/d_{\text{LJ}} = 1.66\,\text{Å}^{-1}$ (d_{LJ} is the equilibrium distance between LJ particles, corresponding to the lattice parameter of the elementary cell of the 2D fcc surface), and $q_{\parallel} = 2\pi/d_{x,\text{GR}} = 2.55\,\text{Å}^{-1}$ ($d_{x,\text{GR}}$ is the lattice vector in the x direction for the graphene surface). Both surface wave vectors are represented with dotted black lines in Fig. 3.4, where we can see that $S(q_{\parallel})$ can be considered constant with temperature.

With regard to the corrugation force, for graphene walls, we took $f_{q_{\parallel}}$ values from Ref. 40, which are well described by a fit, in arbitrary units, of the form $f_{q_{\parallel}} = B\,\exp(-Az)$, with $A = 5.33\,\text{Å}^{-1}$. For LJ walls, an analytical expression for the force corrugation was

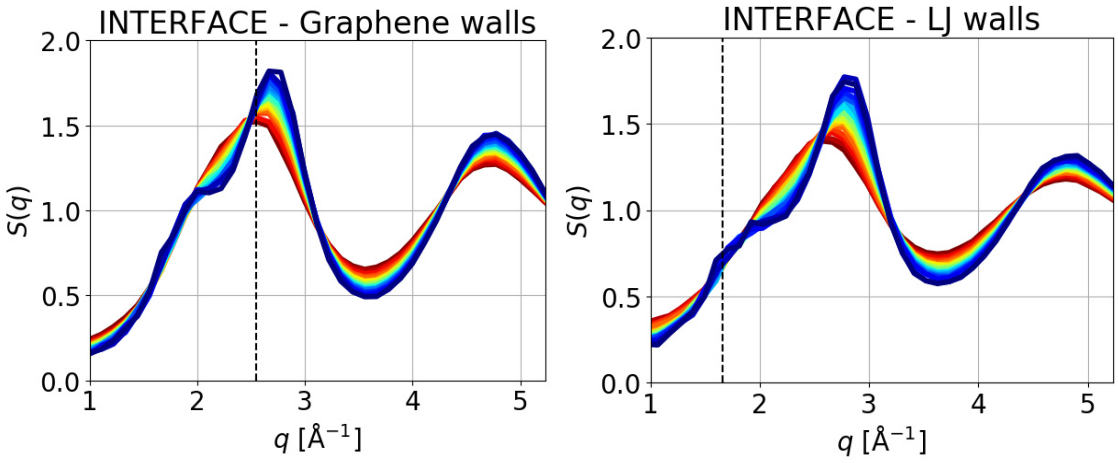

(a) Graphene walls

(b) LJ walls

Figure 3.4: Temperature evolution of the static structure factor for water on (a) graphene and (b) LJ walls; computed in the interfacial region, defined as the liquid region between the wall and the first non-zero minimum of the liquid density profile. Black dashed lines correspond to the shortest wave vector of the solid surface, $q_{\parallel}$. We can observe that $S(q_{\parallel})$ remains constant with temperature. Temperature coloring scheme is the same as in Fig. 3.3.

derived in Ref. 240. In this case,

$$f_{q_{\parallel}}(z) = \frac{4\pi}{d_{\mathrm{LJ}}}\varepsilon_{\mathrm{LJ}}E_1(z), \tag{3.11}$$

where

$$E_1(z) = 2\pi A^6\left[\frac{A^6}{30}\left(\frac{\pi d_{\mathrm{LJ}}}{z}\right)^5 K_5\left(\frac{2\pi z}{d_{\mathrm{LJ}}}\right) - 2\left(\frac{\pi d_{\mathrm{LJ}}}{z}\right)^2 K_2\left(\frac{2\pi z}{d_{\mathrm{LJ}}}\right)\right]; \tag{3.12}$$

where K_n is the modified Bessel function of the nth kind, $\varepsilon_{\mathrm{LJ}}$ and σ_{LJ} the LJ interaction energy and size between liquid and solid atoms, d_{LJ} the equilibrium distance between solid atoms, and $A = \sigma_{\mathrm{LJ}}/d_{\mathrm{LJ}}$. The force corrugation is represented as a function of distance in Fig. 3.5 for both walls, where we can observe a strong decay when increasing the distance from the wall z.

The other structural parameter needed to compute the integral in Eq. (3.9) is the number density profile for the oxygen atoms in the water molecule. Its evolution with temperature can be found in Fig. 3.6 where we observe, for LJ walls, a noisy region of the density profile close to the wall. Such noise, which strongly increases when getting closer to the wall, becomes significant for the highest temperatures when it is multiplied by the force corrugation squared, as we can observe in Fig. 3.7b in dashed lines. In order to decrease this noise, we considered a density behavior close to the wall as $n_{\mathrm{dens}} = A\,\exp(-B/z^n)$, and fitted this function for the LJ walls, obtaining $n \sim 2.5$. We can appreciate in Fig. 3.7b in continuum line the results considering the fitted density profile for LJ wall. No density profile correction was needed for graphene walls, Fig. 3.7a.

In Fig. 3.8b we can compare, for LJ walls, the original data with the fitted results integrals. We see that the main difference between both data sets are for the two highest temperatures (the noisiest ones, $T = \{347, 360\}$ K) while the fitting procedure describes well the rest of the results. In Fig. 3.8 we can observe, for both walls, two different temperature behaviors of the static integral. For the highest temperatures it behaves as a

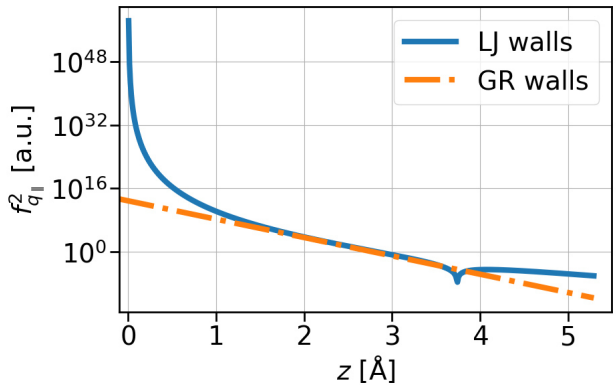

Figure 3.5: Squared force corrugation $f^2_{q_\parallel}(z)$, in arbitrary units, as a function of the distance from the wall for LJ walls and graphene.

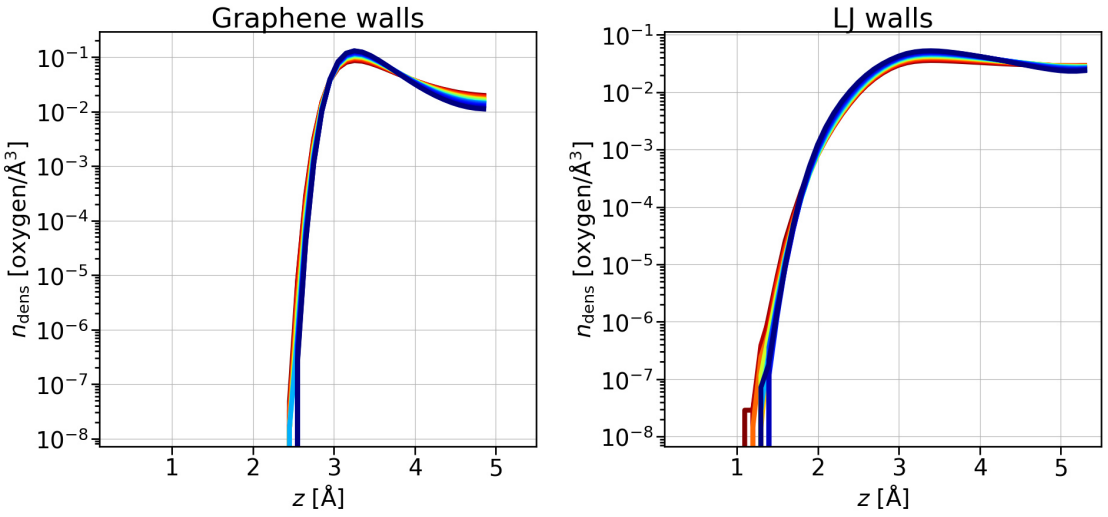

(a) Graphene walls

(b) LJ walls

Figure 3.6: Oxygen number density profiles for (a) water-graphene and (b) water-LJ walls (b) respectively, with the surface wall atoms located at $z = 0\,\text{Å}$, with log scale for the density. Temperature coloring scheme is the same as in Fig. 3.3.

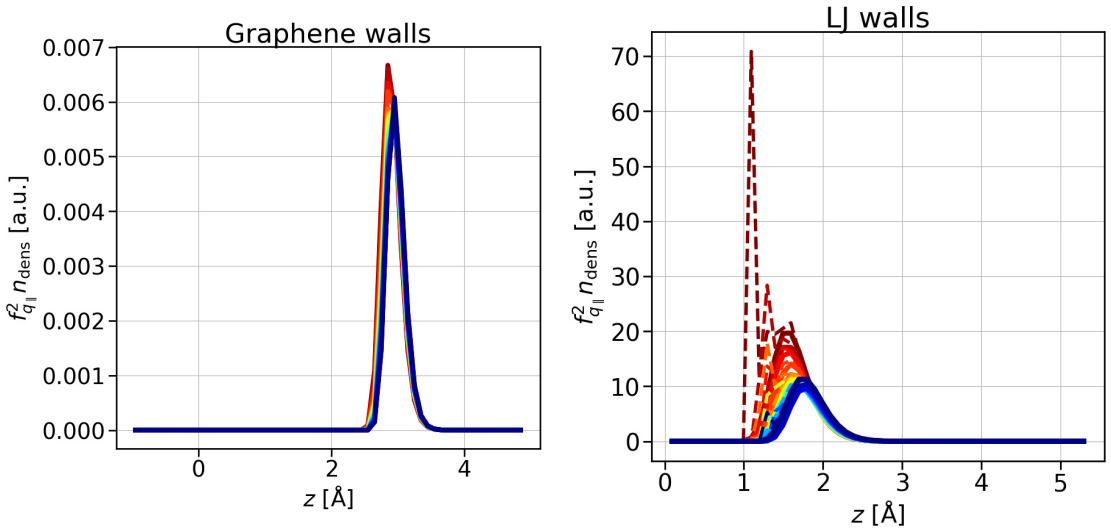

(a) Graphene walls

(b) LJ walls

Figure 3.7: Product of oxygen number density n_{dens} and the squared force corrugation $f_{q_\parallel}^2$, in arbitrary units, as a function of the distance from the wall surface located at $z = 0$ Å, for (a) graphene and (b) LJ walls respectively, for different temperatures. For LJ walls, the original data are represented in dashed lines, and in continuum line are represented the results of fitting the density at short distances as $n_{\mathrm{dens}} = A\exp(-B/z^n)$, in order to remove the noise. No fit was needed for graphene walls, and the original data are represented in continuum line.

power law of the form bx^a, with $a \sim 0.5$ for graphene and $a \sim 3$ for LJ walls. Accordingly, the main static contribution to friction T dependence comes from the integral in Eq. (3.9). For both surfaces, the integral remains constant at low temperatures, and it increases by at most a factor of 2 at higher temperatures. This tendency can be explained by the spreading of the atoms in the contact layer towards the wall due to larger thermal fluctuations; indeed $f_{q_\parallel}(z)$ decreases very fast with z, so that the integral of the static part is dominated by a small fraction of the atoms in the contact layer that are the closest to the wall.

b. Dynamical terms

Overall, the temperature behavior of λ_{STAT} is too weak to explain the exponential decrease of friction for increasing temperature. It is only left to check the dynamical contribution from Eq. (3.9), enclosed in τ_ρ. To measure this parameter we fitted the intermediate scattering function (Fig. 3.9), evaluated at the absolute maximum location $q_{\max}$ of the static structure factor for bulk [241] and at $q_\parallel$ for the interface, following Ref. 242:

$$F(q,t) = [1 - A(q)]\, e^{-(t/\tau_{\mathrm{s}})^2} + A(q)\, e^{-(t/\tau_{\mathrm{l}})^\gamma}, \tag{3.13}$$

considering two characteristic timescales: at short times with $\tau_\beta = \tau_{\mathrm{s}}\Gamma(1/2)/2$ and at long times with $\tau_\alpha = \tau_{\mathrm{l}}\Gamma(1/\gamma)/\gamma$, where $\Gamma(x)$ is the Euler function. The total relaxation time τ_ρ is then defined from Eq. (3.8) as $\tau_\rho = (1 - A(q))\tau_\beta + A(q)\tau_\alpha$.

An intuition on the physical meaning of the α and β relaxation times can be obtained, following Ref. 243, from the times corresponding to the different regimes of the mean squared displacement (MSD). In a fluid, the MSD can be separated into two regimes, one ballistic (without collision, where the MSD scales as t^2) at short times and another one

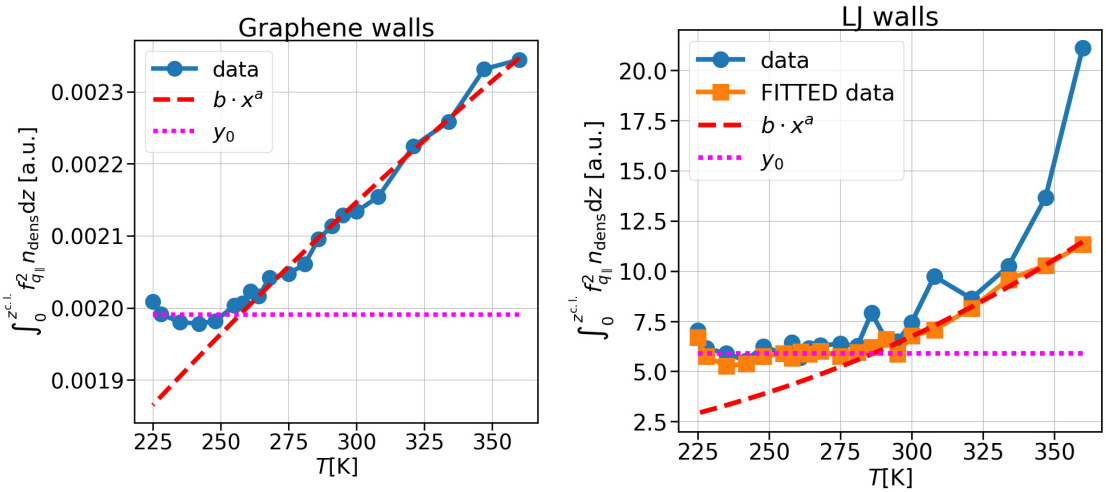

(a) Graphene walls

(b) LJ walls

Figure 3.8: Static part integral from Eq. (3.9) as a function of temperature for (a) water-graphene and (b) water-LJ walls respectively. For LJ walls the original and the fitted density data are plotted. One can observe that the fit is in agreement with the data except for the two highest temperatures, $T = \{347, 360\}$ K. In dashed lines are represented the fits for the two different temperature behaviors observed for both walls: a power law for high temperatures and a constant value at low temperatures.

diffusive (dominated by collisions, where the MSD scales as t) at long times. When the liquid is supercooled, a "plateau"-like regime appears at intermediate times, which becomes longer when lowering the temperature. Picturing the particle enclosed in a *cage* by its neighbors at intermediate times, such plateau region would correspond to a non-ballistic movement of the particle, that despite its collisions with its neighbors cannot escape the cage. This well-known behavior of the MSD remind us of the shape we observe for $F(q,t)$ in Fig. 3.9, which also presents an intermediate region between both decay times whose length increases when decreasing T. In this interpretation, this plateau would correspond to the particle vibrations within the cage, from which it eventually escape (the lower the temperature the longer the time it will take) at a time related to the α relaxation time, which should be T-dependent. In this picture, the β relaxation time would correspond to the time at which the particles start to feel their neighbors, *i.e.* to feel the cage. Thus, this short time should not be affected by the temperature.

Figure 3.10 shows the results for the different characteristic times for bulk and interface obtained from the fit in Eq. (3.13). We can see that τ_α and τ_β are similar at high temperature, but while τ_β remains constant with T, τ_α exponentially increases when lowering T, becoming the main contribution to τ_ρ in the supercooled regime. In Fig. 3.10a we can also observe a small but systematic difference between bulk and interfaces for τ_β. Nevertheless, because the main contribution at low temperatures for the total relaxation time is τ_α, in Fig. 3.10b we observe that τ_ρ is similar for bulk and the different interfaces. Overall, τ_ρ data are well described by a VTF law, analogously to friction (see Chapter 2), showing that the density relaxation is the main interfacial molecular mechanism that controls friction's temperature evolution. The VTF fit results for the total relaxation time τ_ρ are shown in Table 3.1.

With that regard, it is not obvious in previous work on bulk supercooled liquids [235, 204, 206, 234, 236, 244, 245] what time should the viscosity be related to, and different

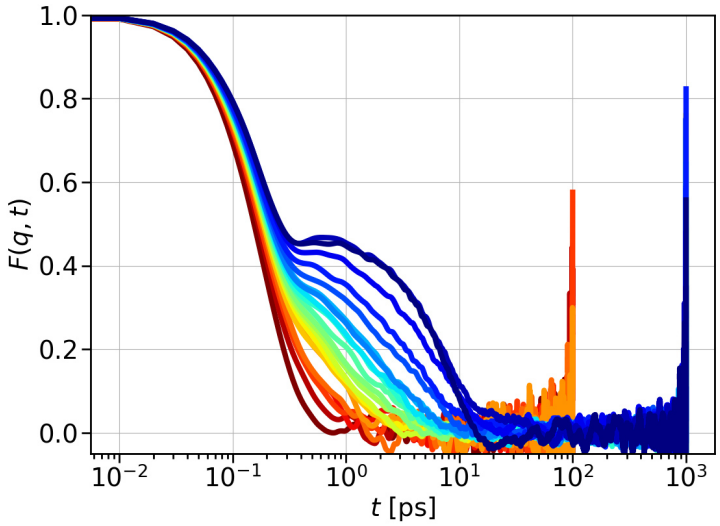

Figure 3.9: Intermediate scattering function $F(q,t)$ computed at the absolute maximum location $q_{\max}$ of the static structure factor for bulk water. The temperature coloring scheme is the same as in Fig. 3.3, with warmer colors corresponding to higher temperatures (temperature range from 225 K to 360 K).

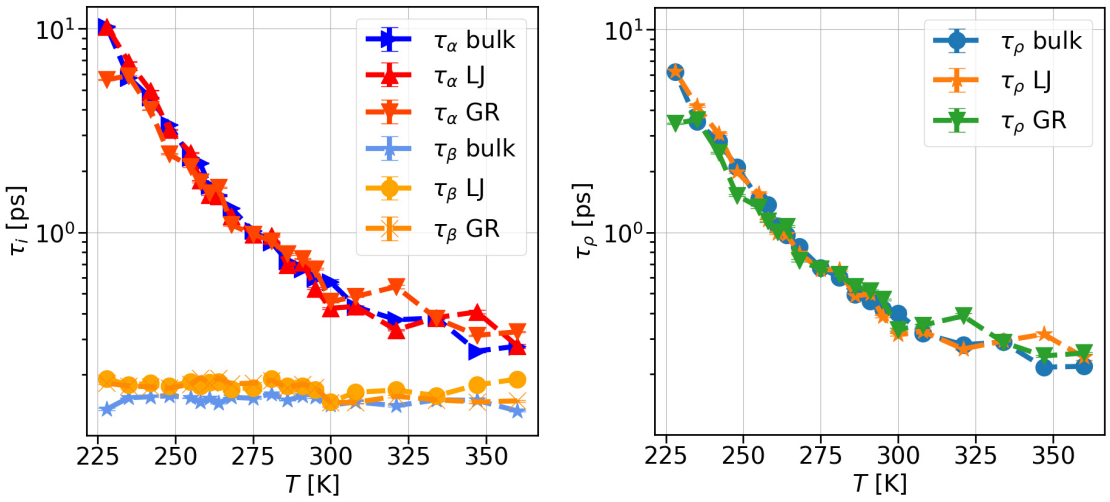

Figure 3.10: Characteristic times (a) τ_α, τ_β and (b) τ_ρ as a function of temperature for bulk water, water-LJ wall and water-graphene(GR) interfaces.

	TIP4P/2005 - VTF parameters		
	T_f (K)	A (K)	X_0 (ps)
τ_ρ bulk	165.69 ± 6.18	322.34 ± 41.23	$3.70 \cdot 10^{-2} \pm 3.70 \cdot 10^{-3}$
τ_ρ LJ walls	144.76 ± 22.49	578.63 ± 213.33	$2.06 \cdot 10^{-2} \pm 1.72 \cdot 10^{-2}$
τ_ρ graphene	157.78 ± 13.86	321.23 ± 83.51	$4.58 \cdot 10^{-2} \pm 1.70 \cdot 10^{-2}$

Table 3.1: Fit parameters of VTF law for the total relaxation time τ_ρ for TIP4P/2005 bulk water and at the interface with two different wall types, LJ walls and graphene.

approaches can be found in the litterature. On the one hand, the question of which characteristic time is the main contribution to viscosity temperature dependence remains open, *i.e.* whether the total decay time τ_ρ or only the long time behavior τ_α is needed. On the other hand, we can also wonder about the suitability of different approaches to measure the τ_α decay time. As discussed in Section 3.2.1; usually, only τ_α is considered, and typically an effective τ_α is defined as the time for which the self or coherent intermediate scattering function equals $1/e$ (*i.e.* assuming $\gamma = 1$ in Eq. (3.13); see $1/e$ approach in Fig. 3.11a). Nevertheless, a better agreement should be found with Eq. (3.13) by considering the weight $A(q)$ (τ_α from A/e approach in Fig. 3.11a). For friction, however, it is clear in the derivation of Eq. (3.9) that the total relaxation time τ_ρ should be used [195], and indeed we showed in Fig. 3.2 that Eq. (3.9) predicted correctly the temperature evolution of λ only when using τ_ρ. Different bulk relaxation times are compared in Fig. 3.11a, where we can see that, globally, viscosity exponential decay with temperature is captured by all the characteristic times measured from the different approaches. Nevertheless, large differences between the different proposed times are reported. Indeed, the approach $1/e$ fails as an approximation of the $F(q,t)$ fit, while more similar results were obtained when computing τ_α from the A/e approach. In order to distinguish subtle differences, in Fig. 3.11b we compare the different τ_α measurements with the characteristic time chosen to describe bulk dynamics in our work: τ_ρ. We can see that the temperature behavior of τ_α is different than the one of τ_ρ, specially in the supercooled regime, for any of the different approaches chosen, even for τ_α from the full $F(q,t)$ fit.

3.2.3 Slip length contributions

Once we understand the molecular mechanisms that control friction, it is interesting to address how do they compare with the ones that control bulk viscosity. In order to understand the temperature dependence of the slip length $b = \lambda/\eta$, we will decompose the viscosity into a static and a dynamic part in the same manner as for the friction coefficient: $\eta = \eta_{\mathrm{STAT}} \cdot \eta_{\mathrm{DYN}}$, with $\eta_{\mathrm{DYN}} = \tau_\rho^{\mathrm{B}}/(2k_{\mathrm{B}}T)$ (in analogy with the definition of λ_{DYN}), and $\eta_{\mathrm{STAT}} = \eta/\eta_{\mathrm{DYN}}$. The slip length can then be decomposed as follows:

$$b = \frac{\eta}{\lambda} = \eta_{\mathrm{STAT}} \frac{\eta_{\mathrm{DYN}}}{\lambda_{\mathrm{DYN}}} \frac{1}{\lambda_{\mathrm{STAT}}}. \tag{3.14}$$

Fig. 3.12 illustrates the temperature evolution of the three contributions to λ for water on LJ walls and graphene. In this figure, the lines are obtained from the ratios between VTF fits of the simulation results for η, λ, τ_ρ and τ_ρ^{B}; specifically, $\eta_{\mathrm{STAT}} \propto T\eta/\tau_\rho^{\mathrm{B}}$, $\eta_{\mathrm{DYN}}/\lambda_{\mathrm{DYN}} = \tau_\rho^{\mathrm{B}}/\tau_\rho$, and $\lambda_{\mathrm{STAT}} \propto T\lambda/\tau_\rho$. We can observe in Fig. 3.12 that $1/\lambda_{\mathrm{STAT}}$ increases when T decreases for both interfaces. The temperature variation of $1/\lambda_{\mathrm{STAT}}$ is slightly larger for LJ walls (a factor of ~ 2) than for graphene (a factor of ~ 1.5). As mentioned above, $1/\lambda_{\mathrm{STAT}}$ is controlled by $S(q_\parallel)$, which remains almost constant with temperature, and

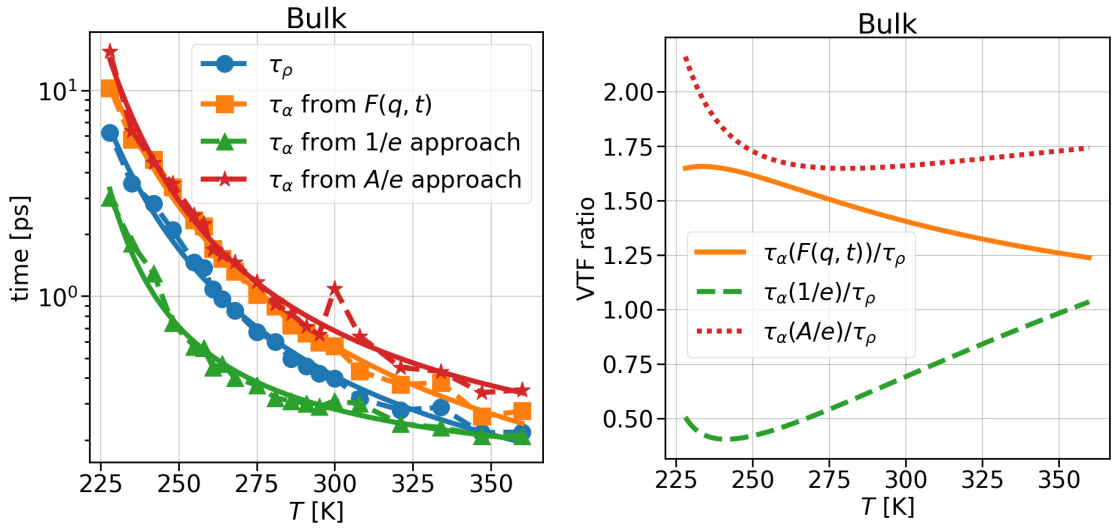

Figure 3.11: (a) Characteristic times measured from different approaches for bulk water as a function of temperature. In continuum lines are represented their respective VTF fits. (b) Characteristic times VTF fit ratio with respect to the characteristic time τ_ρ considered in this work.

by the integral $\int_0^\infty \rho(z) f_{q_\parallel}^2(z)\,\mathrm{d}z$, which increases when the atoms of the contact layer get closer to the wall under larger thermal fluctuations. Therefore, the stronger temperature variation of λ_{STAT} for the LJ walls can be related to the larger extension of the density profiles toward the wall at high temperatures. In bulk, η_{STAT} remains constant at high T, but it increases significantly when water enters in its supercooled regime, for $T < 273\,\mathrm{K}$, providing a large contribution (independent of the wall type) to the significant increase of b in the same T region. As a side note, following our choice to include $1/(k_{\mathrm{B}}T)$ in η_{DYN}, the fact that η_{STAT} is constant in the liquid state corresponds to $\eta \propto \tau_\rho^{\mathrm{B}}/T$; we suggest this correlation could replace more traditional ones used when studying supercooled liquids, $\eta \propto \tau_\alpha$ or $\eta \propto T\,\tau_\alpha$ (as discussed in Section 3.2.1).

Finally, to understand the relative increase of b by a factor ~ 2 for the LJ wall and by a factor ~ 5 for graphene, we looked at the dynamic ratio $\eta_{\mathrm{DYN}}/\lambda_{\mathrm{DYN}}$. In Fig. 3.12b, we can see that for LJ walls the interface relaxation time increases more (*i.e.* slower dynamics) when decreasing T than the bulk one, compensating the static contribution and resulting in a smaller variation of b. In contrast, for graphene, due to the surface smoothness, we see in Fig. 3.12a that there is no contribution from the wall to the slowing down of the interface dynamics with T when compared to the bulk dynamics. Therefore, as for the temperature dependence of λ, we conclude that also with regard to b it is not the interfacial structure which contribute to its different T evolution but the differences in dynamics, which we relate to the different interfacial corrugation at the contact layer. Such interfacial corrugation can be computed in terms of the free energy profile in the contact layer, as discussed in Ref. 45. In Fig. 3.13b we show the elementary cell free energy landscape F in the (x, y) plane for both graphene and LJ walls. In this case the free energy was computed from the relation

$$\Delta F = -k_{\mathrm{B}}T \ln[\mathcal{P}_{\mathrm{O}}(x, y)], \tag{3.15}$$

with $\mathcal{P}_{\mathrm{O}}$ the probability for an oxygen atom to be in the contact layer. Our results for graphene walls show good agreement with previous values obtained from first principles

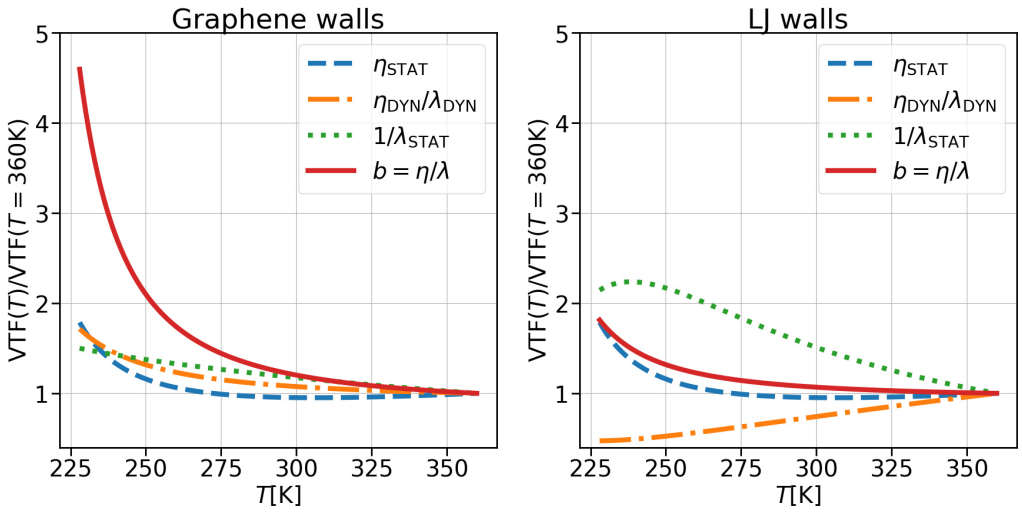

(a) Graphene walls (b) LJ walls

Figure 3.12: Temperature evolution of the static and dynamical contributions to the slip length $b = \eta/\lambda$ of water on (a) graphene and (b) LJ walls, normalized by the values at 360 K. The lines were obtained from VTF fits of the simulation results, see text for details.

calculations [45], and no temperature dependence was appreciated in $F(x, y)$ for any of the two walls considered. In Fig. 3.13 we can observe the surface smoothness of graphene when compared to the LJ wall, which presents larger free energy differences.

Before concluding, it is interesting to comment on a prediction for the temperature dependence of b introduced by Bocquet and Barrat in Ref. 99, who wrote that b should be proportional to $(k_B T)^2/\lambda_{STAT}$, which is in strong disagreement with our results. This formula can be derived from Eqs. (3.9) and (3.10) by relating the density relaxation time τ_ρ to the collective diffusion coefficient $D_{q_\parallel}$,

$$\tau_\rho = \frac{1}{q_\parallel^2 D_{q_\parallel}}; \tag{3.16}$$

so, in terms of temperature dependence, we obtain $\lambda \propto \lambda_{STAT}/(D_{q_\parallel} k_B T)$. With respect to bulk properties temperature dependence, the self-diffusion coefficient D_0 can be related to the viscosity through the Stokes-Einstein relation Eq. (3.5): $D_0 \propto k_B T/\eta$. Combining these two relations we obtain: $b = \eta/\lambda \propto D_{q_\parallel}(k_B T)^2/(D_0 \lambda_{STAT})$. Then, the authors identify the collective diffusion coefficient with the self-diffusion coefficient, $D_{q_\parallel} = D_0$, finally obtaining $b \propto (k_B T)^2/\lambda_{STAT}$. In Fig. 3.14 we show the different temperature evolution for both diffusion coefficients, with $D_{q_\parallel}$ computed from Eq. (3.16) and D_0 values taken from Ref. 216. However, while we found that indeed $D_{q_\parallel} \simeq D_0$ at room temperature, the diffusion coefficients temperature evolution is quite different, specially in the supercooled regime. Indeed, both diffusion coefficients arise from processes that happen at different scales and their relation is non-trivial: while $D_{q_\parallel}$ is related to collective diffusion in the sense that it is a function of all the atomic positions, D_0 is referred to the diffusion of one molecule of $2\,R_h$ size.

3.2.4 Conclusions

In order to understand the molecular mechanisms that control friction, we decomposed the friction coefficient λ into the product of a static contribution λ_{STAT} and a dynamical one

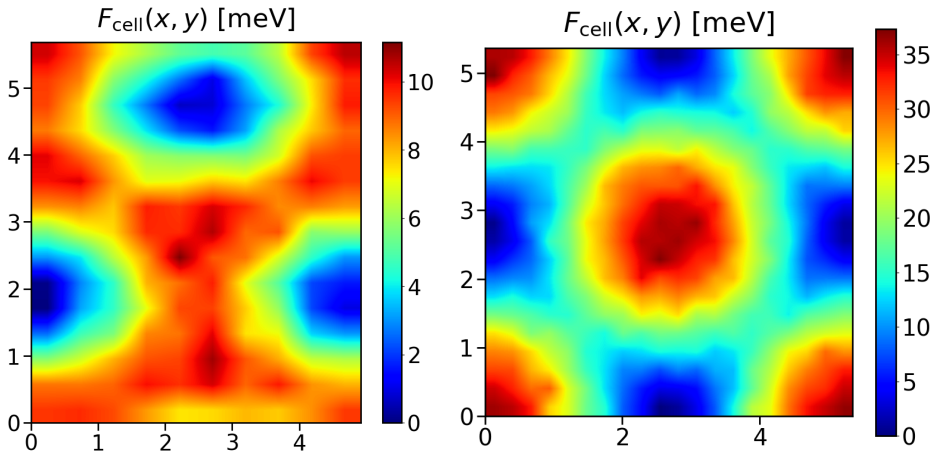

(a) Graphene wall (b) LJ walls

Figure 3.13: Free energy landscape in meV of the elementary cell in the (x, y) plane for (a) graphene walls and (b) LJ walls at 300 K.

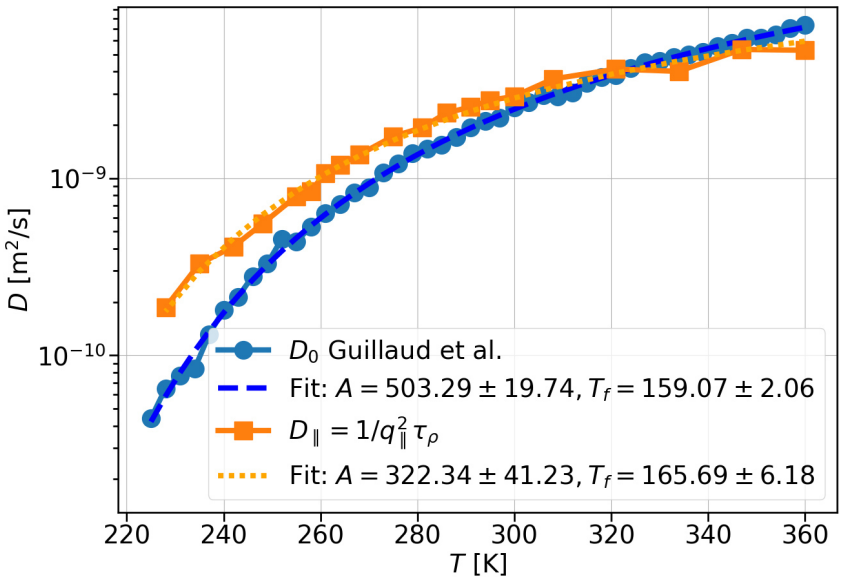

Figure 3.14: Self-diffusion coefficient D_0 from Ref. 216 and collective diffusion coefficient $D_{q_\parallel}$ as a function of the temperature. The respective fits by a VTF law are represented in continuum lines.

λ_{DYN}, in the form of an interface density relaxation time τ_ρ. We observed a small variation of the static part with T, but the main contribution to the temperature dependence of friction came from the dynamical term. In order to explain the temperature dependence of the slip length $b = \eta/\lambda$, we also decomposed the viscosity η into a static term η_{STAT} and a dynamical term η_{DYN}, controlled by the bulk density relaxation time τ_ρ^{B}. The slip length could then be decomposed into three contributions: first, the interfacial static contribution $1/\lambda_{\mathrm{STAT}}$; second, the bulk static contribution, η_{STAT}; and third, the ratio between the bulk and interfacial dynamical terms $\eta_{\mathrm{DYN}}/\lambda_{\mathrm{DYN}} = \tau_\rho^{\mathrm{B}}/\tau_\rho$. We observed that the viscosity static part, while it remained constant at high temperatures, increased significantly in the supercooled regime, representing a major contribution (independent of the wall type) to the slip length temperature evolution. We could finally relate the different slip length temperature dependence on LJ walls and graphene to the differences in interfacial dynamics on these two surfaces.

We suggest that the promising predictions presented here should be within reach of experimental verification, with the recent accurate characterization of liquid-solid slip on new 2D materials and their derivative [31, 191, 34, 192], and investigation of supercooled water dynamics down to very small temperatures [205, 207, 204, 225, 211, 107, 208], e.g. $\sim 230\,\mathrm{K}$ in bulk [107] and $\sim 130\,\mathrm{K}$ in confinement [225].

Moreover, beyond liquid-solid slip, many other new behaviors could arise in the promising field of supercooled nanofluidics. In particular, due to the high slip values obtained at ambient temperature for carbon nanotubes (CNT) [31], comparable to the ones of the present study for graphene at the lower temperatures, we find as an interesting perspective the study of the curvature effect in combination to the supercooling of the liquid. Additionally, nanopatterned superhydrophobic surfaces have shown increased slip compared to flat surfaces [246]. Exploring the effect of supercooling on slip at superhydrophobic surfaces therefore is another relevant venue.

Not only superhydrophobic surfaces are associated with large slippage but also with iceophobicity [212]. Thus, examining the coupling between ice nucleation and slippage at such interfaces may be a further direction to embark on, which could be relevant for the development of anti-freezing coatings. Indeed, one of the proposed mechanisms for hindering ice formation of water droplets on superhydrophobic surfaces is to ensure a minimal contact time between the bouncing droplet and the surface. It will be interesting to see whether the increase in water viscosity at low temperature would promote ice nucleation due to increased contact time of a bouncing droplet [247], or instead whether the increase in water slip (as observed here) would actually decrease the contact time [248], thus hindering ice nucleation. An additional mechanism at play on anti-icing coatings is that of retardation of ice nucleation due to the presence of air pockets between nanoscale patterns, which act as insulating layers [212], while the main reason for the increase in slip length observed in nanopatterned surfaces at room temperature is due to the absence of friction at the vapor–liquid interface [246]. Therefore, it would be interesting to understand whether the friction reduction at nanopatterned surfaces also slows ice nucleation at such interfaces. Further, in this work we found that the interfacial water dynamics is key to the increase in water slip under supercooled conditions. Because the microscopic dynamics of bulk water has been reported to influence homogeneous ice nucleation [226], it is possible that the interfacial dynamics may instead have an impact on heterogeneous ice nucleation.

Overall, we hope the findings obtained and presented in this section by investigating water friction as a function of temperature down to the supercooled regime, will help understanding generally the molecular mechanisms underlying both interfacial and bulk hydrodynamic transport in this fascinating liquid, and motivate experimentalists to find

protocols to measure water slippage under supercooling.

3.3 Interfacial thermal transport

When water is in contact with a solid heat source, if the solid surface is heated above the boiling point of water T_s, the fluid starts to dissipate a large amount of heat flux at the liquid-solid interface. This process is first characterized by nucleate boiling, when air bubbles start to form in the liquid at the interface. In this stage, the removal of heat flux is proportional to the number of bubble nucleation sites formed, and to the temperature difference with respect to T_s [249]. As the temperature and the heat flux increase, the number of vapor bubbles increase as well, covering a larger amount of the interface and acting as a thermal insulator due to the smaller vapor thermal conductivity when compared to the liquid one. This effect will lead to reaching a maximum critical heat flux at a given temperature after which, when increasing the temperature, the heat flux quickly decreases and the heat transfer is too fast for normal boiling to occur, producing a violent liquid-vapor transition, called explosive boiling. Controlling the appearance of such transition can be critical in preventing material damage due to vapor explosions, as may happen in nuclear power plants accidents [250].

A parallel treatment of macro- and nano-scale boiling have been already established experimentally [249], motivated by the high relevance of nanofluidics in the recent years. Seeking to prevent explosive boiling, the effect of texturing a superhydrophobic surface on the temperature at which explosive boiling occurs has also been studied experimentally [251], and it has been shown that the use of such surface can prevent violent film boiling by stabilizing a vapor layer separating the heated surface from the liquid (also known as Leidenfrost effect [252]). Molecular dynamics (MD) approaches to study explosive boiling have also been carried [253, 254] focusing in increasing the temperature at which explosive boiling occurs. For instance, it has been demonstrated for a planar gold surface and ethanol solution containing gold nanoparticles, that increasing the interfacial resistance significantly shifts to higher temperatures the temperature at which explosive boiling occurs when compared to the pure ethanol solution [255]. Also, the effect of roughness on water boiling has been assessed, showing a heat transfer enhancement during the explosive boiling process [254]. The main idea of these studies is to reduce the thermal conductance of the interface (or analogously increasing its thermal resistance), proportional to the heat flux dissipation of the system.

In the recent years, several works have sought to develop new materials and structures with high liquid-solid thermal interfacial resistance (so-called Kapitza resistance R). With that regard, there has been a general interest in understanding the different parameters that control R. Several experiments can be found studying thermal liquid-solid interfacial properties at the nanoscale, assessing the effect on heat transport of different gold nano-scale objects immersed on different solutions [256, 257], of water-solid interactions for walls with different wetting properties [258], or determining interfacial thermal transport properties for gold walls with different liquids such as water or ethanol [259, 260] as well as its enhancement through the insertion of self-assembled monolayers [261]. In addition, from a fundamental point of view, the physical processes controlling interfacial heat transfer between solid and fluid have also been addressed by developing different analytical models, allowing to correctly reproduce the differences in thermal resistance obtained for surfaces with different wettings [127], rationalizing the effect of the bonding strength and viscoelastic properties for water [262], or proposing coarse grained models, with applications for large scale systems modelling, which produce similar results for the conductance

than those obtained via atomistic simulations [263].

MD simulations have also been used to explore how R is related to different physical properties such as solid-liquid interaction energy [128, 264, 265] and roughness [264, 266, 267], the interfacial vibrational coupling [268, 269] or the liquid structure [255]. MD simulations have been the tool of choice to simulate a large variety of water-solid interfaces, such as carbon nanotubes [270] or planar gold-water or silicon-water interfaces [271], with good agreement within experimental results [258]. Of special interest has been the case of water-graphene systems [272, 273], where the proportionality of the thermal resistance to the number of graphene layers has been assessed (up to a threshold increase where R is constant with the number of layers, equivalent to a graphite wall) as well as how it is strongly dependent on the layering of water at the interface [274, 275]. Another way to employ graphene explored in MD simulations is to reduce the interfacial conductance of a material such as copper or silicon by intercalating graphene layers at the interface taking advantage of its high interfacial resistance [276, 277].

The originality of our work is to propose the use of a graphene sheet to cover the nanostructured surface of a solid (gold in our case) to trap air or vacuum at the graphene-solid interface and exploit their low thermal conductivity to achieve low interfacial conductance between water and gold. One alternative path to achieve high Kapitza resistance is the use of superhydrophobic surfaces which, in the case of Cassie (or fakir) state materials, present a high thermal resistance due to the air trapping between the liquid and the solid [278, 279, 251]. Nevertheless, such fakir states are characteristic of very non-wetting surfaces which can be obtained by special chemical treatments, limiting the choice of materials. Also, stability is another major problem of Cassie states, which are not very robust under variations of pressure or the presence of flows in the channel. Contrarily, as we will see, graphene coated nanopillars present an alternative which can be extended to a wide range of common materials, such as gold and copper, and graphene stability can be improved by adding a great number of graphene layers.

In this section, after assessing the stability of the suspended graphene state, which does not bend filling the gold nanopatterns, we verify that the conductance is proportional to the contact surface fraction of graphene and gold, with a smaller conductance for thinner nanopillars (bigger air bubbles trapped). After proposing a linear scaling law of conductance, arising from the idea of understanding the water-graphene and graphene-gold interfaces as a set of resistances connected in series, we verify a universal scaling of the resistance with the effective surface fraction related to the effective gold-carbon interactions. A huge Kapitza length ($\ell_K \sim 200$ nm, proportional to the Kapitza resistance) is measured for the smallest surface fraction, being two orders of magnitude larger than the one reported for water-planar gold interface in simulations [271] and experiments [258] ($\ell_K \sim 6$ nm) and one order of magnitude larger than the largest reported values (to our knowledge) in previous simulations on carbon nanotubes and graphite ($\ell_K \sim 30$ nm and $\ell_K \sim 50$ nm respectively) [270, 276]. The huge thermal resistance we obtain presents promising applications in delaying the temperature at which the boiling crisis occurs, and shows an alternative route to efficiently control thermal dissipation in nanofluidic systems.

3.3.1 Thermal transport equations

Although the physical processes that control thermal transport (*i.e.* of heat) are different than the ones controlling the hydrodynamic transport (*i.e.* of momentum), the fields characterizing both transports (temperature T for heat and velocity v for momentum) are described by equivalent Laplacian equations (heat equation and Stokes equation respectively). In Fig. 3.15 we can see that, as we generated a simple linear velocity profile in

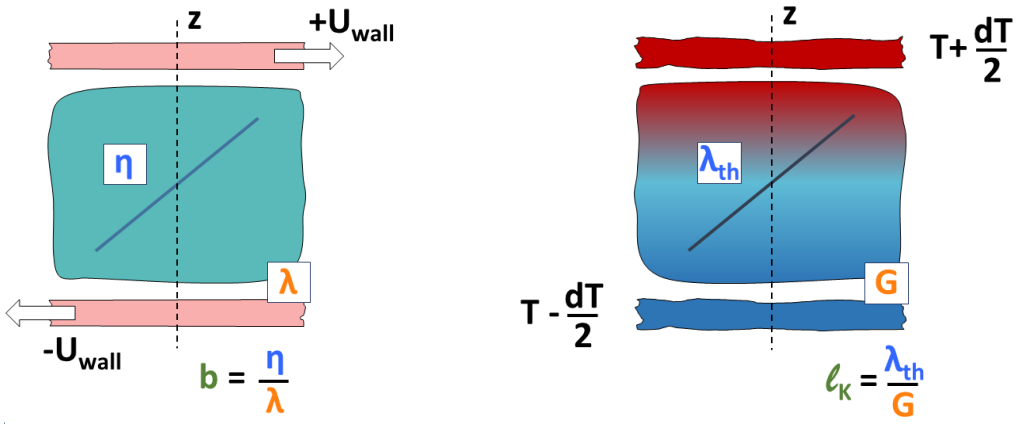

(a) Hydrodynamic transport

(b) Thermal transport

Figure 3.15: Hydrodynamic and thermal transport schematics. We can measure the hydrodynamic transport coefficients by applying a constant shear velocity U_{wall} generating a linear velocity profile in bulk. Analogously we can measure thermal transport coefficients by applying a difference of temperature dT between both walls generating a linear temperature profile in bulk.

the bulk by applying a constant shear velocity U_{wall} in opposite directions (Fig. 3.15a), an equivalent linear temperature profile (typically characterized by its derivative, the temperature gradient $\partial_z T$) is generated by applying a temperature difference dT between both walls (Fig. 3.15b). In the case of thermal transport, the coefficient that characterizes the bulk transport is the thermal conductivity λ_{th}, defined from the Fourier's law $j_{\text{h}} = -\lambda_{\text{th}}\partial_z T$, with j_{h} the heat flux density. With regard to the interface, which we will suppose located at z_{int}, a temperature jump ΔT occurs analogously to the velocity jump v_{slip} observed for hydrodynamic transport. As determined by Kapitza in 1941 [280], the interfacial thermal resistance (also known as Kapitza resistance) is then defined from the relation $j_{\text{h}} = (1/R)\Delta T$, which can be also described in terms of thermal conductance $G = 1/R$. Finally, both interfacial and bulk transport coefficients can be put together in one single equation by imposing continuity of the heat flux at the interface, obtaining:

$$\Delta T = \ell_{\text{K}} \left.\frac{\partial T}{\partial z}\right|_{z=z_{\text{int}}}, \tag{3.17}$$

defining at the interface position z_{int} (which by trivial extension of hydrodynamic transport equations can be proven to be determined in terms of a Gibbs dividing plane, see Chapter 2) the characteristic length $\ell_{\text{K}} = \lambda_{\text{th}}/G$, typically referred to as Kapitza length. The analogue equations between thermal and hydrodynamic transport are represented in Table 3.2.

3.3.2 Simulation details

a. Planar gold wall simulations

We performed MD simulations with the LAMMPS package [144] of TIP4P/2005 water [172] confined between different solid structures in order to determine the system configuration which better enhances interface thermal resistance. First, we enclosed 4096 water molecules between two parallel planar gold walls of dimensions $L_x = L_y = 58.422$ Å, structured as a FCC crystal with lattice parameter $a = 4.173$ Å. Periodic boundary conditions

Hydrodynamic transport	**Thermal transport**
Fields:	
velocity v shear stress τ	temperature T heat flux density j_h
In bulk:	
shear rate $\partial_z v$ shear viscosity $\eta = \tau/\partial_z v$	temperature gradient $\partial_z T$ thermal conductivity $\lambda_\mathrm{th} = j_\mathrm{h}/\partial_z T$
At the interface:	
slip velocity v_slip friction coefficient $\lambda = \tau/v_\mathrm{slip}$	temperature jump ΔT thermal conductance $G = 1/R$ thermal resistance $1/R = j_\mathrm{h}/\Delta T$
Boundary condition at the interface:	
$\tau = \eta\partial_z v = \lambda v_\mathrm{slip}$ $v_\mathrm{slip} = b\partial_z v$	$j_\mathrm{h} = \lambda_\mathrm{th}\partial_z T = (1/R)\Delta T$ $\Delta T = \ell_\mathrm{K}\partial_z T$
Characteristic lengths:	
slip length $b = \eta/\lambda$	Kapitza length $\ell_\mathrm{K} = \lambda_\mathrm{th}R$

Table 3.2: Hydrodynamic and thermal transport equations, disposed to highlight the mathematical analogy between both transports. z corresponds to the direction normal to the surface.

were set in the directions parallel to the wall. The gold-gold interactions were taken from Ref. 281, and the gold-water interactions from Ref. 282. For adding the supported graphene in our simulations with periodic boundary conditions, we had to change the gold wall lattice parameter for it to have the same dimensions than the supported graphene wall. With that regard, we run a planar gold-water simulations analogous to the previous one just changing the gold structure with new lattice parameters: $\{a_x, a_y, a_z\} = \{4.216, 4.260, 4.173\}$ Å, and wall dimensions $L_x = 59.028$ Å and $L_y = 59.640$ Å, in order to determine how this new wall structure affects interfacial thermal transport. After, we added graphene to the planar wall structure with the modified lattice parameters. The graphene wall dimensions were the same than for gold ($L_x = 59.028$ Å and $L_y = 59.640$ Å). Carbon-carbon interactions were modelled with the LCBOP force-field [283], carbon-water interactions from Ref. 40 and carbon-gold interactions from Ref. 284. The simulation details were the same for all the systems described above. A cutoff was applied to the Lennard-Jones interactions at 12 Å, and all the equations of motion were integrated using the velocity-Verlet algorithm with a simulation timestep of 1 fs. In all the simulations, we first performed an equilibration run of 0.9 ns where we settled the pressure to 1 atm, using the piston equilibration described in Chapter 2, so that the distance between the two innermost solid layers was $H \sim 38$ Å, with a well defined bulk region in the middle of the channel. During the first 0.3 ns of such equilibration we applied a Nosé-Hoover thermostat to the fluid and carbon atoms at $T = 300$ K and we turned it off afterwards. After, a production run of 0.5 ns was performed. In both simulation steps we applied a Nosé-Hover thermostat to all the wall atoms except the ones in the outermost layers which were frozen. The top and bottom walls were thermalized at $T \pm \mathrm{d}T/2$ respectively, with $T = 300$ K and $\mathrm{d}T = \{40, 60, 80\}$ K, which corresponded to the linear response regime as we verified.

Before performing the structured gold and supported graphene simulations, we checked the validity of our parameters choice by comparing the measured thermal transport coefficients with the ones obtained for equivalent systems in the literature. All the transport

system	λ_{th} $\left(\frac{\text{W}}{\text{K m}}\right)$	G $\left(\frac{\text{MW}}{\text{K m}^2}\right)$	ℓ_{K} (nm)	Δ (Å)
planar gold	$8.63 \times 10^{-1} \pm 5.14 \times 10^{-2}$	106.66 ± 1.84	8.10 ± 0.14	1.26 ± 0.02
gold modified	$8.05 \times 10^{-1} \pm 2.81 \times 10^{-2}$	117.23 ± 2.84	6.88 ± 0.16	0.75 ± 0.01
supported GR	–	51.76 ± 1.73	15.6 ± 0.05	1.58 ± 0.03

Table 3.3: Thermal transport coefficients measured for planar gold walls for three different system parameters: original FCC lattice (planar gold), modified lattice without supported graphene (gold modified) and modified lattice with supported graphene (supported GR). For this latter system λ_{th} couldn't be accurately determined and we considered the one measured for the gold modified system to determine ℓ_{K}.

coefficients were determined from three different values of temperature jumps dT between walls that belonged to the linear response regime, and three independent simulations (with three different initial configurations) were run for each temperature jump. Taking into account the symmetry of the system (so both top and bottom wall provide independent measures) a total of 18 independent measures were performed and the error bars were computed within 95% of confidence level. The interface position was considered at a distance Δ from the innermost solid layer, and it was determined from the density profiles using the Gibbs dividing plane approach (see Chapter 2). The simulation results can be found in Table 3.3, where we can observe that the bulk value of water thermal conductivity λ_{th} was the same (as it should be) for both planar gold and planar gold modified systems within the error bars, and it is in agreement with previous non-equilibrium measurements [285] and slightly higher than the experimental value obtained for bulk water, $\lambda_{\text{th}} \sim 0.6$ W/(K·m) [286]. Also, we observe that changing the lattice parameter of the planar gold wall has a minor impact on the conductance G and on the Kapitza length ℓ_{K}, where the value of 6.88 nm is in agreement with previous experiments [258] and simulation work for a gold-water interface modelled with different interaction parameters ($\ell_{\text{K}} \sim 6.5$ nm) [271]. Such Kapitza length was increased a factor of ~ 2.5 when adding a graphene layer supported on the planar (modified) gold walls (Table 3.3); which is an increase similar to the one observed for a graphene-coated copper structure (when compared with the no-graphene case) [276]. Because of the difficulty of accurately computing the thermal conductivity for systems with high Kapitza resistances (the temperature profile tends to be flat so it is difficult to determine its gradient precisely), we considered $\lambda_{\text{th}} = 8.05 \times 10^{-1} \pm 2.81 \times 10^{-2}$ W/(K·m), as we will do in the following.

b. Nanopatterned gold wall simulations

After testing our system parameters, we proceeded to nanopattern the gold wall (with the modified lattice parameters $\{a_x, a_y, a_z\} = \{4.216, 4.260, 4.173\}$ Å) by adding pillars to a planar gold base. Before determining the interfacial thermal transport and how it is affected by the pillar geometry, we performed preliminary tests by running MD simulations of a finite graphene sheet, supported on different gold structures. The objective was to test the stability of the suspended state and to make the pillar separation as big as possible while limiting graphene bending (see Fig. 3.16a). To avoid the graphene from sliding we adjusted the center of mass velocities in the x and y directions to cancel the linear momentum, preventing graphene to diffuse globally in those directions. Using this procedure, we verified that the graphene sheet was still able to bend for specific geometries. We observed that with holes of depth $\geq 3a_z = 12.519$ Å, the graphene layer did not bend for any $x - y$ separation between pillars. To check this statement we went to pillar separations of up to

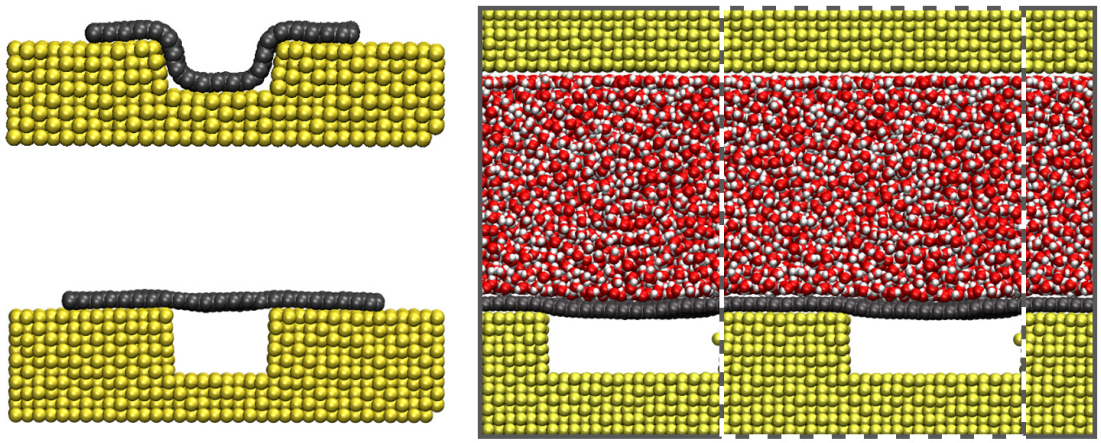

(a) (b)

Figure 3.16: (a) MD system snapshots of the graphene bending test for different gold nanopillars structures. The top figure corresponds to a pillar height of $2a_z$ and the bottom one to $3a_z$. (b) MD system representation of the graphene coated nanopillars system. The original simulation box is represented in white dashed lines.

$30a_x$ (126.48 Å), we also made some extra tests accounting for long-range interactions for the Lennard-Jones potential [287], and we finally confirmed that including water on top of graphene did not affect our results.

Because the graphene structure did not bend for holes deeper than $3a_z$, we decided to impose periodic boundary conditions for the graphene sheet. The system configuration, shown in Fig. 3.16b, consisted in water enclosed between a nano-structured gold surface coated with a graphene layer at the bottom, and planar gold at the top, used for piston equilibration. In this figure one periodic image is represented in order to illustrate the gold structure, and the original simulation box is represented delimited by dashed lines. The system equilibration and production run were the same as those described for planar gold simulations, with the exception that, to avoid graphene bending due to strong perturbations at the beginning of the simulation due to the piston equilibration, we froze it during the first 0.2 ns of the equilibration run. Afterwards we unfroze it and proceeded as detailed for planar gold for the rest of the simulation steps.

With regard to the gold wall structures, we imposed a pillar height of $3a_z$ (Fig. 3.17a) although, as we will see in the next section, equivalent results were obtained for taller pillars of height $6a_z$. Two different structure types were studied. First we explored the effect of 1D structures (Fig. 3.17b) for two different box sizes: $(L_x, L_y) = (14a_x, 14a_y)$ enclosing 5120 water molecules, and $(L_x, L_y) = (28a_x, 14a_y)$ enclosing 10240 water molecules. The width of the pillar l_x was varied between $3a_x$ and $20a_x$ in these simulations. Secondly, we explored the effect of 2D structures (Fig. 3.17c), where the system consisted in 10240 water molecules in a box size of lateral dimensions $(L_x, L_y) = (28a_x, 28a_y)$. The pillar area was imposed such as $\{l_x, ly\} = \{ma_x, ma_y\}$, with m varied between 6 and 9.

3.3.3 Results

The objective of our work is to establish the effect on interfacial heat transfer of texturing a gold surface with supported graphene on top. Let's recall that the main motivation of nanopatterning the gold surface is to reduce the conductance (*i.e.* to increase the resistance) between water and gold by maintaining a Fakir state between the graphene and the

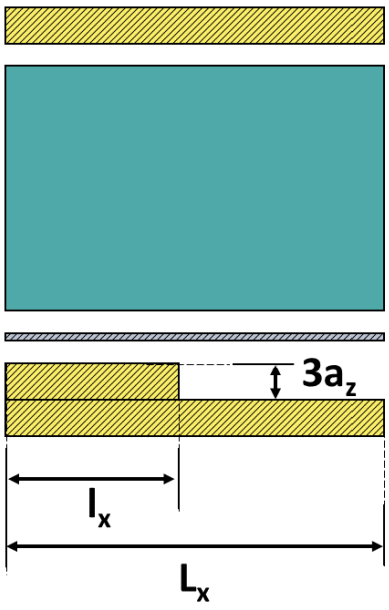

(a) Front view

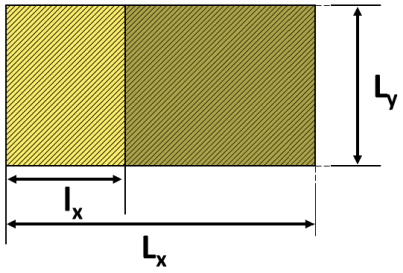

(b) Top view 1D structures

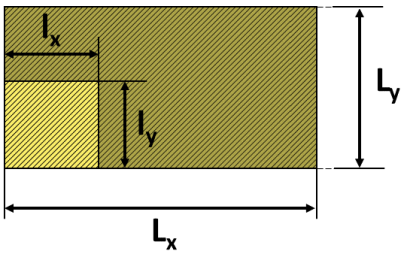

(c) Top view 2D structures

Figure 3.17: Illustration of the nanopillar structure. (a) Front view for 1D and 2D structures in the $x - z$ direction. The pillar height is $3a_z$ (a test was also performed for $6a_z$). (b) Top view of the 1D nanostructure were the surface fraction was varied changing the l_x parameter. (c) Top view of the 2D nanostructure where the surface fraction was varied changing l_x, l_y parameters.

gold walls exploiting the low thermal conductivity of air (or vacuum in our simulations). With that regard, we represent in Fig. 3.18a the measured water-gold (w-Au) conductance as a function of the graphene-gold contact surface fraction $\phi_s = l_x l_y/(L_x L_y)$. In this figure we can see that we measured the conductance for a large variety of 1D and 2D geometries, and that globally the decrease of the contact surface between gold and graphene decreases the efficiency of heat transfer due to the presence of vacuum as indicated above. We also observe equivalent results for different wall sizes, $14a_x$ and $28a_x$, for the 1D structures, as well as no effect of the pillar height (we varied it from $3a_z$ to $6a_z$). To analyze the different contributions to heat transfer between the three different systems (water at the carbon-gold interface), in Fig. 3.18b we show the Kapitza resistance $R = 1/G$ (for all the system geometries) obtained from the temperature jumps between the different groups. We observe that the water-carbon resistance is very low and not affected by the surface fraction, while the carbon-gold resistance mostly determined the total R between water and gold.

Once we assessed the interesting effect of the carbon-gold contact surface fraction on the transfer of heat, we propose a simple model in order to describe our results. We start from the continuity condition of the temperature jumps at the water-carbon-gold interfaces and that, by definition, $\Delta T_{\mathrm{w-Au}} = \Delta T_{\mathrm{w-C}} + \Delta T_{\mathrm{C-Au}}$ (with $\Delta T_{\mathrm{A-B}} = T_{\mathrm{B}} - T_{\mathrm{A}}$). Taking into account that the thermal resistance is given by $R = \Delta T/j_{\mathrm{h}}$ and that j_{h} is the same in the whole channel, it is then a necessary condition that the water-carbon and carbon-gold interfaces act as a pair of resistances connected in series, so for the planar gold wall $R_{\mathrm{w-Au}} = R_{\mathrm{w-C}} + R_{\mathrm{C-Au}}$. We can introduce the effect of the contact surface fraction by supposing that it will affect the carbon-gold thermal resistance as $R_{\mathrm{w-Au}}/\phi_{\mathrm{s,eff}}$, where $\phi_{\mathrm{s,eff}}$ refers to an effective surface fraction. Such $\phi_{\mathrm{s,eff}}$ intends to account for the extension

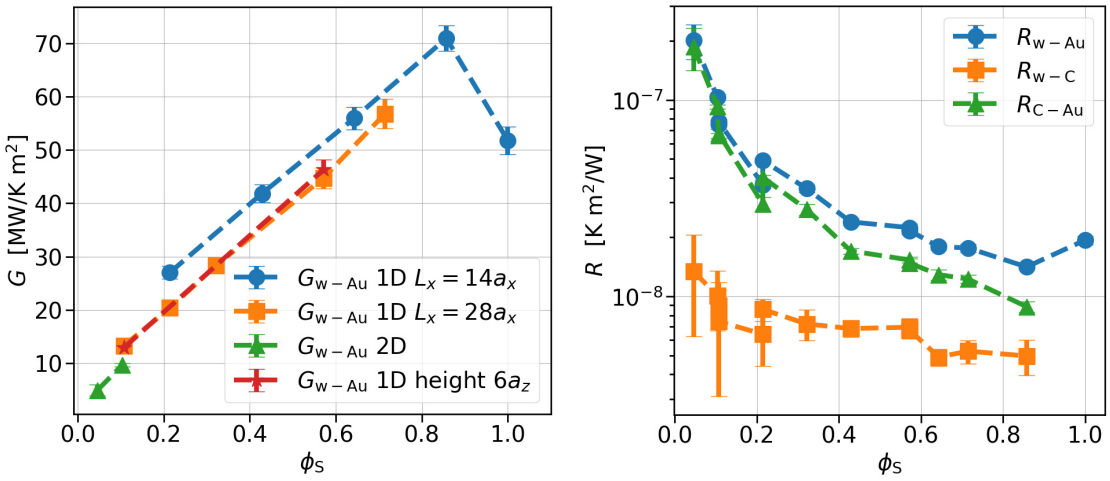

(a) (b)

Figure 3.18: (a) Total water-gold thermal conductance of the nanostructured system as a function of the graphene-gold contact surface fraction. The results are represented for different geometries including 1D pillars with different box sizes, 2D nanostructures and 1D structures with taller pillars. (b) Kapitza resistance $R = 1/G$ as a function of the surface fraction measured from the water-gold (circles), water-carbon (squares) and carbon-gold (triangles) temperature jumps.

of the graphene-gold surface of contact over a small distance r_c, related to the effective extension of the carbon-gold atomic interactions. In this way,

$$R_{w-Au} = R_{w-C} + \frac{R_{C-Au}}{\phi_{s,eff}}, \tag{3.18}$$

with $\phi_{s,eff}$ for a 1D structure:

$$\phi_{s,eff} = \frac{l_x + 2r_c}{L_x};$$

and $\phi_{s,eff}$ for a 2D structure:

$$\phi_{s,eff} \simeq \frac{(l_x + 2r_c)(l_y + 2r_c) - 4r_c^2}{L_x L_y};$$

where we subtract a $4r_c^2$ area to not overestimate the real r_c effect by just considering the rectangle area given by $(l_x + 2r_c)(l_y + 2r_c)$.

We fitted with Eq. (3.18) the $1/G_{w-Au}$ values represented in Fig. 3.18a. The fit results were $R_{w-C} = 3.84 \times 10^{-10} \pm 7.67 \times 10^{-10}$ Km^2/W, $R_{C-Au} = 1.42 \times 10^{-8} \pm 9.47 \times 10^{-10}$ (in agreement with the measured value for $\phi_s = 1$) and $r_c = 5.12 \pm 0.54$ Å. Although the error bars in the fitted water-carbon resistance are big, we can test the goodness of the fit by ploting the measured G_{w-Au} represented in Fig. 3.18a as a function of the effective surface fraction $\phi_{s,eff}$. The results for all the 1D and 2D structures are plotted in Fig. 3.19a. We can see that all the results collapse to the same curve with $r_c = 5.12$ Å, verifying the G_{w-Au} scaling with the effective surface fraction for the all the different geometries considered. In Fig. 3.18a we also observe a deviation from the fit for the point corresponding to $\phi_s = 1$ ($\phi_{s,eff} \sim 1.2$), corresponding to the planar gold wall case. Although we don't expect the fit in terms of effective surface fraction to work well for effective contact surfaces larger than 1, one could expect a plateau in G obtained for $\phi_{s,eff} > 1$. Nevertheless, this result is out

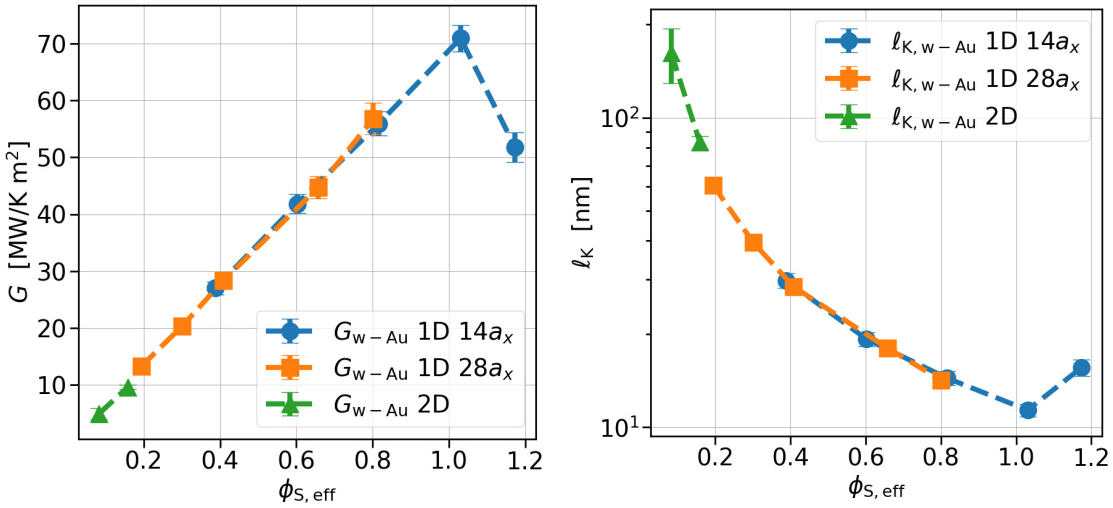

(a) (b)

Figure 3.19: Total water-gold (a) conductance G and (b) Kapitza length ℓ_K scaling with the effective graphene-gold contact surface area.

of the error bars for our measures, and further work should be carried out to understand the conductance decrease for this geometry with respect to the nanopatterned surface.

It is interesting to quantify the contribution of the graphene coated nanopillars in increasing the thermal resistance via the characteristic length of the system, the Kapitza length $\ell_K = \lambda_{th}/G$ with λ_{th} the thermal conductivity of water at 300 K (see Section 3.3.2). The objective of a large body of work in heat transfer is to find affordable structures with a large ℓ_K value. We see in Fig. 3.19b that the Kaptiza lengths measured in our system range from 10 to 200 nm, and even a higher ℓ_K can be predicted by lowering the effective surface fraction. We would like to highlight the great ℓ_K values obtained for our supported graphene simulations for the smallest $\phi_{s,eff}$. As far as we know, they are significantly higher than the exceptional values obtained for more complex structures, such as CNT with $\ell_K \sim 30$ nm for the most confined system [270] or $\ell_K \sim 50$ nm for graphite supported on planar copper [276]. Therefore, nanostructured coated systems are promising to realize interfaces with high Kapitza resistance.

3.3.4 Conclusions

We explored, via non-equilibrium molecular dynamics simulations, the effect on solid-liquid (gold and water) interfacial heat transfer of nanopatterning the solid wall and covering it with a graphene sheet. In the case of planar gold walls, we observed that the Kapitza length increased a factor of ~ 2.5 by adding a graphene layer at the gold-water interface, in agreement with previous results for copper-graphene-water interface [276]. The novelty of the presented work was to introduce nanopatterning to such wall, with the idea of exploring the effect of the wall roughness on thermal transport. First, we observed that graphene did not bend around the wall nanopillars for holes of depth greater than ~ 12.5 Å, independently of the pillar separation, trapping air bubbles between the gold and the graphene layer. Therefore, we performed non-equilibrium simulations of a graphene layer supported on nanopatterned gold with periodic boundary conditions in the directions parallel to the walls. We saw that nanopatterning the gold surface produced an increase of the interfacial Kapitza resistance R by vacuum trapping between both solid interfaces,

due to air's low thermal conductivity. Once we assessed this effect we studied the effect of the gold-graphene contact surface fraction on the resistance by defining an effective surface fraction which accounts for an extension r_c of the effective interactions between gold and graphene atoms. We modelled the total interfacial water-gold R as a set of resistances at the intermediate interfaces connected in series, with the carbon-gold R weighted by the inverse of the effective surface fraction. Measuring the partial resistances, we saw that the water-gold total R was mostly determined by the carbon-gold R, due to the very low water-carbon R (one order of magnitude smaller than for carbon-gold). We observed very good agreement of our results with the model for $r_c = 5.12$Å, with a perfect linear dependency of the thermal conductance $G = 1/R$ with the effective surface fraction. Also, importantly, very high Kapitza lengths were observed for the smaller surface fraction systems, with a maxima of $\ell_K \sim 200$ nm, much higher as compared to previous values obtained for CNT ($\ell_K \sim 30$ nm [270]) or graphite-planar copper ($\ell_K \sim 50$ nm [276]) interfaces.

These promising results (with a predicted higher Kapitza length for even smaller surface fractions) pave the way to efficient design of nanomaterials to control heat dissipation. Particularly, the proposed structure presents promising applications in systems where a high Kapitza resistance is needed. Such is the case of delaying the temperatures at which the boiling crisis occurs (increasing the thermal resistance decreases the heat flux dissipation) which is critical in avoiding vapor explosions in the case of nuclear power plants accidents [250]. The proposed system presents a cheap and robust alternative to superhydrophobic surfaces were the Kapitza resistance is increased for so-called "Cassie materials" for which air is trapped below the liquid drop due to the liquid-solid wetting properties [278, 279]. Moreover, because the main idea of the system is to trap air bubbles at the interface, the presented results can be extended to any type of material with equivalent structure than the gold wall. Also, it could be an interesting perspective to assess the effect of considering other 2D materials, cheaper and stiffer than graphene, or adding more graphene layers to improve the system stability and increase further the Kapitza resistance.

3.4 Summary and conclusions

We have addressed in this chapter the study of two common interface transport mechanisms, hydrodynamic and thermal transport, which present jumps at the interface in their respective fields, velocity and temperature, defining the slip and the Kapitza characteristic lengths from their bulk and interfacial transport coefficients.

In the first part, we have continued the work presented in the previous chapter about the temperature dependence of the hydrodynamic transport coefficients, specifically viscosity and liquid-solid friction, as well as its ratio given by the slip length, focusing on water cooled down into its supercooled regime. After decomposing the friction coefficient, and subsequently the viscosity, into a static and a dynamic contribution, three main messages can be highlighted in this study. First, the main contribution to friction temperature dependence came from the dynamical term, particularly from the density relaxation time of the water molecules at the interface. Second, that the static contribution to viscosity significantly increased for water when lowering the temperature and entering in the supercooled regime, representing a major contribution to the slip length temperature dependence. Third, that the different slip temperature dependencies observed for LJ walls and graphene arose from the different interfacial dynamics on these two surfaces. In particular, for LJ walls we observed slower interfacial dynamics, as compared to bulk, when decreasing the temperature, while for graphene no significant slowing down was observed (again as compared to the bulk one), which we related to the smoothnes of the graphene

surface.

With regard to thermal transport, we proposed a graphene-coated nanopatterned gold structure as an alternative to enhance thermal resistance, which takes advantage of the low air thermal conductivity when compared to the one of water. The idea consists in using the gold roughness to trap air bubbles in between the graphene layer and the nanostructured solid wall. We indeed observed a global decrease in the thermal conductance, proportional to the effective contact surface fraction in between both walls. With interesting applications in delaying the so-called boiling crisis, related to vapor explosions in nuclear power plants, we proposed a simple scaling of our results by considering the different interfacial resistances as a set of resistances connected in series.

Although both thermal and hydrodynamic transport are controlled by different physical processes (mostly phonon transfer and momentum transfer respectively), the effect of wetting or nanopatterning in their respective transport coefficients have been widely studied, specifically via MD simulations. Aside of the fundamental interest, a better understanding of such interfacial processes facilitates the development of new nano-materials and predicts the most favorable and cost-effective system structures to use depending on the physical properties and signals we are interested in detect, strengthen, or mitigate.

Chapter 4

Determining the temperature dependence of bulk transport coefficients from *ab initio* molecular dynamics

"If we were to name the most powerful assumption of all, which leads one on and on in an attempt to understand life, it is that all things are made of atoms, and that everything that living things do can be understood in terms of the jigglings and wigglings of atoms."

Richard P. Feynman, *The Feynman Lectures on Physics* 1964

Contents

4.1 Introduction

Water is an ubiquitous liquid, essential for life development, and therefore one of the most important chemical substances. Due to its critical relevance with regard to energy harvesting and water purification, several efforts have been carried in order to obtain molecular insights about water behavior under multiple different physical conditions. Water molecular interactions arise from a balance between var der Waals and hydrogen bonding forces [288, 66], thus a complete description exclusively from classical force field simulations may

hinder some critical mechanisms. *Ab initio* molecular dynamics (AIMD), which explicitly accounts for electronic interactions, may play a key role in understanding some important physical processes for bulk and confined water. The quantum calculation of the electronic structure, originally formulated by Schrödinger in terms of electronic wave functions, can be performed with different first principle methods. One important approach is the one proposed by density functional theory (DFT), based on a formulation of the quantum mechanical problem in terms of energy functionals of the electronic density. DFT methods are a blooming field, and a broad bibliography can be found in order to assess the density functional which better reproduces the structural and dynamical properties of bulk water [289] with particular interest on reproducing its radial distribution functions $g(r)$, diffusion coefficient and hydrogen bond dynamics [290, 65, 291]. Less bibliography can be found with regard to liquid's shear viscosity [233], specifically water [66]. In terms of bulk transport, further understanding of water viscosity molecular mechanisms are needed to characterize water properties distinctive of its temperature evolution in the supercooled regime, such as shear viscosity viscoelastic properties [53, 292, 52] or, by comparison of viscosity and diffusion temperature evolution, to obtain molecular insights about the breaking of the Stokes-Einstein relation at low temperatures [29]. Also in terms of confined water, were efforts in discerning the atomic processes that control liquid-solid friction [230, 193, 293] have been carried via classical and AIMD, viscosity understanding plays a critical role in enlightening the characteristic of slippage, characterized by the slip length which is defined as the ratio between both transport coefficients. With such motivating perspectives, it becomes crucial to find the density functional which better describes not only water viscosity at a given temperature but also its temperature evolution, with special interest in the temperature range in which the fluid is in its supercooled state.

In the way through finding the best density functional for water, the importance of considering van der Walls interactions [67, 66] or nuclear quantum effects [294, 295, 296, 297] (critical at low temperatures) is often discussed. But also, due to the broad literature focusing on the reproduction of water structural properties such as the $g(r)$, the establishment of a thermodynamic link between structure and dynamics would be not only of great scientific interest but additionally very useful for functional developing and comparison. Such connection has already been explored in the literature via *e.g.* free-volume models [298, 299], relationships between $g(r)$ and glass transition temperature [300], and the proposition of different structural descriptors [301], among which the entropy excess scaling stands out [302, 303, 241]. The excess of entropy, which can be decomposed on different interparticle interactions in terms on the $N-$body radial distribution functions [304], has been proven to exhibit an exponential relation with the diffusion coefficient for multiple systems [305, 306], among which glass forming liquids such as supercooled binary mixtures and water, for which the approximation of the entropy excess to its two body contribution (related to an integral of a function of $g(r)$) has been proven to work well for a broad range of temperatures [307, 308, 309, 241, 310]. One of the main limitations for AIMD is its great need of resources as compared to their classical counterparts. Nevertheless, if the link between dynamics and structure is established, we would be able to predict the transport coefficients value from structural properties which require shorter simulation times to converge [311]. Aside of this, entropy excess scaling has also been used as a tool to bring insights into some fluid molecular mechanisms in the study of the Stokes-Einstein relation [310].

The present chapter is organized as follows. After a brief introduction about first principles MD, the main DFT concepts are introduced, such as Hohenberg-Kohn theorems, Kohn-Sham equations, basis sets and pseudopotentials. A detailed description of both

AIMD and classical MD simulation settings can be found in the methods section, together with the procedure carried to characterize the transport coefficients. Also, a general picture on the entropy excess is presented along with a physical argumentation in terms of scaling to understand the connection between the entropy excess and the transport coefficients. Afterwards, the main results are described and discussed, first by presenting the bulk transport coefficients measures for water at different temperatures and for different functionals, and second by stating the verification of the excess-entropy scaling for all the functionals.

4.2 First principles molecular dynamics

In previous chapters, we have introduced classical molecular dynamics (MD) simulations as a powerful tool to describe processes in the nanometric scale. We particularly focused on the case of force field (FF) simulations, where the interactions between two atoms are described by an explicit function of their positions r, as in the case of the Lennard-Jones potential,

$$V_{\mathrm{LJ}}(r) = 4\varepsilon\left[\left(\frac{\sigma}{\varepsilon}\right)^{12} - \left(\frac{\sigma}{\varepsilon}\right)^{6}\right], \tag{4.1}$$

with σ the effective particle diameter and ε the interaction energy. In this example, (σ, ε) can be adjusted to reproduce experimental interatomic distances, vibration frequencies, etc. This is why we may refer to FFMD as empirical calculations. Such empirical approach may pose some practical difficulties, as the impossibility to predict the interaction parameters in the case of inaccessible systems such as the earth center or new materials. We may also wonder about the fundamental reliability of these methods, due to the failure in describing atomically equivalent systems within the same parameters, like diamond, graphite, graphene and fullerenes. Furthermore, the theoretical background underlying FFMD, based on parametrizations of atomic forces, becomes problematic in the case of chemically complex systems where many different particles are considered (*i.e.* where many different interactions should be parametrized, as for complex molecules or proteins), or where the electronic structure changes qualitatively in the course of the simulation.

A solution for these problems can be the use of first-principles calculations, also called *ab initio* MD (AIMD), where no adjustable parameter needs to be introduced. The main idea underlying AIMD is to consider the electronic variables as active degrees of freedom, thus the atomic interactions (*i.e.* the forces used to propagate the classical nuclei) are obtained from explicit electronic structure calculations. Most of the *ab initio* methods are based on the adiabatic and Born-Oppenheimer approximations [312] by assuming that, because the nucleus is far more massive than the electron, the electrons adiabatically follow the nuclei (*i.e.* they adapt quasi-instantaneously to a variation of the nuclear configuration) and, due to such mass difference, the electronic and nuclear motion can be treated separately. Together with both approximations, most of the *ab initio* methods work under the so-called Ehrenfest MD [313], which assumes that the average nuclear motion is determined by Newton's equations. The validity of this approximation can be stated in terms of de Broglie thermal length $\lambda_{\mathrm{th}} = h/\sqrt{2\pi m k_{\mathrm{B}} T}$, which posses problems at room temperature for the hydrogen atom, for which $\lambda_{\mathrm{th}} \sim 1$ Å is of order of the atomic radius and nuclear quantum effects may not be negligible [296]. The two main formulations in *ab initio* methods to solve the electronic structure are the Hartree-Fock formalism, which approximates the atomic wave function by a single determinant of the orbitals, and the Kohn-Sham formalism, which approximates the interacting electrons by non-interacting auxiliary electrons embedded in an auxiliary potential. Nuclear quantum effects, which

may become important at low temperatures, can be considered within a path integral formulation (PIMD) [314]. Although *ab initio* methods are proven to be a powerful tool which allows us to explore some configurations which cannot be modelled from a classical perspective, the correlation lengths and relaxation times that are accessible via AIMD are much smaller than those affordable with FFMD. Nevertheless, due to the increasing power of computational resources with time, it is expected that AIMD simulations will continue increasing their importance as a tool to tackle different problems in theoretical chemistry, physics and biology [315].

4.2.1 Density functional theory

Density functional theory (DFT) is a type of *ab initio* method based on the Kohn-Sham formulation of the electronic structure problem. In order to introduce and discuss the main concepts underlying this theory, let's start with the well known time-dependent Shrödinger equation:

$$\mathcal{H}\Phi = i\hbar\frac{\partial\Phi}{\partial t}, \tag{4.2}$$

with $\Phi = \Phi(\{\mathbf{r}_i\},\{\mathbf{R}_I\};t)$ the wave function as a function of the electronic coordinates $\{\mathbf{r}_i\}$, the ions coordinates $\{\mathbf{R}_I\}$ and the time t (for a simpler description we will neglect the electronic spin), and the Hamiltonian:

$$\begin{aligned}\mathcal{H} = &\left(-\frac{\hbar^2}{2M_I}\sum_I \nabla_I^2 + \frac{1}{4\pi\varepsilon_0}\sum_{I<J}\frac{Z_I Z_J e^2}{|\mathbf{R}_I-\mathbf{R}_J|}\right)\\ &+\left(-\frac{\hbar^2}{2m_\mathrm{e}}\sum_i \nabla_i^2 + \frac{1}{4\pi\varepsilon_0}\sum_{i<j}\frac{e^2}{|\mathbf{r}_i-\mathbf{r}_j|}\right) - \frac{1}{4\pi\varepsilon_0}\sum_{i,I}\frac{Z_I e^2}{|\mathbf{r}_i-\mathbf{R}_I|},\end{aligned} \tag{4.3}$$

where M_I and m_e refer to the ionic and the electronic mass respectively, Z_I is the atomic number of the I-th nucleus, e the electron charge and ε_0 the vacuum permittivity. The first two terms in Eq. (4.3) refer to the nuclear kinetic energy T_R and potential energy V_R, the third and the fourth terms refer to the electronic kinetic T_r and potential V_r energies, and the last term refers to the interaction energy between the electrons and the collection of atom nuclei. For simplicity, we will denote Eq. (4.3) as:

$$\mathcal{H} = (T_R + V_R) + (T_r + V_r) + V_{r,R}. \tag{4.4}$$

Because of the Hamiltonian shape, we can see that the solution Eq. (4.2) is a $3N$ dimensional problem. The main objective of DFT is to reduce the problem dimension, up to a 3 dimensional problem. The first step is to work within the Born-Oppenheimer approximation, which consists in considering the nuclei and the electrons as two different mathematical problems. Within this approximation, we can then expand the many body wave function Φ in a separate product (neglecting cross terms) of a complete basis set for nuclei χ_k and electrons Ψ_k as:

$$\Phi(\mathbf{r},\mathbf{R};t) = \sum_k \chi_k(\mathbf{R};t)\cdot\Psi_k(\mathbf{r};\mathbf{R}), \tag{4.5}$$

where we denoted, for simplicity, $(\{\mathbf{r}_i\},\{\mathbf{R}_i\}) \equiv (\mathbf{r},\mathbf{R})$, and we considered the electronic wave function $\Psi(\mathbf{r};\mathbf{R})$ adiabatic, so it only depends parametrically on the nuclear positions $\mathbf{R}$. Eq. (4.5) allows us to consider the atomic motion as two separate problems: on the one

hand an electron structure problem, by considering the nucleus fixed in space and solving the stationary electronic Schrödinger equation:

$$\mathcal{H}_{\rm e}\Psi_k(\mathbf{r};\mathbf{R}) = \varepsilon_k(\mathbf{R})\Psi_k(\mathbf{r};\mathbf{R}), \tag{4.6}$$

with $\mathcal{H}_{\rm e} = T_r + V_r + V_{r,R}$. On the other hand, a nuclear problem, consisting in solving the time-dependent Schrödinger equation for the nuclear degrees of freedom:

$$\mathcal{H}_I\,\chi_k(\mathbf{R};t) = i\hbar\frac{\partial\chi_k(\mathbf{R};t)}{\partial t}, \tag{4.7}$$

with $\mathcal{H}_I = T_R + V_R + \varepsilon_k(\mathbf{R})$, where $\varepsilon_k(\mathbf{R})$ has been determined from Eq. (4.6). The solution to Eq. (4.7) remains trivial when considering the nuclei as a classical object, where it can be proven [313] that it rewrites as

$$M_I\ddot{\mathbf{R}}_I(t) = -\nabla_I V_k^{\rm BO}(\mathbf{R}), \tag{4.8}$$

which is simply Newton's second equation from classical mechanics expressed in terms of an effective potential, $V_k^{\rm BO}$, determined by the energy surface $\varepsilon_k(\mathbf{R})$.

a. Hohenberg-Kohn theorems

Several theoretical efforts have then focused on the solution to Eq. (4.6) and in reducing its associated $3N$ dimensional problem. We will discuss here the one from the Kohn-Sham DFT theory, based on the Hohenberg-Kohn (HK) theorems [316, 317]. The **first HK theorem** states that the ground state energy from Schrödinger's equation can be calculated from a universal functional of the electron density $n_{\rm e}(\mathbf{r})$. This theorem ensures the existence of $n_{\rm e}$ and, for known $n_{\rm e}$ (which only depends on the 3 spacial variables), the complete determination of the Hamiltonian ensures the determination of the many-body wave functions for all the states, and thus all properties of the system will be fully determined. So now we know that the total energy is a universal functional of $n_{\rm e}$ $E = E[n_{\rm e}(\mathbf{r})]$; but, how can we determine $n_{\rm e}$ if the many-body wave functions remain unknown? The **second HK theorem** states that the correct electron density is the one that minimizes the energy of the overall functional. This theorem hints that, if the functional shape is known, we can employ the variational principle in order to find the ground-state electron density by means of minimizing the energy from the functional. Such energy functional can be decomposed in a universal contribution, $F[n_{\rm e}(\mathbf{r})]$, and a system dependent contribution as

$$E[n_{\rm e}(\mathbf{r})] = F[n_{\rm e}(\mathbf{r})] + \int V_{\rm ext}(\mathbf{r})n_{\rm e}(\mathbf{r})\mathrm{d}^3r, \tag{4.9}$$

where the term with $V_{\rm ext}$ represents the Coulombic interactions between the electrons and the nuclei. The universal contribution to the energy functional will be given by

$$F[n_{\rm e}(\mathbf{r})] = -\frac{\hbar^2}{m_{\rm e}}\sum_i\int\Psi_i^*\nabla^2\Psi_i\mathrm{d}^3r + \frac{e^2}{2}\int\int\frac{n_{\rm e}(\mathbf{r})n_{\rm e}(\mathbf{r}')}{|\mathbf{r}-\mathbf{r}'|}\mathrm{d}^3r\,\mathrm{d}^3r' + E_{\rm XC}[n_{\rm e}(\mathbf{r})], \tag{4.10}$$

where the first term corresponds to the electronic kinetic energies and the second one to the Coulomb electron-electron interactions. Because in this second term we are accounting for the interaction of an electron with itself, the exchange-correlation contribution $E_{\rm XC}$ is introduced as a non-classical self-interaction correction. Therefore, all the terms in Eq. (4.9) are known but $E_{\rm XC}$. It is important to note that all the terms in Eqs. (4.9) and (4.10) are functionals of the electronic density except the kinetic term, which has to be expressed in terms of the electronic wave functions due to the absence of direct link from the density to the kinetic energy. Therefore, this approach remains exact but impractical and we need further simplification in order to tackle the problem: the Kohn-Sham formulation.

b. Kohn-Sham equations

The main idea in the Kohn-Sham (KS) formulation is to replace the original many-body problem of interacting electrons by a system of non-interacting particles in an effective potential with the same density as the original system. Such non-interacting particles define a set of auxiliary functions $\{\phi_i(\mathbf{r})\}$, denominated the Kohn-Sham orbitals, which are fictitious states. We can then consider the electrons as independent particles via the Hartree product of single electronic wave functions:

$$\phi(\mathbf{r}) = \phi_1(\mathbf{r}) \cdot \phi_2(\mathbf{r}) \cdot ... \cdot \phi_n(\mathbf{r}). \tag{4.11}$$

The electronic density will be then given by the expression:

$$n_{\mathrm{e}}(\mathbf{r}) = 2\sum_i \phi_i^*(\mathbf{r})\phi_i(\mathbf{r}), \tag{4.12}$$

where the prefactor 2 comes from Pauli's principle which states that two electrons with opposite spin can occupy the same spacial location. Then, the total ground state energy of the non-interacting system will be given by the minimum of the Kohn-Sham energy [318, 319]:

$$E^{\mathrm{KS}}[\{\phi_i\}] = T_0[\{\phi_i\}] + \int V_{\mathrm{ext}}(\mathbf{r})n_{\mathrm{e}}(\mathbf{r})\mathrm{d}^3r + E_{\mathrm{H}}[n_{\mathrm{e}}(\mathbf{r})] + E_{\mathrm{XC}}[n_{\mathrm{e}}(\mathbf{r})]; \tag{4.13}$$

with T_0 the kinetic energy of the non-interacting particles, V_{ext} the external potential from the nuclei, E_{H} the classical Coulombic electron-electron interactions, also called the Hartree energy:

$$E_{\mathrm{H}}[n(\mathbf{r})] = \frac{e^2}{2}\int\int \frac{n_{\mathrm{e}}(\mathbf{r})n_{\mathrm{e}}(\mathbf{r}')}{|\mathbf{r}-\mathbf{r}'|}\mathrm{d}^3r\,\mathrm{d}^3r', \tag{4.14}$$

and E_{XC} the self-interaction correction term.

Finally the Kohn-Sham one-electron orbitals provide a set of equations, the Kohn-Sham equations, where one equation involves only one particle, reducing the problem dimension from $3N$ in Eq. (4.2) to only 3 dimensions (associated to the three spacial coordinates):

$$\left[-\frac{\hbar^2}{2m_{\mathrm{e}}}\boldsymbol{\nabla}^2 + V_{\mathrm{ext}}(\mathbf{r}) + V_{\mathrm{H}}(\mathbf{r}) + V_{\mathrm{XC}}(\mathbf{r})\right]\phi_i(\mathbf{r}) = \varepsilon_i\phi_i(\mathbf{r}), \tag{4.15}$$

where the Hartree potential is given by

$$V_{\mathrm{H}}(\mathbf{r}) = e^2\int\int \frac{n_{\mathrm{e}}(\mathbf{r}')}{|\mathbf{r}-\mathbf{r}'|}\mathrm{d}^3r' \tag{4.16}$$

and V_{XC} is the local exchange-correlation potential, given by the functional derivative:

$$\frac{\delta E_{\mathrm{XC}}[n_{\mathrm{e}}]}{\delta n_{\mathrm{e}}(\mathbf{r})} = V_{\mathrm{XC}}(\mathbf{r}). \tag{4.17}$$

But, what is the shape of E_{XC}? The exchange-correlation functional is defined as

$$E_{\mathrm{XC}}[n_{\mathrm{e}}(\mathbf{r})] = \int n_{\mathrm{e}}(\mathbf{r})\,\varepsilon_{\mathrm{XC}}[n_{\mathrm{e}}(\mathbf{r})]\mathrm{d}^3r, \tag{4.18}$$

where the energy $\varepsilon_{\mathrm{XC}}$ will be determined by the level of accuracy chosen for our system. In Fig. 4.1 the different approaches taken for $\varepsilon_{\mathrm{XC}}$ are schematized, typically represented as a "Jacob's ladder" [320] where each step corresponds to different accuracy levels which go

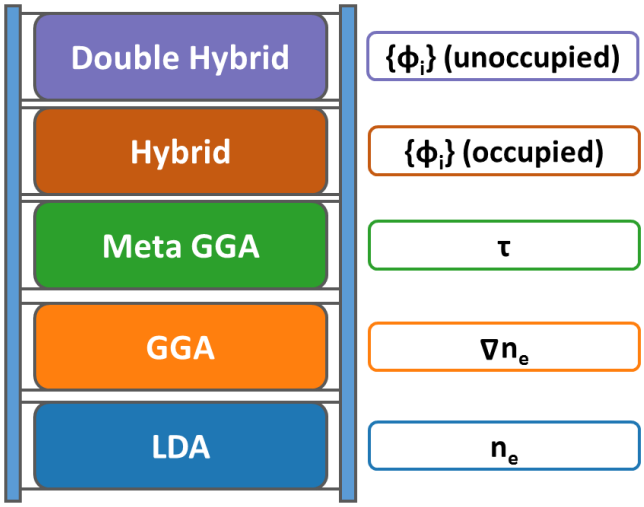

Figure 4.1: Jacob's ladder schematics of the different accuracy levels taken in DFT for the implementation of the exchange-correlation functional. In this representation, the ladder would take us from the "Hartree world", where no exchange-correlation interactions are taken into account, up to the perfect chemically accurate simulation. Each step in the ladder accounts for all the approximations of the previous steps.

from the ground level $\varepsilon_{\mathrm{XC}} = 0$ (*Hartree's world*, where the only internal interactions considered are the ones from V_{H} and the kinetic interactions) to the maximum level of chemical accuracy, where all the inter-atomic interactions are accounted. Therefore, the exchange-correlation functional choice is a key element to the success of DFT and we should find, depending on the system we want to simulate, an equilibrium between the approximation level and the computational resources. The simplest choice for E_{XC} corresponds to the local density approximation (LDA, first step in Fig. 4.1), where the exchange-correlation energy is the one of a homogeneous electron gas of density n_{e}, so the functional only depends on the local density at a given point. The next step would be the generalized gradient approximations (GGA), where the functional only depends on the local density n_{e} and its gradient $\boldsymbol{\nabla} n_{\mathrm{e}}$. Meta GGA functionals are those where the functional also includes the second derivative of the electron density $\boldsymbol{\nabla}^2 n_{\mathrm{e}}$ although they are typically developed [321] to include a dependence on the kinetic energy density τ:

$$\tau(\mathbf{r}) = \frac{1}{2}\sum_i |\nabla\phi_i(\mathbf{r})|^2, \tag{4.19}$$

where the sum on i is performed over the occupied orbitals. The next step in the ladder corresponds to the Hybrid functionals, which explicitly account for the occupied molecular orbitals (typically in form of Hartree-Fock exchange). In the last step of the ladder, before finally reaching the chemical accuracy, we can find the double hybrid functionals, which also include the unoccupied virtual molecular orbitals in their implementation. The Jacob's ladder image is a simple way to schematize the different approximations for E_{XC} in DFT, although it is an incomplete scheme. Different intermediate steps could be added by functionals that, for example, include the van der Waals interactions, which allows an improvement of GGA and hybrid functionals [297].

Bringing to a conclusion, the Kohn-Sham formalism establishes a way to obtain the ground-state energy by finding the electronic density n_{e}, or the Kohn-Sham orbital set $\{\phi_i\}$, which minimizes E^{KS}. In practice, the way to proceed to solve the minimization

problem is via a self-consistent loop where, in a given loop iteration k:

1. We give an initial guess for the electronic density $n_{\mathrm{e}}^{(k)}(\mathbf{r})$, typically a superposition of the atomic densities for $k = 1$, or the electronic density obtained in the previous loop iteration $(k-1)$ otherwise.

2. For the trial electron density chosen, we evaluate the effective Kohn-Sham potential

$$V^{\mathrm{KS}}(\mathbf{r}) = V_{\mathrm{ext}}(\mathbf{r}) + V_{\mathrm{H}}[n_{\mathrm{e}}^{(k)}(\mathbf{r})] + V_{\mathrm{XC}}[n_{\mathrm{e}}^{(k)}(\mathbf{r})].$$

3. For the given potential, we solve the Kohn-Sham equations:

$$\left[-\frac{\hbar^2}{2m_{\mathrm{e}}}\boldsymbol{\nabla}^2 + V^{\mathrm{KS}}[n_{\mathrm{e}}^{(k)}(\mathbf{r})]\right]\phi_i(\mathbf{r}) = \varepsilon_i\phi_i(\mathbf{r}).$$

4. We evaluate the actual density for the $\{\phi_i\}$ obtained,

$$n_{\mathrm{e}}(\mathbf{r}) = 2\sum_i \phi_i^*(\mathbf{r})\phi_i(\mathbf{r}).$$

5. Finally, we check the consistency between the obtained electron density and the trial one for a given precision δ:

$$\left|\left|n_{\mathrm{e}}^{(k)}(\mathbf{r}) - n_{\mathrm{e}}(\mathbf{r})\right|\right| < \delta.$$

   If the precision condition is verified, we finish the self-consistency loop and we can proceed to compute the energy, forces, stresses... Otherwise, we repeat the loop for $k \to k+1$.

c. Basis sets and pseudopotentials

The self-consistency loop described involves solving the Kohn-Sham single electron equations for the molecular orbitals $\{\phi_i\}$. To do so, we need to expand the wave functions $\{\phi_i\}$ in a basis set, which can consist in a linear combination of atomic orbitals:

$$\phi_i(\mathbf{r}) = \sum_\alpha c_{\alpha,i}\,\varphi_\alpha(\mathbf{r}). \tag{4.20}$$

A typical set of functions used in quantum chemistry are the **Gaussian type orbitals** (GTO), where the primitive function is given by:

$$\varphi(\mathbf{r}) = r^l Y_{lm}(\theta,\phi)\exp\left[-\alpha(r-R_I)^2\right], \tag{4.21}$$

constituted by the scalar product of the $Y_{lm}(\theta,\phi)$ spherical harmonic functions in the angular spherical coordinates times a Gaussian exponential centered at the atomic position. GTOs represent a compact basis set which allows an efficient parallel implementation (much reduced optimization problem) as compared to other basis sets. Also, GTOs choice allows analytical integration and efficient derivation for many operators. Nevertheless, because they are a localized non-orthogonal basis set, they can lead to basis set superposition error, which can become critical for binding energy computations (although typically not for MD) [313]. Also, typically molecules and solids have different requirements in terms of basis sets, and GTOs which are good for both cases are difficult to find.

Another common basis set choice are plane waves (PW) basis sets defined as:

$$\varphi(\mathbf{r}) = \frac{1}{\sqrt{\Omega}} \exp[i\mathbf{G}\cdot\mathbf{r}], \tag{4.22}$$

where Ω is the volume of the simulation cell and $\mathbf{G}$ the wave vector in the reciprocal space. PWs form an orthonormal and complete basis set, independent of the atoms positions, and thus any periodic function can be extended in this basis:

$$\psi(\mathbf{r}) = \psi(\mathbf{r}+\mathbf{L}) = \frac{1}{\sqrt{\Omega}} \sum_{\mathbf{G}} \psi(\mathbf{G}) \exp[i\mathbf{G}\cdot\mathbf{r}]. \tag{4.23}$$

Such is the case of the Kohn-Sham orbitals solution of the Kohn-Sham potential of a periodic system ($V^{\mathrm{KS}}(\mathbf{r}) = V^{\mathrm{KS}}(\mathbf{r}+\mathbf{L})$). Nevertheless, in actual calculations, we will never go to a basis set constituted by an infinite number of PWs, and a cutoff has to be introduced in order to truncate the infinite sum over $\mathbf{G}$ vectors. The idea is to include in the calculation all the plane waves with less kinetic energy than a certain cutoff energy:

$$\frac{1}{2}G^2 \leq E_{\mathrm{cut}}. \tag{4.24}$$

Then, the number of plain waves will be approximately given by [313]:

$$N_{\mathrm{PW}} \approx \frac{1}{2\pi^2}\Omega E_{\mathrm{cut}}^{3/2}, \tag{4.25}$$

with Ω and E_{cut} given in atomic units.

Because the accuracy and efficiency of the density expansion will be given by the choice of E_{cut}, with PW calculations we can have problems with functions that are very local because they need a very high cutoff to converge. The way out is the use of **pseudopotentials**. The idea under the pseudopotential introduction is to replace the inactive electronic degrees of freedom in the Hamiltonian by an effective potential. Most of the pseudopotentials are based on atomic calculations and on the frozen core approximation, which consists in considering the core electrons chemically inert, thus the pseudopotential replaces the Hartree and exchange-correlation potentials due to the core electrons. The new potential should be additive and transferable. In order to ensure transferability, pseudopotentials are typically implemented for atoms, not for molecules. Then, the addition condition allows us to define the total molecular pseudopotential from the sum of the atomic pseudopotentials. Pseudopotentials let us to reduce the size of the PW basis set (implying an effective speed up of the calculation), to reduce the number of electrons (and therefore reduce the number of orbitals to calculate), and to partially include relativistic effects into effective potentials. The main idea underlying the use of pseudopotentials is to explicitly account for the valence electrons, and approximate the nuclei and core electrons by the pseudopotential. Therefore they are particularly useful for PW calculations and basis sets related to a grid, although their extension to other type of basis sets, such as GTOs, may also help in the efficiency of the computation.

4.3 Methods

4.3.1 Simulation details

We performed *ab initio* molecular dynamics (AIMD) simulations of 32 water molecules in bulk using DFT with the CP2K code [322], which employs Gaussian and Plane waves

(GPW) method in order to solve the Kohn-Sham equation Eq. (4.15). Three different density functionals were considered: PBE [323] functional with Grimme's D3 corrections [324, 325] (namely PBE-D3, GGA functional with vdW interactions), optB88-vdW [326, 327] (GGA functional with vdW interactions) and SCAN [328] (metaGGA functional). The electronic structure problem was solved within the Born-Oppenheimer approximation for 5 different temperatures ($T = \{260, 270, 300, 330, 360\}$ K (the two lowest ones corresponding to the expected supercooled regime) controlled via the Nosé-Hoover thermostat. We worked at constant volume with a box size such as $\rho = 1\,\mathrm{g/cm^3}$ ($L_{\mathrm{box}} = 9.85\,\text{Å}$ for 32 water molecules). The running time was $\simeq 120\,\mathrm{ps}$ for all functionals and temperatures but optB88-vdW and $T = \{260, 270\}$ K, with running time $\simeq 240\,\mathrm{ps}$. The timestep considered was 0.5 ps. The initial configuration for all the functionals corresponded to the steady state at the given temperature obtained from force field (FF) MD after a running time of 200 ps. The energy cutoff for plane waves was 600 Ry for PBE-D3 and optB88-vdW, and 800 Ry for SCAN, and the localized Gaussian basis set was short range molecularly optimized double-ζ valence polarized (DZVP-MOLOPT-SR) [329] for all PBE-D3 and optB88-vdW, and its SCAN optimization DZVP-MOLOPT-SCAN, available from the developers of CP2K.

We also performed force field (classical MD) simulations via the LAMMPS package [144]. Analogously to AIMD, we worked in the (N, V, T) ensemble with the temperature controlled via a Nosé-Hoover thermostat and with a volume such as $\rho = 1\,\mathrm{g/cm^3}$. Three different box sizes were considered: 32 water molecules ($L_{\mathrm{box}} = 9.85\,\text{Å}$), 64 water molecules ($L_{\mathrm{box}} = 12.42\,\text{Å}$) and 128 water molecules ($L_{\mathrm{box}} = 15.64\,\text{Å}$). The water model considered in all the cases was TIP4P/2005 [172].

4.3.2 Transport coefficients determination

a. Viscosity and Diffusion

For all the simulations, we determined the shear viscosity from its Green-Kubo relation:

$$\eta_{\mathrm{GK}} = \frac{V}{k_{\mathrm{B}}T} \int_0^\infty \langle p_{ij}(t) p_{ij}(0) \rangle \, \mathrm{d}t, \tag{4.26}$$

with V the volume, k_{B} the Boltzmann constant, T the temperature and $p_{ij} = \{p_{xy}, p_{xz}, p_{yz}\}$ the non-diagonal components of the stress tensor. The other two independent traceless components of the stress tensor, $(p_{xx} - p_{yy})/2$ and $(p_{yy} - p_{zz})/2$, were non-equivalent to the diagonal ones for 32 water molecules, implying a breaking of the rotational invariance for small simulation boxes [233]. This invariance was recovered for 128 water molecules boxes.

We also computed the mean squared displacement, $\left\langle r^2 \right\rangle = \left\langle |\mathbf{r}(t) - \mathbf{r}(0)|^2 \right\rangle$, defined as the ensemble average of the squared deviation of the position of a particle with respect to $\mathbf{r}(0)$ over time. At short times, ballistic motion dominates the dynamics of the particles (due to the lack of collisions) and $\left\langle r^2 \right\rangle \propto t^2$. Nevertheless, for long enough times, the liquid particles dynamics will be dominated by Brownian motion. In this diffusive regime, Einstein's relation for diffusion [145] states that $\left\langle r^2 \right\rangle = 6Dt$, with D the diffusion coefficient. In practice, because of hydrodynamic interactions between the periodic image boxes, a finite size correction to the diffusion coefficient has to be introduced [330, 331, 108]. For a cubic simulation box of size L_{box} with periodic boundary conditions:

$$D = D_{\mathrm{PBC}} + 2.837 \frac{k_{\mathrm{B}}T}{6\pi\eta L_{\mathrm{box}}}, \tag{4.27}$$

where η is the bulk shear viscosity and

$$D_{\mathrm{PBC}} = \frac{1}{6}\frac{\mathrm{d}\left\langle r^2\right\rangle}{\mathrm{d}t}. \tag{4.28}$$

From Eq. (4.27) we can see that $D = D_{\mathrm{PBC}}$ when $L_{\mathrm{box}} \to \infty$.

We could run a limited amount of simulations due to the high computation time required for *ab initio* MD, and for both viscosity a diffusion, the error bars were computed within 60% of confidence level. For viscosity, the total MD stress was divided in three time slots of equal length, each of them containing three independent measures of η. Because of the short simulation times, η_{GK} was measured at the time where $\eta(t)$ running integral reached a time plateau (see Fig. 4.2a). Therefore 9 independent viscosity values were computed for each functional at a given temperature. For the diffusion coefficient, the first 20 ps were removed from the trajectory so the system equilibration from the initial configuration does not affect the mean squared displacement results. From them, 3 independent measures of D_{PBC} were obtained from the three independent Cartesian components.

b. Two-body excess entropy s_2

As discussed in the introduction section, let's study the connection between the presented transport coefficients and the structure via the two-body excess entropy. In thermodynamic equilibrium when working in the (N, V, T) ensemble, we can quantify our ignorance about the system's microscopic state with the system's entropy $S(n, T)$, with $n = N/V$ the density of the system. Defining the entropy per particle as $s = S/N$, we can define $s = k_{\mathrm{B}} \ln(\Gamma_{\mathrm{V}})$, where k_{B} is the Boltzmann constant and Γ_{V} is the phase-space volume of the microscopic state consistent with the macroscopic given condition. For example, for an ideal gas system, the particles will be distributed all over the space with the same probability and therefore its entropy s_{id} will be maximum (our ignorance about the system's microscopic state is maximum because the system is maximally disordered). Thus, it is interesting to define the entropy excess as the difference between our system's entropy and the one of an ideal gas system: $s_{\mathrm{ex}} = s - s_{\mathrm{id}}$. Because the possible maximum entropy of any system is s_{id}, then $s_{\mathrm{ex}} \leq 0$ always and $s_{\mathrm{ex}} \to 0$ as $T \to \infty$.

We can decompose the equilibrium entropy in terms of the partial N-particle correlation functions as $s_{\mathrm{ex}} = s_2 + s_3 + s_4 + ...$ [332]. By systematically expanding s_{ex} in terms of partial N-particle distribution functions it can be proven [304] that the two-particle contribution writes:

$$\frac{s_2}{k_{\mathrm{B}}} = -2\pi n \int_0^\infty r^2 (g(r) \ln g(r) - g(r) + 1)\, \mathrm{d}r, \tag{4.29}$$

with $g(r)$ the radial distribution function. In the following, we will suppose $s_{\mathrm{ex}} \simeq s_2$, which has been proven to work well for water and supercooled binary mixtures [307, 308, 309, 310], although it fails for other systems, such as liquid metals, where higher order expansion coefficients should be considered [302, 303, 305, 306].

When considering a liquid, its excess of entropy can be estimated as

$$s_{\mathrm{ex}} = k_{\mathrm{B}} \ln\left(\frac{\sqrt{\left\langle x^2\right\rangle}}{l_0}\right), \tag{4.30}$$

where $l_0 = n^{-1/3}$ is the average inter-particle distance and $\left\langle x^2\right\rangle$ is the vibrational mean squared displacement. The average kinetic energy per degree of freedom due to the particles vibrations will then be $\frac{1}{2} m \omega_0^2 \left\langle x^2\right\rangle$, where ω_0 is the effective vibration frequency,

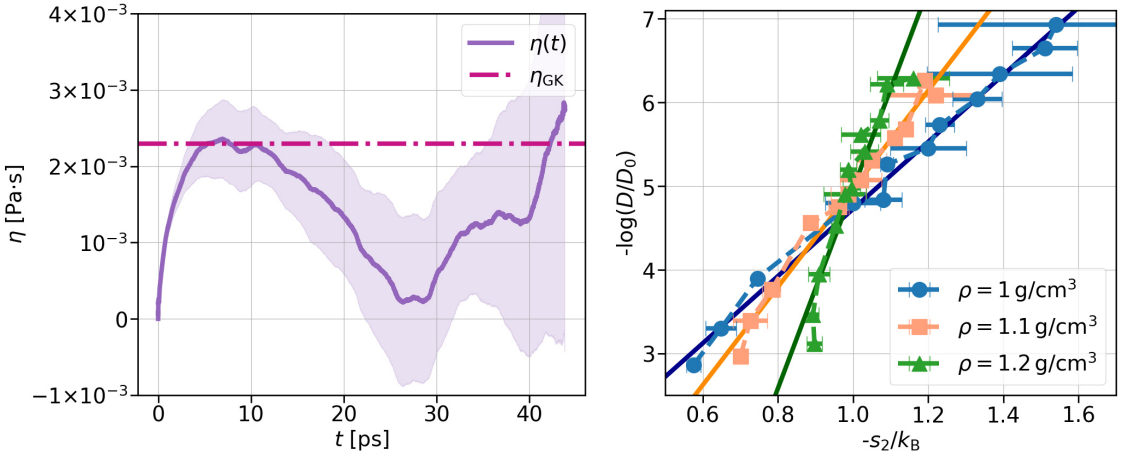

(a) (b)

Figure 4.2: (a) Typical viscosity Green-Kubo running integral with its standard deviation for nine independent measures (the figure example corresponds to SCAN functional at $T = 300\,\mathrm{K}$). Dash-dotted line corresponds to the plateau value considered, measured at $t \sim 10\,\mathrm{ps}$. (b) Reduced diffusion coefficient D/D_0 as a function of the dimensionless two-body entropy for FF simulations of 128 water molecules at different densities. Continuous lines correspond to the data fit with Eq. (4.32).

defined as the inverse of the time between collisions. The equipartition theorem states that $m\omega_0^2 \langle x^2 \rangle = k_\mathrm{B}T$, which, substituting in Eq. (4.30), gives:

$$\exp(s_\mathrm{ex}/k_\mathrm{B}) = \frac{1}{l_0\omega_0}\sqrt{\frac{k_\mathrm{B}T}{m}}. \tag{4.31}$$

We can establish a relation of s_ex with the diffusion coefficient D, by considering $D \sim l_0^2\omega_0$. We can then see that it is expected that the dimensionless diffusion coefficient D/D_0 will scale as:

$$\frac{D}{D_0} = A\exp(-B\, s_2/k_\mathrm{B}), \tag{4.32}$$

with $D_0 = l_0\sqrt{k_\mathrm{B}T/m}$ and A and B dimensionless constants at a given ρ. In Fig. 4.2b we can see that such exponential behavior is verified for FF simulations of water at different densities. Analogously, we can connect diffusion and viscosity through the Stokes-Einstein relation:

$$D = \frac{k_\mathrm{B}T}{6\pi\eta R_\mathrm{h}}, \tag{4.33}$$

with k_B Boltzmann constant and R_h the hydrodynamic radius corresponding to the drag force experienced by a perfect sphere moving through a liquid with viscosity η. From Eq. (4.33) and assuming $R_\mathrm{h} \sim l_0$, we can expect a scaling for the dimensionless viscosity η/η_0 as:

$$\frac{\eta}{\eta_0} = A'\exp\big(-B'\, s_2/k_\mathrm{B}\big), \tag{4.34}$$

with $\eta_0 = \sqrt{mk_\mathrm{B}T}/l_0^2$. From the Stokes-Einstein relation one expects $B' = -B$.

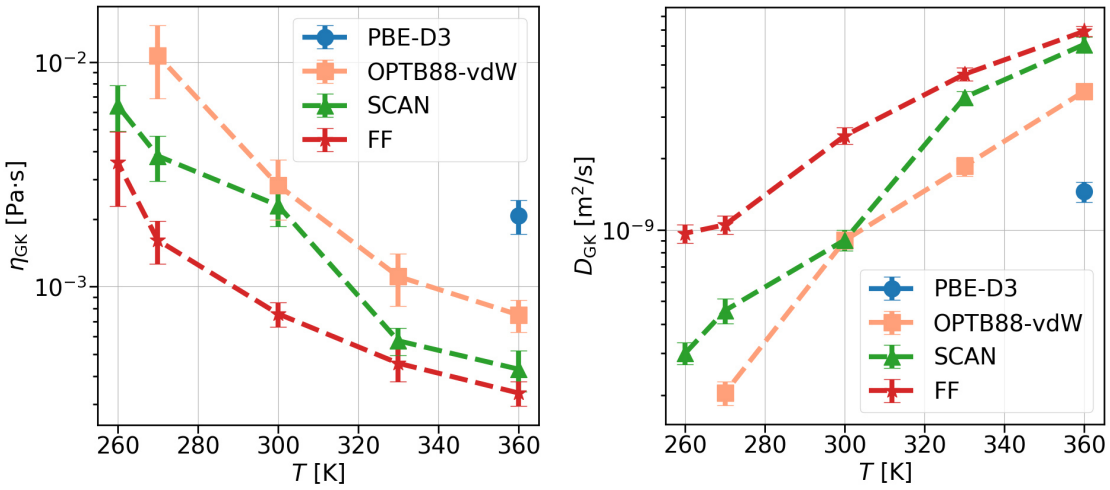

(a) (b)

Figure 4.3: Temperature evolution for different functionals of (a) shear viscosity from Eq. (4.26) and (b) diffusion coefficient from Eq. (4.27) with η_{GK}. To benchmark the results, force field (FF) MD simulations measures are represented in red stars; they are in good agreement with experiments [331, 216, 56].

4.4 Results

4.4.1 Temperature dependence of transport coefficients

We display in Fig. 4.3a the shear viscosity temperature evolution determined from the long-time plateau of the Green-Kubo integral, η_{GK} in Eq. (4.26), for the different functionals. No plateau was observed for PBE-D3 at $T < 360\,\mathrm{K}$ and optB88-vdW at $T = 260\,\mathrm{K}$. To benchmark the results, the same procedure was carried for FF simulations of 32 water molecules simulated with TIP4P/2005, a model which provides good agreement with previous experiments for both bulk transport coefficients (discussed in [331, 216, 56] and in Chapter 2). In Fig. 4.3a we observe that the functional that better describes viscosity is SCAN, specially at high temperatures, although it fails at recovering η_{GK} temperature evolution, implying a failure of the functional at low temperatures. In general, we can see that all the functionals overpredict η_{GK} value.

In Fig. 4.4 we can see the mean squared displacement results as a function of time for all the temperatures, employed to obtain the size-dependent diffusion coefficient D_{PBC} from Eq. (4.28) by fitting $\langle r^2 \rangle$ slope at long times when the system is in the diffusive regime. D_{PBC} could not be determined within our simulation times for PBE-D3 at $T < 360\,\mathrm{K}$ and optB88-vdW at $T = 260\,\mathrm{K}$ because the system has not entered in the diffusive regime. This result is in agreement with the absence of plateau for η_{GK}. The corrected diffusion coefficient D_{GK} was obtained from D_{PBC} results applying Eq. (4.27) correction with $\eta \equiv \eta_{GK}$. The results are displayed in Fig. 4.3a. In analogy to η_{GK}, we observe in Fig. 4.3b that SCAN is the functional that better describes water diffusion coefficient at high temperatures, although it fails at low T.

Viscosity η and diffusion D are related through the Stokes-Einstein relation Eq. (4.33). Even though the failure of this relation is well known at low temperatures [333, 204, 244, 206, 234, 236], it still remains valid for a broad range of T. We can verify this statement by computing R_h for FF simulations of 128 water molecules (we worked on a bigger system in order to have smaller error bars). In Fig. 4.5 we can see that R_h remains constant, $R_h \sim 1\,\text{Å}$,

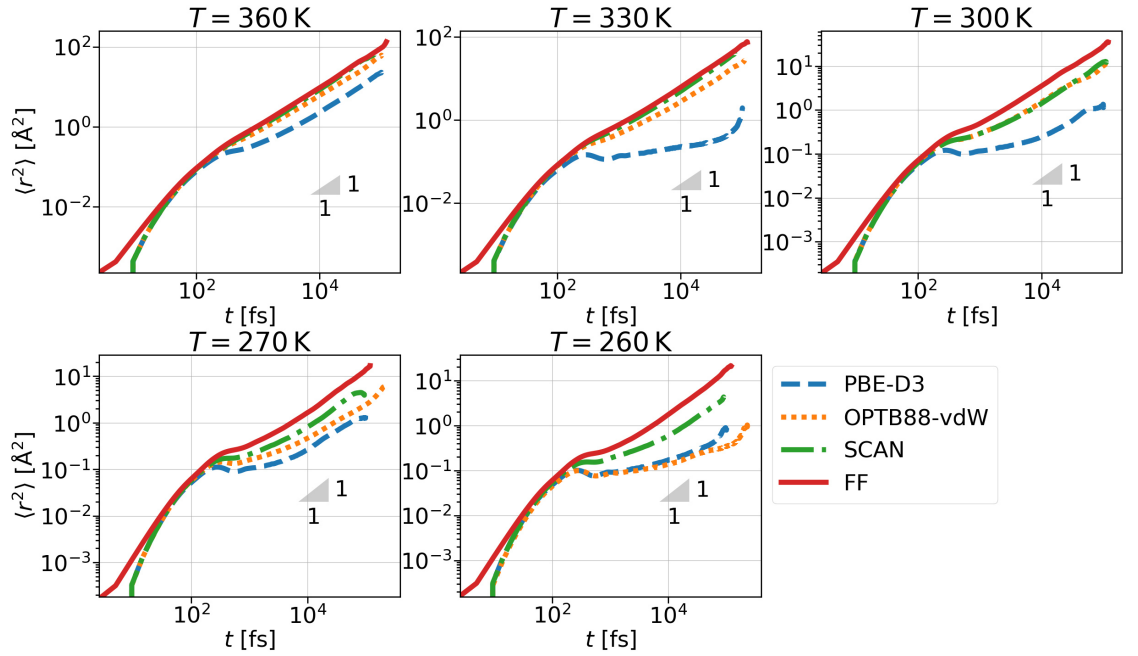

Figure 4.4: Mean squared displacement $\langle r^2 \rangle$ results for different functionals at different temperatures. Force field (FF) results are represented in continuous line. The 1/1 triangle is a guide-to-the-eye for a slope $\propto t$ expected if the diffusive regime is reached at long times.

for a broad range of temperatures, including the ones in our study ($T \in [260, 360]\,\mathrm{K}$), with a failure for the lowest temperature considered $T = 225\,\mathrm{K}$ as well as for the highest one $T = 360\,\mathrm{K}$, probably due to thermal fluctuations because the Stokes-Einstein relation is expected to hold at high termperatures where the fluid remains in its liquid state. Taking into account D size correction Eq. (4.27) and Stokes-Einstein relation Eq. (4.33), we can relate viscosity to D_{PBC} and the hydrodynamic radius:

$$\eta_{R_\mathrm{h}} = \frac{k_\mathrm{B}T}{6\pi D_{\mathrm{PBC}}}\left(\frac{1}{R_\mathrm{h}} - \frac{2.837}{L_{\mathrm{box}}}\right). \tag{4.35}$$

In the same way, we can also determine a relation for D_{R_h} independent of η from Eq. (4.27) and Eq. (4.33):

$$D_{R_\mathrm{h}} = \frac{D_{\mathrm{PBC}}}{1 - \frac{2.837 R_\mathrm{h}}{L_{\mathrm{box}}}}. \tag{4.36}$$

Therefore, viscosity and diffusion can be determined exclusively from the slope of the mean squared displacement at long times by imposing the hydrodynamic radius R_h. In order to test the applicability of this prediction, in Fig. 4.6 we display the results for η_{R_h} from Eq. (4.35) and D_{R_h} from Eq. (4.36) by imposing $R_\mathrm{h} = 1\,\text{Å}$ (value in agreement with the FF measures in Fig. 4.5). In Fig. 4.6 we can see a good agreement between the Green-Kubo and the hydrodynamic radius measures for both transport coefficients and for all the functionals considered, meaning that, although all the functionals fail in predicting viscosity and diffusion temperature dependence, all of them verify the Stokes-Einstein relation and the hydrodynamic radius remains constant independently of the water functional chosen.

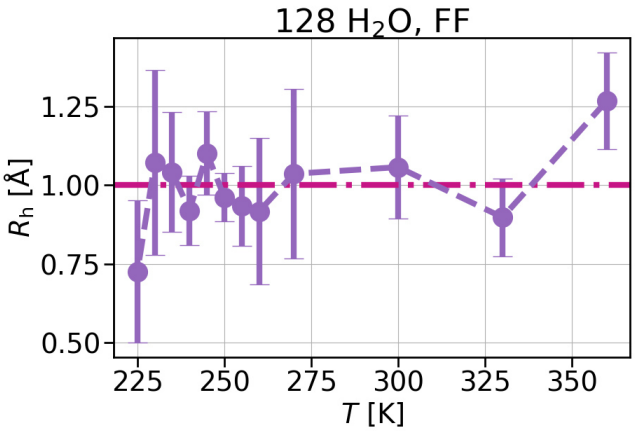

Figure 4.5: Hydrodynamic radius prediction from force field (FF) results for 128 water molecules, computed from the Stokes-Einstein relation. Dash-dotted line is a guide-to-the-eye at $R_\mathrm{h} = 1\,\text{Å}$.

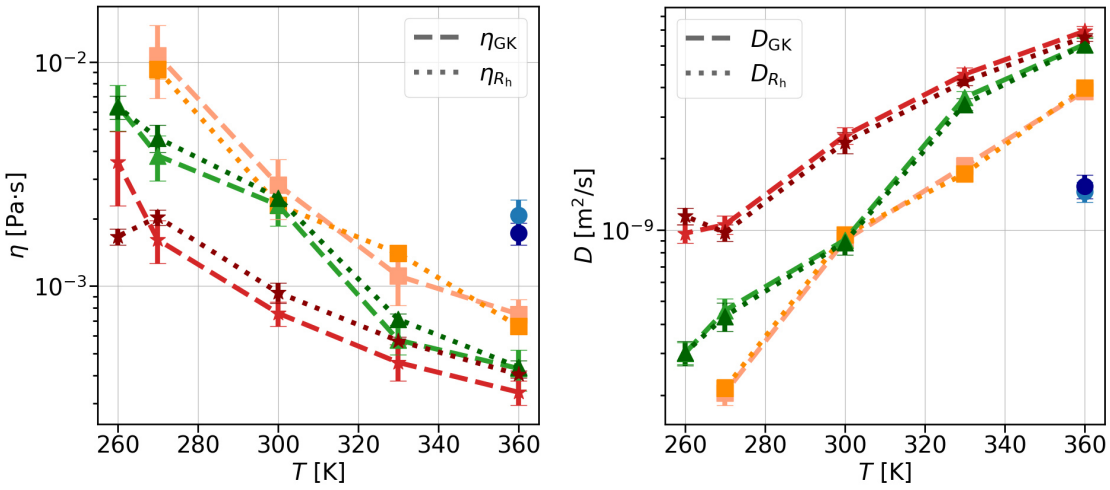

(a) (b)

Figure 4.6: Temperature evolution for different functionals of (a) shear viscosity from Eq. (4.35) and (b) diffusion coefficient from Eq. (4.36) with $R_\mathrm{h} = 1\,\text{Å}$. A good agreement is found between the hydrodynamic radius measures (dotted lines) and the Green-Kubo ones (dashed lines), implying all the functionals verify Stokes-Einstein relation with the same hydrodynamic radius R_h. The color and marker style representing the different functionals is the same as in Fig. 4.3.

4.4.2 Relation between structure and dynamics

Once the dynamic transport has been determined for the different functionals, we can explore its connection with structure. To understand the differences encountered between the different functionals, we show in Fig. 4.7 the radial distribution function $g(r)$ comparison. We observe in this graph that PBE-D3 corresponds to the most structured liquid, even at $T = 360\,\mathrm{K}$, in agreement with the high viscosity observations. We can also see that optB88-vdW and SCAN present similar $g(r)$ at the highest temperatures, although when lowering the temperature optB88-vdW water structures faster than SCAN and FF, which presents small disagreements from the second solvation shell. Due to the strong similarities and connection between the $g(r)$ results in Fig. 4.7 and the η_{GK} and D_{GK} results in Fig. 4.3, we proceed to explore the connection between structure and dynamics via the two-body entropy s_2 defined in Eq. (4.29). The running $s_2(r)$ integrals are represented in Fig. 4.8, where $s_2 = \lim_{r\to\infty} s_2(r)$. In this figure we can observe that the main contribution to the s_2 integral comes from the first solvation shell of the $g(r)$ with a minor contribution from the second and third peaks, with the exception of PBE-D3 for all temperatures and optB88-vdW at low T, which are strongly structured and for which the $g(r)$ does not reach a plateau at 1 within the simulation box, explaining the non-convergence of the $s_2(r)$ results for long r. In Fig. 4.8 the results detailed for the $g(r)$ related to the structural differences between the different functionals become clearer: we observe a close agreement between optB88-vdW, SCAN and FF at high temperatures, although optB88-vdW structures faster than SCAN when lowering the temperature, while SCAN remains close to FF results with small differences from the second solvation shell. It is interesting to note that the largest differences in the long distance plateau of s_2 arise from the long-range part contribution, where the *ab initio* simulations show a much more pronounced structuring and long-range oscillations as temperature is reduced. This is especially clear, from Fig. 4.8, for optB88-vdW, which describes well $g(r)$ first peak when compared to FF while it significantly deviates for the other solvation shells, particularly when the temperature decreases.

Before measuring s_2 from the long distance plateau of the $s_2(r)$ running integrals, we should account for finite size effects (FSE) that may affect our measurements, specially when working with small simulation boxes (as in our case, where we considered 32 water molecules and $L_{\mathrm{box}} = 9.85\,\text{Å}$). With that regard, the $g(r)$ results for FF simulations and different system sizes and water molecules (at fixed density $\rho = 1\,\mathrm{g/cm^3}$) are represented in Fig. 4.9. We can see that a little size effect appears for the third solvation shell at around $7\,\text{Å}$ for a system size of 32 water molecules. This system size effect disappears for 64 and 128 water molecules systems. Therefore, we should add a correction s_2^{FSE} to the s_2 values measured for 32 water molecules boxes. Such s_2^{FSE} value can be determined as the difference between the plateau measures of two different box sizes, for instance $s_2^{\mathrm{FSE}} = s_2(r_{\mathrm{plateau}}, 32\ \text{water}) - s_2(r_{\mathrm{plateau}}, 128\ \text{water})$. Another option, due to the small long distance $g(r)$ contribution to s_2, is to consider a cutoff radius r_{c} for the $g(r)$ so $s_2 = s_2(r_{\mathrm{c}})$ with r_{c} taken before the FSE appears; for instance $r_{\mathrm{c}} = 6.3\,\text{Å}$ (dash-dotted line in Fig. 4.9) in our simulations. In order to measure such correction and assess the validity of both approximations, we can find in Fig. 4.10a a comparison between the different approaches: $s_2(r_{\mathrm{plateau}})$ measures from the long distance $s_2(r)$ plateau (*i.e.* without accounting for FSE), $s_2(r_{\mathrm{c}})$ measures at the cutoff radius and $s_2^{\mathrm{corrected}} = s_2(r_{\mathrm{plateau}}) - s_2^{\mathrm{FSE}}$ for 32 water molecules, together with the $s_2(r_{\mathrm{plateau}})$ measures for 128 water molecules where no FSEs are expected. We see in Fig. 4.10a that both approaches, $s_2^{\mathrm{corrected}}$ and $s_2(r_{\mathrm{c}})$, are compatible with the s_2 measures for 128 water molecules. In the following, we will consider $s_2 \equiv s_2^{\mathrm{corrected}}$ for the different functionals.

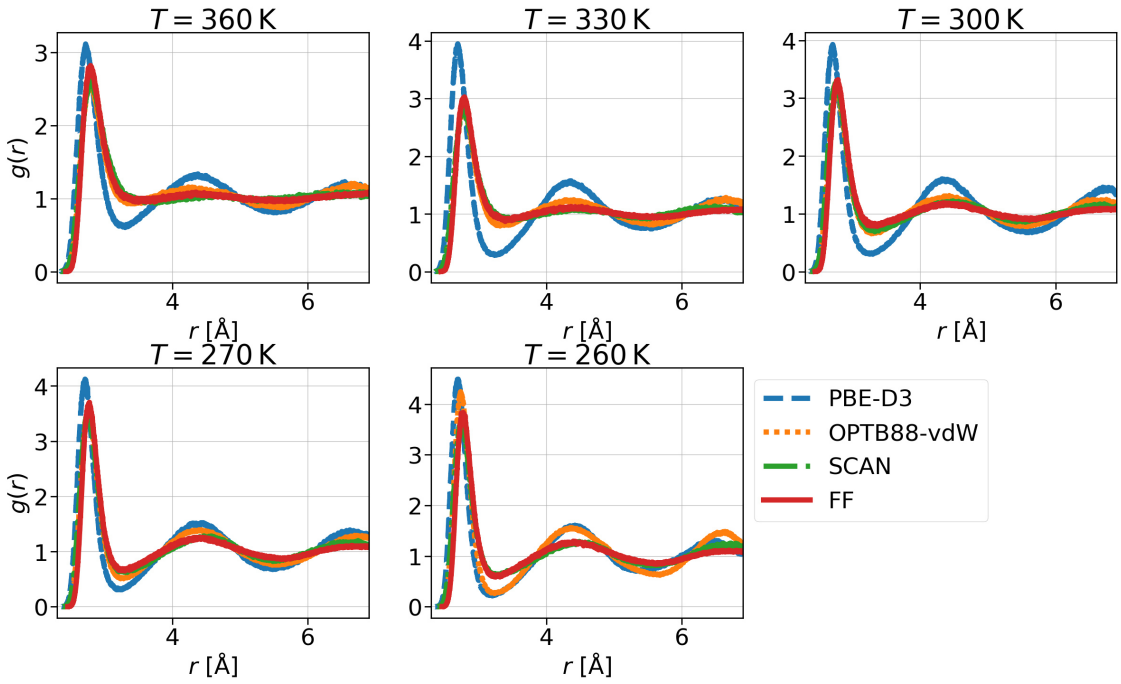

Figure 4.7: Radial distribution function $g(r)$ for different functionals at different temperatures together with FF results.

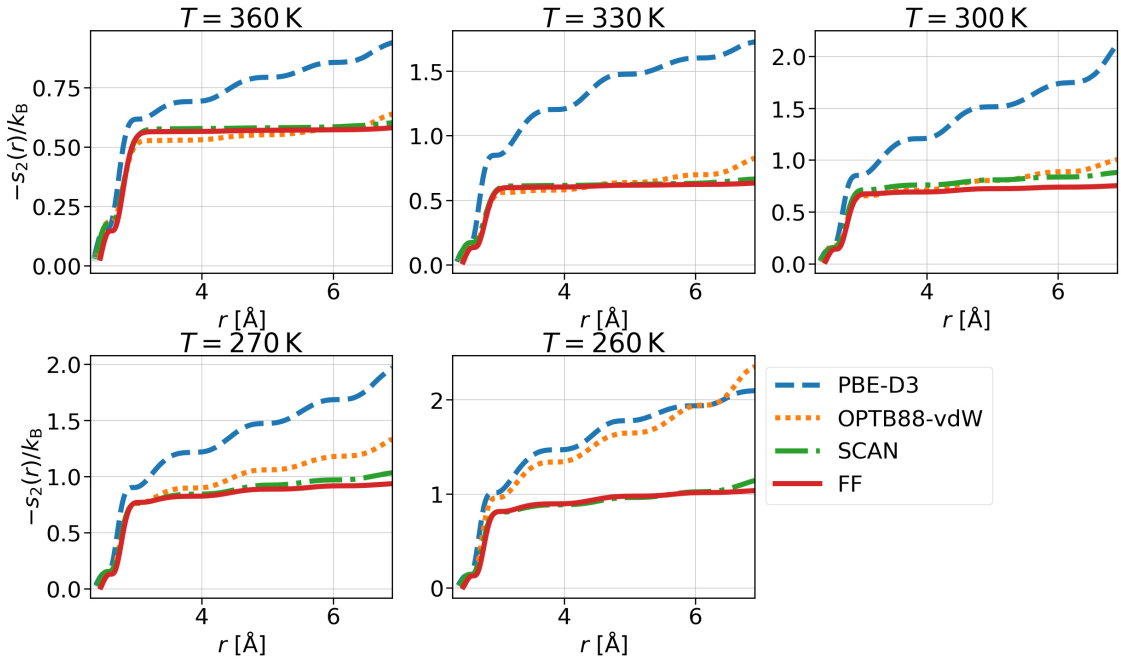

Figure 4.8: Two-body entropy per particle $s_2(r)$ running integral, determined from Eq. 4.29, for different functionals at different temperatures together with FF results.

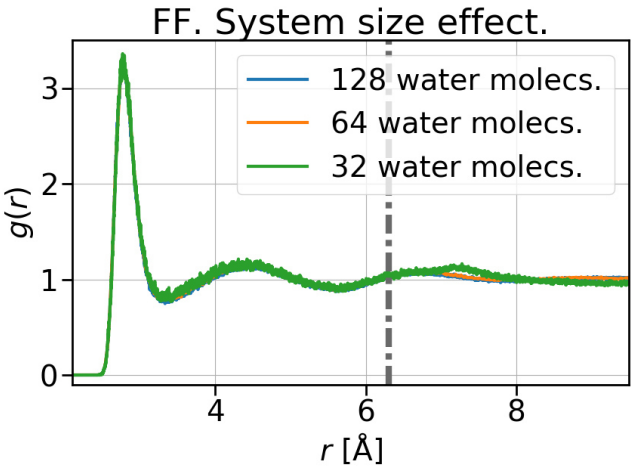

Figure 4.9: Radial distribution function $g(r)$ at $T = 300\,\mathrm{K}$ for FF measures and different system sizes (L_{box} such as $\rho = 1\,\mathrm{g/cm^3}$). We can observe finite size effects for 32 water molecules at around 7 Å. Dash-dotted line is a guide-to-the-eye at $r = 6.3\,\text{Å}$.

In Fig. 4.10b we represent the temperature dependence of the dimensionless two-body entropy s_2/k_{B} for the different functionals, compared with FF results for 32 water molecules (which are in good agreement with previous results [334]). We can observe that SCAN is the functional that better recovers the FF water structure, while optB88-vdW reproduces water structure at the higher temperatures ($T = 360\,\mathrm{K}$) although is highly over structured when the fluid enters in its supercooled regime. PBE-D3 totally fails at recovering the liquid two-body entropy at any temperature, and reaches a plateau for the lowest temperatures hinting a glass transition (the $g(r)$ oscillations amplitude is not significantly affected by temperature [300]).

Finally, in order to establish the relation between structure and transport coefficients for the different functionals, we tested Eq. 4.32 and Eq. 4.34 for the different functionals results from the mean squared displacement and the Green-Kubo integrals: η_{GK} and D_{GK} introduced in Fig. 4.3. In Fig. 4.11 we show the results for the dimensionless transport coefficients as a function of the two-body entropy for the different functionals. We can see that, although the functionals present disagreements between the transport coefficients and the s_2 results, all of them verify an exponential scaling of $\eta_{\mathrm{GK}}/\eta_0$ and D_{GK}/D_0 with s_2. With that regard, we performed the fit in Eqs. (4.32) and Eq. (4.34) for optB88-vdW, SCAN and FF (continuous lines in Fig. 4.11). No fit was performed for PBE-D3 due to the single value measure we could report for this functional. The fit results are indicated in Table 4.1. We can observe that, although out of the error bars, the fit parameters for SCAN and FF are the closest ones and that, for all functionals, $B' = -B$, implying a verification of the Stokes-Einstein relation Eq. 4.33.

Analogously to the R_{h} prediction represented in Fig. 4.6, we could use the s_2 exponential dependency of the transport coefficients in order to predict their value based on the s_2 results. By doing so, once the $\eta(s_2)$ and $D(s_2)$ dependency parameters have been established, we can predict the transport coefficients value from structural properties. Indeed, generally local properties as $g(r)$ require shorter simulations to converge, especially when using force based methods, as the one proposed in Ref. 311, to reduce the variance when compared to the conventional strategies based on particles positions binning. In Fig. 4.12 we can find the Green-Kubo results and their comparison with the s_2 fit predictions. We can see good agreement between measures and predictions for all the data. In particular,

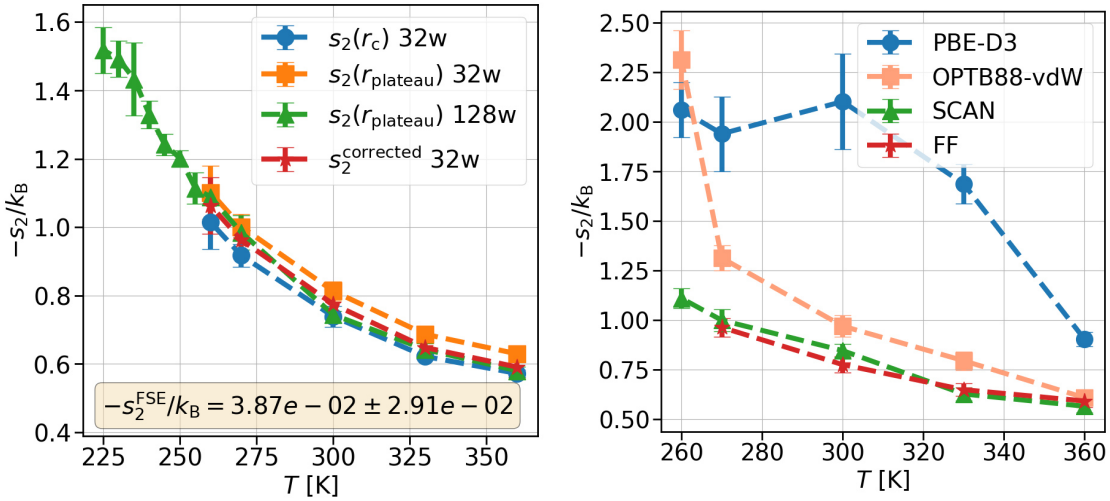

(a) (b)

Figure 4.10: Dimensionless two-body entropy s_2/k_B for (a) FF simulations of different box sizes measured from different approaches in order to account for FSEs for small simulation boxes (32 water molecules in this case); (b) different functionals and FF as a function of the temperature.

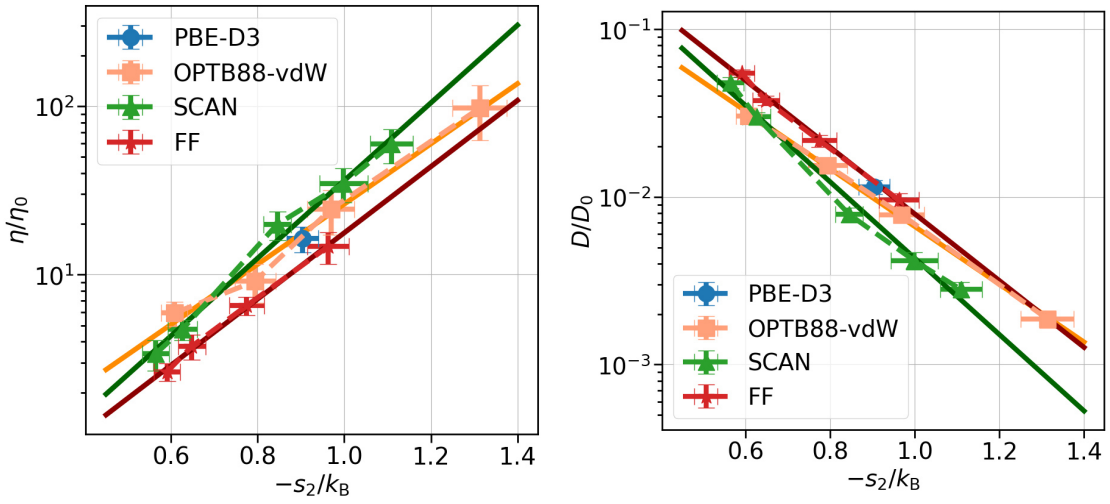

(a) (b)

Figure 4.11: Reduced (a) viscosity η/η_0 and (b) diffusion D/D_0, defined in Eqs. (4.32) and (4.34), as a function of the dimensionless two-body entropy s_2/k_B for different functionals and FF simulations. In continuum line are represented the respective exponential fits for each functional. The fit results are detailed in Table 4.1.

	η_{GK}/η_0		D_{GK}/D_0	
	$A'(\times 10^{-1})$	B'	$A(\times 10^{-1})$	B
optB88-vdW	4.29 ± 1.39	4.11 ± 0.34	3.52 ± 0.29	-3.97 ± 0.09
SCAN	1.79 ± 0.48	5.31 ± 0.31	8.17 ± 2.49	-5.24 ± 0.36
FF	1.92 ± 0.26	4.52 ± 0.18	7.73 ± 1.25	-4.58 ± 0.21

Table 4.1: Fit parameters of $y = A\exp(-Bs_2/k_B)$ with y the dimensionless viscosity η_{GK}/η_0 Eq. (4.34), and diffusion coefficient D_{GK}/D_0 Eq. (4.32), for different functionals and FF simulations.

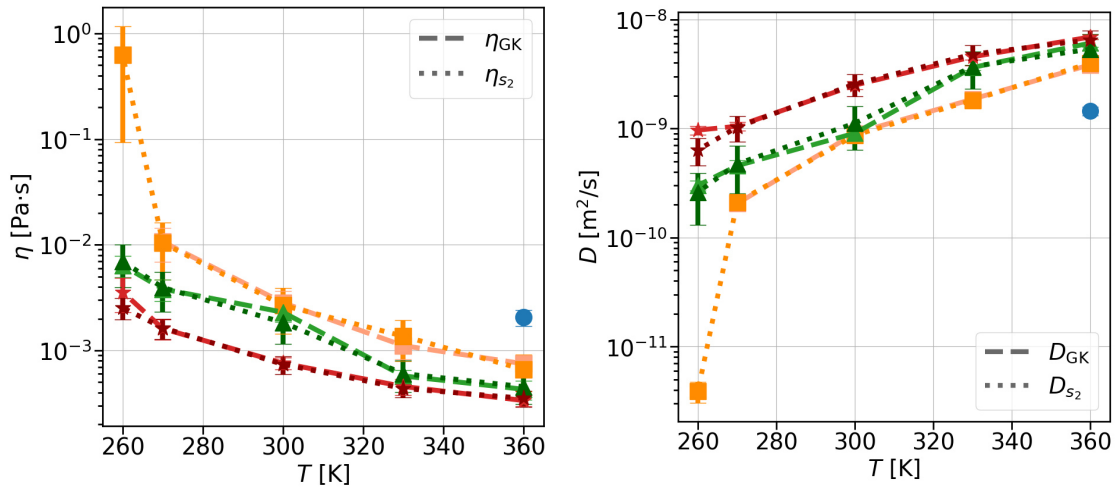

(a) (b)

Figure 4.12: Temperature evolution for different functionals of (a) shear viscosity from Eq. (4.34) and (b) diffusion coefficient from Eq. (4.32) with fit parameters from Table 4.1. A good agreement is found between the s_2 entropy prediction (dotted line) and the Green-Kubo ones (dashed lines), verifying the link between the structure and the transport coefficients. The color and marker style representing the different functionals is the same as in Fig. 4.3.

for optB88-vdW, we can see that, although we could not determine the transport coefficients for the lowest temperature ($T = 260\,\mathrm{K}$), from the s_2 fit we predict a very high viscosity and low diffusion, verifying the failure of the functional in order to reproduce the temperature dependence of both transport coefficients.

4.5 Summary and conclusions

In this chapter we employed density functional theory (DFT) to compute the hydrodynamic bulk transport coefficients, viscosity and diffusion, for water at different temperatures ($T \in [260, 360]\,\mathrm{K}$). We compared the results obtained for three different functionals (PBE-D3, optB88-vdW and SCAN) with FF simulations for TIP4P/2005 water, which shows good agreement with experiments for both viscosity and diffusion [331, 216, 56]. We observed that SCAN is the functional that better compares to FF simulation results with the more acceptable temperature evolution. We detected large discrepancies between functionals, with a major failure of PBE-D3, which is far too viscous when compared to the expected results, and even SCAN, which fails at low temperatures. Nevertheless,

although we disclosed great discrepancies between different functionals for viscosity and diffusion coefficient, both in the value and in the temperature evolution description, we saw that regardless of this, all functionals verified the Stokes-Einstein relation for the temperature range considered and, moreover, all of them predicted the same hydrodynamic radius $R_\mathrm{h} \sim 1\,\text{Å}$. This property, together with the finite size correction for the diffusion coefficient, allowed us to define a viscosity η_{R_h} and diffusion coefficient D_{R_h} measure only dependent on the slope of the mean squared displacement in the diffusive regime D_PBC, for known box size and fixed R_h.

Motivated by a possible connection between dynamic and structure, we computed the radial distribution functions for the different functionals. Analogously to the transport coefficient results, we observed that SCAN radial distribution function is the one that better compares to FF, with little differences at the lowest temperatures in the second and third solvation shells, whereas PBE-D3 was far more structured that SCAN and optB88-vdW at high temperatures, in agreement with the high viscosity value measured for this functional. An explicit relationship between dynamic and structure can be established through the two-body entropy excess, which is an integral of a function of the radial distribution. Supposing that the main contribution to the total entropy excess comes from this two-body interaction (*i.e.* $s_\mathrm{ex} \simeq s_2$, which has been proven to work well for water and supercooled-binary mixtures [307, 308, 309, 310]), it is expected that the reduced viscosity and diffusion coefficient will present an exponential excess-entropy scaling independent of temperature. We verified this exponential dependency on s_2 for both reduced bulk transport coefficients and, although the dependency was not universal (different fit parameters were used for the different functionals) we observed similar orders of magnitude in the exponential fit parameters.

For finishing, based on the established exponential dependency between the bulk transport coefficients, we computed both viscosity and diffusion coefficient from the s_2 results and the exponential fit parameters. This allowed us to estimate transport coefficients for functionals strongly structured (for instance optB88-vdW at 260 K), which present such a high viscosity value that longer simulations are needed in order to observe a well-defined plateau in the Green-Kubo integral. Therefore we propose here, once the exponential dependency has been determined for a few points, a method to determine viscosity and diffusion coefficient from only structural properties, which typically require shorter simulation times to converge [311]. This can be a useful technique to apply in the determination of transport coefficients for very viscous systems, where the associated time-scales are far from the ones computationally reachable nowadays with AIMD simulations. The connection between transport coefficients and the radial distribution function via the two-body entropy excess also establishes some guidelines to choose a functional for simulations of nanofluidic systems, where a functional which better reproduces water's structure will more likely reproduce its dynamical properties. The s_2 parameter can be also employed as a rule of thumb to develop better functionals, where the comparison between different s_2 values becomes more straightforward than the comparison between two $g(r)$ profiles, or just the value of the $g(r)$ minimum or maximum, which does not ensure a full structure correlation. Indeed, from the $s_2(r)$ running integrals, we showed the importance of reproducing not only the first solvation shell of the $g(r)$ but also the long range structure, which is a non-negligible contribution to s_2 value. This feature, together with the bulk transport coefficients entropy scaling, hint that it is important for the functionals to reproduce not only $g(r)$ first peak, but also its long range behavior, critical to obtain an accurate description of dynamical properties such as viscosity and diffusion coefficient.

It is still left to understand the origin of the discrepancies in terms of temperature

evolution of viscosity and diffusion temperature evolution, specially striking for the SCAN functionals, which shows good agreement at high temperatures with FF and experimental results but fails at low temperatures. Such failure at low T points may have two different origins. First, maybe the given functional overestimates the glass transition temperature of water, *i.e.* the viscosity deviates from the Arrhenius behavior at a larger temperature than the expected one. Secondly, and more interestingly, there can be a link between the low temperature functional description at low temperatures and the nuclear quantum effects (NQEs). Standard AIMD methods, including DFT, treat the nuclei as classical particles, and solve the quantum mechanics equations only for the electrons. However, de Broglie thermal length (inversely proportional to $\sqrt{T}$) becomes larger at low temperatures, and the NQEs may not be negligible any more. There are currently different methods to implement such NQEs [297, 295], and the difficulty arises in terms of the longer computation times needed to solve the nuclear quantum equations, which add to the longer simulation times needed at low T for the dynamical properties to converge. A possible way out can be the development and use of machine learning potentials, trained to mimic the desired functional and which require less expensive simulations.

Chapter 5

Modelling fast and versatile thermo-osmotic flows

"God made the bulk; the surface was invented by the devil."
Wolfgang Pauli, Nobel Prize in Physics, 1945

Contents

5.1 Introduction

In previous chapters, we have studied bulk and interfacial mechanisms, addressing different physical processes characteristic of the molecular scale. Among those processes, slip has appeared as a fundamental mechanism resulting from the competition between bulk and interfacial transport at the nanoscale. But what is the role of slip in energy conversion and how can it help us to understand and conceive nanofluidic systems with applications in optimizing the energy conversion in those systems?

Due to the increasing world energy consumption and the need of new clean energies, waste heat harvesting is a major challenge for the decades to come. Some of the most common difficulties to harvest waste heat come from the small temperature differences

between the source and the environment ($< 50\,^\circ$C) [83], as well as from the need to use rare, expensive and often toxic thermoelectric materials [335]. Alternatively, thermo-osmotic flows (generated at liquid-solid interfaces by temperature gradients) can be used to transform waste heat into electricity via a turbine [336], or to pump water for desalination [8, 337]. Historically, Derjaguin and Sidorenkov measured the first reported water flow by applying a temperature gradient through porous glass [338]. Since then, a broad literature has been devoted to the measure of the thermo-osmotic response, whether from experiments [339, 340, 341, 342] or molecular dynamics simulations [343, 344, 345, 346]. Nevertheless, some disagreements have been reported in the results for aqueous electrolytes, with a finite thermo-osmotic response reported for pure water and uncharged membranes [340], and disagreements in the flow direction (towards the hot or the cold side) for similar systems [347, 348, 349, 350]. Such differences cannot be understood by the classical theory [351] developed by Derjaguin and Sidorenkov [338, 352], and by Ruckenstein for thermophoresis [353]. This theory, based on the electrostatic enthalpy of the electric double layer appearing close to charged walls, predicts that the flow is controlled by the surface charge, and always goes to the hot side.

Thermo-osmosis has seen a renewed interest due to the massive thermo-osmotic responses predicted by the use of novel materials, such as soft nanochannels [354], carbon-nanotubes [337, 345, 84] or graphene [344], together with novel experiments by Bregulla et al. [350], which first reported a microscale observation of thermo-osmotic flows. Thermo-osmotic flows could in particular be boosted by the failure of the no-slip boundary condition (BC), which considers that the fluid velocity vanishes in contact with the wall, when working with nano and micro-systems [99]. In this case, as we have already discussed in previous chapters, a velocity jump $v_{\rm slip}$ is reported, and the BC is described by a more general expression first proposed by Navier [19, 101]:

$$v_{\rm s} = b \left. \frac{\partial v}{\partial z} \right|_{z=z_{\rm s}}, \tag{5.1}$$

where $z_{\rm s}$ corresponds to the shear plane position and b is the slip length. The role of interfacial hydrodynamics for thermo-osmosis modelling has already been explored in the literature [343, 344, 355]. Furthermore, in recent work on thermo-electricity, the critical role of the solvent enthalpy in describing the response has been highlighted for a modelled, highly hydrophobic surface [85].

Following this work, we propose in this chapter an analytical framework with the objective to predict thermo-osmosis of aqueous electrolytes confined by charged surfaces, extendable to thermoelectricity and thermophoresis processes. The solvent contribution and the electrostatic ionic interactions are shown to play the leading role along with hydrodynamic slip. We apply the new model to a wide range of systems, varying the wetting interaction, salt type and concentration, and the surface charge. We report large thermo-osmotic responses, comparable to the highest responses predicted for special systems from previous simulations [343, 344, 337, 84], as well as a change of sign in the flow direction, which cannot be predicted by only considering electrostatic interactions, and which can be crucial in order to interpret the different experimental results reported in the literature.

5.2 Analytical framework derivation

In order to account for the different contributions to the thermo-osmotic response coefficient, we will briefly introduce some general concepts in response theory we will

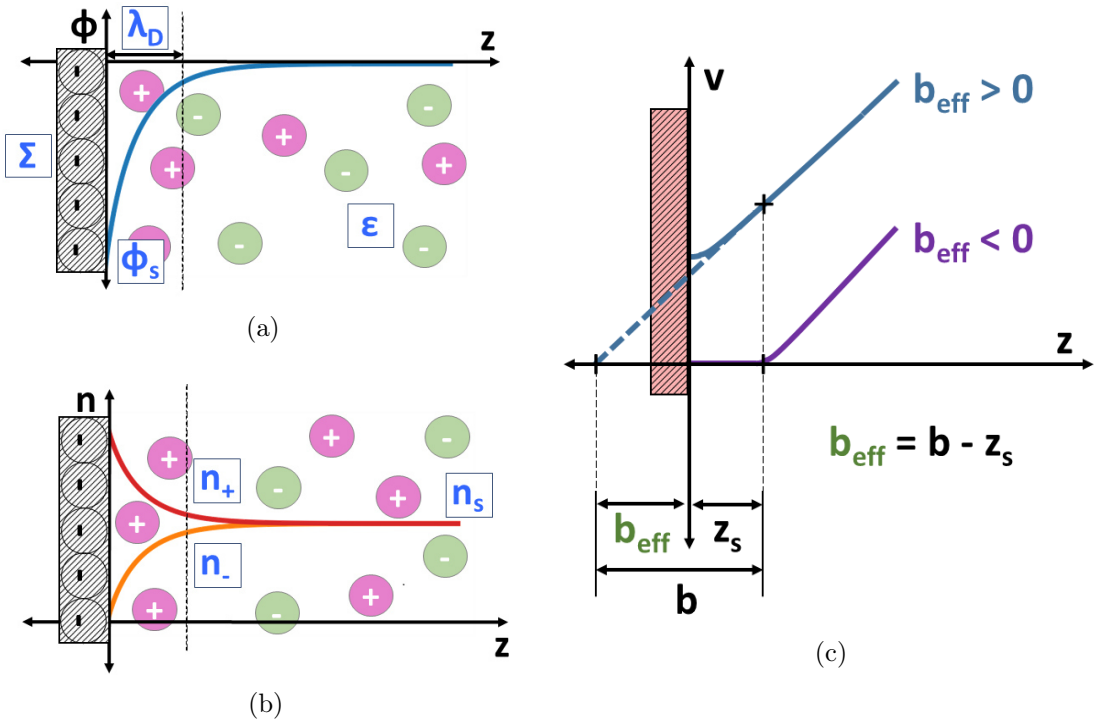

Figure 5.1: a-b) Local picture of the electrical double layer at a charged wall: (a) Profile of reduced electric potential ϕ, with ϕ_s the value at the wall; (b) Profiles of cation n_+ and anion n_- densities, with n_s the bulk value. (c) Schematics of the effective slip length b_{eff} as a function of the slip length b and the shear plane position z_s. We distinguish between the slip situation $b_{\text{eff}} > 0$, when the velocity profile is non-zero in the channel, and the stagnant layer situation $b_{\text{eff}} < 0$, when the velocity profile vanishes in the channel.

work with. We can describe the thermodynamics of irreversible processes which occur in systems out of global equilibrium but stationary (with local equilibrium). Non-equilibrium thermodynamics is based on the local entropy production S given by, following the second law of thermodynamics:

$$S = \sum_i J_i X_i \geq 0, \tag{5.2}$$

where J_i and X_i are the flux-force pairs in the system, the flux being the rate of a flow per unit area. If the system is driven not too far from equilibrium, we can assume that each flux is a linear combination of all the forces [356]:

$$J_i = \sum_{j=1}^{n} M_{ij} X_j, \tag{5.3}$$

with n the number of independent flux-force pairs. The different M_{ij} coefficients in Eq. (5.3) form the so-called response matrix of a stationary non-equilibrium thermodynamic system, and it describes the system response to a perturbation. Let's consider for example a fluid system, described in terms of temperature, matter density and pressure. If we apply a pressure difference to this system, it will generate a matter flow from the high pressure regions towards the low pressure regions. Analogously, by imposing a temperature difference in the fluid, it will generate a heat flow. But, what will happen if pressure and temperature vary at the same time? If a temperature gradient is applied at constant

pressure it will cause a matter flow (as in convection) and if a pressure gradient is applied at constant temperature it will produce a heat flow in the system. What is remarkable is that such matter flow per unit of temperature difference is equal to the heat flow per unit of pressure difference. This equality, which can written in terms of response coefficients as

$$M_{ij} = M_{ji}, \tag{5.4}$$

was proven necessary via statistical mechanics by Lars Onsager as a consequence of the microscropic reversibility of the system [357, 358]. Thanks to these relations, Onsager is typically considered the founder of the field of non-equilibrium thermodynamics, which remains very active nowadays due to its promising applications on heat harvesting and energy production. For instance, let's consider the response matrix for the flow rate density j_{q}, the heat flux density j_{h} and the electric current density j_{e}:

$$\begin{pmatrix} j_{\mathrm{q}} \\ j_{\mathrm{h}} \\ j_{\mathrm{e}} \end{pmatrix} = \begin{pmatrix} \cdot & M_{\mathrm{to}} & M_{\mathrm{eo}} \\ M_{\mathrm{to}} & \cdot & M_{\mathrm{te}} \\ M_{\mathrm{eo}} & M_{\mathrm{te}} & \cdot \end{pmatrix} \begin{pmatrix} -\nabla p \\ -\frac{\nabla T}{T} \\ E \end{pmatrix}, \tag{5.5}$$

with p the pressure, T the temperature and $E = -\nabla V$ the electrostatic field and V the potential. This response matrix describes the response coefficients of three different thermodynamic processes: thermo-osmosis M_{to}, electro-osmosis M_{eo} and thermoelectricity M_{te}, the three of them related to the flow generation by applying a temperature gradient or an electric field, or to the electricity generation by an applied temperature gradient.

As mentioned in the introduction, thermo-osmotic flows (flows generated in micro and nanofluidic systems by thermal gradients) could provide an alternative approach to harvest waste heat. However, such use would require massive thermo-osmotic flows, which are up to now only predicted for special and expensive materials [335]. There is thus an urgent need to design affordable nanofluidic systems displaying large thermo-osmotic coefficients. But first, what controls thermo-osmosis? When a dielectric is plugged in water, a molecule in the surface can be dissociated to release ions when the thermal forces on the order of $k_{\mathrm{B}}T$ are greater than the electrostatic interactions. Such is the case of polar liquids like water, for which the Bjerrum length ℓ_{B} (representing the distance at which the thermal energy is comparable to the electrostatic interaction energy, $\ell_{\mathrm{B}} \sim 7$ Å for water) is comparable to (or smaller than) the interatomic distance [359]. How water molecules and dissolved ions in a solution electrostatically interact with the surface has been extensively investigated, theoretically from the 19th century and more extensively by Gouy and Chapman at the beginning of the 20th century [360, 361], and experimentally in the 1980s [347, 352]. We simply recall here the main ingredients of the well-established and so-called Gouy-Chapman theory, and discuss its limitations. Educational presentations of the Gouy-Chapman theory can be found in books [362, 363, 359], book chapters [364, 365], and articles [366], discussing in particular applications to nanofluidics [87, 29, 367, 368]; useful equations for the description of slit and cylindrical channels are gathered in Appendix B. With the final objective of obtaining a decomposition of the thermo-osmotic response coefficient M_{to} in terms of different contributions, an analytical expression in terms of enthalpy density δh is proposed. All these quantities were computed within the Poisson-Boltzmann framework. The range of validity of such framework is also discussed here.

5.2.1 Poisson-Boltzmann framework

Let us consider a charged surface in contact with a Z:Z aqueous electrolyte. Far from the interface, the positive and negative ions are dispersed in the solution, due to

entropy, and will have the same concentration. Nevertheless, close to the wall, the ions of the opposite sign of the ones of the charged surface will tend to accumulate, forming the so-called electrical double layer (EDL).

Gouy and Chapman described the ion repartition near the wall, and the subsequent electrostatic potential induced by the surface charge, under four main hypotheses:

1. The ions are considered as punctual and highly mobile.

2. The solvent dielectric permittivity ε is considered constant throughout the system.

3. The charge density ρ_e and the electric potential V are continuous fields.

4. All the descriptions are mean field: hence, we neglect ion-ion correlations and ion-solvent interactions.

For simplicity, let's consider a smooth charged surface, located at $z = 0$, with uniform surface charge density Σ (Figs. 5.1a and 5.1b). In this case, the electric potential along the channel $V(z)$ will be given by the Poisson equation:

$$\varepsilon \frac{\mathrm{d}^2 V}{\mathrm{d}z^2} = -\rho_\mathrm{e}(z), \tag{5.6}$$

where $\varepsilon = \varepsilon_0 \varepsilon_\mathrm{r}$ is the solvent permittivity, and ρ_e is the charge density along the channel. Such charge density can be expressed in terms of the positive n_+ and negative n_- ion densities as $\rho_\mathrm{e}(z) = q[n_+(z) - n_-(z)]$, where $q = Ze$ is the absolute ionic charge, with e the elementary charge and Z the ion valence. As ions are highly mobile, thermal fluctuations of V and ρ_e are neglected. The only contribution to the ion energy is electrostatic, the ions concentrations along the channel will be given by the Boltzmann equation:

$$n_\pm(z) = n_\mathrm{s} \exp[\mp \beta q V(z)], \tag{5.7}$$

where n_s is the salt concentration far from the wall and $\beta = 1/(k_\mathrm{B} T)$, with T the thermodynamic temperature and k_B the Boltzmann factor. Taking into account Eq. (5.7), the charge density can be expressed as $\rho_\mathrm{e}(z) = q[n_+(z) - n_-(z)] = -2q\, n_\mathrm{s} \sinh[\beta q V(z)]$. Finally, we can substitute this expression for ρ_e in the Poisson Eq. (5.6), resulting in:

$$\frac{\mathrm{d}^2 \phi(z)}{\mathrm{d}z^2} = \frac{2\beta q^2 n_\mathrm{s}}{\varepsilon} \sinh[\phi(z)] = 8\pi n_\mathrm{s} \ell_\mathrm{B} \sinh[\phi(z)], \tag{5.8}$$

where $\phi(z) = \beta q V(z)$ is the reduced potential. This expression involves a system characteristic length, the Bjerrum length $\ell_\mathrm{B} = \frac{\beta q^2}{4\pi\varepsilon}$, previously introduced. By defining the Debye length as

$$\lambda_\mathrm{D} = \frac{1}{\sqrt{8\pi \ell_\mathrm{B} n_\mathrm{s}}}, \tag{5.9}$$

Equation (5.8) can be rewritten as:

$$\frac{\mathrm{d}^2 \phi(z)}{\mathrm{d}z^2} = \frac{1}{\lambda_\mathrm{D}^2} \sinh[\phi(z)]; \tag{5.10}$$

typically referred to as the Poisson-Boltzmann equation.

a. Exact solution for a planar wall

We can solve Eq. (5.10) analytically for some specific geometries and conditions (see Appendix B), as in the case of a planar smooth wall. For this system geometry, assuming a vanishing potential far from the wall, Eq. (5.10) can be integrated as:

$$\phi(z) = 4\,\mathrm{atanh}\Big(\gamma e^{-z/\lambda_\mathrm{D}}\Big); \tag{5.11}$$

with $\gamma = \tanh(\phi_\mathrm{s}/4)$, where ϕ_s is the potential at the wall, represented in Fig. 5.1a. In Fig. 5.1b we can find represented the ions distributions given by Eq. (5.7) with the potential solution for planar walls. From the Poisson-Boltzmann solution for planar walls Eq. (5.11), we can state a relationship between the surface potential ϕ_s, and the surface charge density Σ, by taking into account that at the wall the electric field E_s reads $E_\mathrm{s} = -\frac{\mathrm{d}V}{\mathrm{d}z}\big|_{z=0} = \frac{\Sigma}{\varepsilon}$. The expression which relates ϕ_s and Σ for planar walls is called the Grahame equation:

$$\Sigma = \frac{q}{2\pi\ell_\mathrm{B}\lambda_\mathrm{D}}\sinh\left(\frac{\phi_\mathrm{s}}{2}\right); \tag{5.12}$$

which can be simplified as:

$$\phi_\mathrm{s} = 2\,\mathrm{sgn}(\Sigma)\,\mathrm{asinh}\left(\frac{\lambda_\mathrm{D}}{\ell_\mathrm{GC}}\right), \tag{5.13}$$

where $\ell_\mathrm{GC} = q/(2\pi\ell_\mathrm{B}|\Sigma|)$ is the Gouy-Chapman length.

We can also find an approximate solution to Eq. (5.10) when considering the small Σ limit. This case is analogous to consider small ϕ (*i.e.* $qV \ll k_\mathrm{B}T$), so we can linearize $\sinh[\phi(z)] \sim \phi(z)$, obtaining:

$$\phi^\mathrm{DH}(z) = \phi_\mathrm{s}\exp\left(-\frac{z}{\lambda_\mathrm{D}}\right). \tag{5.14}$$

This small surface charge density limit is known as the Debye-Hückel limit (DH), and can be found from Eq. (5.13) when $\lambda_\mathrm{D} \ll \ell_\mathrm{GC}$, which occurs for low Σ and/or large n_s. The opposite situation, when working under high Σ and/or low n_s, *i.e.* high potential, is known as the Gouy-Chapman limit (GC), and it corresponds to the limit when $\lambda_\mathrm{D} \gg \ell_\mathrm{GC}$.

b. Validity of the hypotheses and limitations of the Poisson-Boltzmann framework

We can now discuss the validity of this modeling and in particular the limits of the different hypotheses underlying in the Gouy-Chapman theory. Let's first consider the case of the ionic correlations. Such ionic correlations can be discarded if the typical Coulombic interaction energy between two ions is small compared to $k_\mathrm{B}T$, which reads if we introduce the so-called plasma parameter Γ [369, 370, 371]:

$$\Gamma = \frac{\beta q^2}{4\pi\varepsilon d_\mathrm{ions}} = \frac{\ell_\mathrm{B}}{d_\mathrm{ions}} < 1, \tag{5.15}$$

where d_ions is the typical inter-ionic distance. At the surface, $1/d_\mathrm{ions}^2 = |\Sigma|/q$, and then we can rewrite Γ as

$$\Gamma = \sqrt{\frac{\ell_\mathrm{B}}{2\pi\ell_\mathrm{GC}}}. \tag{5.16}$$

This ratio between two characteristic system lengths allows us to define a critical surface charge density Σ^{c}, related to $\ell^{\mathrm{c}}_{\mathrm{GC}}$, above which ionic correlations must be taken into account. We can consider non-negligible ion-correlations when $\Gamma \gg 1$, *i.e.* when $\ell_{\mathrm{GC}} \ll \ell^{\mathrm{c}}_{\mathrm{GC}} = \ell_{\mathrm{B}}/(2\pi)$ or, in terms of Σ^{c}:

$$|\Sigma^{\mathrm{c}}| = \frac{q}{\ell_{\mathrm{B}}^2}, \tag{5.17}$$

on the order of $330\,\mathrm{mC/m^2}$ for monovalent ions in water at 300 K.

We can follow the same procedure to obtain a limit in terms of critical salt concentration in the bulk $n_{\mathrm{s}}^{\mathrm{c}}$, by considering the associated bulk inter-ionic distance: $d_{\mathrm{ions}} = (2n_{\mathrm{s}}^{\mathrm{c}})^{-1/3}$ (taking into account that the ion concentration is twice the salt concentration). As previously described, we will consider the limit of the model validity for $\Gamma \sim 1$. Therefore, from Eq. (5.15), we finally obtain:

$$n_{\mathrm{s}}^{\mathrm{c}} = \frac{1}{2\,\ell_{\mathrm{B}}^3}. \tag{5.18}$$

of the order of $n_{\mathrm{s}}^{\mathrm{c}} \simeq 2\,\mathrm{M}$ for a monovalent salt in water at 300 K.

Finally, it is important to note that, for monovalent ions in water at room temperature, $\ell_{\mathrm{B}} \sim 7\,\text{Å}$ is greater than the ionic size, so that there will be no steric repulsion effects, when $\Gamma = \ell_{\mathrm{B}}/d_{\mathrm{ions}} < 1$.

Other assumptions for the Gouy-Chapman theory, aside of the discussed ionic correlations effects, can pose a problem when working under the Poisson-Boltzmann framework. Different adjustments to the model can be performed for a more accurate description of reality, by taking into account the spatial heterogeneities due to the molecular solvent structure, which affect several parameters such as the dielectric permittivity along the channel or the non-electrostatic interaction potential [372], and which one can describe by introducing a position-dependent polarization of the medium in Eq. (5.6) [213]. Although always present, these short-range interactions can significantly affect the ion distribution when the Debye length λ_{D} is of order of the first absorption layer of water (around one molecular diameter). Aside of local effects, other contributions to the ion energy can also be taken into account within the Boltzmann factor, such as the interactions of the ions with the solvent and the wall [373]. Indeed, the ion-size can play a critical role in the ion distribution behavior due to its interaction with the solid, and for instance the density of large ions can be interfacially enhanced due to the inhomogeneties of the solvation energy or solvation enthalpy excess.

Still, the validity of the presented model has been assessed by numerous experiments and simulations under standard conditions and typically for symmetric monovalent salts dissolved in water, which are systems that can be easily found in everyday media (for example sea water), and with a deep theoretical interest due to its multiple and promising applications, as the ones discussed in the following.

5.2.2 The hydrodynamic boundary condition and the osmotic velocity profile

We have already seen in previous chapters, that the standard no-slip boundary condition (BC), which supposes that the fluid velocity vanishes when in contact to the wall, needs to be refined at the nanoscale. Two different situations can occur. First, we can consider the presence of a liquid stagnant layer close to the wall (Fig. 5.1c with $b_{\mathrm{eff}} < 0$), implying a vanishing velocity profile inside the channel. The typical size of the stagnant layer, due to the layering of the fluid close to the wall, is of order of one molecular diameter ([185], Chapter 2), $\sigma \sim 2.75\,\text{Å}$ for water.

Second, we can consider an interfacial velocity jump (Fig. 5.1c with $b_{\text{eff}} > 0$), also known as slip velocity v_{slip}, which implies a non vanishing fluid profile at the interface. As detailed in Chapter 2, bulk and interface transport coefficients (namely the shear viscosity η and the liquid-solid friction coefficient λ), can be related via the partial slip BC Eq. (5.1), which introduces the slip length b and the shear plane position z_{s}. We have previously discussed that, although this feature is always present for a confined fluid, it is at the nano- and micro-metric scales that it becomes critical to take it into account, due to the typical order of magnitude of the slip length, $b \sim 10^0 - 10^2$ nm [30, 29, 31].

We can account for both situations by introducing an effective slip length $b_{\text{eff}} = b - z_{\text{s}}$. We can see in Fig. 5.1c that $b_{\text{eff}} \geq 0$ corresponds to the slip situation and $b_{\text{eff}} < 0$ corresponds to the stagnant layer situation. In the last case, $-b_{\text{eff}}$ identifies with the size of the stagnant layer present at the liquid-solid interface, where the liquid velocity vanishes. In terms of wettability, we can expect the presence of a stagnant layer in the most hydrophilic systems, where the liquid molecules have more tendency to accumulate close to the wall, while a slipping system will correspond to hydrophobic interfaces, with small liquid-solid friction coefficient due to the depletion of the liquid atoms from the wall.

The appropriate boundary conditions together with the Stokes equation

$$-\eta \Delta v = -\nabla p + f_{\text{ext}}, \tag{5.19}$$

where p is the pressure and f_{ext} is an applied external force per unit volume, allow us to derive a general expression for the osmotic velocity profile close to a planar wall as a function of the force density profile in the interaction layer. Let us first simplify Eq. (5.19) by considering $f = -\nabla p + f_{\text{ext}}$ the force density generated by the thermodynamic gradients in the interfacial layer. Integrating Stokes Eq. (5.19), in the lubrication limit and supposing force and therefore velocity derivative vanish far from the wall, we obtain:

$$-\eta \frac{\partial v_x(z)}{\partial z} = \int_{+\infty}^{z} f(z')\,\mathrm{d}z'. \tag{5.20}$$

Integrating again between the position z_0 (corresponding to the wall position in the slip situation and to the position where the velocity profile vanishes in the stagnant layer case) and z, we obtain:

$$v_x(z) - v_x(z_0) = \int_{z_0}^{z} \mathrm{d}z' \int_{z'}^{\infty} \frac{1}{\eta} f(z'')\,\mathrm{d}z''. \tag{5.21}$$

We can replace $v_x(z_0)$ by the relevant boundary condition from Eq. (5.1) (with $b = 0$ in the stagnant layer situation) obtaining:

$$v_x(z) = \frac{1}{\eta}\left[\int_{z_0}^{z} \mathrm{d}z' \int_{z'}^{\infty} f(z'')\,\mathrm{d}z'' + (b_{\text{eff}} + z_0)\int_{z_0}^{\infty} f(z)\,\mathrm{d}z\right]; \tag{5.22}$$

which reduces, integrating by parts and taking its limit far from the wall, to:

$$v_{\text{osm}}^{\infty} = \frac{1}{\eta}\int_{z_0}^{\infty} (z + b_{\text{eff}})\, f(z)\,\mathrm{d}z, \tag{5.23}$$

with $z_0 = 0$ in the slip case ($b_{\text{eff}} \geq 0$) and $z_0 = -b_{\text{eff}}$ in the stagnant layer case (see Fig. 5.1c). Osmotic velocity profiles, given by the general expression Eq. (5.23) far from the wall, are of special interest when computing the different coefficients of the response matrix.

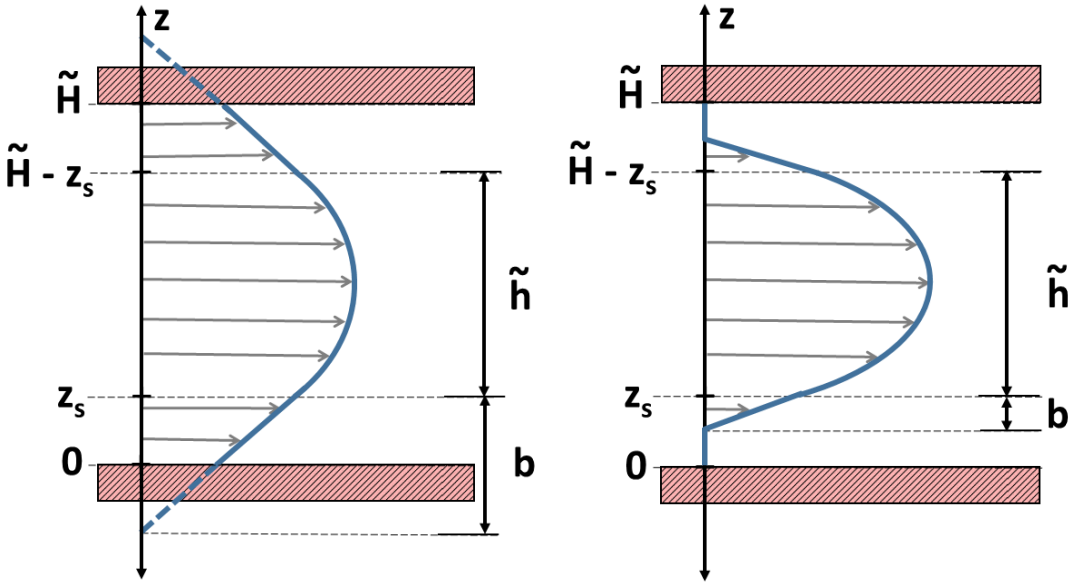

(a) Slip situation (b) Stagnant layer situation

Figure 5.2: Schematics of the Poiseuille velocity profile generated by applying a pressure gradient $-\nabla p$ to the fluid particles in the direction parallel to the wall.

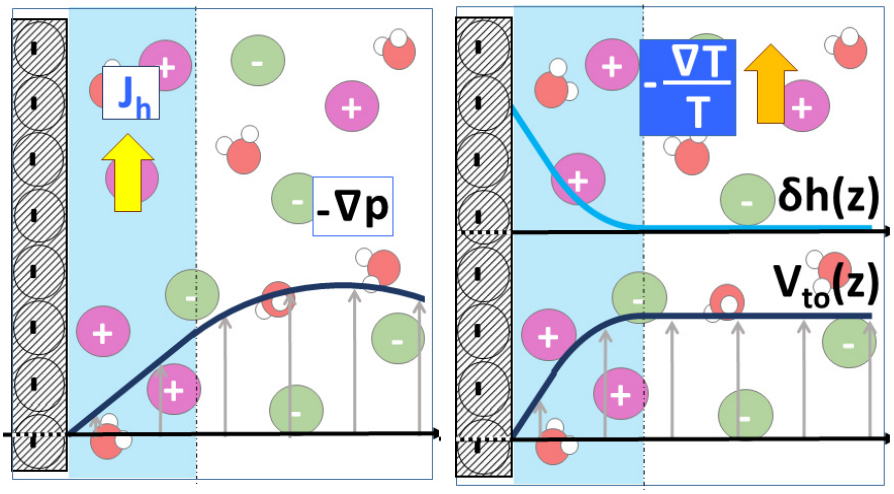

(a) Mechanocaloric effect (b) Thermo-osmotic flow

Figure 5.3: (a) Generation of a heat flux J_{h} by applying a pressure gradient $-\nabla p$ in an aqueous electrolyte. Due to Onsager's reciprocal relations, the response of this system is equivalent to the thermo-osmotic response.(b) Thermo-osmotic flow in an aqueous electrolyte, consisting in the generation of a thermo-osmotic velocity profile v_{to} by applying a temperature gradient $-\nabla T/T$ in the direction parallel to the wall, due to the variations in the enthalpy excess density profile δh.

5.2.3 Thermo-osmotic response

Thermal gradients along liquid-solid interfaces generate a flow, called thermo-osmotic flow. From the response matrix in Eq. (5.5), the elements that contribute to the thermo-osmotic response are:

$$\begin{pmatrix} j_\mathrm{q} \\ j_\mathrm{h} \end{pmatrix} = \begin{pmatrix} \cdot & M_\mathrm{to} \\ M_\mathrm{to} & \cdot \end{pmatrix} \begin{pmatrix} -\nabla p \\ -\frac{\nabla T}{T} \end{pmatrix}, \tag{5.24}$$

where j_q is the flow rate density (*i.e.* the average flow velocity v_osm) and j_h is the heat flux density. Due to Onsager's reciprocal relations, there are two different paths to compute the thermo-osmotic response coefficient M_to: the mechanocaloric route ($j_\mathrm{h} = -M_\mathrm{to}\nabla p$, Fig. 5.3a) and the thermo-osmotic route ($j_\mathrm{q} = -M_\mathrm{to}\nabla T/T$, Fig. 5.3b).

Mechanocaloric route First we will follow the mechanocaloric route, considering $f = -\nabla p$ as the force applied on the system. Supposing a flow in the x direction, $\tilde{H}$ the channel height and L_x, L_y the wall dimensions, the total heat flux J_h will be given by the integral over the cross section of the flux of enthalpy excess density δh (which will be discussed in next Section 5.2.4), within the region where the velocity profile in the z direction is non-zero:

$$J_\mathrm{h} = \int_0^{L_y} \mathrm{d}y \int_{z_0}^{\tilde{H}-z_0} \delta h(z)\, v(z)\, \mathrm{d}z. \tag{5.25}$$

Using the symmetry of the flow around $z = \tilde{H}/2$ and extending the result to a semi-infinite channel (or, analogously, supposing that the walls are far enough and that there is a well defined bulk liquid region in the channel where $\delta h = 0$), Eq. (5.25) writes:

$$J_\mathrm{h} = 2L_y \int_{z_0}^{\infty} \delta h(z) v(z)\, \mathrm{d}z. \tag{5.26}$$

Assuming that $\delta h(z)$ does not vanish in a thin region of liquid close to the wall, where $z - z_\mathrm{s} \ll \tilde{h}$, we can linearize the velocity profile. To determine the shape of such velocity profile we consider a slab channel, with two parallel walls perpendicular to the z axis, located at $z = 0$ and $z = \tilde{H}$ (see Fig. 5.2). We now apply a pressure gradient $f = -\nabla p$ along the x direction, which generates a Poiseuille velocity profile $v(z)$, as we discussed in Chapter 2. This Poiseuille flow will be described by Eq. (5.19) together with the boundary condition $\frac{\mathrm{d}v}{\mathrm{d}z}\big|_{z=\tilde{H}/2} = 0$, consequence of the symmetry of the system. The general solution for the velocity profile is:

$$v(z) = \begin{cases} \frac{f}{2\eta}\left[\tilde{h}(z + b_\mathrm{eff}) - (z - z_\mathrm{s})^2\right] & \text{for } z_0 < z < \tilde{H} - z_0 \\ 0 & \text{otherwise} \end{cases}; \tag{5.27}$$

with $z_0 = 0$ in the slip situation (Fig. 5.2a), and $z_0 = -b_\mathrm{eff} = z_\mathrm{s} - b$ in the stagnant layer situation (Fig. 5.2b). Eq. (5.27) can be thus linearized close to the interface as:

$$v(z) \approx \begin{cases} \frac{f\tilde{h}}{2\eta}(z + b_\mathrm{eff}) & \text{for } z > z_0 \\ 0 & \text{for } z < z_0 \end{cases}. \tag{5.28}$$

Substituting in Eq. (5.26), we subsequently obtain:

$$J_\mathrm{h} = \frac{L_y \tilde{h} f}{\eta} \int_{z_0}^{\infty} \delta h(z)(z + b_\mathrm{eff})\mathrm{d}z. \tag{5.29}$$

Finally, the heat flux per unit area will be $j_{\mathrm{h}} = \frac{J_{\mathrm{h}}}{S_{\perp}} = \frac{J_{\mathrm{h}}}{L_y \tilde{h}}$ and, taking into account from Eq. (5.24) that $j_{\mathrm{h}} = M_{\mathrm{to}}\, f$, we obtain:

$$M_{\mathrm{to}} = \frac{1}{\eta} \int_{z_0}^{\infty} \delta h(z)(z + b_{\mathrm{eff}}) \mathrm{d}z. \tag{5.30}$$

Thermo-osmotic route Equation (5.30) can be also determined, following Onsager reciprocal relations, through the thermo-osmotic route: $v_{\mathrm{osm}} = M_{\mathrm{to}}(-\nabla T/T)$. In this case, the force density driving the flow will be the thermodynamic force, $f = -T\nabla(\frac{\tilde{\mu}}{T})$, with $\tilde{\mu}$ the chemical potential. Taking into account the Gibbs-Helmholtz equation, $\frac{\mathrm{d}\tilde{\mu}/T}{\mathrm{d}T} = -\frac{\delta h}{T^2}$ [350], we obtain that

$$f(z) = -\delta h(z) \frac{\nabla T}{T}. \tag{5.31}$$

Substituting f in Eq. (5.23) we obtain:

$$v_{\mathrm{osm}}^{\infty} = -\frac{\nabla T/T}{\eta} \int_{z_0}^{\infty} \delta h(z)(z + b_{\mathrm{eff}}) \mathrm{d}z. \tag{5.32}$$

Finally, taking into account that $v_{\mathrm{osm}} = M_{\mathrm{to}}(-\nabla T/T)$, the same expression than in Eq. (5.30) is obtained, consistently with Onsager's reciprocal relations [357, 358].

5.2.4 Enthalpy excess density

A fundamental quantity in Eq. (5.30) is the enthalpy excess density δh. Here we introduce some general concepts related to δh such as its classical description [338, 352], given only by the ionic electrostatic interactions, together with some additional contributions that we will account for in the general model we propose to describe the different interactions that play a role in the enthalpy of an aqueous electrolyte.

a. General remarks

In the case of aqueous electrolytes, originally, Derjaguin et al. developed a model for the thermo-osmotic coefficient [338, 352] as in Eq. (5.30) without the slip term, and only considering the electrostatic enthalpy of the ions $\delta h_{\mathrm{el}}(z) = \rho_{\mathrm{e}}(z)V(z) + p(z)$. By taking into account Eq. (5.6) and considering mechanical equilibrium along the z direction $\left(\frac{\mathrm{d}p}{\mathrm{d}z} = -\rho_{\mathrm{e}} \frac{\mathrm{d}V}{\mathrm{d}z}\right)$, we obtain an expression of δh_{el} as a function of the electric potential:

$$\delta h_{\mathrm{el}}(z) = -\varepsilon V(z) \frac{\mathrm{d}^2 V}{\mathrm{d}z^2} + \frac{\varepsilon}{2} \left(\frac{\mathrm{d}V}{\mathrm{d}z}\right)^2. \tag{5.33}$$

Just focusing on this classical theory [352], which only considers the electrostatic interactions between ions ($\delta h \simeq \delta h_{\mathrm{el}}$), substituting Eq. (5.33) in Eq. (5.30), we can solve the integral analytically in the slip situation, obtaining the electrostatic constribution to the thermo-osmotic response as a function of the ratio $x = \lambda_{\mathrm{D}}/\ell_{\mathrm{GC}}$:

$$M_{\mathrm{to}}^{\mathrm{el}} = \frac{1}{2\pi \ell_{\mathrm{B}} \eta \beta} \left\{ -3\ln\left(1-\gamma^2\right) - \mathrm{asinh}^2(x) + \frac{b_{\mathrm{eff}}}{\lambda_{\mathrm{D}}} \left[3x|\gamma| - 2x\,\mathrm{asinh}(x) \right] \right\}, \tag{5.34}$$

with

$$\gamma = \frac{\mathrm{sgn}(\Sigma)}{x} \left(-1 + \sqrt{1 + x^2} \right). \tag{5.35}$$

This expression can be simplified in the Debye-Hückel regime, which was the one considered by Derjaguin [338, 352], then $x \ll 1$:

$$M_{\text{to}}^{\text{el,DH}} = -\frac{x^2}{8\pi\ell_{\text{B}}\eta\beta}\left(1 + 2\frac{b_{\text{eff}}}{\lambda_{\text{D}}}\right), \tag{5.36}$$

and thus scaling as Σ^2 in this regime. A different scaling with x is found for high surface charges, *i.e.* when $x \gg 1$, when the contribution is given by the expression:

$$M_{\text{to}}^{\text{el},x\gg1} = \frac{1}{2\pi\ell_{\text{B}}\eta\beta}\left\{3\ln\left(\frac{x}{2}\right) - \ln^2(2x) + \frac{b_{\text{eff}}}{\lambda_{\text{D}}}x\left[3 - 2\ln(2x)\right]\right\}. \tag{5.37}$$

It is interesting to note that none of these expressions depend on the sign of the surface charge: $M_{\text{to}} < 0$ independently of the range of parameters studied.

Although the model proposed by Derjaguin et al. is useful to quantitatively predict some M_{to} experimental orders of magnitude [350], it fails to describe the amplitude of the responses predicted in the literature [343, 344, 337, 84], the thermo-osmotic response reported for pure water in uncharged membranes [340], as well as the experimental discrepancies observed in M_{to} sign [347, 348, 349, 350]. Although electrostatic ionic interactions are for sure an important ingredient controlling the thermodynamical processes of a dissolved salt in a charged channel, other interactions discarded by the classical model may also be critical to describe thermo-osmosis, such as the liquid-solid interactions (*i.e.* the wetting properties), as well as the ion specificity (with a very important impact in the case of very asymmetric salts [213]).

Generally, the atomic enthalpy excess density for an element i can be defined as:

$$\delta h_i(z) = \left[\delta u_i(z) + \delta p_i(z)\right] n_i(z), \tag{5.38}$$

where $\delta\mathcal{A}(z) = \mathcal{A}(z) - \mathcal{A}_{\text{bulk}}$; with $\mathcal{A}_{\text{bulk}}$ the bulk value of the physical property $\mathcal{A}$, u_i the energy per atom, p_i the stress per atom [1], and n_i the atomic number density profile. When working at constant temperature, the kinetic energy per atom $u_{\text{k},i}$ is proportional to $k_{\text{B}}T$ for all z, so $\delta u_{\text{k},i} = 0$ and $\delta u_i = \delta u_{\text{p},i}$ with $u_{\text{p},i}$ the potential energy per atom.

Equation (5.38) can be easily extended to the case of molecular fluids as the sum of the different atomic contributions. Therefore, in the case of water:

$$\delta h_{\text{wat}}(z) = \delta h_{\text{O}}(z) + \delta h_{\text{H}}(z). \tag{5.39}$$

In this case δh_{wat} does not have a simple analytical form and, due to its strong dependence on the wetting properties [343, 344], it has to be computed numerically from simulations for a given wall type.

Note that other contributions to the total thermo-osmotic response could be considered, as the one associated to the depletion of the ions from the wall or to the dipole moment of the water molecules in the EDL. In this latter case, for instance, the associated density of enthalpy excess will be

$$\delta h_{\text{dp}}(z) = -\left\langle\mu\right\rangle(z)\, n_{\text{O}}(z)\, E(z), \tag{5.40}$$

with n_{O} the number density of the oxygen atoms, $E = -\frac{\text{d}V}{\text{d}z}$ the electrostatic field, and $\langle\mu\rangle$ the average dipole moment in the direction of the field. $\langle\mu\rangle$ can be computed from Boltzmann statistics, by taking into account that $\langle\mu\rangle(z) = \mu\langle\cos\theta\rangle(z)$, with $\langle\cos\theta\rangle$ the average dipole moment orientation and μ the dipole moment of the solvent, $\mu = 1.85$ D

[1] A practical difficulty with measuring this term will be discussed in Section 5.3.2.

for water. With that regard, denoting $\mathcal{P}_{\mathrm{B}}$ the probability that the molecule will have the angle θ, then

$$\mathcal{P}_{\mathrm{B}} = \frac{e^{\alpha\cos\theta}}{\int \mathrm{d}\Omega\, e^{\alpha\cos\theta}}, \tag{5.41}$$

where Ω is the solid angle and $\alpha = \beta\mu E$. Therefore,

$$\langle\mu\rangle = \int \mathrm{d}\Omega\, \mu\, \mathcal{P}_{\mathrm{B}} \cos\theta = \frac{\mu \int_0^\pi e^{\alpha\cos\theta}\cos\theta\sin\theta\,\mathrm{d}\theta}{\int_0^\pi e^{\alpha\cos\theta}\sin\theta\,\mathrm{d}\theta} = \mu\left(\coth\alpha - \frac{1}{\alpha}\right). \tag{5.42}$$

By linearizing this expression when $\mu E \ll k_{\mathrm{B}}T$ and substituting in Eq. (5.40) we finally obtain:

$$\delta h_{\mathrm{dp}}(z) = -\frac{1}{3\beta}\left(\frac{\mu}{q}\right)^2 n_{\mathrm{O}}(z)\left(\frac{\mathrm{d}\phi}{\mathrm{d}z}\right)^2, \tag{5.43}$$

where ϕ is the reduced potential. We can obtain n_{O} from molecular dynamics simulations and $\phi(z)$ solving Eq. (5.10) for the corresponding geometry.

One of the objectives of this chapter is to present a general model that accounts for the different interactions taking place in a liquid electrolyte, namely the solute and solvent electrostatic interactions (in the presence of a charged surface) and purely neutral interactions (due to the solid wetting properties).

b. Proposed model

The main idea in the model we propose here is, following the ideas of Ref. 85, to include the additional contributions to δh related to the solvent (water in the present work) and the ions, along with the electrostatic enthalpy of ions δh_{el} considered by the standard approach.

The **water contribution** in the case of a neutral surface ($\Sigma = 0$), will be given exclusively by the sum of the oxygen and hydrogen atomic enthalpies, which can be directly determined from equilibrium MD simulations following Eqs. (5.38) and (5.39), so $\delta h^0_{\mathrm{wat}} = \delta h^0_{\mathrm{O}} + \delta h^0_{\mathrm{H}}$. In the case of a charged surface Σ, we should also account for the dipole moment contribution, $\delta h^{\Sigma}_{\mathrm{dp}}$ from Eq. (5.43), writing the total water enthalpy contribution as $\delta h^0_{\mathrm{wat}} + \delta h^{\Sigma}_{\mathrm{dp}}$.

Analogously, the **ions contribution** for a neutral surface will write $\delta h^0_{\mathrm{ions}} = \delta h^0_+ + \delta h^0_-$, where

$$\delta h^0_\pm = \left(\delta u^0_\pm + \delta p^0_\pm\right) n^0_\pm, \tag{5.44}$$

with the ions distribution given by an exponential of the potential energy variation; for symmetric salts depleted from the wall:

$$n^0_\pm = n^0_{\mathrm{s}} \exp\left(-\beta\delta u^0_\pm\right); \tag{5.45}$$

$n^0_\pm$ can also be determined from equilibrium MD simulations at a reference bulk concentration n^0_{s}.

We can extend this description to a charged surface, by including the potential (described within the Poisson-Boltzmann framework) in Eq. (5.44):

$$\delta h^{\Sigma}_{\mathrm{ions}} = \left(\delta u^0_+ + \delta p^0_+ + qV\right) n^{\Sigma}_+ + \left(\delta u^0_- + \delta p^0_- - qV\right) n^{\Sigma}_-; \tag{5.46}$$

where the ionic concentrations will be given by the Boltzmann distribution:

$$n^{\Sigma}_\pm = n_{\mathrm{s}} \exp\left[-\beta\left(\delta u^0_\pm \pm qV\right)\right] = n_\pm \exp\left(-\beta\delta u^0_\pm\right), \tag{5.47}$$

with $n_\pm$ the ion distributions within the Poisson-Boltzmann framework, given by Eq. (5.7). Rearranging terms in Eq. (5.46) we obtain:

$$\begin{aligned}\delta h^{\Sigma}_{\text{ions}} &= \frac{\delta h^0_+}{n^0_{\text{s}}} n_+ + \frac{\delta h^0_-}{n^0_{\text{s}}} n_- + q\left(n^{\Sigma}_+ - n^{\Sigma}_-\right) V \\ &= \delta h^{\Sigma}_{\text{sol}} + \delta h^{\Sigma}_{\text{mix}} + \delta h^{\Sigma}_{\text{ES}},\end{aligned} \tag{5.48}$$

from where we defined the solvation enthalpy as the enthalpy contribution from the first two terms:

$$\delta h^{\Sigma}_{\text{sol}} = \frac{\delta h^0_+}{n^0_{\text{s}}} n_+ + \frac{\delta h^0_-}{n^0_{\text{s}}} n_-. \tag{5.49}$$

The potential term in Eq. (5.48) is in turn decomposed into a purely electrostatic contribution:

$$\delta h^{\Sigma}_{\text{ES}} = q\left(n_+ - n_-\right) V, \tag{5.50}$$

and a mixed term

$$\delta h^{\Sigma}_{\text{mix}}(z) = q\left[n_+\left(\frac{n^0_+}{n^0_{\text{s}}} - 1\right) - n_-\left(\frac{n^0_-}{n^0_{\text{s}}} - 1\right)\right] V, \tag{5.51}$$

which acts as a compensation term for $\delta h^{\Sigma}_{\text{ES}}$ in the region where the ions are depleted from the wall. Indeed, when the salts are depleted from the wall (typically symmetric salts), their density profile for neutral walls can be approximated by a step function with $n^0_\pm = n^0_{\text{s}}$ in bulk and $n^0_\pm = 0$ close to the wall, so $\delta h^{\Sigma}_{\text{mix}} = 0$ in bulk and $\delta h^{\Sigma}_{\text{mix}} = -\delta h^{\Sigma}_{\text{ES}}$ at the interface.

A full picture will be completed by considering the electrostatic pressure contribution $\delta p^{\Sigma}_{\text{ES}} = \frac{\varepsilon}{2}\left(\frac{\mathrm{d}V}{\mathrm{d}z}\right)^2$ which, together with $\delta h^{\Sigma}_{\text{ES}}$, form the classical electrostatic term from Eq. (5.33), $\delta h_{\text{el}} = \delta h^{\Sigma}_{\text{ES}} + \delta p^{\Sigma}_{\text{ES}}$. In conclusion, dropping the enthalpies super indexes related to the surface charge in order to light notation, the total enthalpy excess density writes:

$$\delta h(z) = \delta h_{\text{wat}}(z) + \delta h_{\text{dp}}(z) + \delta h_{\text{sol}}(z) + \delta h_{\text{mix}}(z) + \delta h_{\text{el}}(z). \tag{5.52}$$

As discussed, the classical picture within δh_{el} is a continuum description which does not account for the depletion of the ions in the vicinity of the wall. Defining the characteristic depletion length as d_ℓ, we could also think in accounting for this effect, instead with the compensation term δh_{mix}, by imposing a vanishing potential in the interfacial region where there are no ions. This defines, for a semi-infinite channel:

$$\delta h^*_{\text{el}} = \begin{cases} \delta h_{\text{el}} & \text{for } z > d_\ell \\ 0 & \text{for } z \leq d_\ell \end{cases}. \tag{5.53}$$

In this way, we can approximate for symmetric salts $\delta h^*_{\text{el}} \approx \delta h_{\text{mix}} + \delta h_{\text{el}}$, and thus the total enthalpy can be expressed as:

$$\delta h(z) = \delta h_{\text{wat}}(z) + \delta h_{\text{sol}}(z) + \delta h_{\text{dp}}(z) + \delta h^*_{\text{el}}(z). \tag{5.54}$$

In this equation we can distinguish a contribution related to the solvent (water in this work) δh_{wat}, another one related to the ion solvation δh_{sol}, and two electrostatic contributions, δh_{dp} and δh^*_{el}, related to the solvent and the ions electrostatic interactions respectively.

5.2.5 Thermoelectric response

The process of generating an electric current by applying a temperature gradient is known as thermoelectricity. In order to compute the thermoelectric response, the elements that contribute from the response matrix in Eq. (5.5) are:

$$\begin{pmatrix} j_{\mathrm{h}} \\ j_{\mathrm{e}} \end{pmatrix} = \begin{pmatrix} \cdot & M_{\mathrm{te}} \\ M_{\mathrm{te}} & \cdot \end{pmatrix} \begin{pmatrix} -\frac{\nabla T}{T} \\ E \end{pmatrix}, \tag{5.55}$$

where j_{h} is the heat flux density, j_{e} is the electric flux density and E is the external electric field parallel to the interface. In order to compute the thermoelectric response coefficient M_{te}, we will follow the relation $j_{\mathrm{h}} = M_{\mathrm{te}}E$ although, due to Onsager's reciprocal relations, the same result is obtained from the relation $j_{\mathrm{e}} = -M_{\mathrm{te}}\nabla T/T$. Analogously to the thermo-osmotic response computation through the mechanocaloric route in the limit of thin interaction layers, the heat flux will be given by Eq. (5.25), although in this case the velocity field we should consider is the one induced by an electric field, also known as electro-osmotic velocity profile, which is given by Eq. (5.22) with $f = \rho_{\mathrm{e}}E$ the electric force. Substituting ρ_{e} by its relation with the potential given by Eq. (5.6), the solution of Eq. (5.22), supposing a vanishing potential far from the wall, yields:

$$v_{\mathrm{EO}}(z) = \begin{cases} \frac{\varepsilon E}{\eta}\left[V(z) - V(z_0) + b_{\mathrm{eff}}\left.\frac{\mathrm{d}V}{\mathrm{d}z}\right|_{z=z_0}\right] & \text{for } z_0 < z < \tilde{H} - z_0 \\ 0 & \text{otherwise} \end{cases}. \tag{5.56}$$

Taking into account that the heat flux density $j_{\mathrm{h}} = \frac{J_{\mathrm{H}}}{S_\perp}$, and that $M_{\mathrm{te}} = \frac{j_{\mathrm{h}}}{E}$, we finally obtain that

$$M_{\mathrm{te}} = \frac{q}{2\pi\ell_{\mathrm{B}}\tilde{h}\eta}\int_{z_0}^{\infty}\mathrm{d}z\,\delta h(z)\left[\phi(z) - \phi(z_0) + b_{\mathrm{eff}}\left.\frac{\mathrm{d}\phi}{\mathrm{d}z}\right|_{z=z_0}\right], \tag{5.57}$$

with $\phi = \beta q V$. As for the thermo-osmotic response, the main contributions to $\delta h(z)$ will be given by Eq. (5.54). We can compute the classical electrostatic contribution to the thermoelectric response in the slip situation. In this case, $\left.\frac{\mathrm{d}\phi}{\mathrm{d}z}\right|_{z=0} = -\frac{2\mathrm{sgn}(\Sigma)}{\ell_{\mathrm{GC}}}$ (see Appendix B), and the integral in Eq. (5.57) can be performed analytically, giving:

$$\begin{aligned} M_{\mathrm{te}}^{\mathrm{el}} = -\frac{q}{2\pi^2\ell_{\mathrm{B}}^2\tilde{h}\eta\beta}\frac{\mathrm{sgn}(\Sigma)x}{\lambda_{\mathrm{D}}}\Bigg\{ & 5\left[1 - \frac{\mathrm{asinh}(x)}{x}\right] - 2|\gamma|\mathrm{asinh}(x) \\ & + \frac{b_{\mathrm{eff}}}{\lambda_{\mathrm{D}}}\left[3|\gamma|x - 2x\mathrm{asinh}(x)\right]\Bigg\}; \end{aligned} \tag{5.58}$$

with $x = \lambda_{\mathrm{D}}/\ell_{\mathrm{GC}}$ and γ defined in Eq. (5.35). As for thermo-osmosis, it is interesting to obtain the simplified expression corresponding to low and high surface charge limits. Therefore, in the Debye-Hückel regime (when $x = \lambda_{\mathrm{D}}/\ell_{\mathrm{GC}} \ll 1$):

$$M_{\mathrm{te}}^{\mathrm{el,DH}} = \frac{q}{12\pi^2\ell_{\mathrm{B}}^2\tilde{h}\eta\beta}\frac{\mathrm{sgn}(\Sigma)x^3}{\lambda_{\mathrm{D}}}\left(1 + 3\frac{b_{\mathrm{eff}}}{\lambda_{\mathrm{D}}}\right); \tag{5.59}$$

which, instead of scaling as Σ^2 like the thermo-osmotic response Eq. (5.36), scales as Σ^3. In the Gouy-Chapman regime corresponding to high surface charges, *i.e.* when $x \gg 1$, the scaling changes:

$$M_{\mathrm{te}}^{\mathrm{el},x\gg1} = -\frac{q}{2\pi^2\ell_{\mathrm{B}}^2\tilde{h}\eta\beta}\frac{\mathrm{sgn}(\Sigma)x}{\lambda_{\mathrm{D}}}\left\{5 - 2\ln(2x) + \frac{b_{\mathrm{eff}}}{\lambda_{\mathrm{D}}}x\left[3 - 2\ln(2x)\right]\right\}. \tag{5.60}$$

5.3 Methods

After exposing the theoretical framework under which we will obtain the different contributions to the thermo-osmotic response, we will perform MD simulations with the objective of determining the solvent and solute atomic enthalpies as a function of the wetting properties of the system. MD simulations are a useful and necessary tool to obtain such atomic enthalpy profiles, although they present some limitations that are also discussed here.

5.3.1 Simulation details

We used the LAMMPS package [144] to determine the enthalpy excess density profiles from equilibrium molecular dynamics (EMD) simulations of an aqueous electrolyte constituted by 2080 water molecules, simulated with the SPC/E water model [169], and 80 ions (40 anions and 40 cations) of three different salt types, NaCl, KCl and NaI, such as the bulk salt concentration was $n_s \sim 1\,\mathrm{M}$, following Ref. 373. In this paper, the authors performed MD simulations to study electro-osmotic flow in hydrophobic channels and proposed a theoretical model, extended in Ref. 213, in good agreement with their simulation results. Therefore, we intended to reproduce their system in order to study thermo-osmotic flows. All atomic interactions were modeled with a Lennard-Jones potential characterized by an interaction energy ε_{ij} and size σ_{ij}. The system parameters were the ones indicated in Ref. 373, namely the water-ions interactions were taken from [374] except for the biggest ion, I^-, for which we considered $\sigma_{II} = 6.00\,\text{Å}$ [373, 213]. We imposed periodic boundary conditions in the x and y directions parallel to the walls with lateral sizes $L_x = 48.21\,\text{Å}$ and $L_y = 32.14\,\text{Å}$. The structure of the walls consisted in three atomic layers structured as a face centered cubic crystal exhibiting a (001) face to the fluid, with a lattice parameter $a = 5.356\,\text{Å}$, equivalent to the LJ wall structure in previous chapters. The solid wall atoms were frozen and the oxygen-solid (LS) interactions were varied between the hydrophobic and hydrophilic values given in Ref. 373, with $\varepsilon_{LS} = \{0.160, 0.231, 0.323, 0.416, 0.568\}$ kcal/mol. These wettings are characterized by the respective contact angles $\theta \sim \{140°, 130°, 110°, 90°, 50°\}$, determined from additional sessile drop simulations (see Chapter 2). The exact values for the contact angles, measured at 298 K from three independent simulations for a given wetting, can be found in Table 5.1. Lorentz-Berthelot mixing rules were applied for all the cross-interactions.

For all the simulations we imposed a timestep of 2 fs and we ran an equilibration stage of 500 ps where we fixed the temperature at 298 K via a Nosé-Hoover thermostat with a damping time of 200 fs. Following Ref. 373, we also set the pressure to 10 atm by using the top wall as a piston, exerting an external force proportional to the desired pressure multiplied by the wall surface. We then continued applying the thermostat, and fixed the top wall at its equilibrium position in the production run. The average distance between the walls for all the runs was $\tilde{H} \sim 45$ Å.

The slip length was determined for an aqueous electrolyte from non-equilibrium molecular dynamics (NEMD) simulations of 1 M of NaCl dissolved in SPC/E water at 10 atm. With that regard, we applied a constant shear velocity U_{wall} to both walls in opposite x directions, generating far from the wall a linear velocity profile with constant shear rate. The friction coefficient was determined from the relation $\tau = \lambda v_{slip}$ between the shear stress τ and the velocity jump at the interface, $v_{slip} = U_{wall} - v_x(z_s)$, with z_s measured from the Gibbs dividing plane method, see Chapter 2. The slip length was then $b = \eta/\lambda$, with η corresponding to the bulk viscosity obtained from the relation $\tau = \eta \frac{\mathrm{d}v_x}{\mathrm{d}z}$. Further details about the slip boundary condition can be found in Chapters 2 and 3.

θ (deg)	$\varepsilon_{\mathrm{LS}}$ (kcal/mol)	b (Å)	z_{s} (Å)	b_{eff} (Å)
142.16 ± 16.49	0.160	54.89 ± 6.99	1.44 ± 0.02	53.45
127.90 ± 6.20	0.231	23.50 ± 1.82	1.07 ± 0.06	22.43
108.41 ± 0.81	0.323	6.94 ± 2.05	0.83 ± 0.05	6.11
87.25 ± 8.29	0.416	3.98 ± 0.53	0.59 ± 0.13	3.39
51.46 ± 2.65	0.568	0.0 (-0.47 ± 0.34)	0.33 ± 0.03	-0.33

Table 5.1: Slip length b and shear plane position z_{s} along with the effective slip $b_{\mathrm{eff}} = b - z_{\mathrm{s}}$, for the different wetting angles θ considered in our study, which are controlled by the interaction energy $\varepsilon_{\mathrm{LS}}$ between liquid and solid atoms.

For a given wetting angle, determined by $\varepsilon_{\mathrm{LS}}$, 3 independent shears in the linear response regime were applied, $U_{\mathrm{wall}} = \{10, 15, 20\}$ m/s, and for a given shear three independent simulations were performed, giving (taking into account the possibility of independently measuring τ for the top and the bottom wall) 18 independent measures of viscosity and friction, with a production time of 4 ns. The error of both transport coefficients corresponded to the statistical error within 95% of confidence level and the error on b was determined from error propagation computation:

$$\Delta b = b \sqrt{\left(\frac{\Delta \eta}{\eta}\right)^2 + \left(\frac{\Delta \lambda}{\lambda}\right)^2}. \tag{5.61}$$

Good agreement was found between the simulated viscosity and the experimental value for all the wettings [375, 376]. The slip length and shear plane position values are shown in Table 5.1, where we note that the most hydrophilic situation ($\theta \sim 50°$) is considered as a no-slip situation with $b = 0.0$ Å corresponding to a stagnant layer ($b_{\mathrm{eff}} < 0$).

Aside of EMD and NEMD simulations of different aqueous electrolytes enclosed between LJ walls, we also performed an extra set of simulations of 1 M of NaCl dissolved in SPC/E water confined between graphene walls with size $L_x = 46.73$ Å and $L_y = 34.08$ Å. The solution parameters were the same than the ones for LJ walls and the oxygen-carbon interactions were modelled as described in Ref. 377, with a contact angle of $\theta = 84.98° \pm 5.57°$. The slip length of this configuration, measured analogously as for LJ walls, was $b = 539.53 \pm 41.23$ Å and $z_{\mathrm{s}} = 0.76 \pm 0.20$ Å.

5.3.2 About enthalpy excess density determination

Generality of our model The only contributions to δh in Eq. (5.54) that cannot be computed analytically are the solvent and solute contributions, δh_{wat} and δh_{sol} respectively. In Fig. 5.4 we can find represented the total enthalpy excess densities computed directly from the aqueous electrolyte solutions following Eq. (5.38) for NaCl, KCl (Fig. 5.4a) and NaI (Fig. 5.4b) for a concentration $n_{\mathrm{s}} = 1\,\mathrm{M}$, together with the profiles for pure water simulations (with no dissolved ions). In Fig. 5.4 we can see that in the case of symmetric salts (Fig. 5.4a) the solute enthalpy, even at large concentrations, does not affect the total enthalpy profile, which is controlled by the solvent. However, in the case of very asymmetric salts (Fig. 5.4b), the solute enthalpy density profile presents a non negligible contribution. To overcome this problem, one can introduce a modified Poisson-Boltzmann equation, which accounts for the position-dependent polarization of the medium together with an external potential contribution to the ionic densities distributions in the Boltzmann factor, as done in Ref. 213 for electro-osmosis. With that regard the ion specifity is quantified by

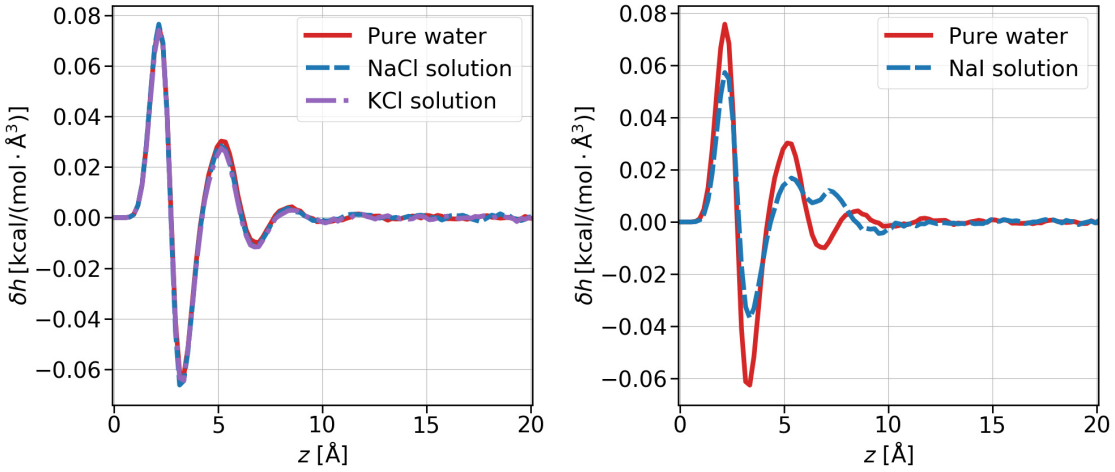

(a) (b)

Figure 5.4: Enthalpy excess density profiles of pure water (continuous line) simulations together with the profiles corresponding to an aqueous solution of (a) two symmetric salts: NaCl and KCl; and (b) one assymetric salt NaI, with a bulk salt concentration $n_s \sim 1$ M.

the function

$$f(z) = \frac{1}{2\lambda_D^2 q}\left[U_{ext}^{+}(z) - U_{ext}^{-}(z)\right],$$

where $U_{ext}^{\pm}$ is the external potential action on the ions due to the interactions other than the electrostatic potential V. From the comparison of this model with their simulation results, the authors conclude that the ion-specific function $f(z)$ is critical to describe the results for very asymmetric salts such as NaI. Nevertheless, for symmetric salts such as NaCl, the Debye-Hückel model, analogous to consider $f(z) = 0$, works well for low surface potentials (as discussed in Section 5.2.1b.) and for solution concentration of approximately 1 M, which is the upper consideration in this work. Therefore, in the following, we will present the different enthalpies results for NaCl dissolved in water within a 1 M concentration, although they are equivalent to pure water simulation results and thus extendable to any other symmetric salt type and lower concentrations. The fact that the solution profile is mostly dominated by water is due to the depletion of the ions from the wall, characteristic of symmetric salts, which implies that only the water molecules are affected by the interactions with the solid atoms (Fig. 5.5). Therefore, we decided to approximate the ion density profiles (in Fig. 5.5b) by a smooth step function (because the classical Heaviside function is not differentiable at the step, causing minimization issues) given by, for half the channel, $1/\{1 + \exp\left[(d_\ell - x)/(1\ \text{Å})\right]\}$, which allowed us to determine the size of the depletion layer d_ℓ. Tipically, $d_\ell \sim 5$ Å (see Fig. 5.5b).

Local pressure profile in MD Before studying the simulation results, it is important to comment on one important aspect about the enthalpy excess density determination in MD simulations. In the model proposed in Section 5.2.4 for the enthalpy excess density contributions, we discussed that the enthalpy contributions related to the liquid-solid interactions, namely δh_{wat} and δh_{sol} in Eq. (5.54), cannot be *a priori* described by an analytical formula due to the lack of a mathematical model for the wetting properties of the system, and therefore both contributions have to be determined from MD simulations using the atomic enthalpy profiles given by Eq. (5.38). Nevertheless, in this equation, the

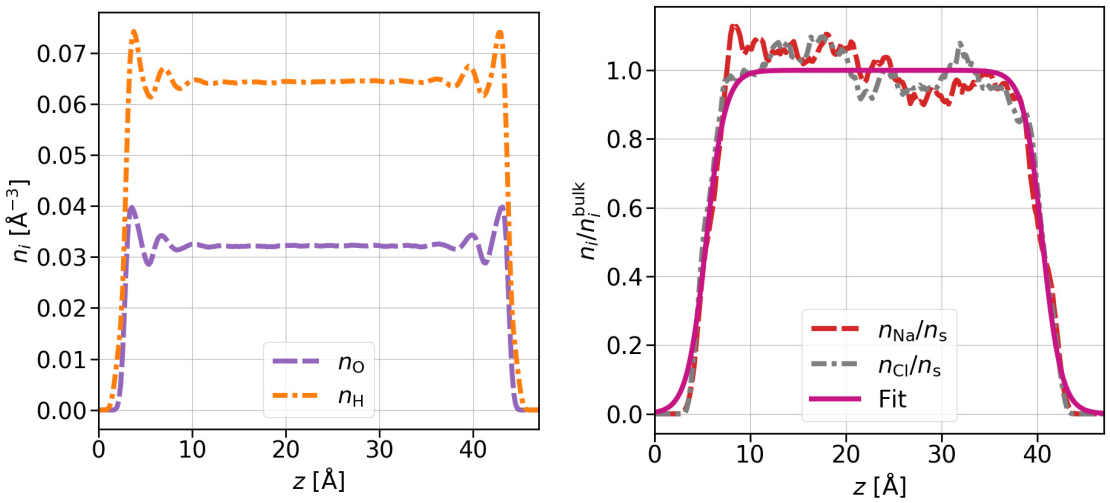

(a) (b)

Figure 5.5: Number density profiles for an aqueous electrolyte enclosed between LJ walls ($\theta \sim 140°$) of (a) oxygen and hydrogen atoms; (b) Na^+ and Cl^- ions normalized by their bulk concentration n_s. The fit by a smooth step function is also represented in solid line.

enthalpy excess density profile is given as a function of the *local* pressure differences $\delta p(z)$, which are not well defined in molecular dynamics simulations [343]. Indeed, although the total system pressure is well defined in MD simulations from the total virial of the system (see Chapter 2),

$$P = nk_BT - \frac{1}{3V}\left\langle \sum_{i<j} \mathbf{r}_{ij} \cdot \mathbf{f}_{ij} \right\rangle, \tag{5.62}$$

where $n = N/V$ is the density of the system, V its volume, and $\left\langle \sum_{i<j} \mathbf{r}_{ij} \cdot \mathbf{f}_{ij} \right\rangle$ the expected value of the sum of the products of the interparticle distance among atoms and the forces acting on them, the local definition of the stress in a liquid is not unique [378]. The pressure $P(\mathbf{R}, t)$ in a fluid, omitting additional contributions such as those due to external forces, is given by the change of the momentum density $\mathbf{J}(\mathbf{R}, t)$ in the relation

$$\frac{\partial \mathbf{J}(\mathbf{R}, t)}{\partial t} = -\boldsymbol{\nabla} P(\mathbf{R}, t). \tag{5.63}$$

The ambiguities in the definition arise because any term $\delta P(\mathbf{R}, t)$ such as $\boldsymbol{\nabla}\delta P = 0$ may be added to $P(\mathbf{R}, t)$ verifying the momentum conservation in Eq. (5.63). Although it can be proven that the vagueness of the local pressure tensor definition have no effect on physical properties such as the solid-liquid surface tension [379], it has been already discussed and showed in previous work that the choice of the local pressure definition affects the computed thermo-osmotic response coefficient M_{to} [343]. In a recent work in Ref. 380, the authors propose an alternative route to compute M_{to} by directly computing the thermo-osmotic force profile, well defined, from non equilibrium simulations, by tuning the mass of the fluid particles in the Hamiltonian and setting it to infinite in the temperature gradient direction in order to avoid the cancellation of the thermo-osmotic force with the gradient shear force due to the necessary condition of a vanishing net force on all fluid particles in the steady state. However, in this paper, the authors show that many different initial configurations are needed in order to eliminate the noise in the thermo-osmotic force profile. Because it has

been shown that the different proposed methods to determine δh, including those based on different local stress gradient definitions, provided relatively similar $M_{\rm to}$ results [343, 380], we decided to measure the local enthalpy profile from the stress per atom definition based on the virial formulation, easier to implement in MD simulations and which works well to give a general and qualitative picture in terms of orders of magnitude for the different contributions of the thermo-osmotic response, which is the main objective of the present work.

In the presented results we choose a definition of the stress per atom given by the virial-like expression:

$$p_{\alpha\beta i} = m_i v_{\alpha i} v_{\beta i} + \frac{1}{2}\sum_{j\neq i} r_{\alpha ij} f_{\beta ij}, \tag{5.64}$$

where $p_{\alpha\beta i}$ denotes the stress tensor component for the atom i in the $\alpha\beta$ direction with $\{\alpha,\beta\} = \{x,y,z\}$. In the following, we will drop the spatial coordinates to light notation. In a MD simulation, the local pressure profile is obtained dividing the space in bins (which for simplicity we will suppose of the same size) and averaging over the $N(z_{\rm bin})$ particles in the bin:

$$p(z_{\rm bin}) = \frac{\sum_{i\in{\rm bin}} p_i}{N(z_{\rm bin})}.$$

The total pressure acting on the system will be then given by the sum to all the bins of the average pressure tensor multiplied by the number of particles in the bin:

$$\sum_{\rm bin} p(z_{\rm bin}) N(z_{\rm bin}) = \sum_{\rm bin}\sum_{i\in{\rm bin}} p_i.$$

Taking into account from the equipartition theorem that $m\left\langle v^2\right\rangle = k_{\rm B}T$, and Eq. (5.62), it is straightforward that

$$\sum_{\rm bin}\sum_{i\in{\rm bin}} p_i = N k_{\rm B} T + \frac{1}{2}\left\langle \sum_{i<j} r_{ij} f_{ij} \right\rangle = PV.$$

Note that, explicitly accounting for the spatial coordinates, $\sum_\alpha p_{\alpha\alpha} = 3PV$ in a bulk system. We have then proven that the quantity $\int \delta p\, n\, {\rm d}z$ in Eq. (5.38), and therefore the enthalpy excess defined as

$$H^0 = \int_0^\infty \delta h\, {\rm d}z, \tag{5.65}$$

is unambiguous and independent of the local pressure definition. Nevertheless, the thermo-osmotic response coefficient, given by Eq. (5.30), can be decomposed as

$$M_{\rm to} = \frac{1}{\eta}\left(\int_{z_0}^\infty \delta h(z)\, z\, {\rm d}z + b_{\rm eff} H\right), \tag{5.66}$$

where

$$H = \int_{z_0}^\infty \delta h\, {\rm d}z. \tag{5.67}$$

In the slip situation $H = H^0$ and then it will be well defined. However, the integral of $\delta h\, z$ will depend on the local pressure definition and is only expected to predict the real thermo-osmotic response of the system quantitatively for very slipping systems (when the $b_{\rm eff} H$ term dominates). It will be thus useful to explore the different $M_{\rm to}$ contributions studying how do they compare to H.

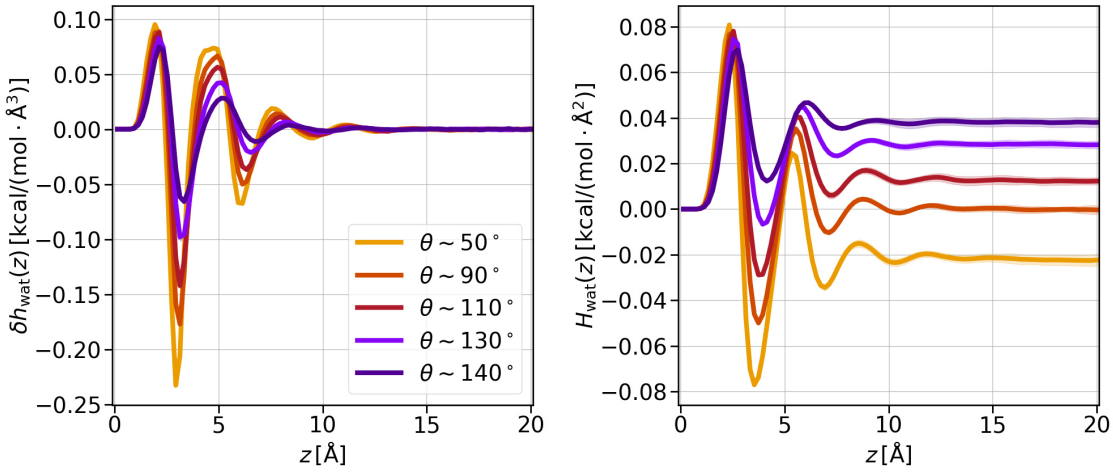

(a) (b)

Figure 5.6: (a) Enthalpy density profiles for different wettings. (b) Enthalpy excess running integral for different wettings with the same legend as in Fig. 5.6a.

5.3.3 About enthalpy excess and its comparison with the thermo-osmotic response

Let's explore the effect of wetting on the enthalpy excess (per unit area) and how it compares to the predicted thermo-osmotic response coefficient. Because the ions are depleted from the wall, the wall-ions interactions are almost negligible and the wetting effects mostly affect the water enthalpy excess density profiles, δh_{wat}. As detailed in Section 5.3.1, we controlled the wetting by varying the liquid-solid interaction energy $\varepsilon_{\mathrm{LS}} = \{0.160, 0.231, 0.323, 0.416, 0.568\}$ kcal/mol, corresponding respectively to contact angles $\theta \sim \{140°, 130°, 110°, 90°, 50°\}$. In Fig. 5.6a we can observe the enthalpy excess density profile for different contact angles. We see that δh_{wat} vanishes in the bulk and in the wall region, and that it presents strong oscillations close to the interface, which are more pronounced for the hydrophilic situations. In Fig. 5.6b we can see the running integral of the δh_{wat} profiles presented in Fig. 5.6a. We observe that H_{wat} converges in the bulk region for all the wettings, and that it recovers the strong oscillations at the interface present in δh_{wat}.

The water enthalpy values represented in Fig. 5.7a are obtained by considering a semi-infinite system constituted by a wall and a homogeneous bulk region far from the interface. We can do so by splitting δh_{wat} profiles in two (one for each wall) and extending the bulk value to infinite. The enthalpy excess is then measured from Eq. (5.67) with z_0 related to the effective slip determined from NEMD simulations (Table 5.1): $z_0 = 0$ (slip situation) for $\theta \sim \{140°, 130°, 110°, 90°\}$; and $z_0 = -b_{\mathrm{eff}}$ for $\theta \sim 50°$ (stagnant layer situation). In Fig. 5.7a we observe that the enthalpy excess increases (from -0.02 kcal/molÅ to 0.04 kcal/molÅ) with the wetting and that it changes sign for $\theta \sim 90°$. Nevertheless, it is interesting to note that a stagnant layer can be present for any wetting due to *e.g.* nano-asperities of the surface. This situation is the typical one in experiments, where some defects and bumps are present in the wall due to the difficulty of obtaining perfectly smooth surfaces with experimental techniques. Therefore, it is interesting to study the effect of different stagnant layers sizes (*i.e.* different integral lower boundaries z_0 in Eq. (5.67)) for all the wettings considered in this study. The values obtained for H_{wat} as a function of b_{eff} for different contact angles are represented in Fig. 5.7b. In this figure we observe a

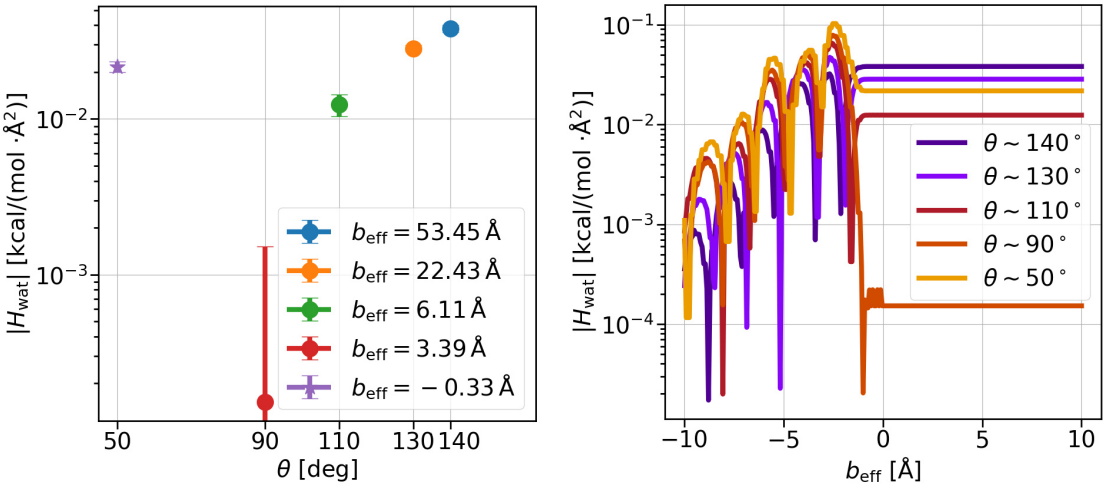

(a) (b)

Figure 5.7: Enthalpy excess water contribution for different wettings (a) measured for a given effective slip determined from NEMD, stars correspond to $H_{wat} < 0$ and circles to $H_{wat} > 0$; (b) as a function of the effective slip b_{eff}. The oscillations for $b_{eff} < 0$ are due to the oscillations of the enthalpy density profile close to the wall.

strong decrease of the water enthalpy of the system when increasing the stagnant layer size (namely $-b_{eff}$). This is due to the strong oscillations close to the wall of the running integral discussed in Fig. 5.6b, which significantly contribute to the H_{wat} integral value. For $\theta \sim 90°$ we observe a significant increase of H_{wat} in the stagnant layer situation ($b_{eff} < 0$) when compared to the slip situation ($b_{eff} > 0$). This is due to the very small value obtained for this wetting in the slip situation, related to the H_{wat} change of sign with the contact angle. Aside of this effect, we also observe for this wetting a H_{wat} decrease when increasing the stagnant layer size.

With regard to the thermo-osmotic response coefficient, in Fig. 5.8a we observe a similar wetting effect in its water contribution, which produces a change of sign in M_{to}^{wat} in this case also for a contact angle of $\theta \sim 90°$. In Fig. 5.8b the value of M_{to}^{wat} is represented as a function of the effective slip. We observe that, analogously to H_{wat} in Fig. 5.7b, the presence of a stagnant layer ($b_{eff} < 0$) significantly reduces the thermo-osmotic response, up to three orders of magnitude for the most hydrophobic systems. We also observe a small effect of slip ($b_{eff} > 0$) in the value of M_{to}^{wat}, due to the contribution $b_{eff} H_{wat}$ in Eq. (5.66) (with H_{wat} constant for $b_{eff} > 0$, see Fig. 5.7b). This slip contribution is negligible in the case of $\theta \sim 90°$, because $H_{wat} \sim 0$ for this case. To simplify the coming discussion, in the following, when referring to H_{wat} and M_{to}^{wat}, we will restrict to the values shown in Figs. 5.7a and 5.8a respectively, obtained for the b_{eff} values from NEMD simulations.

The other non-analytical term in Eq. (5.54) is the one related to the solvation enthalpy of the ions δh_{sol}, defined in Eq. (5.49). From δh_{sol} we can define H_{sol} and M_{to}^{sol}, and study how do they compare to the other non-electrostatic and non-analytical term: the water contribution. Because of the depletion of the ionic density profiles from the wall for a neutral surface charge (Fig. 5.5b), the wetting effect on both H_{sol} and M_{to}^{sol} is very small, and the solvation contribution is mostly affected by the Debye length λ_D and the surface charge density Σ. We can see in Fig. 5.9a that, at a given λ_D, H_{sol} increases when increasing Σ and that it is not affected by λ_D at high Σ, while for low Σ it can vary up to 3 orders of magnitude. In general, we observe that $H_{wat} \gg H_{sol}$ for all the λ_D and Σ range

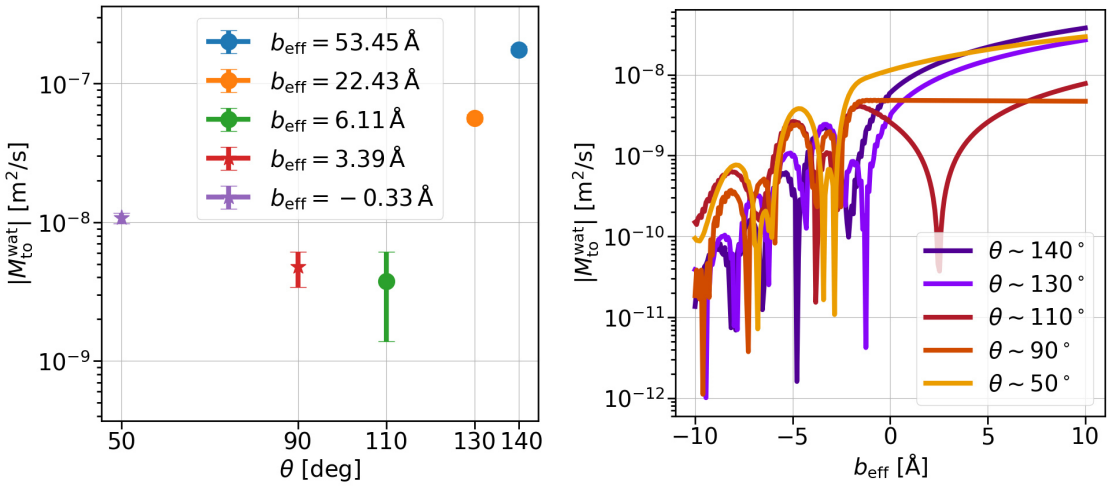

(a) (b)

Figure 5.8: Thermo-osmotic response coefficient water contribution for different wettings (a) measured for a given effective slip determined from NEMD, stars correspond to $M_{\text{to}}^{\text{wat}} < 0$ and circles to $M_{\text{to}}^{\text{wat}} > 0$; (b) as a function of the effective slip b_{eff}.

considered, except for the wetting $\theta \sim 90°$, where the water enthalpy excess is close to 0, and a competition between water and solvation contributions may happen depending on λ_{D} and Σ values. Nevertheless, such competition never happens for the predicted solvation contribution to the thermo-osmotic response coefficient ($M_{\text{to}}^{\text{sol}}$ in Fig. 5.9b), where for the range of parameters studied $M_{\text{to}}^{\text{wat}} \gg M_{\text{to}}^{\text{sol}}$. Therefore we can consider, in terms of the thermo-osmotic response coefficient, a negligible solvation contribution.

It is then left to study how the water contribution compares to the electrostatic enthalpy contributions in Eq. (5.54), namely δh_{dp} and δh_{el}^* (given by Eqs. (5.43) and (5.53) respectively). But first, it is interesting to assess the effect that the consideration of a depletion layer of thickness d_ℓ has in the classical electrostatic term δh_{el} (defined in Eq. (5.33)). With that regard, we can see in Fig. 5.10 the comparison between the classical and the modified electrostatic terms for the enthalpy excess and the thermo-osmotic response. We observe a similar behavior for H and M_{to}, where the electrostatic (H_{el}, $M_{\text{to}}^{\text{el}}$) and modified electrostatic term (H_{el}^*, $M_{\text{to}}^{\text{el}*}$) identify at low Σ and high λ_{D}. This is because the classical electrostatic potential decays for distances of order of the minimum of λ_{D} or ℓ_{GC}. Then, for the potential to decay for distances larger than d_ℓ (so the depletion layer has a smaller impact in the total integral, see Fig. 5.1a) it is needed a large λ_{D} (or low n_{s}) and a large ℓ_{GC} (small Σ). In general terms we see that considering the modified electrostatic term implies a decrease of the electrostatic contribution of up to one order of magnitude for the largest Σ considered.

At last, we find represented in Fig. 5.11 how the modified electrostatic contribution compares to the solvent dipole contribution. Again, a similar global behavior is observed for both H and M_{to}. In Fig. 5.11a, we see that for all Σ and for a broad range of λ_{D}, $H_{\text{el}}^* \gg H_{\text{dp}}$, and that both terms are comparable only for the smallest λ_{D} values considered. In general we see that both contributions increase when increasing λ_{D} and Σ. We also note that the region where both terms are comparable is when they reach an absolute value smaller than the measured H_{wat} in Fig. 5.7a, with the exception of $\theta \sim 90°$, when $H_{\text{wat}} \sim 0$ and, as we observed also in terms of solvation contribution, a more detailed description is needed for this specific wetting. This detailed description is not required

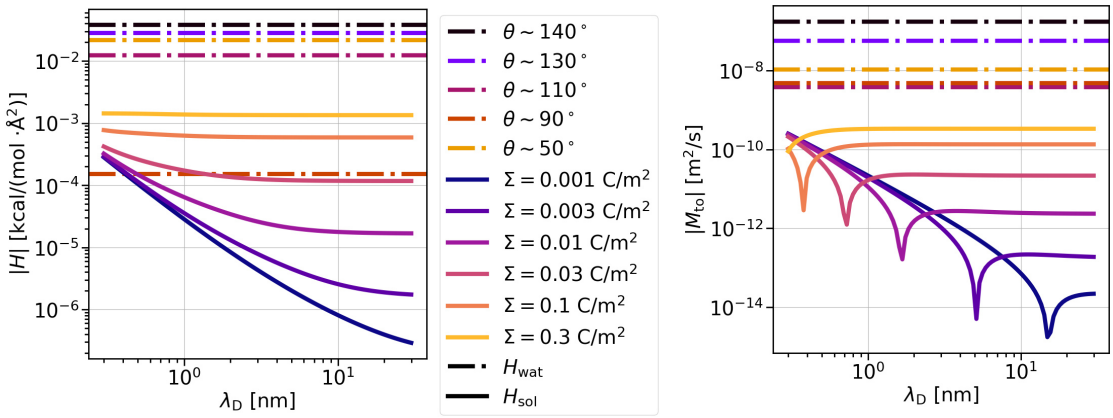

(a) (b)

Figure 5.9: Comparison between water (dash-dotted lines) and solvation (solid lines) contributions for different wettings θ and different surface charges Σ as a function of the Debye length, respectively for (a) enthalpy excess H; (b) thermo-osmotic response coefficient M_{to}.

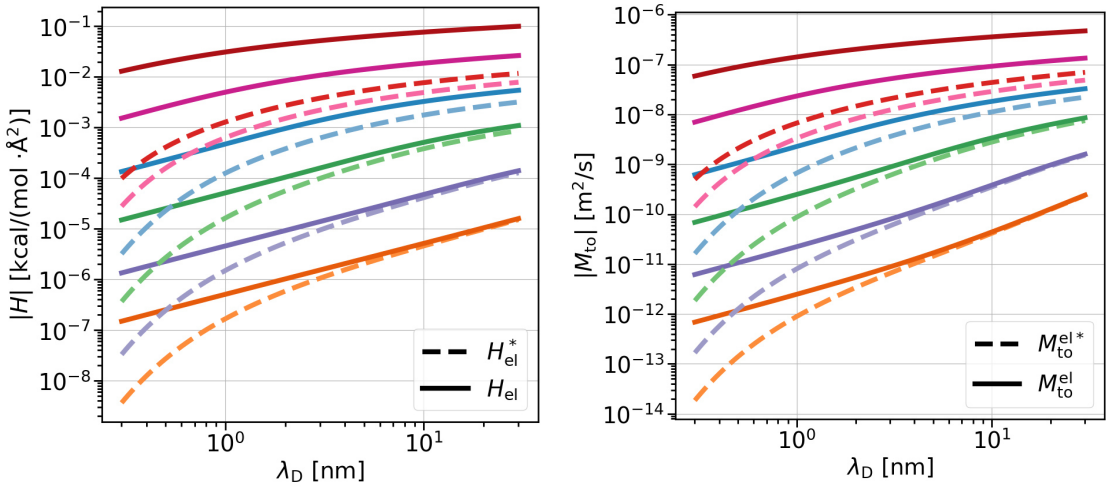

(a) (b)

Figure 5.10: Comparison between modified electrostatic (dashed lines) and classical electrostatic (solid lines) contributions for different surface charges Σ at a given wetting, as a function of the Debye length, respectively for (a) enthalpy excess H; (b) thermo-osmotic response coefficient M_{to}. The color code is the same as in Fig. 5.12 (increasing absolute value with increasing surface charge).

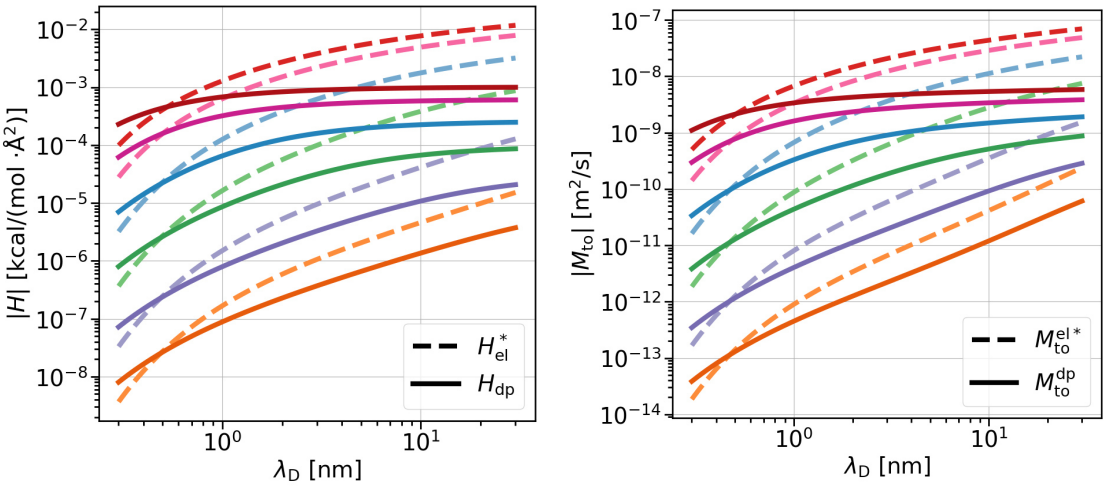

(a) (b)

Figure 5.11: Comparison between modified electrostatic (dashed lines) and dipole moment (solid lines) contributions for different surface charges Σ at a given wetting, as a function of the Debye length, respectively for (a) enthalpy excess H; (b) thermo-osmotic response coefficient $M_{\rm to}$. The color code is the same as in Fig. 5.12 (increasing absolute value with increasing surface charge).

in terms of $M_{\rm to}$ contributions, where we can see, by comparing the water contribution values in Fig. 5.8a with the ones corresponding to $M_{\rm to}^{\rm el*}$ and $M_{\rm to}^{\rm dp}$ contributions reported in Fig. 5.11b, that the values for the lower $\lambda_{\rm D}$ values where $M_{\rm to}^{\rm el*}$ and $M_{\rm to}^{\rm dp}$ are comparable are much smaller than the reported values of $M_{\rm to}^{\rm wat}$, on the order of $10^{-8} - 10^{-9}$ m^2/s and thus, we can consider $M_{\rm to}^{\rm el*} \gg M_{\rm to}^{\rm dp}$.

We can hence conclude that the main contributions to the thermo-osmotic response coefficient $M_{\rm to}$ come from the water and the electrostatic term, considering negligible the solvation and the dipole moment contributions. We can then focus our discussion considering:

$$M_{\rm to} \simeq M_{\rm to}^{\rm wat} + M_{\rm to}^{\rm el*}, \tag{5.68}$$

and studying how do these contributions affect the total thermo-osmotic response of the system.

5.4 Results: Fast and versatile thermo-osmotic flows

The objective of this study is to present a general simple model, and with that regard we have applied some approximations in order to explore a broad range of parameters and to obtain a simple general picture of the physical processes that control the thermo-osmotic response. We have discussed in previous sections the validity of such approximations, let's now explore how do wetting, salt concentration and surface charge affect the thermo-osmotic response coefficient for an aqueous electrolyte composed by a symmetric salt (NaCl, KCl) dissolved in water.

We can first focus on the wetting interactions corresponding to a slip situation ($b_{\rm eff} > 0$). In this case, as previously discussed, the lower limit in the integral (5.30) is $z_0 = 0$. When exploring in the previous section the different contributions to $M_{\rm to}$, we have concluded that the response should be mostly dominated by a modified electrostatic contribution

$M_{\rm to}^{\rm el*}$, equivalent to the classical Derjaguin's contribution integrated from the depletion layer position d_ℓ instead of from the wall; together with the water contribution $M_{\rm to}^{\rm wat}$, *i.e.* $M_{\rm to}$ is given by Eq. (5.68). Therefore $M_{\rm to}$ is controlled by the competition between water and electrostatics contributions, depending on wetting, Σ and $n_{\rm s}$ (or analogously $\lambda_{\rm D}$). In Fig. 5.12 the total thermo-osmotic response is represented in solid lines for all the wettings considered, together with $M_{\rm to}^{\rm wat}$ in dash-dotted lines (independent of $\lambda_{\rm D}$ and Σ) and $M_{\rm to}^{\rm el*}$ in dashed lines (which presents a very small wetting effect). We observe in this figure the rich behavior resulting from of that competition, where the water term mostly dominates for the most hydrophobic surface ($\theta \sim 140°$), while for the most hydrophilic surfaces ($\theta \sim \{90°, 50°\}$) electrostatic dominates for the larger $\lambda_{\rm D}$. We can also see a large variation of $M_{\rm to}$ for the different wettings, ranging from 10^{-9} to 10^{-7} m^2/s for most hydrophobic case.

A striking result from Fig. 5.12 is the transition for intermediate wettings (for $\theta \sim 110°$ in our parameters range) between a thermophobic behavior ($M_{\rm to} > 0$) at high salt concentration (small $\lambda_{\rm D}$) to a thermophilic behavior ($M_{\rm to} < 0$) at low salt concentration. In agreement with previous predictions [350], the electrostatic contribution $M_{\rm to}^{\rm el*}$ is independent of the sign of the surface charge. In contrast, the water term exhibits a change of sign when varying the wetting (see Sec. 5.3.3). Such change of sign for $M_{\rm to}^{\rm wat}$ happens at $\theta \sim 110°$ and thus, for $\theta \gtrsim 110°$, $\mathrm{sgn}\big(M_{\rm to}^{\rm wat}\big) = -\mathrm{sgn}\big(M_{\rm to}^{\rm el*}\big)$ resulting in a change of sign of $M_{\rm to}$ for $\lambda_{\rm D}$ such as $\big|M_{\rm to}^{\rm wat}\big| = \big|M_{\rm to}^{\rm el*}\big|$. Although this change of behavior happens for all $\theta \gtrsim 110°$, for the most hydrophobic cases it takes place for $\lambda_{\rm D}$ values higher than the ones considered in this study and far from the limits of validity of the Poisson-Boltzmann framework considered in the computation of $M_{\rm to}^{\rm el^*}$. Even so, within our parameters range, we can still observe for $\theta \sim \{130°, 140°\}$ a decrease of the total response for high $\lambda_{\rm D}$, which goes against the standard expectation and can only happen if water and electrostatic contributions have opposite signs. Besides, for the most hydrophilic cases $\theta \sim \{90°, 50°\}$, $\mathrm{sgn}\big(M_{\rm to}^{\rm wat}\big) = \mathrm{sgn}\big(M_{\rm to}^{\rm el*}\big)$ and $M_{\rm to}$ does not change sign for any $\lambda_{\rm D}$ value.

It is interesting to note that a similar change of sign has been found in the context of thermophoresis experiments [381, 382, 383]. This change of sign is commonly attributed to the so-called thermopotential ψ_0 [384]. Such thermopotential appears for ions having an asymmetric mobility, from imposing no ionic flux in the channel, and it generates an electro-osmotic flow, which can go against the thermo-osmotic flow and reverse the total flow direction. Nevertheless, ψ_0 should disappear by allowing ionic fluxes through the channel, and as a consequence the change of sign would disappear. By introducing the water contribution to the thermo-osmotic response, we propose a more fundamental understanding of such change of sign, which should persist regardless of any constrain on the fluxes through the channel.

The proposed $M_{\rm to}^{\rm el*}$ and $M_{\rm to}^{\rm wat}$ decomposition allows us to obtain agreement with the experimental results of $M_{\rm to}$ [350], on the order of $10^{-10} - 10^{-9}$ m^2/s. Such agreement is specially significant in the stagnant layer situation, typical of experiments due to the presence of imperfections in the solid surface, when $M_{\rm to}^{\rm wat}$ decreases and $M_{\rm to}^{\rm el*}$ may dominate for a broader range of $\lambda_{\rm D}$. Therefore, we have assessed good experimental agreement within the suggested model but, is there some parameter range or system properties which may allow to obtain a great thermo-osmotic response? Because we should not further explore the range of the parameters that control the electrostatic contribution (Σ and $\lambda_{\rm D}$) without modifying the underlying Poisson-Boltzmann description, one interesting perspective is to improve the system properties to boost the water contribution response. Because $M_{\rm to}^{\rm wat}$ increases when increasing the slip, one interesting surface is the one constituted by graphene, with an effective slip length of $b_{\rm eff} = 538.77\,$Å, which we obtained in NEMD simulations

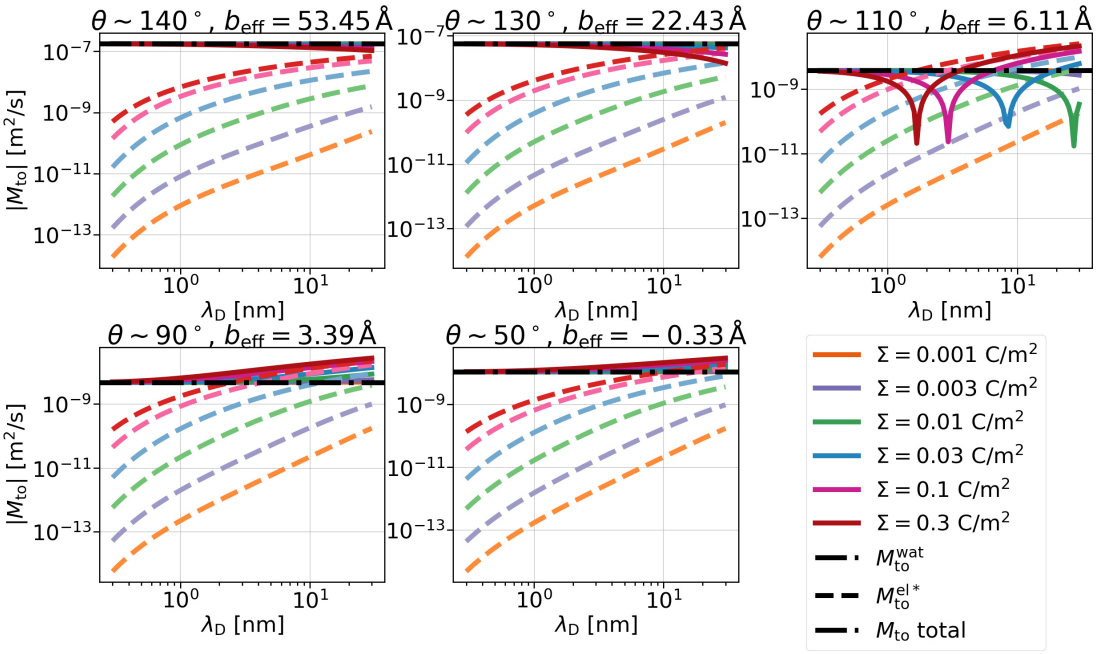

Figure 5.12: Total thermo-osmotic response coefficient (solid lines) for different wettings and surface charges as a function of the Debye length. In all the graphs the two main contributions, water (dash-dotted lines) and modified electrostatic (dashed lines), are also represented.

for NaCl aqueous solution at room temperature. In Fig. 5.13a we can observe a significant increase in both electrostatic and water thermo-osmotic response contributions, resulting in a large value of the total response $M_{\text{to}} \sim 10^{-6}$ m^2/s for this interface. Because $M_{\text{to}}^{\text{el}}$ does not vary significantly with wetting and the total response is dominated by the water contribution, we can expect $M_{\text{to}} \sim M_{\text{to}}^{\text{wat}}$ for graphene. In Fig. 5.13b we see how $M_{\text{to}}^{\text{wat}}$ is affected by the effective slip. In this figure we show that high M_{to} value may be obtained for very slipping systems, although it is important to note that the presence of a stagnant layer or defects in the surface (resulting in smaller b_{eff}) may decrease the large predicted M_{to} response, up to 10^{-9} m^2/s.

In conclusion, we predict much larger values for hydrophobic LJ and graphene walls than the ones reported in experiments (for surfaces less atomically smooth and with smaller slip, such as glass in [350]), with orders of magnitude comparable to the ones predicted by MD simulations for water thermo-osmosis in CNTs [337, 84] or on uncharged planar walls [343, 344]. Therefore, our analysis predicts that very strong thermo-osmotic flows can be obtained not only for special systems such as carbon nanotubes, but also with more common hydrophobic charged surfaces, ensuring the absence of a liquid stagnant layer at the interface so that slip can boost the response. We have also seen that, for some intermediate wettings, just by tuning the salt concentration we can change the flow direction due to M_{to} change of sign. This opens the way to manipulate thermally induced nanoscale flows with a pinch of salt.

5.5 Summary and conclusions

We proposed here an analytical framework aimed at predicting the thermo-osmotic response of aqueous electrolytes for a wide range of systems and experimental conditions.

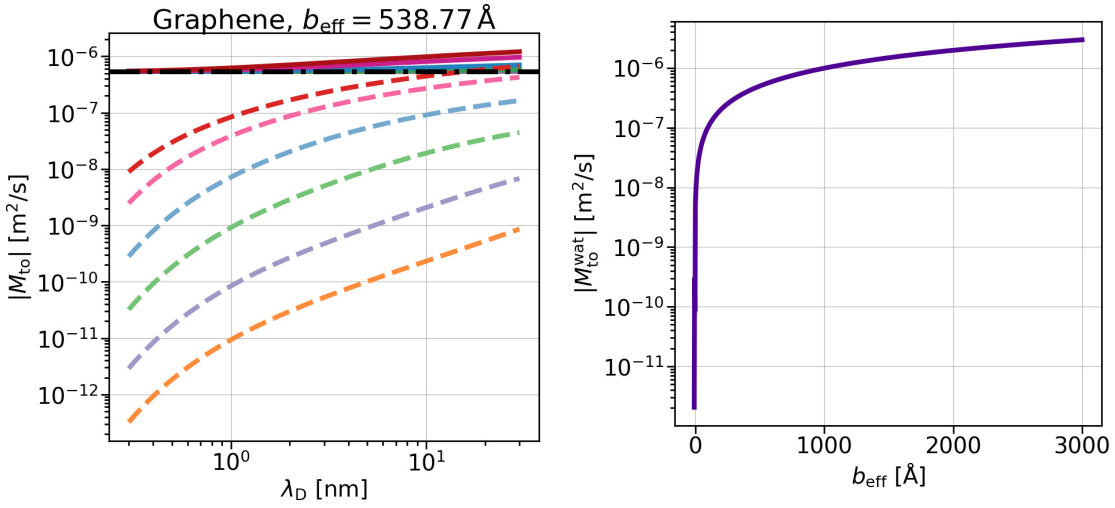

(a) (b)

Figure 5.13: (a) Total thermo-osmotic response coefficient (solid line) for graphene walls, as a function of the Debye length for different surface charges as in Fig. 5.12. The water (dash-dotted) and modified electrostatic (dashed) contributions are also represented. (b) Water contribution to the total thermo-osmotic response for graphene walls as a function of the effective slip.

While the standard picture relates the response to the ion electrostatic enthalpy in the electrical double layer close to charged walls, we show first that this contribution to the interfacial enthalpy may be negligible when compared to the water contribution for a broad range of parameters, and second that it should be slightly lowered due to the depletion of the ions from the solid surface.

The competition between the modified electrostatic and water contributions and the impact of the hydrodynamic boundary condition leads to a rich phenomenology that we illustrated here. First, our theory predicts a higher thermo-osmotic response at low λ_D than the one expected from only considering the electrostatic contribution. Second, the proposed model also predicts a transition between a thermophobic behavior at low salt concentrations to a thermophilic behavior at high salt concentrations for intermediate wettings. Such transition has also been observed in thermophoresis experiments [381, 382, 383], and is commonly attributed to the existence of a thermopotential which is, however, limited to particular boundary conditions imposing no ionic fluxes in the bulk liquid. In contrast, our interpretation of the change of sign is more general and independent on the nanofluidic channel boundary conditions. Third, we predict intense thermally induced flows, comparable to those predicted using very specific channel walls such as carbon nanotubes. These flows were obtained in this work by employing slipping surfaces such as hydrophobic generic Lennard-Jones walls or planar graphene, paving the way to explore other common and affordable charged surfaces. These predictions call for future experimental verification, and could be exploited for the design of innovative solutions for heat harvesting applications.

The importance of the solute contribution in thermo-osmosis of aqueous electrolytes, together with a modification of the classical electrostatic term, opens the way to several perspectives. First, an accurate description of thermo-osmosis should take into account spatial heterogenities of the dielectric and viscosity profiles at the interface [372], as well as the impact of the surface charge and its distribution on water contribution to the response. For very asymmetric salts, such as NaI, the ion-size-dependent hydrophobic solvation term

should be considered, *e.g.* though the modified Poisson-Boltzmann framework described in Refs. 373, 213. Also one should take into account the limits of considering pure water simulations as an approximation of the water enthalpy contribution. For high concentrations, steric effects should be accounted for, and ions can affect water viscosity [69]. Nevertheless such effects correspond to extreme n_s values (whose validity has been discused in Sec. 5.2.1) and they should not understate one of the main results of the present chapter: the great M_{to} value found for slipping surfaces. To consider explicitly systems containing both water and ions, it could be useful to employ other kind of approaches such as Monte Carlo simulations [385], integral equations [386] or classical density functional theory [387]. Secondly, it is straightforward to extend the current model to predict the thermoelectric [388, 389, 390] and thermodiffusive [391] response, with promising applications for electricity production from waste heat or to refine large-scale continuum descriptions [392]. Third, an insightful direction concerns the study of thermo-osmosis in ultra-confined systems [393], where the system height is much smaller than the Debye length. This ultra-confined situation, for which the Poisson-Boltzmann framework still holds, offers another opportunity to modulate thermal nanoscale flows using common surfaces. It would be also interesting to exploit the large thermo-osmotic responses predicted for very slipping systems by using CNTs, where slip values of $b \sim 300$ nm have been reported at room temperature for tube radius of $R \sim 15$ nm [31]. For such confinement, although the theoretical description is beyond the thin Debye layer limit, the Poisson-Boltzmann framework is still valid, and the electrostatic equations can be approximately solved in the cylindrical geometry.

Chapter 6

Conclusions and Outlook

> *"[The cabin; by the stern windows; Ahab sitting alone, and gazing out.] I leave a white and turbid wake; pale waters, paler cheeks, where'er I sail. The envious billows sidelong swell to whelm my track; let them; but first I pass."*
>
> Herman Melville, *Moby Dick* 1851

My thesis work has been devoted to the study of interfacial transport, focusing on liquid-solid friction and slip, intending to provide some fundamental insights on the molecular mechanisms that take place at the interface.

Summary and Applications We started from the critical failure of the no-slip boundary condition due to the presence of a velocity jump at the interface, quantified by the slip velocity v_{slip}. Then, we presented the partial slip boundary condition, first proposed by Navier in 1823 [19]:

$$v_{\text{slip}} = b \left. \frac{\partial v}{\partial z} \right|_{z=z_{\text{s}}} . \tag{6.1}$$

This equation introduces a system characteristic length at the interface (located at z_{s}): the slip length b, defined from the ratio between the bulk and the interfacial transport coefficients, namely viscosity η and liquid-solid friction coefficient λ, so $b = \eta/\lambda$. For a full characterization of the boundary condition, two parameters have to be determined: the slip length b and also the location where the boundary condition applies, z_{s}, what we referred to as the shear plane position.

In the first part of this work (Chapters 2 and 3), we employed classical molecular dynamics (MD) simulations, based on modelling the atomic and molecular physical interactions with empirical force fields, to fully characterize the fluid transport properties under confinement. First, we focused on studying the position z_{s} where the boundary condition applies, and showed that it can be well defined by the Gibbs dividing plane corresponding to the partitioning between a region full of homogeneous fluid and vacuum. Furthermore, because the fluid density profile should not be affected (in the linear response regime) by the forcing applied, we proved that the Gibbs dividing plane position determined from the density profile of equilibrium simulations, identified with the boundary position obtained from gravity-like flow measurements, consisting in applying a constant per atom forcing to all the fluid atoms in the slab. As a consequence, the Gibbs dividing plane characterization of the boundary position appears as a simple, fast and accurate method, in contrast to previous analytical approaches proposed, based on complicated expressions and difficult to

apply to finite size systems [122, 184]. It is also straightforward to extend this method to cylindrical geometries, mixtures, multicomponent fluids and thermalized walls.

We then proceeded to study the temperature dependence of the transport coefficients, viscosity, liquid-solid friction coefficient, and their ratio, the slip length. First we determined the viscosity and the friction coefficient from non-equilibrium MD for a broad range of temperatures, from 225 K to 360 K, two different fluids, methanol and water, and two different wall types, Lennard-Jones (LJ) walls and graphene. We saw that the friction coefficient temperature dependence was weakly affected by the wall type (although at a given temperature LJ walls presented one order of magnitude larger friction than graphene) and mostly determined by the fluid type, where the temperature behavior could be fitted by the same laws for both viscosity and friction, with an Arrhenius law for methanol and a Vogel-Tammann-Fulcher law (modified Arrhenius law, with a divergency at a finite temperature $T_f \neq 0$ K) for water. We highlighted the differences between $\eta(T)$ and $\lambda(T)$ by considering their ratio, which defines the slip length $b(T)$. We observed an increase of slip when decreasing the temperature. Such increase of slip became specially striking when water entered in its supercooled regime, below 273 K. For water, we also observed some quantitative differences in the slip increase (from $T = 360$ K to $T = 225$ K) between different wall types, with it being on the order of 2 for LJ walls and on the order of 5 for graphene walls.

After determining the hydrodynamic transport coefficients in Chapter 2, in Chapter 3 we proceeded to understand the molecular mechanisms controlling friction and slip, focusing on supercooled water. To do so, we decomposed friction, following Ref. 137, into a static and a dynamic contribution, with the dynamics being controlled by the relaxation time of the density autocorrelation, determined from the time decay of the intermediate scattering function. We observed that the temperature evolution of the friction coefficient was mostly controlled by the dynamics of the fluid atoms in the contact layer, defined as the region between the solid surface and the first non-zero minimum of the density profile, *i.e.* the first absorption layer. Following friction decomposition, we also distinguished static and dynamic contributions to viscosity, with the dynamics being controlled in this case by the total relaxation time of the density corresponding to the liquid particles in bulk. With the objective of understanding the temperature evolution of the slip length, controlled by the ratio $\eta(T)/\lambda(T)$, we decomposed slip as the product of η and λ dynamic and static ratios. We observed that viscosity static contribution significantly increased by decreasing temperature when water entered in its supercooled regime, becoming the major contribution to $b(T)$. We also rationalized the differences between graphene and LJ walls from the different friction dynamics (as compared to the bulk ones) between both walls. These interesting results, particularly the great slip values predicted at low temperatures ($b \sim 230$ nm for water on graphene walls), are seeking for experimental validation, where such low temperatures have already been achieved in experiments for water on nanopores, for bulk water, or for droplets on anti-icing surfaces [212, 226, 56].

In Chapter 3, we also characterized thermal transport, by studying the interfacial heat transfer between water and gold, nanostructuring the gold surface and coating it with a graphene sheet. By trapping air (or vacuum in our simulations) between graphene and the nanopatterned gold, we observed an increase in the interfacial resistance as compared to the planar gold situation, which was shown to scale with the effective graphene-gold contact surface (the less contact surface the higher the resistance). The large thermal resistance values we predicted present promising applications in delaying the temperature at which the boiling crisis occurs, using a robust alternative to superhydrophobic Cassie materials. Also, because the low thermal conductance is achieved mostly due to geometrical properties

(air trapping), it is trivial to extend our results to any material with equivalent structure to that of the nanopatterned gold wall we presented.

In Chapter 4 we used *ab initio* MD to characterize the temperature dependence of bulk transport properties (viscosity and diffusion coefficient) for water, in a temperature range $T \in [260, 360]$ K. By comparing different exchange-correlation functionals (PBE-D3, optB88-vdW and SCAN) and benchmarking our results with force-field (FF) simulations (for a water model in good agreement with experiments), we saw that SCAN was the functional that better described viscosity and diffusion coefficient temperature dependence, although it deviated from FF results for the lower temperatures considered. Independently of the failure or success in recovering water's transport properties in bulk, we observed that all the functional predictions verified the Stokes-Einstein relation with the same hydrodynamic radius, $R_{\mathrm{h}} \sim 1$ Å. Motivated by exploring the connection between dynamic transport and structural properties, we also characterized the structure for the different functionals by computing the radial distribution function. In this case SCAN was again the functional whose results better compared to FF. Finally, we recalled excess entropy scaling laws, which predict an exponential dependency of the reduced (dimensionless) diffusion coefficient and viscosity on the excess of entropy. We approximated the excess of entropy to the 2-pair contribution, related to the radial distribution function, and concluded that all the functionals were in agreement with the expected scaling although with different fit parameters. From these results we established the importance of reproducing the radial distribution function for all the solvation shells, *i.e.* including its long-range behavior, in contrast to the common procedure carried in functional development that only focuses on a good description of its first peak. Therefore, we hope that our results could be used to develop better functionals. Also, we suggested the employment of entropy-scaling laws for a fast and practical characterization of the temperature dependence of bulk transport properties. Once the entropy scaling fit parameters have been determined for a given functional, diffusion coefficient and viscosity could be predicted at fixed density from only structural properties, which typically need shorter times to converge as compared to their dynamic counterparts [311].

Lastly, in Chapter 5 we proposed an analytical framework to describe the thermo-osmotic response coeeficient, controlled by enthalpy excess density, of an aqueous electrolyte in a nanochannel. We obtained that the thermo-osmotic response was mostly determined from the competition between the solvent contribution (water, which had to be determined from classical MD simulations) and a modification of the classical ion electrostatic term, corrected to take into account the depletion of the ions from the wall. Three main results were obtained in contrast with the classical theory, which only accounts for the electrostatic enthalpy of the ions and where no depletion layer is considered. First, we determined that at small Debye lengths (high salt concentrations), the response was mostly dominated by the water contribution, being orders of magnitude greater than the values expected from the classical electrostatic theory. We also observed a change of sign in the response coefficient for intermediate and hydrophobic wettings: at fixed surface charge, when varying the salt concentration, the response evolved from a thermophobic behavior at low concentrations to a thermophilic behavior at high concentrations. Such behavior arises from the different signs for the water and the electrostatic contributions, and thus it cannot be predicted by only considering electrostatic interactions. We also remarked that the change of sign has already been observed in thermophoresis experiments, and could explain the sign disagreements reported in thermo-osmosis experiments. Finally, we also reported high thermo-osmotic responses, specially for graphene walls, with interesting applications in heat harvesting by *e.g.* using the osmotic flow generated by the temperature

gradient to drive a turbine, transforming waste heat into mechanical power.

Perspectives Although all thesis work has to lead to a conclusion, I would like to finish this manuscript highlighting some of the interesting perspectives I could not explore by lack of time, together with some questions that arouse at some moment of the development of my thesis and that remain to be answered.

For instance, when characterizing the hydrodynamic boundary position, one could explore the interesting case of nanopattering the wall surface. As previously mentioned in Chapter 2, we proposed a hydrodynamic justification to employ the Gibbs dividing plane approach to determine the interface position by identifying this method with the gravity-like flow measures. Nevertheless, one could wonder if both measures still identify in the case of a rough wall, modelled with nanopillars, which would impose an absence of flow at the interface in the holes of the nanostructure.

Also, because it has been already assessed that nanopattering an interface can imply an increase in the slip length with respect to the planar wall situation [246], an interesting venue is to explore the temperature effect on slippage for a nanostructured wall, extending the procedure proposed to characterize $\lambda(T)$ and $b(T)$ when driving the liquid (water) to its supercooled regime. In this case, from a possible coupled effect between wall structure and temperature, one could expect an even higher slip increase than the one we presented for planar walls. Another interesting and promising way of broadening the slippage results in supercooled water would be to extend the presented analysis to the case of carbon nanotubes (CNTs), for which a similar order of magnitude than the one we measure at 225 K has been assessed experimentally at room temperature [31]. The effect of the characteristic cylindrical geometry together with the effect we assessed related to the supercooled state at low temperatures, could imply a massive slip, of special interest for the community and with a large set of applications as those discussed in the introduction, Chapter 1. In this project on supercooled water and liquid-solid friction, it also remains to fundamentally explore the quantitative failure of the friction static/dynamic decomposition proposed by Bocquet and Barrat [137], which only provided a good qualitative description in terms of temperature dependence.

For thermal transport, it is left for a full completeness of the study to extend the results by adding graphene layers between the water and the gold nanopillars, until recovering graphite structures. It has been already assessed for planar walls that the thermal interfacial resistance is affected by the number of graphene layers [274, 275]. By then showing the suitability of graphite to locate at the interface to trap air bubbles, we should expect even higher thermal resistance values than the ones presented in this manuscript, which would be achieved with a cheaper and stiffer material than graphene.

When exploring *ab initio* simulations of bulk water and how the transport coefficients are affected by temperature, we showed a failure of the SCAN functional at low temperatures, which remains to be understood. One possible explanation is the importance of the nuclear quantum effects (not modelled in our DFT simulations) at such low temperatures. These quantum nuclear effects could be implemented via path-integral molecular dynamics (PIMD) or a quantum thermostat. Since these methods are very demanding, one could reduce the overall cost of the simulations by replacing DFT by machine learning potentials, and implement the nuclear effects on them. For a fully completion of this work one could also explore the validity of our approximation $s_{\text{ex}} \simeq s_2$, whose range of validity can become delicate under extreme pressure and temperature conditions [394, 309, 306]. Although a more precise measure of s_{ex} based on the three, four, etc,-body contributions is difficult to implement, different ways of determining s_{ex} have been proposed in the literature. Of

special interest, due to its simplicity, would be to construct s_2 from the oxygen-oxygen, oxygen-hydrogen, and hydrogen-hydrogen pair distributions, which is expected to estimate better s_{ex}, following Ref. 395. Finally, a difficult and non-trivial perspective is to understand the physical meaning of the fit parameters in the excess entropy scaling relations, which have been proven to be affected by the density, and which may be an interesting way to explore the breaking of the Stokes-Einstein relation at low temperatures [310].

Last, but not least, several improvements could be performed in the analytical framework we proposed to describe the enthalpy excess density profiles. It would be interesting to assess the importance of taking into account in the model the inhomogeneties of the permittivity and viscosity at the interface. Equivalent venues have already been taken in Refs. 372, 213, and the extension of their results to our system should not be too difficult to implement. Also one could explore the extension to multicomponent fluids (as water) of the thermo-osmotic force determination technique proposed in Ref. 380, which would provide an accurate determination of the local velocity profiles without going through the ambiguities related to the local definition of the pressure tensor in MD simulations. One could also wonder about how the water enthalpy is affected by the sign, magnitude and distribution of the surface charge, and to extend the current model to encounter for the ion specificity, critical in the case of very asymmetric salts, as done in Refs. 373, 213 for electro-osmosis. The extension of our analysis of the thermo-osmotic response to the thermoelectric response is also a trivial issue, all with important applications on heat harvesting. With that regard, the formulas controlling the thermoelectric response coefficient have been already presented in this manuscript. Also, Appendix B details important formulas describing the no-coions regime (corresponding to an electric double layer overlap of the top and bottom wall), and cylindrical geometries within the Poisson-Boltzmann framework. These expressions can be useful in the study and modelling of ultraconfined systems and nanotubes.

Overall, in this manuscript we tried to highlight the richness of behaviors related to flows at the nanoscale. We mostly focused on the slip boundary condition, stated by Navier and rediscovered in the 70's for polymers and in the late 90's for simple fluids. We tried to better characterize and to understand the molecular mechanisms related to interfacial hydrodynamic and heat transport. We also studied hydrodynamic bulk transport properties and their deep and non trivial connection with structure. Finally, we showed, via a proposed analytical model, the power of slip and liquid-solid interactions, which can translate into large system responses as we predicted in the case of thermo-osmosis. Together with the answers we suggest, new and intriguing questions appeared, which we hope will be addressed in the future. On the whole, we hope to have presented the transport at the nanoscale as the land of opportunities it is. Being at the crossroad of many characteristic lengths, nanofluidics encloses innovative and unique fluid transport behavior, with promising perspectives to tackle some of the great challenges faced by our society. It is, for sure, an exciting time.

Appendix A

Ewald sums

Typically, the most costly stage in a molecular dynamics simulation is the computation of the set of forces between all the particles in the system. For short-range interactions like Lennard-Jones interactions, we simply define a cutoff radius around each particle, beyond which the interactions are neglected. In contrast, to compute long-range interactions (in particular Coulomb interactions) it is not possible to simply truncate the potential. The Ewald sums method allows us to efficiently calculate the electrical interactions between charged particles in the system. We present in this section a general introduction to this method, of which further detail can be found on general textbooks on molecular simulations as in Ref. [146].

A.1 General idea: charge smearing

Let's first consider as basic cell a system with periodic boundary conditions, of volume $V = L^3$, and with partial charges q_i such as $\sum_i q_i = 0$ with $i = 1, ..., N$. The Ewald sums or Ewald summation method consists in considering the basic cell surrounded by an infinite number of identical copies of itself. Therefore, the total Coulombic interactions will we be obtained from summing the interaction energy of each charge in the central volume (i.e. our basic cell) with all the images of the other charges. We want to compute the electrostatic energy

$$\mathcal{U}_{\mathrm{C}} = \frac{1}{2} \sum_{i=1}^{N} q_i \phi(\mathbf{r}_i), \tag{A.1}$$

where $\phi(\mathbf{r}_i)$ corresponds to the electrostatic potential at the position of the ion i, which will be itself equal to the sum over all the periodic images $\mathbf{n}$,

$$\phi(\mathbf{r}_i) = \sum_{\mathbf{n}} \sum_{j=1}^{N} \frac{q_j}{|\mathbf{r}_{ij} + \mathbf{n}L|}, \tag{A.2}$$

with $j \neq i$ if $\mathbf{n} = \mathbf{0}$ (the ion i interacts with all the periodic images but not with itself). The punctual charges and its periodic images define the charge density creating the potential, given by:

$$\rho(\mathbf{r}) = \sum_{\mathbf{n}} \sum_{j=1}^{N} q_j \delta(\mathbf{r}) = \sum_{\mathbf{n}} \sum_{j=1}^{N} q_j \delta(|\mathbf{r} - (\mathbf{r}_j + \mathbf{n}L)|). \tag{A.3}$$

This $\rho(\mathbf{r})$ expression corresponds to a periodic function of period L but, because it is very sharp (due to its dependence on the delta function), its Fourier representation will never

converge. To solve this problem, we can smear all the charges by considering each point charge surrounded by a diffusive charge distribution of equal magnitude and opposite sign. This new charge distribution is conveniently taken as a Gaussian of width $\sqrt{2/\alpha}$:

$$\rho_{\text{Gauss}}(\mathbf{r}) = -q_i\Big(\frac{\alpha}{\pi}\Big)^{3/2} e^{-\alpha r^2}. \tag{A.4}$$

Let's first compute the electrostatic energy of the smeared charges given by $-\rho_{\text{Gauss}}$. This charge distribution will be determined by the periodic sum of Gaussians:

$$\rho(\mathbf{r}) = \sum_{\mathbf{n}}\sum_{j=1}^{N} q_j\Big(\frac{\alpha}{\pi}\Big)^{3/2} \exp\Big[-\alpha|\mathbf{r} - (\mathbf{r}_j + \mathbf{n}L)|^2\Big], \tag{A.5}$$

which converges to Eq. (A.3) for large α. In order to compute the electrostatic potential of a given charge distribution $\rho(\mathbf{r})$, we should use the Poisson equation:

$$\nabla^2\phi(\mathbf{r}) = -4\pi\rho(\mathbf{r}); \tag{A.6}$$

which, in the reciprocal space writes:

$$k^2\phi(\mathbf{k}) = -4\pi\rho(\mathbf{k}), \tag{A.7}$$

with $\rho(\mathbf{k})$ the Fourier transform of the charge density:

$$\rho(\mathbf{k}) = \frac{1}{V}\int_V \mathrm{d}\mathbf{r}\, e^{-i\mathbf{k}\cdot\mathbf{r}}\rho(\mathbf{r}) = \frac{1}{V}\sum_{j=1}^{N} q_j e^{-i\mathbf{k}\cdot\mathbf{r}_j} e^{-k^2/4\alpha}. \tag{A.8}$$

Substituting this expression in Eq. (A.7) and inverting the transform to recover the real-space potential, we finally obtain:

$$\phi(\mathbf{r}) = \sum_{\mathbf{k}\neq 0}\phi(\mathbf{k})e^{i\mathbf{k}\cdot\mathbf{r}} = \frac{1}{V}\sum_{\mathbf{k}\neq 0}\sum_{j=1}^{N}\frac{4\pi q_j}{k^2} e^{i\mathbf{k}\cdot(\mathbf{r}-\mathbf{r}_j)} e^{-k^2/4\alpha}. \tag{A.9}$$

From the point charges in this expression for the potential of smeared charges, we can now obtain the electrostatic energy, given by the expression:

$$\mathcal{U}_q = \frac{1}{2}\sum_i q_i\phi(\mathbf{r}) = \frac{1}{2}\sum_{\mathbf{k}\neq 0}\sum_{i,j=1}^{N}\frac{4\pi q_i q_j}{Vk^2} e^{-k^2/4\alpha} e^{i\mathbf{k}\cdot(\mathbf{r}_i-\mathbf{r}_j)}. \tag{A.10}$$

Multiplying and dividing by V and taking into account that $\rho(\mathbf{k}) = \sum_j q_j e^{-i\mathbf{k}\cdot\mathbf{r}_j}/V$, then $\mathcal{U}_q$ can be written as:

$$\mathcal{U}_q = \frac{1}{2}\sum_{\mathbf{k}\neq 0}\frac{4\pi V}{k^2} e^{-k^2/4\alpha}|\rho(\mathbf{k})|^2. \tag{A.11}$$

A.2 Potential corrections

It is important to note that, for $\mathcal{U}_q$ to identify with the Coulombic potential $\mathcal{U}_{\text{C}}$ in Eq. (A.1), two corrections are needed: one correction related to the self interactions and another one due to the charge smearing introduced.

a. Self-interaction correction

Let's focus first on the correction for self-interaction. Eq. (A.11) was estimated by replacing each point charge by a smeared Gaussian centered on that charge. This implies that a given point charge also interacts with its smeared representation (i.e. we overcounted the contribution $\mathbf{n} = 0$ in Eq. (A.5)) and, in order to recover the real electrostatic energy, we need to subtract this contribution from $\mathcal{U}_q$. To do so, we will work in real space in order to deal with the self term. The solution to the Poisson Eq. (A.6) is

$$\phi(\mathbf{r}) = \frac{q_j}{\mathbf{r}}\mathrm{erf}\big(\sqrt{\alpha}\mathbf{r}\big); \tag{A.12}$$

where

$$\mathrm{erf}(x) = \frac{2}{\sqrt{\pi}}\int_0^x e^{-u^2}\mathrm{d}u,$$

is the error function. In particular, the potential due to the self-interaction, ϕ_{self}, is

$$\phi_{\mathrm{self}} = \phi(\mathbf{0}) = 2q_j\sqrt{\frac{\alpha}{\pi}}. \tag{A.13}$$

Therefore, the self correction to be subtracted from $\mathcal{U}_q$ for each charge will be:

$$\mathcal{U}_{\mathrm{self}} = \frac{1}{2}\sum_{j=1}^{N} q_j\phi(\mathbf{0}) = \sqrt{\frac{\alpha}{\pi}}\sum_{j=1}^{N} q_j^2; \tag{A.14}$$

which does not depend on the particles positions, i.e. it is independent of the configuration.

b. Smear correction

The second correction we have to introduce to Eq. (A.11) is related to the introduced smear. This is an additive contribution, because it is related to the electrostatic energy due to the point charges screened by oppositely charged Gaussians. To do so, we add the correct field related to the point charges, $\phi_j^{\mathrm{pc}}(\mathbf{r})$,and subtract the approximate one related to the Gaussians, $\phi_j^{\mathrm{G}}(\mathbf{r})$, introduced:

$$\Delta\phi_j(\mathbf{r}) = \phi_j^{\mathrm{pc}}(\mathbf{r}) - \phi_j^{\mathrm{G}}(\mathbf{r}) = \frac{q_j}{|\mathbf{r}-\mathbf{r}_j|}\mathrm{erfc}\big(\sqrt{\alpha}|\mathbf{r}-\mathbf{r}_j|\big), \tag{A.15}$$

with $\mathrm{erfc}(x) = 1 - \mathrm{erf}(x)$ the complementary error function. Because $\Delta\phi_j$ is short ranged for large α (narrow Gaussians), it is often referred as $\phi_{\mathrm{short-range}}$ [145]. The correction to the electrostatic energy will be then given by $\Delta\mathcal{U} = \frac{1}{2}\sum_{\mathbf{n}}\sum_{i\neq j} q_i\Delta\phi_j(\mathbf{r}_{ij})$, and therefore:

$$\Delta\mathcal{U} = \frac{1}{2}\sum_{\mathbf{n}}\sum_{i\neq j}^{N}\frac{q_iq_j}{\mathbf{r}_{ij}}\mathrm{erfc}\big(\sqrt{\alpha}\mathbf{r}_{ij}\big). \tag{A.16}$$

Finally, the total Coulomb energy is given by the expression:

$$\mathcal{U}_{\mathrm{C}} = \mathcal{U}_q(\alpha) - \mathcal{U}_{\mathrm{self}}(\alpha) + \Delta\mathcal{U}(\alpha), \tag{A.17}$$

where each term depends on α but, if enough lattice vectors are used in the reciprocal and real space sums, the sum will be independent of it.

Appendix B

Poisson-Boltzmann formulary

The Poisson-Boltzmann equation provides a mean-field theory of electrolyte solutions at interfaces and in confinement, with numerous applications ranging from colloid science to nanofluidics. This formulary gathers important formulas for the Poisson-Boltzmann description of a Z:Z electrolyte solution inside slit and cylindrical channels. Different approximated solutions and their range of validity are discussed, together with the full solution for the slit channel. This formulary is meant to continuously evolve following feedback from the readers and it has been published as an arXiv preprint (*arXiv:2105.00720*).

B.1 Introduction

When an electrolyte solution meets a solid surface, several mechanisms can generate a surface charge, together with an opposite charge carried by ions in the liquid (typical mechanisms include dissociation of surface groups and specific adsorption of charged species) [362, 363, 359]. In the vicinity of a charged wall, ions reorganize to form a diffuse charged layer, the electrical double layer (EDL), which screens the surface electric field over the so-called Debye length denoted λ_D, see Fig. B.1(a-b). The EDL plays a key role in many aspects of soft condensed matter, as it controls the stability and dynamics of charged objects in solution [362, 363, 359]. In particular, the EDL is at the origin of the so-called electrokinetic effects, where gradients and fluxes of different types (hydrodynamic, electrical, chemical, thermal) are coupled in the presence of charged interfaces [366]. Such electrokinetic effects are central to the very active field of nanofluidics [87, 29, 367, 368].

The ion distribution and electric potential profile in the EDL can be computed by combining the Poisson equation for electrostatics and the Boltzmann distribution of the ions into the so-called Poisson-Boltzmann (PB) equation, under certain assumptions [364, 365]:

- the Poisson equation is written assuming that the solvent has a local, homogeneous and isotropic dielectric permittivity;
- the Boltzmann distribution of the ions is written assuming that the energy of the ions results only from their Coulomb interactions with the other ions and the wall, described at a mean-field level.

Educational presentations of the PB theory can be found in books [362, 363, 359], book chapters [364, 365], and articles [366], discussing in particular applications to nanofluidics [87, 29, 367, 368].

In contrast, this formulary simply gathers important formulas for the description of the EDL with the PB equation, focusing on a Z:Z electrolyte solution inside slit and cylindrical

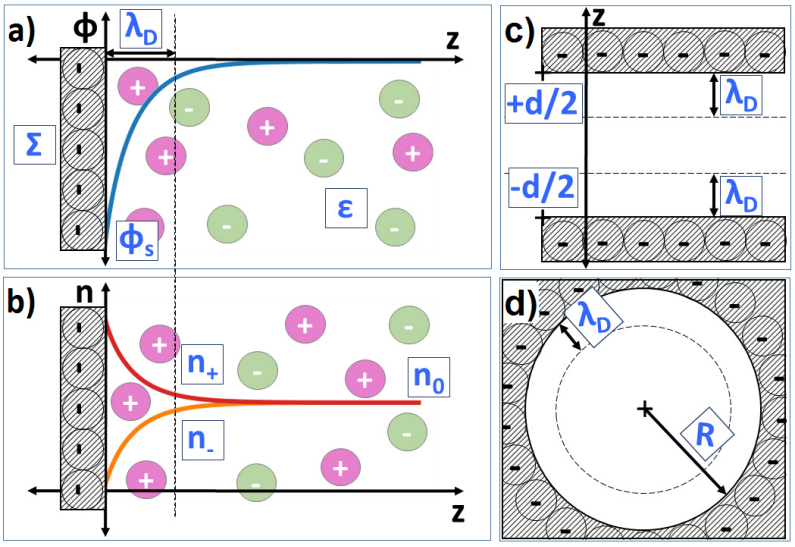

Figure B.1: a-b) Local picture of the electrical double layer at a charged wall (z is the distance from the wall, Σ the surface charge density, ε the solvent dielectric permittivity, and λ_D the Debye length): a) Profile of reduced electric potential ϕ, with ϕ_s the value at the wall; b) Profiles of cation n_+ and anion n_- densities, with n_0 the bulk value. c) Schematics of the slit channel. d) Schematics of the cylindrical channel.

channels, see Fig. B.1(c) and Fig. B.1(d), respectively. After introducing the notations (Sec. B.2) and important characteristic lengths (Sec. B.3), the formulary describes the cases of a slit channel (Sec. B.4) and of a cylindrical channel (Sec. B.5). For both geometries, different approximated solutions are discussed: the thin EDL limit, where λ_D is small as compared to the channel size; the no co-ion limit, where the EDLs overlap and the surface charge is large enough that co-ions are excluded; the Debye-Hückel limit at low surface charge, where the PB equation can be linearized. The range of validity of these approximations is then discussed; for the slit channel only, the general solution is presented. Finally the limits of the PB framework are briefly discussed in Sec. B.6.

B.2 Notations

- inverse thermal energy $\beta = 1/(k_B T)$, with k_B the Boltzmann constant and T the temperature
- absolute ionic charge $q = Ze$, with e the elementary charge and Z the ion valence
- electrostatic potential V
- reduced potential $\phi = \beta q V$
- their value at the wall V_s and ϕ_s
- ion densities $n_\pm$
- charge density ρ_e
- solvent dielectric permittivity ε
- salt concentration $n_0 = n_+ = n_-$ in the bulk/reservoirs

- surface charge density Σ

B.3 Characteristic lengths

Solvent permittivity ε: Bjerrum length $\ell_\mathbf{B}$ – The Bjerrum length is the distance at which the electrostatic interaction energy between two ions is equal to the thermal energy $k_\mathrm{B}T$.

$$\ell_\mathrm{B} = \frac{\beta q^2}{4\pi\varepsilon} \quad \Leftrightarrow \quad \varepsilon = \frac{\beta q^2}{4\pi\ell_\mathrm{B}} \tag{B.1}$$

For a monovalent salt in water at room temperature, $\ell_\mathrm{B} \sim 0.7\,\mathrm{nm}$.

Bulk salt concentration n_0: Debye length $\lambda_\mathbf{D}$ – The Debye length is the range of the exponential screening of the electric field in an electrolyte.

$$\lambda_\mathrm{D} = \frac{1}{\sqrt{8\pi\ell_\mathrm{B} n_0}} \quad \Leftrightarrow \quad n_0 = \frac{1}{8\pi\ell_\mathrm{B}\lambda_\mathrm{D}^2} \tag{B.2}$$

For a monovalent salt in water at room temperature, $\lambda_\mathrm{D} \sim 0.3\,\mathrm{nm}/\sqrt{n_0(\mathrm{mol/L})}$.

Surface charge density Σ: Gouy-Chapman length $\ell_\mathbf{GC}$ – The Gouy-Chapman length is the distance at which the electrostatic interaction energy between an ion and a charged surface is comparable to the thermal energy $k_\mathrm{B}T$.

$$\ell_\mathrm{GC} = \frac{q}{2\pi\ell_\mathrm{B}|\Sigma|} \quad \Leftrightarrow \quad \Sigma = \mathrm{sgn}(\Sigma)\frac{q}{2\pi\ell_\mathrm{B}\ell_\mathrm{GC}} \tag{B.3}$$

For monovalent ions in water at room temperature, $\ell_\mathrm{GC} \sim 36\,\mathrm{nm}/|\Sigma|(\mathrm{mC/m^2})$.

In the following, it will appear that many quantities can be expressed as a function of the ratio $\lambda_\mathrm{D}/\ell_\mathrm{GC}$, which is proportional to the absolute value of the surface charge, and inversely proportional to the square root of the bulk salt concentration:

$$\frac{\lambda_\mathrm{D}}{\ell_\mathrm{GC}} = 2\pi\ell_\mathrm{B}\lambda_\mathrm{D}\frac{|\Sigma|}{q} = \frac{|\Sigma|/q}{\sqrt{n_0}}\sqrt{\frac{\pi\ell_\mathrm{B}}{2}}$$

B.4 Slit channel

This section gathers the equations describing a Z:Z electrolyte solution confined between two planar parallel walls at a distance d, see Fig. B.1(c).

B.4.1 Thin EDLs: one wall with salt

When the distance d between the surfaces is much larger than the thickness of the EDLs, one can solve the PB equation for a single charged wall, and superimpose the potentials of the two walls to obtain the full potential in the channel. The limits of validity of this approximation will be quantified in section B.4.4.

Accordingly, this section gathers formulas for the description of a Z:Z electrolyte solution in contact with a single planar wall, where $z \geq 0$ is the distance from the wall, see Fig. B.1(a) and (b).

a. Poisson-Boltzmann equation: derivation

Poisson equation:

$$-\varepsilon\frac{\mathrm{d}^2V}{\mathrm{d}z^2} = \rho_\mathrm{e}(z) = q\{n_+(z) - n_-(z)\}$$

Boltzmann distribution:

$$n_\pm(z) = n_0\,\exp\{\mp\beta q V(z)\}$$

Poisson-Boltzmann equation

$$\frac{\mathrm{d}^2\phi}{\mathrm{d}z^2} = \frac{1}{\lambda_\mathrm{D}^2}\sinh\{\phi(z)\} \tag{B.4}$$

b. Poisson-Boltzmann equation: solution

Multiplying both sides of Eq. (B.4) by $\mathrm{d}\phi/\mathrm{d}z$ and integrating between $z=\infty$ and z, imposing that $\mathrm{d}\phi/\mathrm{d}z|_{z=\infty} = \phi(\infty) = 0$:

$$\frac{1}{2}\left(\frac{\mathrm{d}\phi}{\mathrm{d}z}\right)^2 = \frac{1}{\lambda_\mathrm{D}^2}\{\cosh(\phi) - 1\} \tag{B.5}$$

Noting that $\cosh(\phi) - 1 = 2\sinh^2(\phi/2)$, and that ϕ and $\mathrm{d}\phi/\mathrm{d}z$ are of opposite sign:

$$\frac{\mathrm{d}\phi}{\mathrm{d}z} = -\frac{2}{\lambda_\mathrm{D}}\sinh\left(\frac{\phi}{2}\right) \tag{B.6}$$

Noting that $\sinh(\phi/2) = 2\sinh(\phi/4)\cosh(\phi/4) = 2\tanh(\phi/4)\cosh^2(\phi/4)$, and integrating like a physicist:

$$\int_{\phi_\mathrm{s}}^{\phi}\frac{\mathrm{d}(\phi/4)}{\tanh(\phi/4)\cosh^2(\phi/4)} = -\int_0^z\frac{\mathrm{d}z}{\lambda_\mathrm{D}} \quad\Rightarrow\quad \ln\left|\tanh\left(\frac{\phi}{4}\right)\right| - \ln\left|\tanh\left(\frac{\phi_\mathrm{s}}{4}\right)\right| = -\frac{z}{\lambda_\mathrm{D}}$$

Noting that ϕ and ϕ_s have the same sign:

$$\tanh\left(\frac{\phi}{4}\right) = \tanh\left(\frac{\phi_\mathrm{s}}{4}\right)e^{-\frac{z}{\lambda_\mathrm{D}}}$$

Noting that $\mathrm{atanh}(x) = \frac{1}{2}\ln\left(\frac{1+x}{1-x}\right)$, and denoting

$$\gamma = \tanh\left(\frac{\phi_\mathrm{s}}{4}\right) \tag{B.7}$$

one finally gets:

$$\phi(z) = 4\,\mathrm{atanh}\left\{\gamma e^{-\frac{z}{\lambda_\mathrm{D}}}\right\} = 2\ln\left(\frac{1+\gamma e^{-\frac{z}{\lambda_\mathrm{D}}}}{1-\gamma e^{-\frac{z}{\lambda_\mathrm{D}}}}\right) \tag{B.8}$$

c. Surface charge and surface potential

Electrostatics at the interface:

$$-\left.\frac{\mathrm{d}V}{\mathrm{d}z}\right|_{z=0} = \frac{\Sigma}{\varepsilon} \quad \Rightarrow \quad \left.\frac{\mathrm{d}\phi}{\mathrm{d}z}\right|_{z=0} = -4\pi\ell_\mathrm{B}\frac{\Sigma}{q} = -\frac{2\,\mathrm{sgn}(\Sigma)}{\ell_\mathrm{GC}}$$

Using Eq. (B.6), one obtains *Grahame equation* relating ϕ_s and Σ:

$$\sinh\left(\frac{\phi_\mathrm{s}}{2}\right) = 2\pi\ell_\mathrm{B}\lambda_\mathrm{D}\frac{\Sigma}{q} = \mathrm{sgn}(\Sigma)\frac{\lambda_\mathrm{D}}{\ell_\mathrm{GC}} \tag{B.9}$$

so that ϕ_s can be expressed as:

$$\phi_\mathrm{s} = 2\,\mathrm{sgn}(\Sigma)\,\mathrm{asinh}\left(\frac{\lambda_\mathrm{D}}{\ell_\mathrm{GC}}\right) = 2\,\mathrm{sgn}(\Sigma)\ln\left\{\frac{\lambda_\mathrm{D}}{\ell_\mathrm{GC}} + \sqrt{1+\left(\frac{\lambda_\mathrm{D}}{\ell_\mathrm{GC}}\right)^2}\right\}$$

One can also express $\gamma = \tanh(\phi_\mathrm{s}/4)$ as a function of Σ:

$$\gamma = \frac{\mathrm{sgn}(\Sigma)}{\lambda_\mathrm{D}/\ell_\mathrm{GC}}\left\{-1+\sqrt{1+\left(\frac{\lambda_\mathrm{D}}{\ell_\mathrm{GC}}\right)^2}\right\} \tag{B.10}$$

d. A few integrals

Electrostatic energy $\mathcal{E}$

$$\begin{aligned}\mathcal{E} &= \frac{\varepsilon}{2}\int_0^\infty \left(\frac{\mathrm{d}V}{\mathrm{d}z}\right)^2 \mathrm{d}z = \frac{1}{8\pi\ell_\mathrm{B}\beta}\int_0^\infty \left(\frac{\mathrm{d}\phi}{\mathrm{d}z}\right)^2 \mathrm{d}z \\ &= \frac{1}{2\pi\ell_\mathrm{B}\lambda_\mathrm{D}\beta}\left\{-1+\sqrt{1+\left(\frac{\lambda_\mathrm{D}}{\ell_\mathrm{GC}}\right)^2}\right\} = \frac{|\gamma|}{2\pi\ell_\mathrm{B}\ell_\mathrm{GC}\beta}\end{aligned} \tag{B.11}$$

Ionic densities

Total density excess Using Eq. (B.5),

$$n_+ + n_- - 2n_0 = 2n_0\left\{\cosh(\phi)-1\right\} = \frac{1}{8\pi\ell_\mathrm{B}}\left(\frac{\mathrm{d}\phi}{\mathrm{d}z}\right)^2$$

Therefore,

$$\int_0^\infty (n_+ + n_- - 2n_0)\,\mathrm{d}z = \beta\mathcal{E} \tag{B.12}$$

Density difference Electroneutrality imposes that:

$$\int_0^\infty \rho_\mathrm{e}(z)\,\mathrm{d}z = -\Sigma$$

Remembering that $\rho_\mathrm{e} = q(n_+ - n_-)$, one gets:

$$\int_0^\infty (n_+ - n_-)\,\mathrm{d}z = -\frac{\Sigma}{q} = -\frac{\mathrm{sgn}(\Sigma)}{2\pi\ell_\mathrm{B}\ell_\mathrm{GC}} \tag{B.13}$$

Thickness of the EDL The thickness of the EDL is often identified with the Debye length λ_D. However, at high $|\Sigma|$, the charge of the EDL is concentrated in a region much thinner than λ_D. The characteristic thickness of the charged region can be defined as:

$$\lambda = \frac{\int_0^\infty z\,\rho_e(z)\,\mathrm{d}z}{\int_0^\infty \rho_e(z)\,\mathrm{d}z} = \frac{\varepsilon V_s}{\Sigma} = \frac{V_s}{-\left.\frac{\mathrm{d}V}{\mathrm{d}z}\right|_{z=0}} = \frac{\phi_s}{-\left.\frac{\mathrm{d}\phi}{\mathrm{d}z}\right|_{z=0}}$$

Using Eq. (c.) and Eq. (c.), one gets:

$$\lambda = \ell_{GC}\frac{|\phi_s|}{2} = \ell_{GC}\ln\left\{\frac{\lambda_D}{\ell_{GC}} + \sqrt{1+\left(\frac{\lambda_D}{\ell_{GC}}\right)^2}\right\} \tag{B.14}$$

Note that the characteristic scale for the variation of the electric field can also be written, following Ref. 396:

$$\lambda' = \frac{-\left.\frac{\mathrm{d}\phi}{\mathrm{d}z}\right|_{z=0}}{\left.\frac{\mathrm{d}^2\phi}{\mathrm{d}z^2}\right|_{z=0}} = \frac{\lambda_D}{\sqrt{1+\left(\frac{\lambda_D}{\ell_{GC}}\right)^2}} \tag{B.15}$$

The limits at low and high surface charge of these characteristic scales are reported in next section e.

More integrals Denoting $x = \lambda_D/\ell_{GC}$,

$$\mathcal{F} = \int_0^\infty (\phi_s - \phi)\left(\frac{\mathrm{d}\phi}{\mathrm{d}z}\right)^2 \mathrm{d}z = \frac{8\,\mathrm{sgn}(\Sigma)}{\ell_{GC}}\left\{1 - \frac{\mathrm{asinh}(x)}{x}\right\} \tag{B.16}$$

$$\mathcal{G} = \int_0^\infty z\left(\frac{\mathrm{d}\phi}{\mathrm{d}z}\right)^2 \mathrm{d}z = -4\ln\left(1-\gamma^2\right) \tag{B.17}$$

e. Low and high surface charge limits

Critical surface charge When the surface charge $|\Sigma|$ is low enough that the reduced potential $|\phi|$ is much lower than 1 everywhere, and therefore when $|\phi_s| = \max(|\phi|) \ll 1$, the PB equation can be linearized; this is the Debye-Hückel (DH) regime.

Using Grahame equation, Eq. (B.9), it appears that this regime is found when $\lambda_D \ll \ell_{GC}$. The related critical surface charge for which $\lambda_D = \ell_{GC}$ writes:

$$|\Sigma|_c = \frac{q}{2\pi\ell_B\lambda_D} = \sqrt{\frac{8\varepsilon n_0}{\beta}} \tag{B.18}$$

For instance, for a monovalent salt in water at room temperature:

$$|\Sigma|_c \sim \frac{36\,\mathrm{mC/m^2}}{\lambda_D(\mathrm{nm})} \sim 120\,\mathrm{mC/m^2}\sqrt{n_0(\mathrm{mol/L})} \tag{B.19}$$

In practice the linearized equation only provides a fair description for $|\Sigma| \lesssim 0.2|\Sigma|_c = 24\,\mathrm{mC/m^2}\sqrt{n_0(\mathrm{mol/L})}$. Thus, except at very high salt concentration, the DH regime is only found for very low surface charge.

Quantity	$\lambda_D \ll \ell_{GC}$	$\lambda_D \gg \ell_{GC}$
ϕ_s	$\mathrm{sgn}(\Sigma)\dfrac{2\lambda_D}{\ell_{GC}} = \beta q\dfrac{\Sigma\lambda_D}{\varepsilon}$	$2\,\mathrm{sgn}(\Sigma)\ln\left(\dfrac{2\lambda_D}{\ell_{GC}}\right)$
γ	$\mathrm{sgn}(\Sigma)\dfrac{\lambda_D}{2\ell_{GC}} = \beta q\dfrac{\Sigma\lambda_D}{4\varepsilon}$	$\mathrm{sgn}(\Sigma)$
$\mathcal{E}$	$\dfrac{\lambda_D}{4\pi\beta\ell_B\ell_{GC}^2} = \dfrac{\Sigma^2\lambda_D}{4\varepsilon}$	$\dfrac{1}{2\pi\beta\ell_B\ell_{GC}} = \dfrac{\lvert\Sigma\rvert}{\beta q}$
λ	λ_D	$\ell_{GC}\ln\left(\dfrac{2\lambda_D}{\ell_{GC}}\right)$
λ'	λ_D	ℓ_{GC}
$\mathcal{F}$	$\dfrac{4\,\mathrm{sgn}(\Sigma)\lambda_D^2}{3\ell_{GC}^3}$	$\dfrac{8\,\mathrm{sgn}(\Sigma)}{\ell_{GC}}$
$\mathcal{G}$	$\left(\dfrac{\lambda_D}{\ell_{GC}}\right)^2$	$4\ln\left(\dfrac{\lambda_D}{2\ell_{GC}}\right)$

Table B.1: One wall with salt: limits of ϕ_s, γ, $\mathcal{E}$, λ, λ', $\mathcal{F}$ and $\mathcal{G}$ for $\lambda_D \ll \ell_{GC}$ (low surface charge, DH regime) and for $\lambda_D \gg \ell_{GC}$ (high surface charge regime).

Debye-Hückel regime When $\lambda_D \ll \ell_{GC}$, the PB equation can be linearized and its solutions simplified:

- the PB equation becomes: $\dfrac{\mathrm{d}^2\phi}{\mathrm{d}z^2} = \dfrac{1}{\lambda_D^2}\phi$
- the potential becomes: $\phi(z) = \phi_s\,\mathrm{e}^{-z/\lambda_D}$
- γ becomes $\phi_s/4$
- the Grahame relation becomes: $V_s/\lambda_D = \Sigma/\varepsilon$

Some limits at low and high surface charge The limits of ϕ_s, γ, $\mathcal{E}$, λ, λ', $\mathcal{F}$ and $\mathcal{G}$ at low and high surface charge are reported in Table B.1.

B.4.2 Strong EDL overlap: two walls, no co-ion

When the EDLs overlap and for large enough surface charges (these conditions will be quantified in section B.4.4), co-ions are excluded from the channel and the PB equation can be solved with counter-ions only.

a. Poisson-Boltzmann equation: derivation

Let's consider counter-ions with density $n(z)$ confined between two parallel walls located at $z = -d/2$ and $z = d/2$, baring the same surface charge density Σ.

In order to make the equations describing a negative surface charge (with positive counter-ions) or a positive surface charge (with negative counter-ions) identical, one can define an auxiliary reduced potential ψ, which will always be negative:

$$\psi = -\mathrm{sgn}(\Sigma)\times\phi = -\mathrm{sgn}(\Sigma)\times\beta qV. \tag{B.20}$$

The potential in the middle of the channel is arbitrarily fixed to zero: $\psi_{\mathrm{m}} = \psi(z=0) = 0$. Denoting n_{m} the counter-ion density at $z = 0$, and introducing a new characteristic length K^{-1},

$$K^{-1} = \frac{1}{\sqrt{2\pi\ell_{\mathrm{B}} n_{\mathrm{m}}}} \quad \Leftrightarrow \quad n_{\mathrm{m}} = \frac{K^2}{2\pi\ell_{\mathrm{B}}}, \tag{B.21}$$

one can derive the PB equation.

Poisson equation:

$$qn(z) = -\frac{\varepsilon}{\beta q}\frac{\mathrm{d}^2\psi}{\mathrm{d}z^2}$$

Boltzmann distribution:

$$n(z) = n_{\mathrm{m}}\,\mathrm{e}^{-\psi(z)}$$

Poisson-Boltzmann equation:

$$\frac{\mathrm{d}^2\psi}{\mathrm{d}z^2} = -2K^2\,\mathrm{e}^{-\psi(z)} \tag{B.22}$$

b. Poisson-Boltzmann equation: solution

$$\psi(z) = \ln\left\{\cos^2(Kz)\right\} \tag{B.23}$$

$$\frac{\mathrm{d}\psi}{\mathrm{d}z} = -2K\tan(Kz) \tag{B.24}$$

$$n(z) = \frac{n_{\mathrm{m}}}{\cos^2(Kz)} = \frac{K^2}{2\pi\ell_{\mathrm{B}}\cos^2(Kz)} \tag{B.25}$$

c. Surface charge and surface potential

To fully determine the potential and ion density profiles, one needs to express K as a function of the surface charge.

Electrostatics at the interface:

$$\left.\frac{\mathrm{d}V}{\mathrm{d}z}\right|_{z=d/2} = \frac{\Sigma}{\varepsilon} \quad \Rightarrow \quad \left.\frac{\mathrm{d}\psi}{\mathrm{d}z}\right|_{z=d/2} = -\frac{2}{\ell_{\mathrm{GC}}} \tag{B.26}$$

Using Eq. (B.24), one obtains:

$$Kd\,\tan\left(\frac{Kd}{2}\right) = \frac{d}{\ell_{\mathrm{GC}}}. \tag{B.27}$$

Equation (B.27) only provides an implicit expression for K, but a very accurate explicit approximation (error below 0.05 %) can be written:

$$\frac{Kd}{2} \approx \pi\sqrt{\frac{x(x+\alpha)}{4x^2+4x(4+\alpha)+2\pi^2\alpha}}, \tag{B.28}$$

with $x = d/\ell_{\mathrm{GC}}$ and $\alpha \approx 4.8955$. Simpler approximate expressions can also be derived in the low and high surface charge limits, see Sec. e..

d. A few integrals

Electrostatic energy $\mathcal{E}$

$$\mathcal{E} = \frac{\varepsilon}{2}\int_{-d/2}^{d/2}\left(\frac{\mathrm{d}V}{\mathrm{d}z}\right)^2 \mathrm{d}z = \frac{K}{\pi\ell_\mathrm{B}\beta}\left[\tan\left(\frac{Kd}{2}\right) - \frac{Kd}{2}\right] \tag{B.29}$$

Ionic density

$$\int_{-d/2}^{d/2} n(z)\,\mathrm{d}z = \frac{2|\Sigma|}{q} = \frac{1}{\pi\ell_\mathrm{B}\ell_\mathrm{GC}} \tag{B.30}$$

e. Low and high surface charge limits

Low surface charge When Σ is small enough that $d/\ell_\mathrm{GC} \ll 1$, Eq. (B.27) simplifies:

$$Kd \approx \sqrt{2d/\ell_\mathrm{GC}}, \tag{B.31}$$

which is accurate within 1 % up to $d/\ell_\mathrm{GC} \approx 0.12$.

Note that when $d/\ell_\mathrm{GC} \ll 1$, $Kd \ll 1$, so that $\psi \approx 0$ and the ion density is approximately homogeneous in the channel:

$$n \approx \frac{K^2}{2\pi\ell_\mathrm{B}} = \frac{1}{\pi d\ell_\mathrm{B}\ell_\mathrm{GC}}. \tag{B.32}$$

This is commonly called the *ideal gas* regime. In practice, the ion density varies by less than 10 % over the channel thickness as long as $d/\ell_\mathrm{GC} < 0.2$; the boundaries of the ideal gas regime are illustrated in Fig. B.2.

High surface charge When Σ is large enough that $d/\ell_\mathrm{GC} \gg 1$, Eq. (B.27) simplifies:

$$Kd \approx \frac{\pi}{1 + \frac{2\ell_\mathrm{GC}}{d}}, \tag{B.33}$$

which is accurate within 1 % down to $d/\ell_\mathrm{GC} \approx 7$.

Eventually, when $d/\ell_\mathrm{GC} \to \infty$, $Kd \to \pi$, and the potential and ion density profiles reach a limit, sometimes referred to as the "Gouy-Chapman limit":

$$\psi(z) = \ln\left\{\cos^2(\pi z/d)\right\} \tag{B.34}$$

$$n(z) = \frac{\pi}{2d^2\ell_\mathrm{B}\cos^2(\pi z/d)} \tag{B.35}$$

B.4.3 General case: two walls with salt

a. Exact solution

In the general case of an aqueous electrolyte confined between two symmetrical parallel walls located at $z = -d/2$ and $z = d/2$, the potential profile can be written in terms of the Jacobi elliptic functions cd, sn, cn and dn.

As for the no co-ion regime (see Sec. B.4.2), one can define an auxiliary reduced potential ψ, which is always negative:

$$\psi = -\mathrm{sgn}(\Sigma) \times \phi = -\mathrm{sgn}(\Sigma) \times \beta q V. \tag{B.36}$$

The auxiliary potential writes:

$$\psi(y) = 2\ln\left\{\sqrt{m}\ \mathrm{cd}\left(\frac{yr_1}{2\sqrt{m}}, m^2\right)\right\}, \tag{B.37}$$

where $y = z/d \in [-0.5; 0.5]$ is the reduced position, $r_1 = d/\lambda_\mathrm{D}$, and $m = \exp(\psi_\mathrm{m})$ with ψ_m the potential in the middle of the slab. m is the solution of:

$$r_2 = \frac{1-m^2}{2\sqrt{m}} \times \frac{\mathrm{sn}\left(\frac{r_1}{4\sqrt{m}}, m^2\right)}{\mathrm{cn}\left(\frac{r_1}{4\sqrt{m}}, m^2\right)\mathrm{dn}\left(\frac{r_1}{4\sqrt{m}}, m^2\right)}, \tag{B.38}$$

where $r_2 = \lambda_\mathrm{D}/\ell_\mathrm{GC}$; for a given r_1, m lies in the interval $]m_0, 1[$, where m_0 the solution of $4\sqrt{m}K(m^2) = r_1$ (with $K(x)$ the complete elliptic integral of the first kind).

b. Debye-Hückel limit

When the reduced potential $|\phi|$ is small everywhere, the PB equation can be linearized (DH regime, already encountered when considering only one wall in Sec. B.4.1).

With the conditions:

$$\left.\frac{\mathrm{d}\phi}{\mathrm{d}z}\right|_{z=0} = 0 \quad \text{and} \quad \left.\frac{\mathrm{d}\phi}{\mathrm{d}z}\right|_{z=d/2} = \frac{2\,\mathrm{sgn}(\Sigma)}{\ell_\mathrm{GC}},$$

the solution to the linearized PB equation, $\frac{\mathrm{d}^2\phi}{\mathrm{d}z^2} = \phi/\lambda_\mathrm{D}^2$, writes:

$$\phi = \mathrm{sgn}(\Sigma)\,\frac{2\lambda_\mathrm{D}}{\ell_\mathrm{GC}}\,\frac{\cosh\left(\frac{z}{\lambda_\mathrm{D}}\right)}{\sinh\left(\frac{d}{2\lambda_\mathrm{D}}\right)} = \mathrm{sgn}(\Sigma)\,2r_2\,\frac{\cosh\left(yr_1\right)}{\sinh\left(\frac{r_1}{2}\right)}. \tag{B.39}$$

B.4.4 Validity of the approximate solutions

In section B.4.3, it appeared that the potential profile is uniquely determined by the two ratios $r_1 = d/\lambda_\mathrm{D}$ and $r_2 = \lambda_\mathrm{D}/\ell_\mathrm{GC}$. Here we will discuss the range of r_1 and r_2 where the different approximate solutions presented in the previous sections can safely be used. Following Ref. 365, we will illustrate the domains of validity of the approximate solutions in a $r_2 - r_1$ diagram, see Fig. B.2.

a. Debye-Hückel limit

In practice, the DH potential introduced in Sec. b. is an excellent approximation to the exact potential as long as the surface potential, $|\phi_\mathrm{s}| = \max(|\phi|) = |\phi(y = 1/2)|$ remains under a (somehow arbitrary) critical value $\phi_\mathrm{c} = 0.4$. This corresponds to $r_2 \leq \tanh(r_1/2) \times \phi_\mathrm{c}/2$. This boundary is represented with a blue dashed line in Fig. B.2.

One can then simplify the relation between r_1 and r_2 by considering two limits: for thin EDLs, $r_1 \gg 1$, the DH solution can be used up to $r_2 \leq \phi_\mathrm{c}/2$; for overlapping EDLs, $r_1 \ll 1$, the DH solution can be used up to $r_2 \leq r_1 \times \phi_\mathrm{c}/4$.

b. Thin EDLs limit

When the distance d between the surfaces is much larger than the Debye length (corresponding to well-separated EDLs), one can solve the PB equation for a single charged

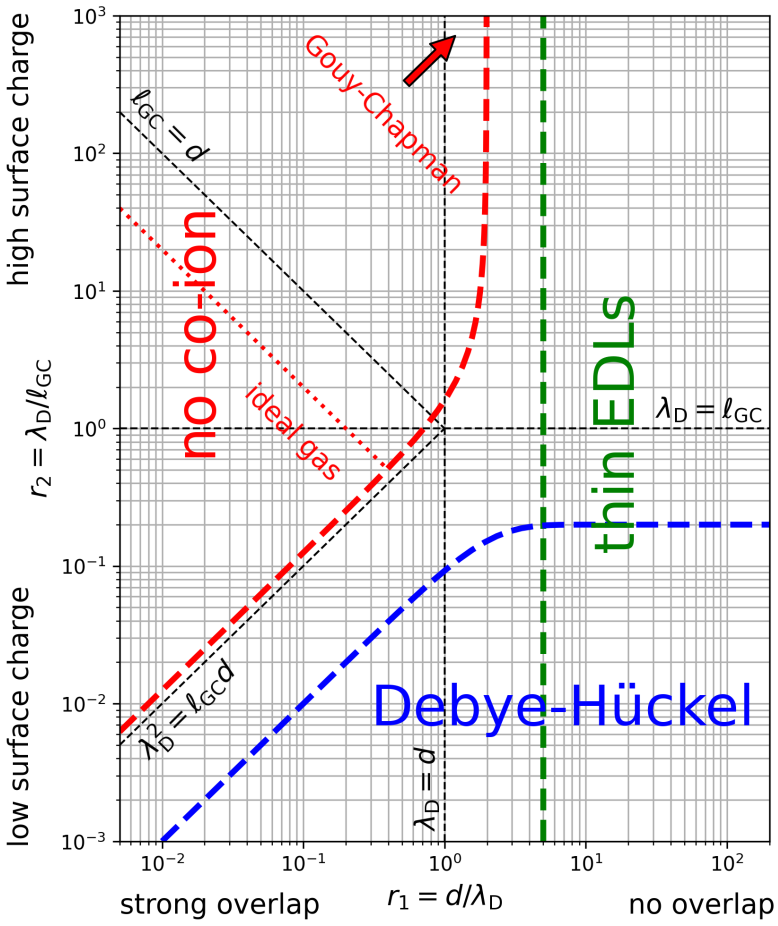

Figure B.2: Domains of validity of the different approximate solutions to the PB equation for an electrolyte solution confined between two planar walls, as a function of the ratios $r_1 = d/\lambda_D$ and $r_2 = \lambda_D/\ell_{GC}$, where d is the distance between the walls, λ_D the Debye length, and ℓ_{GC} the Gouy-Chapman length.

wall (see Sec. B.4.1), and superimpose the potentials of the two walls to obtain the full potential in the channel.

In practice, this approach provides an an accurate representation of the exact solution as long as $r_1 = d/\lambda_D > 5$. This boundary is represented with a green dashed line in Fig. B.2.

c. No co-ion limit

When the EDLs overlap and for large enough surface charges, co-ions are excluded from the channel and the PB equation can be solved with counter-ions only, see Sec. B.4.2. To that aim an auxiliary reduced potential $\psi = -\text{sgn}(\Sigma) \times \phi$ was computed, given by Eq. (B.23). The counter-ion density profile $n(z)$ was given by Eq. (B.25). Both ψ and n depended on an inverse length K related to the surface charge via Eq. (B.27).

To determine the limits of applicability of this regime, one needs to acknowledge that the channel is connected to an external salt reservoir with salt concentration n_0 and corresponding Debye length λ_D. To simply the expressions, let's consider negatively charged walls, $\Sigma < 0$, so that $\psi = \phi$, counter-ions are cations, and co-ions are anions.

Denoting $Kd = r_3$, and moving the reference of potential to the reservoir, $\phi_0 = 0$, Eq. (B.23) and Eq. (B.27) become:

$$\phi = \phi_m + \ln\left(\cos^2(r_3 y)\right), \tag{B.40}$$

$$r_3 \tan\left(\frac{r_3}{2}\right) = r_1 r_2. \tag{B.41}$$

One can then compute the counter-ion density n_m^+ and corresponding potential ϕ_m in the middle of the channel, noting that $n_0 = 1/(8\pi\ell_B\lambda_D^2)$ and $n_m^+ = K^2/(2\pi\ell_B)$:

$$\frac{n_m^+}{n_0} = \exp\{-\phi_m\} = \frac{4r_3^2}{r_1^2}. \tag{B.42}$$

Accordingly, the ratio η between counter-ions and co-ion densities in the middle of the channel writes:

$$\eta = \frac{n_m^+}{n_m^-} = \exp\{-2\phi_m\} = \left(\frac{4r_3^2}{r_1^2}\right)^2. \tag{B.43}$$

One can consider that co-ions are efficiently excluded from the channel when η is above a critical value η_c, that we will arbitrarily fix to 100. Combining Eq. (B.41) and Eq. (B.43), one can see that $\eta = \eta_c$ corresponds to:

$$r_2 = \frac{\eta_c^{1/4}}{2} \tan\left(\frac{r_1 \eta_c^{1/4}}{4}\right). \tag{B.44}$$

This boundary is represented with a red dashed line in Fig. B.2.

One can simplify the relation between r_1 and r_2 by considering two limits: for small surface charges, $r_2 \ll 1$, the no co-ion approximation can be used for $r_2 \geq r_1\eta_c^{1/2}/8 \approx 1.25 r_1$; for large surface charges, $r_2 \gg 1$, the no co-ion approximation can be used for $r_1 \leq 2\pi/\eta_c^{1/4} \approx 1.99$.

B.5 Cylindrical channel

This section gathers the equations describing a Z:Z electrolyte solution confined inside a cylindrical channel of radius R, see Fig. B.1(d). More detailed discussions can be found in e.g. Refs. 397, 398, 399.

B.5.1 Thin EDL

When the channel radius R is much larger than the thickness of the EDL, one can neglect the wall curvature at the scale of the EDL, and solve the PB equation for a single planar charged wall, see section B.4.1, where the distance to the wall is $z = R - r$.

Accordingly, the integrals computed per unit surface for a single planar wall in Sec. d. can simply be multiplied by $2\pi R$ to obtain the corresponding integral per unit length of the cylindrical channel.

The limits of validity of this approximation will be quantified in section B.5.5.

B.5.2 Debye-Hückel limit

When the reduced potential $|\phi|$ is small everywhere, the PB equation can be linearized (DH regime).

With the conditions:

$$\left.\frac{\mathrm{d}\phi}{\mathrm{d}r}\right|_{r=0} = 0 \quad \text{and} \quad \left.\frac{\mathrm{d}\phi}{\mathrm{d}r}\right|_{r=R} = \frac{2\,\mathrm{sgn}(\Sigma)}{\ell_{\mathrm{GC}}},$$

the solution to the linearized PB equation in cylindrical coordinates, $\frac{1}{r}\frac{\mathrm{d}}{\mathrm{d}r}\left(r\frac{\mathrm{d}\phi}{\mathrm{d}r}\right) = \phi/\lambda_{\mathrm{D}}^2$, writes:

$$\phi(r) = \mathrm{sgn}(\Sigma)\,\frac{2\lambda_{\mathrm{D}}}{\ell_{\mathrm{GC}}}\,\frac{\mathrm{I}_0\left(\frac{r}{\lambda_{\mathrm{D}}}\right)}{\mathrm{I}_1\left(\frac{R}{\lambda_{\mathrm{D}}}\right)}, \tag{B.45}$$

where $\mathrm{I}_0(x)$ and $\mathrm{I}_1(x)$ are the modified Bessel functions of the first kind of order zero and one. Therefore,

$$\frac{\mathrm{d}\phi}{\mathrm{d}r} = \mathrm{sgn}(\Sigma)\,\frac{2}{\ell_{\mathrm{GC}}}\,\frac{\mathrm{I}_1\left(\frac{r}{\lambda_{\mathrm{D}}}\right)}{\mathrm{I}_1\left(\frac{R}{\lambda_{\mathrm{D}}}\right)} \tag{B.46}$$

The corresponding potential V writes:

$$V(r) = \frac{\Sigma\lambda_{\mathrm{D}}}{\varepsilon}\,\frac{\mathrm{I}_0\left(\frac{r}{\lambda_{\mathrm{D}}}\right)}{\mathrm{I}_1\left(\frac{R}{\lambda_{\mathrm{D}}}\right)}. \tag{B.47}$$

The limits of validity of this approximation will be quantified in section B.5.5.

a. A few integrals

Electrostatic energy $\mathcal{E}$ (per unit length of the cylindrical channel) Denoting $u = R/\lambda_{\mathrm{D}}$,

$$\mathcal{E} = \frac{\varepsilon}{2}\int_0^R 2\pi r\left(\frac{\mathrm{d}V}{\mathrm{d}r}\right)^2 \mathrm{d}r = \frac{R^2}{2\beta\ell_{\mathrm{B}}\ell_{\mathrm{GC}}^2}\left[1 - \frac{I_0(u)I_2(u)}{I_1(u)^2}\right]. \tag{B.48}$$

B.5.3 Strong EDL overlap: no co-ion

When the EDLs overlap and for large enough surface charges (these conditions will be quantified in section B.5.5), co-ions are excluded from the channel and the PB equation can be solved with counter-ions only.

a. Poisson-Boltzmann equation: derivation

As for the slit channel, the counter-ion density is denoted $n(r)$, and one can define an auxiliary reduced potential ψ, which is always negative:

$$\psi = -\mathrm{sgn}(\Sigma) \times \phi = -\mathrm{sgn}(\Sigma) \times \beta q V.$$

The potential in the middle of the channel is arbitrarily fixed to zero: $\psi_\mathrm{m} = \psi(r=0) = 0$. Denoting n_m the counter-ion density at $r = 0$, one can define the same characteristic length K^{-1} as for the slit geometry,

$$K^{-1} = \frac{1}{\sqrt{2\pi\ell_\mathrm{B} n_\mathrm{m}}} \quad \Leftrightarrow \quad n_\mathrm{m} = \frac{K^2}{2\pi\ell_\mathrm{B}},$$

and derive the PB equation for a negative surface charge (with positive counter-ions) or for a positive surface charge (with negative counter-ions).

Poisson equation:

$$qn(r) = -\frac{\varepsilon}{\beta q}\frac{1}{r}\frac{\mathrm{d}}{\mathrm{d}r}\left(r\frac{\mathrm{d}\psi}{\mathrm{d}r}\right)$$

Boltzmann distribution:

$$n(r) = n_\mathrm{m}\,\mathrm{e}^{-\psi(r)}$$

Poisson-Boltzmann equation:

$$\frac{1}{r}\frac{\mathrm{d}}{\mathrm{d}r}\left(r\frac{\mathrm{d}\psi}{\mathrm{d}r}\right) = -2K^2\,\mathrm{e}^{-\psi(r)} \tag{B.49}$$

b. Poisson-Boltzmann equation: solution

$$\psi(r) = 2\ln\left[1 - \left(\frac{Kr}{2}\right)^2\right] \tag{B.50}$$

$$\frac{\mathrm{d}\psi}{\mathrm{d}r} = \frac{-K^2 r}{1 - \left(\frac{Kr}{2}\right)^2} \tag{B.51}$$

$$n(r) = \frac{n_\mathrm{m}}{\left[1 - \left(\frac{Kr}{2}\right)^2\right]^2} = \frac{K^2}{2\pi\ell_\mathrm{B}\left[1 - \left(\frac{Kr}{2}\right)^2\right]^2} \tag{B.52}$$

c. Surface charge and surface potential

To fully determine the potential and ion density profiles, one needs to express K as a function of the surface charge.

Electrostatics at the interface:

$$\left.\frac{\mathrm{d}V}{\mathrm{d}r}\right|_{r=R} = \frac{\Sigma}{\varepsilon} \quad \Rightarrow \quad \left.\frac{\mathrm{d}\psi}{\mathrm{d}r}\right|_{r=R} = -\frac{2}{\ell_\mathrm{GC}} \tag{B.53}$$

Using Eq. (B.51), one obtains:

$$\frac{(KR)^2}{1 - \left(\frac{KR}{2}\right)^2} = \frac{2R}{\ell_\mathrm{GC}}, \tag{B.54}$$

which can be solved:

$$\frac{KR}{2} = \sqrt{\frac{R/\ell_{\mathrm{GC}}}{R/\ell_{\mathrm{GC}} + 2}}. \tag{B.55}$$

Hence, in contrast with the slit geometry, an explicit expression of K can be derived in general for a cylindrical channel.

d. A few integrals

Electrostatic energy $\mathcal{E}$ (per unit length of the channel) Denoting $y = KR/2$,

$$\mathcal{E} = \frac{\varepsilon}{2} \int_0^R 2\pi r \,\mathrm{d}r \, \left(\frac{\mathrm{d}V}{\mathrm{d}r}\right)^2 = \frac{2}{\ell_{\mathrm{B}}\beta} \left[\ln(1-y^2) + \frac{y^2}{1-y^2}\right] \tag{B.56}$$

Using Eq. (B.55), $\mathcal{E}$ can be directly written in terms of R/ℓ_{GC}:

$$\mathcal{E} = \frac{2}{\ell_{\mathrm{B}}\beta} \left[\ln\left(\frac{2}{R/\ell_{\mathrm{GC}} + 2}\right) + \frac{R}{2\ell_{\mathrm{GC}}}\right] \tag{B.57}$$

Ionic density

$$\int_0^R 2\pi r \,\mathrm{d}r \; n(z) = 2\pi R \frac{|\Sigma|}{q} = \frac{R}{\ell_{\mathrm{B}}\ell_{\mathrm{GC}}} \tag{B.58}$$

e. Low and high surface charge limits

Low surface charge When Σ is small enough that $R/\ell_{\mathrm{GC}} \ll 1$, Eq. (B.55) simplifies:

$$KR \approx \sqrt{2R/\ell_{\mathrm{GC}}}, \tag{B.59}$$

which is accurate to within 1 % up to $R/\ell_{\mathrm{GC}} \approx 0.04$.

Note that when $R/\ell_{\mathrm{GC}} \ll 1$, $KR \ll 1$, so that $\psi \approx 0$ and the ion density is approximately homogeneous in the channel:

$$n \approx \frac{K^2}{2\pi\ell_{\mathrm{B}}} = \frac{1}{\pi R \ell_{\mathrm{B}} \ell_{\mathrm{GC}}}. \tag{B.60}$$

This is commonly called the *ideal gas* regime. In practice, the ion density varies by less than 10 % over the channel thickness as long as $R/\ell_{\mathrm{GC}} < 0.1$; the boundaries of the ideal gas regime are illustrated in Fig. B.3.

High surface charge When Σ is large enough that $R/\ell_{\mathrm{GC}} \gg 1$, Eq. (B.55) simplifies:

$$KR \approx \frac{2}{1 + \frac{\ell_{\mathrm{GC}}}{R}}, \tag{B.61}$$

which is accurate to within 1 % down to $R/\ell_{\mathrm{GC}} \approx 7$.

Eventually, when $R/\ell_{\mathrm{GC}} \to \infty$, $KR \to 2$, and the potential and ion density profiles reach a limit, sometimes referred to as the "Gouy-Chapman limit":

$$\psi(r) = 2\ln\left[1 - \left(\frac{r}{R}\right)^2\right], \tag{B.62}$$

$$n(r) = \frac{2}{\pi\ell_{\mathrm{B}}R^2\left[1 - \left(\frac{r}{R}\right)^2\right]^2}. \tag{B.63}$$

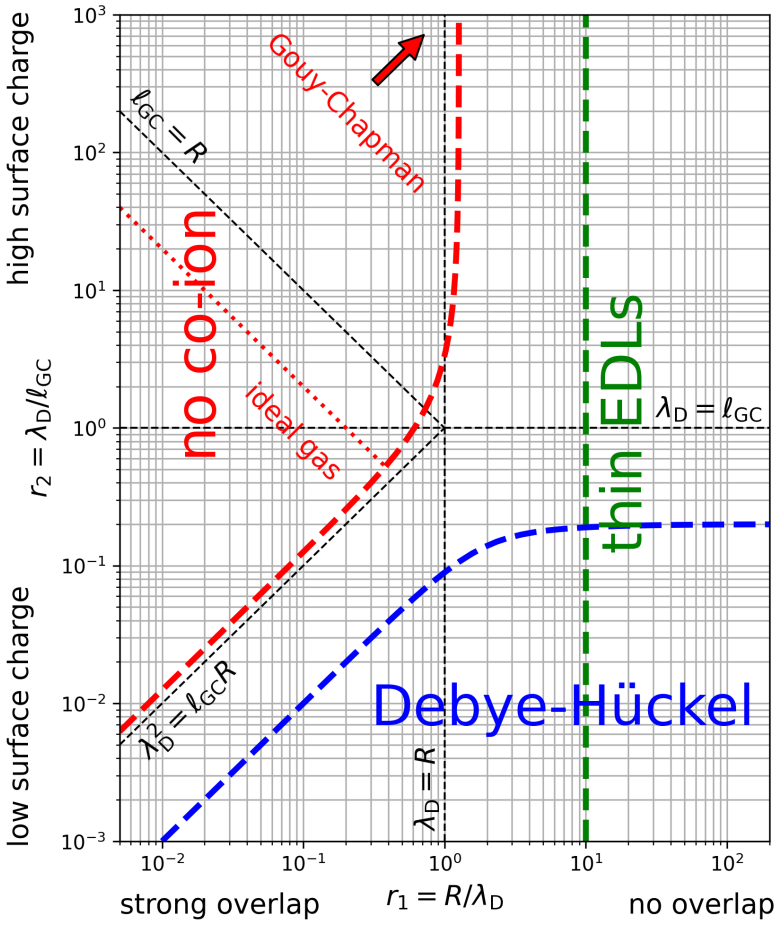

Figure B.3: Domains of validity of the different approximate solutions to the PB equation for an electrolyte solution confined inside a cylindrical channel, as a function of the ratios $r_1 = R/\lambda_D$ and $r_2 = \lambda_D/\ell_{GC}$, where R is the channel radius, λ_D the Debye length, and ℓ_{GC} the Gouy-Chapman length.

B.5.4 General case

In a cylindrical channel, we are not aware of a usable analytical solution for the general case, and the PB equation has to be solved numerically.

B.5.5 Validity of the approximate solutions

Like in the slit case, the potential profile is uniquely determined by two ratios $r_1 = R/\lambda_D$ and $r_2 = \lambda_D/\ell_{GC}$. We will in the following bound the regions in the $r_1 - r_2$ diagram where the different approximate solutions can safely be used, see Fig. B.3.

a. Debye-Hückel limit

Like in the slit case, the DH potential introduced in Sec. B.5.2 is an excellent approximation to the exact potential as long as the surface potential, $|\phi_s| = \max(|\phi|) = |\phi(r = R)|$ remains under a (somehow arbitrary) critical value $\phi_c = 0.4$. This corresponds to:

$$r_2 \leq \frac{\mathrm{I}_1(r_1)}{\mathrm{I}_0(r_1)} \times \frac{\phi_c}{2}. \tag{B.64}$$

This boundary is represented with a blue dashed line in Fig. B.3.

One can then simplify the relation between r_1 and r_2 by considering two limits: for thin EDLs, $r_1 \gg 1$, the DH solution can be used up to $r_2 \leq \phi_c/2$; for overlapping EDLs, $r_1 \ll 1$, the DH solution can be used up to $r_2 \leq r_1 \times \phi_c/4$.

b. Thin EDL limit

When the channel radius R is much larger than λ_D, one can neglect the wall curvature at the scale of the EDL, and solve the PB equation for a single planar charged wall.

However this approximation should be taken with caution. Even when the EDL is significantly thinner than the channel radius ($R/\lambda_D > 10$), the planar wall solution only provides a fair description of the exact potential profile. Still, this boundary is represented with a green dashed line in Fig. B.2.

c. No co-ion limit

When the EDL extends over the whole channel and for large enough surface charges, co-ions are excluded from the channel and the PB equation can be solved with counter-ions only, see Sec. B.5.3. To that aim an auxiliary reduced potential $\psi = -\mathrm{sgn}(\Sigma) \times \phi$ was computed, given by Eq. (B.50). The counter-ion density profile $n(r)$ was given by Eq. (B.52). Both ψ and n depended on an inverse length K related to the surface charge via Eq. (B.55).

To determine the limits of applicability of this regime, one needs to acknowledge that the channel is connected to an external salt reservoir with salt concentration n_0 and corresponding Debye length λ_D. To simply the expressions, let's consider negatively charged walls, $\Sigma < 0$, so that $\psi = \phi$, counter-ions are cations, and co-ions are anions.

Denoting $KR = r_3$ and $y = r/R$, and moving the reference of potential to the reservoir, $\phi_0 = 0$, Eq. (B.50) and Eq. (B.55) become:

$$\phi = \phi_m + 2\ln\left[1 - \left(\frac{r_3 y}{2}\right)^2\right], \tag{B.65}$$

$$r_3 = 2\sqrt{\frac{r_1 r_2}{r_1 r_2 + 2}}. \tag{B.66}$$

One can then compute the counter-ion density n_m^+ and corresponding potential ϕ_m in the middle of the channel, noting that $n_0 = 1/(8\pi\ell_B\lambda_D^2)$ and $n_m^+ = K^2/(2\pi\ell_B)$:

$$\frac{n_m^+}{n_0} = \exp\{-\phi_m\} = \frac{4r_3^2}{r_1^2}. \tag{B.67}$$

Accordingly, the ratio η between counter-ions and co-ion densities in the middle of the channel writes:

$$\eta = \frac{n_m^+}{n_m^-} = \exp\{-2\phi_m\} = \left(\frac{4r_3^2}{r_1^2}\right)^2. \tag{B.68}$$

One can consider that co-ions are efficiently excluded from the channel when η is above a critical value η_c, that we will arbitrarily fix to 100. Combining Eq. (B.66) and Eq. (B.68), one can see that $\eta = \eta_c$ corresponds to:

$$r_2 = \frac{2r_1\eta_c^{1/2}}{16 - r_1^2\eta_c^{1/2}}. \tag{B.69}$$

This boundary is represented with a red dashed line in Fig. B.3.

One can simplify the relation between r_1 and r_2 by considering two limits: for small surface charges, $r_2 \ll 1$, the no co-ion approximation can be used for $r_2 \geq r_1 \eta_c^{1/2}/8 \approx 1.25 r_1$; for large surface charges, $r_2 \gg 1$, the no co-ion approximation can be used for $r_1 \leq 4/\eta_c^{1/4} \approx 1.26$.

B.6 Limits of the PB framework

In the first molecular layers of liquid close to the wall, the hypotheses underlying the PB equation generally fail. The reader can find detailed discussions on the limits of the PB theory in e.g. Refs. 362, 363, 359, 364, 365, 366, 87, 372, 367, 400, 368.

Here we will simply present a criterion for the validity of the mean field approximation. The importance of ionic correlations can be quantified by the plasma parameter Γ [369, 370, 371], which compares the typical interaction energy between two ions and the thermal energy $k_B T$:

$$\Gamma = \frac{\beta q^2}{4\pi\varepsilon d_{\text{ion}}} = \frac{\ell_B}{d_{\text{ion}}}, \tag{B.70}$$

where d_{ion} is the typical inter-ionic distance.

This typical inter-ionic distance can be related to surface or bulk properties, imposing respectively a critical surface charge density $|\Sigma|^c$ or a critical salt concentration n_0^c above which the applicability of the PB framework should be taken with care.

At the surface, assuming that counter-ions organize into a monolayer screening the surface charge, $1/d_{\text{ion}}^2 = |\Sigma|/q$, and $\Gamma^{\text{surface}} = \sqrt{|\Sigma|\ell_B^2/q}$. Ionic correlations cannot be neglected when $\Gamma^{\text{surface}} > 1$ [369, 370], corresponding to:

$$|\Sigma| > |\Sigma|^c = \frac{q}{\ell_B^2}. \tag{B.71}$$

In bulk, because the total ionic concentration is twice the salt concentration, the inter-ionic distance is $d_{\text{ion}} = (2n_0)^{-1/3}$, and $\Gamma^{\text{bulk}} = (2n_0\ell_B^3)^{1/3}$. Ionic correlations cannot be neglected when $\Gamma^{\text{bulk}} > 1$ [369, 370], corresponding to:

$$n_0 > n_0^c = \frac{1}{2\ell_B^3}. \tag{B.72}$$

For a monovalent salt in water at room temperature, $|\Sigma|^c \simeq 330\,\text{mC/m}^2$, and $n_0^c \simeq 2\,\text{M}$. Also in these conditions, $\ell_B \sim 7\,\text{Å}$ is greater than the ionic size, so that there will be no steric repulsion effects while $\Gamma < 1$.

Bibliography

[1] A. S. Verkman, "Role of aquaporin water channels in eye function," 2003.

[2] J. Mathé, A. Aksimentiev, D. R. Nelson, K. Schulten, and A. Meller, "Orientation discrimination of single-stranded DNA inside the α-hemolysin membrane channel," *Proceedings of the National Academy of Sciences of the United States of America*, vol. 102, no. 35, 2005.

[3] S. Park and K. Hamad-Schifferli, "Nanoscale interfaces to biology," 2010.

[4] A. Zijlstra and D. D. Vizio, "Size matters in nanoscale communication," *Nature Cell Biology*, vol. 20, no. 3, 2018.

[5] S. Marbach and L. Bocquet, "Active osmotic exchanger for efficient nanofiltration inspired by the kidney," *Physical Review X*, vol. 6, no. 3, 2016.

[6] R. Greger and U. Windhorst, "Comprehensive human physiology," *From Cellular Mechanisms to Integration*, p. 1996, 1996.

[7] M. Elimelech and W. A. Phillip, "The future of seawater desalination: Energy, technology, and the environment," 2011.

[8] K. Zhao and H. Wu, "Fast Water Thermo-pumping Flow Across Nanotube Membranes for Desalination," *Nano Letters*, vol. 15, no. 6, pp. 3664–3668, 2015.

[9] T. Ahmad and D. Zhang, "A critical review of comparative global historical energy consumption and future demand: The story told so far," *Energy Reports*, vol. 6, pp. 1973–1991, 2020.

[10] B. Wilson, *History of Tribology (2nd ed.)*, vol. 50. John Wiley & Sons, Ltd, 1998.

[11] A. Fall, B. Weber, M. Pakpour, N. Lenoir, N. Shahidzadeh, J. Fiscina, C. Wagner, and D. Bonn, "Sliding friction on wet and dry sand," *Physical Review Letters*, vol. 112, no. 17, 2014.

[12] E. Popova and V. L. Popov, "The research works of Coulomb and Amontons and generalized laws of friction," *Friction*, vol. 3, no. 2, pp. 183–190, 2015.

[13] G. Amontons, "De la résistance causée dans les machines," *Mémoires de L'Academie Royale des sciences*, pp. 206–227, 1699.

[14] L. Euler, "Sur le frottement des corps solides," *Mémoires de l'académie des sciences de Berlin*, vol. 4, pp. 122–132, 1750.

[15] M. Coulomb, "Theorie des Machines Simples," *Academie des Sciences*, vol. 10, p. 166, 1781.

[16] I. Newton, *Analysis per Quantitatum Series, Fluxiones, ac Diferentias: cum Enumeratione Linearum Tertii Ordinis.* sumptibus Societatis, 1711.

[17] R. W. Johnson, *Handbook of Fluid Dynamics: Second Edition.* Crc Press, 2016.

[18] L. D. Landau and E. M. Lifshitz, "Fluid mechanics, vol. 6," *Course of Theoretical Physics*, pp. 227–229, 1987.

[19] C. L. Navier, "Mémoire sur les lois du mouvement des fluides," *Mémoires de l'Académie des sciences de l'Institut de France*, vol. 6, 1823.

[20] G. K. Batchelor, *An Introduction to Fluid Dynamics*, vol. 12. Cambridge university press, 1959.

[21] P. G. de Gennes and T. A. Witten, *Scaling Concepts in Polymer Physics* , vol. 33. Cornell university press, 1980.

[22] K. B. Migler, H. Hervet, and L. Leger, "Slip transition of a polymer melt under shear stress," *Physical Review Letters*, vol. 70, no. 3, pp. 287–290, 1993.

[23] E. Durliat, H. Hervet, and L. Leger, "Influence of grafting density on wall slip of a polymer melt on a polymer brush," *Europhysics Letters*, vol. 38, no. 5, pp. 383–388, 1997.

[24] H. Hervet and L. Léger, "Flow with slip at the wall: From simple to complex fluids," *Comptes Rendus Physique*, vol. 4, no. 2, pp. 241–249, 2003.

[25] E. Lauga, M. P. Brenner, and H. A. Stone, "Microfluidics: the no-slip boundary condition," *arXiv preprint cond-mat/0501557*, 2005.

[26] C. Cottin-Bizonne, B. Cross, A. Steinberger, and E. Charlaix, "Boundary slip on smooth hydrophobic surfaces: Intrinsic effects and possible artifacts," *Physical Review Letters*, vol. 94, no. 5, 2005.

[27] L. Joly, C. Ybert, and L. Bocquet, "Probing the nanohydrodynamics at liquid-solid interfaces using thermal motion," *Physical Review Letters*, vol. 96, no. 4, 2006.

[28] D. M. Huang, C. Sendner, D. Horinek, R. R. Netz, and L. Bocquet, "Water slippage versus contact angle: A quasiuniversal relationship," *Physical Review Letters*, vol. 101, no. 22, pp. 1–4, 2008.

[29] L. Bocquet and E. Charlaix, "Nanofluidics, from bulk to interfaces," *Chemical Society Reviews*, vol. 39, no. 3, pp. 1073–1095, 2010.

[30] J. K. Holt, H. G. Park, Y. Wang, M. Stadermann, A. B. Artyukhin, C. P. Grigoropoulos, A. Noy, and O. Bakajin, "Fast mass transport through sub-2-nanometer carbon nanotubes," *Science*, vol. 312, no. 5776, 2006.

[31] E. Secchi, S. Marbach, A. Niguès, D. Stein, A. Siria, and L. Bocquet, "Massive radius-dependent flow slippage in carbon nanotubes," *Nature*, vol. 537, no. 7619, 2016.

[32] M. Majumder, N. Chopra, R. Andrews, and B. J. Hinds, "Nanoscale hydrodynamics: Enhanced flow in carbon nanotubes," *Nature*, vol. 438, no. 7064, p. 44, 2005.

[33] M. Whitby and N. Quirke, "Fluid flow in carbon nanotubes and nanopipes," 2007.

[34] R. H. Tunuguntla, R. Y. Henley, Y. C. Yao, T. A. Pham, M. Wanunu, and A. Noy, "Enhanced water permeability and tunable ion selectivity in subnanometer carbon nanotube porins," *Science*, vol. 357, no. 6353, 2017.

[35] T. B. Sisan and S. Lichter, "The end of nanochannels," *Microfluidics and Nanofluidics*, vol. 11, no. 6, pp. 787–791, 2011.

[36] D. Mattia and F. Calabrò, "Explaining high flow rate of water in carbon nanotubes via solid-liquid molecular interactions," *Microfluidics and Nanofluidics*, vol. 13, no. 1, pp. 125–130, 2012.

[37] M. Majumder, A. Siria, and L. Bocquet, "Flows in one-dimensional and two-dimensional carbon nanochannels: Fast and curious," *MRS Bulletin*, vol. 42, no. 4, 2017.

[38] J. A. Thomas and A. J. H. McGaughey, "Reassessing fast water transport through carbon nanotubes," *Nano Letters*, vol. 8, no. 9, 2008.

[39] J. A. Thomas and A. J. H. McGaughey, "Water flow in carbon nanotubes: Transition to subcontinuum transport," *Physical Review Letters*, vol. 102, no. 18, 2009.

[40] K. Falk, F. Sedlmeier, L. Joly, R. R. Netz, and L. Bocquet, "Molecular Origin of Fast Water Transport in Carbon Nanotube Membranes: Superlubricity versus Curvature Dependent Friction," *Nano Letters*, vol. 10, no. 10, pp. 4067–4073, 2010.

[41] C. Y. Won and N. R. Aluru, "Water permeation through a subnanometer boron nitride nanotube," *Journal of the American Chemical Society*, vol. 129, no. 10, 2007.

[42] M. E. Suk, A. V. Raghunathan, and N. R. Aluru, "Fast reverse osmosis using boron nitride and carbon nanotubes," *Applied Physics Letters*, vol. 92, no. 13, 2008.

[43] A. Sam, R. Hartkamp, S. K. Kannam, and S. P. Sathian, "Prediction of fluid slip in cylindrical nanopores using equilibrium molecular simulations," *Nanotechnology*, vol. 29, no. 48, 2018.

[44] H. Li and X. C. Zeng, "Wetting and interfacial properties of water nanodroplets in contact with graphene and monolayer boron-nitride sheets," *ACS Nano*, vol. 6, no. 3, pp. 2401–2409, 2012.

[45] G. Tocci, L. Joly, and A. Michaelides, "Friction of water on graphene and hexagonal boron nitride from Ab initio methods: Very different slippage despite very similar interface structures," *Nano Letters*, vol. 14, no. 12, pp. 6872–6877, 2014.

[46] N. Kavokine, A. Robert, M.-L. Bocquet, and L. Bocquet, "Fluctuation-induced quantum friction in nanoscale water flows," *arXiv preprint arXiv:2105.03413*, 2021.

[47] S. Gravelle, "Nanofluidics: a pedagogical introduction," *HAL*, vol. 0, no. March, pp. 1–16, 2016.

[48] J.-L. Barrat and F. Chiaruttini, "Kapitza resistance at the liquid—solid interface," *Molecular Physics*, vol. 101, no. 11, pp. 1605–1610, 2003.

[49] S. Alosious, S. K. Kannam, S. P. Sathian, and B. D. Todd, "Prediction of Kapitza resistance at fluid-solid interfaces," *The Journal of Chemical Physics*, vol. 151, no. 19, p. 194502, 2019.

[50] J. Happel and H. Brenner, *Low Reynolds number hydrodynamics - with special applications to particulate media.*, vol. 1. Springer Science & Business Media, 1983.

[51] N. M. Lacevic and J. E. Sader, "Viscoelasticity of glycerol at ultra-high frequencies investigated via molecular dynamics simulations," *Journal of Chemical Physics*, vol. 144, no. 5, 2016.

[52] T. J. O'Sullivan, S. K. Kannam, D. Chakraborty, B. D. Todd, and J. E. Sader, "Viscoelasticity of liquid water investigated using molecular dynamics simulations," *Physical Review Fluids*, vol. 4, no. 12, p. 123302, 2019.

[53] J. C. F. Schulz, A. Schlaich, M. Heyden, R. R. Netz, and J. Kappler, "Molecular interpretation of the non-Newtonian viscoelastic behavior of liquid water at high frequencies," *Physical Review Fluids*, vol. 5, no. 10, p. 103301, 2020.

[54] T. Omori, N. Inoue, L. Joly, S. Merabia, and Y. Yamaguchi, "Full characterization of the hydrodynamic boundary condition at the atomic scale using an oscillating channel: Identification of the viscoelastic interfacial friction and the hydrodynamic boundary position," *Physical Review Fluids*, vol. 4, no. 11, p. 114201, 2019.

[55] H. Oga, T. Omori, C. Herrero, S. Merabia, L. Joly, and Y. Yamaguchi, "Theoretical framework for the atomistic modeling of frequency-dependent liquid-solid friction," *Physical Review Research*, vol. 3, no. 3, p. L032019, 2021.

[56] C. Herrero, G. Tocci, S. Merabia, and L. Joly, "Fast increase of nanofluidic slip in supercooled water: the key role of dynamics," *Nanoscale*, vol. 12, no. 39, pp. 20396–20403, 2020.

[57] P. G. Debenedetti, "Supercooled and glassy water," *Journal of Physics Condensed Matter*, vol. 15, no. 45, 2003.

[58] A. Covington, "Water: A comprehensive treatise," *Electrochimica Acta*, vol. 21, no. 6, p. 453, 1976.

[59] V. F. Petrenko and R. W. Whitworth, *Physics of Ice*. OUP Oxford, 2010.

[60] J. L. Abascal, E. Sanz, R. G. Fernández, and C. Vega, "A potential model for the study of ices and amorphous water: TIP4P/Ice," *Journal of Chemical Physics*, vol. 122, no. 23, 2005.

[61] P. Gallo, K. Amann-Winkel, C. A. Angell, M. A. Anisimov, F. Caupin, C. Chakravarty, E. Lascaris, T. Loerting, A. Z. Panagiotopoulos, J. Russo, J. A. Sellberg, H. E. Stanley, H. Tanaka, C. Vega, L. Xu, and L. G. M. Pettersson, "Water: A Tale of Two Liquids," *Chemical Reviews*, vol. 116, no. 13, pp. 7463–7500, 2016.

[62] P. G. Debenedetti, F. Sciortino, and G. H. Zerze, "Second critical point in two realistic models of water," *Science*, vol. 369, no. 6501, pp. 289–292, 2020.

[63] R. Shi, J. Russo, and H. Tanaka, "Origin of the emergent fragile-to-strong transition in supercooled water," *Proceedings of the National Academy of Sciences of the United States of America*, vol. 115, no. 38, pp. 9444–9449, 2018.

[64] R. Shi, J. Russo, and H. Tanaka, "Common microscopic structural origin for water's thermodynamic and dynamic anomalies," *Journal of Chemical Physics*, vol. 149, no. 22, 2018.

[65] M. Chen, H. Y. Ko, R. C. Remsing, M. F. Calegari Andrade, B. Santra, Z. Sun, A. Selloni, R. Car, M. L. Klein, J. P. Perdew, and X. Wu, "Ab initio theory and modeling of water," *Proceedings of the National Academy of Sciences of the United States of America*, vol. 114, no. 41, pp. 10846–10851, 2017.

[66] T. Morawietz, A. Singraber, C. Dellago, and J. Behler, "How van der waals interactions determine the unique properties of water," *Proceedings of the National Academy of Sciences of the United States of America*, vol. 113, no. 30, pp. 8368–8373, 2016.

[67] I. C. Lin, A. P. Seitsonen, I. Tavernelli, and U. Rothlisberger, "Structure and dynamics of liquid water from ab initio molecular dynamics-comparison of BLYP, PBE, and revPBE density functionals with and without van der Waals corrections," *Journal of Chemical Theory and Computation*, vol. 8, no. 10, pp. 3902–3910, 2012.

[68] I. M. Zeron, J. L. Abascal, and C. Vega, "A force field of Li+, Na+, K+, Mg2+, Ca2+, Cl-, and S O 4 2 - In aqueous solution based on the TIP4P/2005 water model and scaled charges for the ions," *Journal of Chemical Physics*, vol. 151, no. 13, p. 134504, 2019.

[69] J. S. Kim, Z. Wu, A. R. Morrow, A. Yethiraj, and A. Yethiraj, "Self-diffusion and viscosity in electrolyte solutions," *Journal of Physical Chemistry B*, vol. 116, no. 39, 2012.

[70] R. Dashtpour and S. N. Al-zubaidy, "Energy Efficient Reverse Osmosis Desalinaton Process," *International Journal of Environmental Science and Development*, vol. 3, no. 4, p. 339, 2012.

[71] A. Siria, M. L. Bocquet, and L. Bocquet, "New avenues for the large-scale harvesting of blue energy," *Nature Reviews Chemistry*, vol. 1, no. 11, 2017.

[72] S. E. Skilhagen, "Osmotic power - A new, renewable energy source," *Desalination and Water Treatment*, vol. 15, no. 1-3, 2010.

[73] J. Veerman, M. Saakes, S. J. Metz, and G. J. Harmsen, "Reverse electrodialysis: Performance of a stack with 50 cells on the mixing of sea and river water," *Journal of Membrane Science*, vol. 327, no. 1-2, pp. 136–144, 2009.

[74] A. Alkaisi, R. Mossad, and A. Sharifian-Barforoush, "A Review of the Water Desalination Systems Integrated with Renewable Energy," in *Energy Procedia*, vol. 110, 2017.

[75] T. Lee, E. Charrault, and C. Neto, "Interfacial slip on rough, patterned and soft surfaces: A review of experiments and simulations," *Advances in Colloid and Interface Science*, vol. 210, pp. 21–38, 2014.

[76] A. Siria, P. Poncharal, A. L. Biance, R. Fulcrand, X. Blase, S. T. Purcell, and L. Bocquet, "Giant osmotic energy conversion measured in a single transmembrane boron nitride nanotube," *Nature*, vol. 494, no. 7438, pp. 455–458, 2013.

[77] S. Chou, R. Wang, L. Shi, Q. She, C. Tang, and A. G. Fane, "Thin-film composite hollow fiber membranes for pressure retarded osmosis (PRO) process with high power density," *Journal of Membrane Science*, vol. 389, pp. 25–33, 2012.

[78] S. J. Kim, S. H. Ko, K. H. Kang, and J. Han, "Direct seawater desalination by ion concentration polarization," *Nature Nanotechnology*, vol. 5, no. 4, pp. 297–301, 2010.

[79] J. Feng, M. Graf, K. Liu, D. Ovchinnikov, D. Dumcenco, M. Heiranian, V. Nandigana, N. R. Aluru, A. Kis, and A. Radenovic, "Single-layer MoS2 nanopores as nanopower generators," *Nature*, vol. 536, no. 7615, pp. 197–200, 2016.

[80] L. Bocquet, "Nanofluidics coming of age," *Nature materials*, vol. 19, no. 3, 2020.

[81] J. Gao, X. Liu, Y. Jiang, L. Ding, L. Jiang, and W. Guo, "Understanding the giant gap between single-pore-and membrane-based nanofluidic osmotic power generators," *Small*, vol. 15, no. 11, p. 1804279, 2019.

[82] L. Wang, Z. Wang, S. K. Patel, S. Lin, and M. Elimelech, "Nanopore-based power generation from salinity gradient: Why it is not viable," *ACS nano*, vol. 15, no. 3, pp. 4093–4107, 2021.

[83] A. P. Straub, N. Y. Yip, S. Lin, J. Lee, and M. Elimelech, "Harvesting low-grade heat energy using thermo-osmotic vapour transport through nanoporous membranes," *Nature Energy*, vol. 1, no. 7, 2016.

[84] L. Fu, S. Merabia, and L. Joly, "Understanding Fast and Robust Thermo-osmotic Flows through Carbon Nanotube Membranes: Thermodynamics Meets Hydrodynamics," *The Journal of Physical Chemistry Letters*, vol. 9, no. 8, pp. 2086–2092, 2018.

[85] L. Fu, L. Joly, and S. Merabia, "Giant Thermoelectric Response of Nanofluidic Systems Driven by Water Excess Enthalpy," *Physical Review Letters*, vol. 123, no. 13, pp. 1–15, 2019.

[86] F. J. Kahn, *States of matter*, vol. 35. Courier Corporation, 1982.

[87] R. B. Schoch, J. Han, and P. Renaud, "Transport phenomena in nanofluidics," *Reviews of Modern Physics*, vol. 80, no. 3, pp. 839–883, 2008.

[88] D. Y. Chan and R. G. Horn, "The drainage of thin liquid films between solid surfaces," *The Journal of Chemical Physics*, vol. 83, no. 10, pp. 5311–5324, 1985.

[89] J. M. Georges, S. Millot, J. L. Loubet, and A. Tonck, "Drainage of thin liquid films between relatively smooth surfaces," *The Journal of Chemical Physics*, vol. 98, no. 9, pp. 7345–7360, 1993.

[90] A. Maali, T. Cohen-Bouhacina, G. Couturier, and J.-P. Aimé, "Oscillatory dissipation of a simple confined liquid," *Physical review letters*, vol. 96, no. 8, p. 086105, 2006.

[91] R. Piccirelli and T. A. Litovttz, "Ultrasonic Shear and Compressional Relaxation in Liquid Glycerol," *Journal of the Acoustical Society of America*, vol. 29, no. 9, pp. 1009–1020, 1957.

[92] K. Meier, A. Laesecke, and S. Kabelac, "Transport coefficients of the Lennard-Jones model fluid. I. Viscosity," *The Journal of chemical physics*, vol. 121, no. 8, pp. 3671–3687, 2004.

[93] A. Saugey, L. Joly, C. Ybert, J. L. Barrat, and L. Bocquet, "Diffusion in pores and its dependence on boundary conditions," *Journal of Physics Condensed Matter*, vol. 17, no. 49, p. S4075, 2005.

[94] F. Detcheverry and L. Bocquet, "Thermal fluctuations in nanofluidic transport," *Physical Review Letters*, vol. 109, no. 2, p. 24501, 2012.

[95] P. Simonnin, B. Noetinger, C. Nieto-Draghi, V. Marry, and B. Rotenberg, "Diffusion under Confinement: Hydrodynamic Finite-Size Effects in Simulation," *Journal of Chemical Theory and Computation*, vol. 13, no. 6, pp. 2881–2889, 2017.

[96] G. J. Wang and N. G. Hadjiconstantinou, "Molecular mechanics and structure of the fluid-solid interface in simple fluids," *Physical Review Fluids*, vol. 2, no. 9, p. 94201, 2017.

[97] S. Bernardi, B. D. Todd, and D. J. Searles, "Thermostating highly confined fluids," *Journal of Chemical Physics*, vol. 132, no. 24, p. 244706, 2010.

[98] H. Hoang and G. Galliero, "Local viscosity of a fluid confined in a narrow pore," *Physical Review E - Statistical, Nonlinear, and Soft Matter Physics*, vol. 86, no. 2, p. 021202, 2012.

[99] L. Bocquet and J.-L. Barrat, "Flow boundary conditions from nano- to micro-scales," *Soft Matter*, vol. 3, no. 6, p. 685, 2007.

[100] V. S. Craig, C. Neto, and D. R. Williams, "Shear-Dependent boundary slip in an aqueous newtonian liquid," *Physical Review Letters*, vol. 87, no. 5, pp. 54504–1–54504–4, 2001.

[101] B. Cross, C. Barraud, C. Picard, L. Léger, F. Restagno, and É. Charlaix, "Wall slip of complex fluids: Interfacial friction versus slip length," *Physical Review Fluids*, vol. 3, no. 6, pp. 1–9, 2018.

[102] J. Kestin, M. Sokolov, and W. A. Wakeham, "Viscosity of Liquid Water in the Range of -8 °C to 150 °C," *J. Phys. Chem. Ref. Data*, vol. 7, no. 3, pp. 941–948, 1978.

[103] W. Duangthongsuk and S. Wongwises, "Measurement of temperature-dependent thermal conductivity and viscosity of TiO2-water nanofluids," *Experimental Thermal and Fluid Science*, vol. 33, no. 4, pp. 706–714, 2009.

[104] C. Vega, J. L. Abascal, M. M. Conde, and J. L. Aragones, "What ice can teach us about water interactions: A critical comparison of the performance of different water models," *Faraday Discussions*, vol. 141, pp. 251–276, 2008.

[105] E. Sanz, C. Vega, J. L. Abascal, and L. G. MacDowell, "Phase diagram of water from computer simulation," *Physical Review Letters*, vol. 92, no. 25 I, p. 255701, 2004.

[106] P. H. Poole, U. Essmann, F. Sciortino, and H. E. Stanley, "Phase diagram for amorphous solid water," *Physical Review E*, vol. 48, no. 6, pp. 4605–4610, 1993.

[107] A. Dehaoui, B. Issenmann, and F. Caupin, "Viscosity of deeply supercooled Water and its coupling to molecular diffusion," *Proceedings of the National Academy of Sciences of the United States of America*, vol. 112, no. 39, pp. 12020–12025, 2015.

[108] P. M. de Hijes, E. Sanz, L. Joly, C. Valeriani, and F. Caupin, "Viscosity and self-diffusion of supercooled and stretched water from molecular dynamics simulations," *The Journal of Chemical Physics*, vol. 149, no. 9, p. 94503, 2018.

[109] R. J. Speedy, "Stability-limit conjecture. An interpretation of the properties of water," *Journal of Physical Chemistry*, vol. 86, no. 6, pp. 982–991, 1982.

[110] G. G. Simeoni, T. Bryk, F. A. Gorelli, M. Krisch, G. Ruocco, M. Santoro, and T. Scopigno, "The Widom line as the crossover between liquid-like and gas-like behaviour in supercritical fluids," *Nature Physics*, vol. 6, no. 7, pp. 503–507, 2010.

[111] A. T. Celebi, C. T. Nguyen, R. Hartkamp, and A. Beskok, "The role of water models on the prediction of slip length of water in graphene nanochannels," *Journal of Chemical Physics*, vol. 151, no. 17, p. 174705, 2019.

[112] C. Sendner, D. Horinek, L. Bocquet, and R. R. Netz, "Interfacial water at hydrophobic and hydrophilic surfaces: Slip, viscosity, and diffusion," *Langmuir*, vol. 25, no. 18, pp. 10768–10781, 2009.

[113] X. Gu and M. Chen, "Shape dependence of slip length on patterned hydrophobic surfaces," *Applied Physics Letters*, vol. 99, no. 6, p. 63101, 2011.

[114] E. Wagemann, E. Oyarzua, J. H. Walther, and H. A. Zambrano, "Slip divergence of water flow in graphene nanochannels: The role of chirality," *Physical Chemistry Chemical Physics*, vol. 19, no. 13, pp. 8646–8652, 2017.

[115] E. Bonaccurso, M. Kappl, and H. J. Butt, "Hydrodynamic Force Measurements: Boundary Slip of Water on Hydrophilic Surfaces and Electrokinetic Effects," *Physical Review Letters*, vol. 88, no. 7, p. 4, 2002.

[116] C.-H. Choi and C.-J. Kim, "Large slip of aqueous liquid flow over a nanoengineered superhydrophobic surface," *Physical review letters*, vol. 96, no. 6, p. 066001, 2006.

[117] L. Bocquet, P. Tabeling, and S. Manneville, "Comment on "large slip of aqueous liquid flow over a nanoengineered superhydrophobic surface"," *Physical Review Letters*, vol. 97, no. 10, p. 66001, 2006.

[118] S. Kumar Kannam, B. D. Todd, J. S. Hansen, and P. J. Daivis, "Slip length of water on graphene: Limitations of non-equilibrium molecular dynamics simulations," *The Journal of chemical physics*, vol. 136, no. 2, p. 24705, 2012.

[119] B. Ramos-Alvarado, S. Kumar, and G. P. Peterson, "Hydrodynamic slip length as a surface property," *Physical Review E*, vol. 93, no. 2, pp. 1–10, 2016.

[120] P. Español, J. A. De La Torre, and D. Duque-Zumajo, "Solution to the plateau problem in the Green-Kubo formula," *Physical Review E*, vol. 99, no. 2, p. 22126, 2019.

[121] H. Nakano and S.-i. Sasa, "Statistical Mechanical Expressions of Slip Length," *Journal of Statistical Physics*, 2019.

[122] L. Bocquet and J. L. Barrat, "Hydrodynamic boundary conditions, correlation functions, and Kubo relations for confined fluids," *Physical Review E*, vol. 49, no. 4, pp. 3079–3092, 1994.

[123] J. Petravic and P. Harrowell, "On the equilibrium calculation of the friction coefficient for liquid slip against a wall," *Journal of Chemical Physics*, vol. 127, no. 17, p. 174706, 2007.

[124] L. Bocquet and J. L. Barrat, "On the Green-Kubo relationship for the liquid-solid friction coefficient," *Journal of Chemical Physics*, vol. 139, no. 4, p. 44704, 2013.

[125] J. S. Hansen, B. D. Todd, and P. J. Daivis, "Prediction of fluid velocity slip at solid surfaces," *Physical Review E - Statistical, Nonlinear, and Soft Matter Physics*, vol. 84, no. 1, p. 16313, 2011.

[126] K. Huang and I. Szlufarska, "Green-Kubo relation for friction at liquid-solid interfaces," *Physical Review E - Statistical, Nonlinear, and Soft Matter Physics*, vol. 89, no. 3, p. 032119, 2014.

[127] M. E. Caplan, A. Giri, and P. E. Hopkins, "Analytical model for the effects of wetting on thermal boundary conductance across solid/classical liquid interfaces," *The Journal of Chemical Physics*, vol. 140, no. 15, p. 154701, 2014.

[128] A. Giri and P. E. Hopkins, "Spectral analysis of thermal boundary conductance across solid/classical liquid interfaces: A molecular dynamics study," *Applied Physics Letters*, vol. 105, no. 3, p. 33106, 2014.

[129] C. J. Mundy, S. Balasubramanian, and M. L. Klein, "Hydrodynamic boundary conditions for confined fluids via a nonequilibrium molecular dynamics simulation," *The Journal of Chemical Physics*, vol. 105, no. 8, pp. 3211–3214, 1996.

[130] C. J. Mundy, S. Balasubramanian, and M. L. Klein, "Computation of the hydrodynamic boundary parameters of a confined fluid via non-equilibrium molecular dynamics," *Physica A: Statistical Mechanics and its Applications*, vol. 240, no. 1-2, pp. 305–314, 1997.

[131] J. Delhommelle and P. T. Cummings, "Simulation of friction in nanoconfined fluids for an arbitrarily low shear rate," *Physical Review B - Condensed Matter and Materials Physics*, vol. 72, no. 17, p. 172201, 2005.

[132] V. P. Sokhan and N. Quirke, "Slip coefficient in nanoscale pore flow," *Physical Review E*, vol. 78, no. 1, p. 15301, 2008.

[133] D. Camargo, J. A. De La Torre, R. Delgado-Buscalioni, F. Chejne, and P. Español, "Boundary conditions derived from a microscopic theory of hydrodynamics near solids," *Journal of Chemical Physics*, vol. 150, no. 14, p. 144104, 2019.

[134] H. Nakano and S. I. Sasa, "Microscopic determination of macroscopic boundary conditions in Newtonian liquids," *Physical Review E*, vol. 99, no. 1, p. 13106, 2019.

[135] P. A. Thompson and M. O. Robbins, "Shear flow near solids: Epitaxial order and flow boundary conditions," *Physical Review A*, vol. 41, no. 12, pp. 6830–6837, 1990.

[136] P. A. Thompson and S. M. Troian, "A general boundary condition for liquid flow at solid surfaces," *Nature*, vol. 389, no. 6649, pp. 360–362, 1997.

[137] J. L. Barrat and L. Bocquet, "Influence of wetting properties on hydrodynamic boundary conditions at a fluid/solid interface," *Faraday Discussions*, vol. 112, no. 0, pp. 119–127, 1999.

[138] M. Cieplak, J. Koplik, and J. R. Banavar, "Boundary conditions at a fluid-solid interface," *Physical Review Letters*, vol. 86, no. 5, pp. 803–806, 2001.

[139] S. K. Kannam, B. D. Todd, J. S. Hansen, and P. J. Daivis, "Slip flow in graphene nanochannels," *The Journal of Chemical Physics*, vol. 135, no. 14, p. 144701, 2011.

[140] S. K. Kannam, B. D. Todd, J. S. Hansen, and P. J. Daivis, "How fast does water flow in carbon nanotubes?," *Journal of Chemical Physics*, vol. 138, no. 9, p. 94701, 2013.

[141] S. K. Bhatia and D. Nicholson, "Friction between solids and adsorbed fluids is spatially distributed at the nanoscale.," *Langmuir : the ACS journal of surfaces and colloids*, vol. 29, no. 47, pp. 14519–14526, 2013.

[142] S. Nakaoka, Y. Yamaguchi, T. Omori, and L. Joly, "Molecular dynamics analysis of the friction between a water-methanol liquid mixture and a non-polar solid crystal surface," *Journal of Chemical Physics*, vol. 146, no. 17, 2017.

[143] A. R. bin Saleman, H. K. Chilukoti, G. Kikugawa, M. Shibahara, and T. Ohara, "A molecular dynamics study on the thermal energy transfer and momentum transfer at the solid-liquid interfaces between gold and sheared liquid alkanes," *International Journal of Thermal Sciences*, vol. 120, pp. 273–288, 2017.

[144] S. Plimpton, "Fast parallel algorithms for short-range molecular dynamics," *Journal of Computational Physics*, vol. 117, no. 1, 1995.

[145] D. Frenkel and B. Smit, *Understanding molecular simulation: from algorithms to applications*, vol. 1. Elsevier, 2001.

[146] M. P. Allen and D. J. Tildesley, *Computer simulation of liquids: Second edition.* Oxford University Press, 2017.

[147] J. Delhommelle and P. Millié, "Inadequacy of the Lorentz-Berthelot combining rules for accurate predictions of equilibrium properties by molecular simulation," *Molecular Physics*, vol. 99, no. 8, pp. 619–625, 2001.

[148] L. A. Girifalco and V. G. Weizer, "Application of the morse potential function to cubic metals," *Physical Review*, vol. 114, no. 3, pp. 687–690, 1959.

[149] P. P. Ewald, "Die Berechnung optischer und elektrostatischer Gitterpotentiale," *Annalen der Physik*, vol. 369, no. 3, pp. 253–287, 1921.

[150] J. W. Eastwood, R. W. Hockney, and D. N. Lawrence, "P3M3DP—The three-dimensional periodic particle-particle/particle-mesh program," *Computer Physics Communications*, vol. 19, no. 2, pp. 215–261, 1980.

[151] R. W. Hockney and J. W. Eastwood, *Computer Simulation Using Particles.* crc Press, 1988.

[152] L. Verlet, "Computer "experiments" on classical fluids. I. Thermodynamical properties of Lennard-Jones molecules," *Physical Review*, vol. 159, no. 1, pp. 98–103, 1967.

[153] P. H. Hünenberger, "Thermostat algorithms for molecular dynamics simulations," *Advances in Polymer Science*, vol. 173, pp. 105–147, 2005.

[154] L. V. Woodcock, "Isothermal molecular dynamics calculations for liquid salts," *Chemical Physics Letters*, vol. 10, no. 3, pp. 257–261, 1971.

[155] W. T. Ashurst and W. G. Hoover, "Dense-fluid shear viscosity via nonequilibrium molecular dynamics," *Physical Review A*, vol. 11, no. 2, pp. 658–678, 1975.

[156] H. J. Berendsen, J. P. Postma, W. F. Van Gunsteren, A. Dinola, and J. R. Haak, "Molecular dynamics with coupling to an external bath," *The Journal of Chemical Physics*, vol. 81, no. 8, pp. 3684–3690, 1984.

[157] H. A. Posch, W. G. Hoover, and F. J. Vesely, "Canonical dynamics of the Nosé oscillator: Stability, order, and chaos," *Physical Review A*, vol. 33, no. 6, pp. 4253–4265, 1986.

[158] S. Nosé, "A unified formulation of the constant temperature molecular dynamics methods," *The Journal of Chemical Physics*, vol. 81, no. 1, pp. 511–519, 1984.

[159] W. G. Hoover, "Nosé-Hoover nonequilibrium dynamics and statistical mechanics," *Molecular Simulation*, vol. 33, no. 1-2, pp. 13–19, 2007.

[160] W. G. Hoover, "Canonical dynamics: Equilibrium phase-space distributions," *Physical review A*, vol. 31, no. 3, p. 1695, 1985.

[161] H. C. Andersen, "Molecular dynamics simulations at constant pressure and/or temperature," *The Journal of Chemical Physics*, vol. 72, no. 4, pp. 2384–2393, 1980.

[162] M. Parrinello and A. Rahman, "Polymorphic transitions in single crystals: A new molecular dynamics method," *Journal of Applied Physics*, vol. 52, no. 12, pp. 7182–7190, 1981.

[163] T. Chen, B. Smit, and A. T. Bell, "Are pressure fluctuation-based equilibrium methods really worse than nonequilibrium methods for calculating viscosities?," *Journal of Chemical Physics*, vol. 131, no. 24, p. 246101, 2009.

[164] H. Oberhofer, C. Dellago, and P. L. Geissler, "Biased sampling of nonequilibrium trajectories: Can fast switching simulations outperform conventional free energy calculation methods?," *Journal of Physical Chemistry B*, vol. 109, no. 14, pp. 6902–6915, 2005.

[165] C. Dellago and G. Hummer, "Computing equilibrium free energies using non-equilibrium molecular dynamics," *Entropy*, vol. 16, no. 1, pp. 41–61, 2014.

[166] K. M. Dyer, J. S. Perkyns, G. Stell, and B. Montgomery Pettitt, "Site-renormalised molecular fluid theory: On the utility of a two-site model of water," *Molecular Physics*, vol. 107, no. 4-6, pp. 423–431, 2009.

[167] I. Shvab and R. J. Sadus, "Atomistic water models: Aqueous thermodynamic properties from ambient to supercritical conditions," *Fluid Phase Equilibria*, vol. 407, pp. 7–30, 2015.

[168] H. J. C. Berendsen, J. P. M. Postma, W. F. van Gunsteren, and J. Hermans, "Interaction Models for Water in Relation to Protein Hydration," in *Intermolecular forces*, pp. 331–342, Springer, 1981.

[169] H. J. Berendsen, J. R. Grigera, and T. P. Straatsma, "The missing term in effective pair potentials," *Journal of Physical Chemistry*, vol. 91, no. 24, pp. 6269–6271, 1987.

[170] W. L. Jorgensen, J. Chandrasekhar, J. D. Madura, R. W. Impey, and M. L. Klein, "Comparison of simple potential functions for simulating liquid water," *The Journal of Chemical Physics*, vol. 79, no. 2, pp. 926–935, 1983.

[171] H. W. Horn, W. C. Swope, J. W. Pitera, J. D. Madura, T. J. Dick, G. L. Hura, and T. Head-Gordon, "Development of an improved four-site water model for biomolecular simulations: TIP4P-Ew," *Journal of Chemical Physics*, vol. 120, no. 20, pp. 9665–9678, 2004.

[172] J. L. Abascal and C. Vega, "A general purpose model for the condensed phases of water: TIP4P/2005," *Journal of Chemical Physics*, vol. 123, no. 23, pp. 1–12, 2005.

[173] M. W. Mahoney and W. L. Jorgensen, "A five-site model for liquid water and the reproduction of the density anomaly by rigid, nonpolarizable potential functions," *Journal of Chemical Physics*, vol. 112, no. 20, pp. 8910–8922, 2000.

[174] H. Nada and J. P. Van Der Eerden, "An intermolecular potential model for the simulation of ice and water near the melting point: A six-site model of H2O," *Journal of Chemical Physics*, vol. 118, no. 16, pp. 7401–7413, 2003.

[175] J. P. Ryckaert, G. Ciccotti, and H. J. Berendsen, "Numerical integration of the cartesian equations of motion of a system with constraints: molecular dynamics of n-alkanes," *Journal of Computational Physics*, vol. 23, no. 3, pp. 327–341, 1977.

[176] G. Ciccotti and J. P. Ryckaert, "Molecular dynamics simulation of rigid molecules," *Computer Physics Reports*, vol. 4, no. 6, pp. 346–392, 1986.

[177] Y. Wu, H. L. Tepper, and G. A. Voth, "Flexible simple point-charge water model with improved liquid-state properties," *Journal of Chemical Physics*, vol. 124, no. 2, p. 24503, 2006.

[178] M. A. González and J. L. Abascal, "A flexible model for water based on TIP4P/2005," *Journal of Chemical Physics*, vol. 135, no. 22, p. 224516, 2011.

[179] T. Qian, X.-P. Wang, and P. Sheng, "Molecular scale contact line hydrodynamics of immiscible flows," *Physical Review E*, vol. 68, no. 1, p. 16306, 2003.

[180] N. V. Priezjev and S. M. Troian, "Molecular Origin and Dynamic Behavior of Slip in Sheared Polymer Films," *Physical Review Letters*, vol. 92, no. 1, p. 4, 2004.

[181] A. Boţan, B. Rotenberg, V. Marry, P. Turq, and B. Noetinger, "Hydrodynamics in clay nanopores," *Journal of Physical Chemistry C*, vol. 115, no. 32, pp. 16109–16115, 2011.

[182] A. Boţan, V. Marry, B. Rotenberg, P. Turq, and B. Noetinger, "How electrostatics influences hydrodynamic boundary conditions: Poiseuille and electro-osmostic flows in clay nanopores," *Journal of Physical Chemistry C*, vol. 117, no. 2, pp. 978–985, 2013.

[183] P. Simonnin, V. Marry, B. Noetinger, C. Nieto-Draghi, and B. Rotenberg, "Mineral- and Ion-Specific Effects at Clay–Water Interfaces: Structure, Diffusion, and Hydrodynamics," *The Journal of Physical Chemistry C*, vol. 122, no. 32, pp. 18484–18492, 2018.

[184] S. Chen, H. Wang, T. Qian, and P. Sheng, "Determining hydrodynamic boundary conditions from equilibrium fluctuations," *Physical Review E*, vol. 92, no. 4, p. 43007, 2015.

[185] C. Herrero, T. Omori, Y. Yamaguchi, and L. Joly, "Shear force measurement of the hydrodynamic wall position in molecular dynamics," *Journal of Chemical Physics*, vol. 151, no. 4, 2019.

[186] M. Morciano, M. Fasano, A. Nold, C. Braga, P. Yatsyshin, D. N. Sibley, B. D. Goddard, E. Chiavazzo, P. Asinari, and S. Kalliadasis, "Nonequilibrium molecular dynamics simulations of nanoconfined fluids at solid-liquid interfaces," *Journal of Chemical Physics*, vol. 146, no. 24, p. 244507, 2017.

[187] I. Hanasaki and A. Nakatani, "Flow structure of water in carbon nanotubes: Poiseuille type or plug-like?," *Journal of Chemical Physics*, vol. 124, no. 14, 2006.

[188] I. Hanasaki and A. Nakatani, "Fluidized piston model for molecular dynamics simulations of hydrodynamic flow," *Modelling and Simulation in Materials Science and Engineering*, vol. 14, no. 5, 2006.

[189] J. A. Thomas, A. J. McGaughey, and O. Kuter-Arnebeck, "Pressure-driven water flow through carbon nanotubes: Insights from molecular dynamics simulation," *International Journal of Thermal Sciences*, vol. 49, no. 2, pp. 281–289, 2010.

[190] D. M. Heyes, "The molecular dynamics study of shear thinning of the Lennard-Jones fluid," *Chemical Physics*, vol. 109, no. 1, pp. 47–65, 1986.

[191] Q. Yang, Y. Su, C. Chi, C. T. Cherian, K. Huang, V. G. Kravets, F. C. Wang, J. C. Zhang, A. Pratt, A. N. Grigorenko, F. Guinea, A. K. Geim, and R. R. Nair, "Ultrathin graphene-based membrane with precise molecular sieving and ultrafast solvent permeation," *Nature Materials*, vol. 16, no. 12, 2017.

[192] Q. Xie, M. A. Alibakhshi, S. Jiao, Z. Xu, M. Hempel, J. Kong, H. G. Park, and C. Duan, "Fast water transport in graphene nanofluidic channels," *Nature Nanotechnology*, vol. 13, no. 3, pp. 238–245, 2018.

[193] G. Tocci, M. Bilichenko, L. Joly, and M. Iannuzzi, "Ab initio nanofluidics: Disentangling the role of the energy landscape and of density correlations on liquid/solid friction," *Nanoscale*, vol. 12, no. 20, 2020.

[194] Y. Xie, L. Fu, T. Niehaus, and L. Joly, "Liquid-Solid Slip on Charged Walls: The Dramatic Impact of Charge Distribution," *Physical Review Letters*, vol. 125, no. 1, 2020.

[195] A. Govind Rajan, M. S. Strano, and D. Blankschtein, "Liquids with Lower Wettability Can Exhibit Higher Friction on Hexagonal Boron Nitride: The Intriguing Role of Solid-Liquid Electrostatic Interactions," *Nano Letters*, vol. 19, no. 3, pp. 1539–1551, 2019.

[196] G. W. Robinson, S. B. Zhu, S. Singh, and M. W. Evans, *Water in biology, chemistry and physics: Experimental Overviews and Computational Methodologies*, vol. 9. World Scientific, 1996.

[197] F. Franks, *Water: A matrix of life, 2nd edition*, vol. 78. Royal Society of Chemistry, 2001.

[198] P. Ball, "Water as an active constituent in cell biology," *Chemical Reviews*, vol. 108, no. 1, pp. 74–108, 2008.

[199] W. Chen, A. S. Foster, M. J. Alava, and L. Laurson, "Stick-slip control in nanoscale boundary lubrication by surface wettability," *Physical Review Letters*, vol. 114, no. 9, p. 95502, 2015.

[200] M. H. Köhler, J. R. Bordin, L. B. Da Silva, and M. C. Barbosa, "Breakdown of the Stokes-Einstein water transport through narrow hydrophobic nanotubes," *Physical Chemistry Chemical Physics*, vol. 19, no. 20, pp. 12921–12927, 2017.

[201] J. Martí, C. Calero, and G. Franzese, "Structure and dynamics of water at carbon-based interfaces," *Entropy*, vol. 19, no. 3, p. 135, 2017.

[202] X. Cai, W. J. Xie, Y. Yang, Z. Long, J. Zhang, Z. Qiao, L. Yang, and Y. Q. Gao, "Structure of water confined between two parallel graphene plates," *Journal of Chemical Physics*, vol. 150, no. 12, p. 124703, 2019.

[203] A. Zaragoza, M. A. Gonzalez, L. Joly, I. López-Montero, M. A. Canales, A. L. Benavides, and C. Valeriani, "Molecular dynamics study of nanoconfined TIP4P/2005 water: How confinement and temperature affect diffusion and viscosity," *Physical Chemistry Chemical Physics*, vol. 21, no. 25, pp. 13653–13667, 2019.

[204] S.-H. Chen, F. Mallamace, C.-Y. Mou, M. Broccio, C. Corsaro, A. Faraone, and L. Liu, "The violation of the Stokes-Einstein relation in supercooled water," *Proceedings of the National Academy of Sciences*, vol. 103, no. 35, pp. 12974–12978, 2006.

[205] A. Buchsteiner, A. Lerf, and J. Pieper, "Water dynamics in graphite oxide investigated with neutron scattering," *Journal of Physical Chemistry B*, vol. 110, no. 45, 2006.

[206] L. Xu, F. Mallamace, Z. Yan, F. W. Starr, S. V. Buldyrev, and H. E. Stanley, "Appearance of a fractional Stokes–Einstein relation in water and a structural interpretation of its onset," *Nature Physics*, vol. 5, no. 8, pp. 565–569, 2009.

[207] S. Cerveny, F. Barroso-Bujans, Á. Alegría, and J. Colmenero, "Dynamics of Water Intercalated in Graphite Oxide," *The Journal of Physical Chemistry C*, vol. 114, no. 6, pp. 2604–2612, 2010.

[208] S. Cerveny, F. Mallamace, J. Swenson, M. Vogel, and L. Xu, "Confined Water as Model of Supercooled Water," *Chemical Reviews*, vol. 116, no. 13, pp. 7608–7625, 2016.

[209] T. Kaneko, J. Bai, T. Akimoto, J. S. Francisco, K. Yasuoka, and X. C. Zeng, "Phase behaviors of deeply supercooled bilayer water unseen in bulk water," *Proceedings of the National Academy of Sciences of the United States of America*, vol. 115, no. 19, pp. 4839–4844, 2018.

[210] L. Mishchenko, B. Hatton, V. Bahadur, J. A. Taylor, T. Krupenkin, and J. Aizenberg, "Design of ice-free nanostructured surfaces based on repulsion of impacting water droplets," *ACS Nano*, vol. 4, no. 12, pp. 7699–7707, 2010.

[211] S. Jung, M. K. Tiwari, N. V. Doan, and D. Poulikakos, "Mechanism of supercooled droplet freezing on surfaces," *Nature Communications*, vol. 3, 2012.

[212] M. J. Kreder, J. Alvarenga, P. Kim, and J. Aizenberg, "Design of anti-icing surfaces: Smooth, textured or slippery?," 2016.

[213] D. M. Huang, C. Cottin-Bizonne, C. Ybert, and L. Bocquet, "Aqueous Electrolytes near Hydrophobic Surfaces: Dynamic Effects of Ion Specificity and Hydrodynamic Slip," *Langmuir*, vol. 24, no. 4, pp. 1442–1450, 2008.

[214] T. Schnabel, A. Srivastava, J. Vrabec, and H. Hasse, "Hydrogen bonding of methanol in supercritical CO2: Comparison between1H NMR spectroscopic data and molecular simulation results," *Journal of Physical Chemistry B*, vol. 111, no. 33, pp. 9871–9878, 2007.

[215] G. Guevara-Carrion, J. Vrabec, and H. Hasse, "Prediction of self-diffusion coefficient and shear viscosity of water and its binary mixtures with methanol and ethanol by molecular simulation," *Journal of Chemical Physics*, vol. 134, no. 7, p. 74508, 2011.

[216] E. Guillaud, S. Merabia, D. de Ligny, and L. Joly, "Decoupling of viscosity and relaxation processes in supercooled water: a molecular dynamics study with the TIP4P/2005f model," *Physical Chemistry Chemical Physics*, vol. 19, no. 3, pp. 2124–2130, 2017.

[217] P. G. Debenedetti and F. H. Stillinger, "Supercooled liquids and the glass transition," *Nature*, vol. 410, no. 6825, pp. 259–267, 2001.

[218] H. Vogel, "The law of the relation between the viscosity of liquids and the temperature," *Phys. Z.*, vol. 22, pp. 645–646, 1921.

[219] G. Tamman and W. Hesse, "The dependence of viscosity upon the temperature of supercooled liquids," *Zeitschrift fuer Anorganische und Allgemeine Chemie*, vol. 156, pp. 245–257, 1926.

[220] G. S. Fulcher, "Analysis of Recent Measurements of the Viscosity of Glasses," *Journal of the American Ceramic Society*, vol. 75, no. 5, pp. 1043–1055, 1992.

[221] R. J. Speedy and C. A. Angell, "Isothermal compressibility of supercooled water and evidence for a thermodynamic singularity at -45°C," *The Journal of Chemical Physics*, vol. 65, no. 3, pp. 851–858, 1976.

[222] H. Bässler, "Viscous flow in supercooled liquids analyzed in terms of transport theory for random media with energetic disorder," *Physical Review Letters*, vol. 58, no. 8, pp. 767–770, 1987.

[223] J. Hallett, "The temperature dependence of the viscosity of supercooled water," *Proceedings of the Physical Society*, vol. 82, no. 6, pp. 1046–1050, 1963.

[224] A. P. Markesteijn, R. Hartkamp, S. Luding, and J. Westerweel, "A comparison of the value of viscosity for several water models using Poiseuille flow in a nano-channel," *The Journal of Chemical Physics*, vol. 136, no. 13, p. 134104, 2012.

[225] J. Sjöström, J. Mattsson, R. Bergman, E. Johansson, K. Josefsson, D. Svantesson, and J. Swenson, "Dielectric secondary relaxation of water in aqueous binary glass-formers," *Physical Chemistry Chemical Physics*, vol. 12, no. 35, pp. 10452–10456, 2010.

[226] M. Fitzner, G. C. Sosso, S. J. Cox, and A. Michaelides, "Ice is born in low-mobility regions of supercooled liquid water," *Proceedings of the National Academy of Sciences*, vol. 116, no. 6, pp. 2009–2014, 2019.

[227] C. Neto, D. R. Evans, E. Bonaccurso, H. J. Butt, and V. S. Craig, "Boundary slip in Newtonian liquids: A review of experimental studies," *Reports on Progress in Physics*, vol. 68, no. 12, pp. 2859–2897, 2005.

[228] H. Oga, Y. Yamaguchi, T. Omori, S. Merabia, and L. Joly, "Green-Kubo measurement of liquid-solid friction in finite-size systems," *The Journal of Chemical Physics*, vol. 151, no. 5, p. 54502, 2019.

[229] H. Nakano and S. I. Sasa, "Equilibrium measurement method of slip length based on fluctuating hydrodynamics," *Physical Review E*, vol. 101, no. 3, p. 33109, 2020.

[230] A. V. Straube, B. G. Kowalik, R. R. Netz, and F. Höfling, "Rapid onset of molecular friction in liquids bridging between the atomistic and hydrodynamic pictures," *Communications Physics*, vol. 3, no. 1, 2020.

[231] M. Grzelka, I. Antoniuk, E. Drockenmuller, A. Chennevière, L. Léger, and F. Restagno, "Viscoelasticity-induced onset of slip at the wall for polymer fluids," *ACS Macro Letters*, vol. 9, no. 7, pp. 924–928, 2020.

[232] J. P. Hansen and I. R. McDonald, *Theory of Simple Liquids: With Applications to Soft Matter: Fourth Edition*. Academic Press, 2013.

[233] D. Alfè and M. J. Gillan, "First-Principles Calculation of Transport Coefficients," *Physical Review Letters*, vol. 81, no. 23, pp. 5161–5164, 1998.

[234] G. Shi, J. Liu, C. Wang, B. Song, Y. Tu, J. Hu, and H. Fang, "Ion enrichment on the hydrophobic carbon-based surface in aqueous salt solutions due to cation-π interactions.," *Scientific reports*, vol. 3, p. 3436, 2013.

[235] R. Yamamoto and A. Onuki, "Dynamics of highly supercooled liquids: Heterogeneity, rheology, and diffusion," *Physical Review E - Statistical Physics, Plasmas, Fluids, and Related Interdisciplinary Topics*, vol. 58, no. 3, pp. 3515–3529, 1998.

[236] T. Kawasaki and K. Kim, "Identifying time scales for violation/preservation of Stokes-Einstein relation in supercooled water," *Science Advances*, vol. 3, no. 8, p. e1700399, 2017.

[237] G. Tarjus and D. Kivelson, "Breakdown of the Stokes–Einstein relation in supercooled liquids," *The Journal of Chemical Physics*, vol. 103, no. 8, pp. 3071–3073, 1995.

[238] A. Ikeda and K. Miyazaki, "Glass transition of the monodisperse Gaussian core model," *Physical Review Letters*, vol. 106, no. 1, pp. 1–4, 2011.

[239] S. D. Overduin and G. N. Patey, "Understanding the structure factor and isothermal compressibility of ambient water in terms of local structural environments," *Journal of Physical Chemistry B*, vol. 116, no. 39, pp. 12014–12020, 2012.

[240] W. A. Steele, "The physical interaction of gases with crystalline solids," *Surface Science*, vol. 36, no. 1, pp. 317–352, 1973.

[241] T. S. Ingebrigtsen and H. Tanaka, "Structural predictor for nonlinear sheared dynamics in simple glass-forming liquids," *Proceedings of the National Academy of Sciences of the United States of America*, vol. 115, no. 1, pp. 87–92, 2018.

[242] P. Gallo, F. Sciortino, P. Tartaglia, and S.-H. H. Chen, "Slow Dynamics of Water Molecules in Supercooled States," *Physical Review Letters*, vol. 76, no. 15, pp. 2730–2733, 1996.

[243] A. Cavagna, "Supercooled liquids for pedestrians," *Physics Reports*, vol. 476, no. 4-6, pp. 51–124, 2009.

[244] P. Kumar, S. V. Buldyrev, S. R. Becker, P. H. Poole, F. W. Starr, and H. E. Stanley, "Relation between the Widom line and the breakdown of the Stokes-Einstein relation in supercooled water," *Proceedings of the National Academy of Sciences of the United States of America*, vol. 104, no. 23, 2007.

[245] D. Jeong, M. Y. Choi, H. J. Kim, and Y. Jung, "Fragility, Stokes-Einstein violation, and correlated local excitations in a coarse-grained model of an ionic liquid," *Physical Chemistry Chemical Physics*, vol. 12, no. 8, 2010.

[246] C. Cottin-Bizonne, J. L. Barrat, L. Bocquet, and E. Charlaix, "Low-friction flows of liquid at nanopatterned interfaces," *Nature Materials*, vol. 2, no. 4, pp. 237–240, 2003.

[247] T. Maitra, C. Antonini, M. K. Tiwari, A. Mularczyk, Z. Imeri, P. Schoch, and D. Poulikakos, "Supercooled water drops impacting superhydrophobic textures," *Langmuir*, vol. 30, no. 36, 2014.

[248] Y. Lu, S. Sathasivam, J. Song, C. R. Crick, C. J. Carmalt, and I. P. Parkin, "Robust self-cleaning surfaces that function when exposed to either air or oil," *Science*, vol. 347, no. 6226, 2015.

[249] T. Jollans and M. Orrit, "Explosive, oscillatory, and Leidenfrost boiling at the nanoscale," *Physical Review E*, vol. 99, no. 6, pp. 1–9, 2019.

[250] G. Berthoud, "Vapor explosions," *Annual Review of Fluid Mechanics*, vol. 32, no. 1, pp. 573–611, 2000.

[251] I. U. Vakarelski, N. A. Patankar, J. O. Marston, D. Y. Chan, and S. T. Thoroddsen, "Stabilization of Leidenfrost vapour layer by textured superhydrophobic surfaces," *Nature*, vol. 489, no. 7415, pp. 274–277, 2012.

[252] D. Quéré, "Leidenfrost dynamics," *Annual Review of Fluid Mechanics*, vol. 45, pp. 197–215, 2013.

[253] H. Han, S. Merabia, and F. Müller-Plathe, "Thermal transport at a solid-nanofluid interface: From increase of thermal resistance towards a shift of rapid boiling," *Nanoscale*, vol. 9, no. 24, pp. 8314–8320, 2017.

[254] R. Liu and Z. Liu, "Rapid thermal transport at rough solid-fluid interface: Evaporation and explosive boiling on concave nanostructure," *International Journal of Heat and Mass Transfer*, vol. 154, p. 119676, 2020.

[255] H. Han, S. Mérabia, and F. Müller-Plathe, "Thermal Transport at Solid-Liquid Interfaces: High Pressure Facilitates Heat Flow through Nonlocal Liquid Structuring," *Journal of Physical Chemistry Letters*, vol. 8, no. 9, pp. 1946–1951, 2017.

[256] J. Park, J. Huang, W. Wang, C. J. Murphy, and D. G. Cahill, "Heat transport between Au nanorods, surrounding liquids, and solid supports," *Journal of Physical Chemistry C*, vol. 116, no. 50, pp. 26335–26341, 2012.

[257] J. Park and D. G. Cahill, "Plasmonic Sensing of Heat Transport at Solid-Liquid Interfaces," *Journal of Physical Chemistry C*, vol. 120, no. 5, pp. 2814–2821, 2016.

[258] Z. Ge, D. G. Cahill, and P. V. Braun, "Thermal conductance of hydrophilic and hydrophobic interfaces," *Physical Review Letters*, vol. 96, no. 18, pp. 1–4, 2006.

[259] T. Stoll, P. Maioli, A. Crut, S. Rodal-Cedeira, I. Pastoriza-Santos, F. Vallée, and N. Del Fatti, "Time-Resolved Investigations of the Cooling Dynamics of Metal Nanoparticles: Impact of Environment," *The Journal of Physical Chemistry C*, vol. 119, no. 22, pp. 12757–12764, 2015.

[260] J. A. Tomko, D. H. Olson, A. Giri, J. T. Gaskins, B. F. Donovan, S. M. O'Malley, and P. E. Hopkins, "Nanoscale Wetting and Energy Transmission at Solid/Liquid Interfaces," *Langmuir*, 2019.

[261] Z. Tian, A. Marconnet, and G. Chen, "Enhancing solid-liquid interface thermal transport using self-assembled monolayers," *Applied Physics Letters*, vol. 106, no. 21, pp. 1–5, 2015.

[262] S. Merabia, J. Lombard, and A. Alkurdi, "Importance of viscoelastic and interface bonding effects in the thermal boundary conductance of solid-water interfaces," *International Journal of Heat and Mass Transfer*, vol. 100, pp. 287–294, 2016.

[263] V. R. Ardham and F. Leroy, "Communication: Is a coarse-grained model for water sufficient to compute Kapitza conductance on non-polar surfaces?," *Journal of Chemical Physics*, vol. 147, no. 15, 2017.

[264] Y. Wang and P. Keblinski, "Role of wetting and nanoscale roughness on thermal conductance at liquid-solid interface," *Applied Physics Letters*, vol. 99, no. 7, pp. 2011–2014, 2011.

[265] L. Xue, P. Keblinski, S. R. Phillpot, S. U. Choi, and J. A. Eastman, "Two regimes of thermal resistance at a liquid-solid interface," *Journal of Chemical Physics*, vol. 118, no. 1, pp. 337–339, 2003.

[266] Y. Chen and C. Zhang, "Role of surface roughness on thermal conductance at liquid-solid interfaces," *International Journal of Heat and Mass Transfer*, vol. 78, pp. 624–629, 2014.

[267] D. Surblys, Y. Kawagoe, M. Shibahara, and T. Ohara, "Molecular dynamics investigation of surface roughness scale effect on interfacial thermal conductance at solid-liquid interfaces," *Journal of Chemical Physics*, vol. 150, no. 11, 2019.

[268] S. Ge and M. Chen, "Vibrational coupling and Kapitza resistance at a solid-liquid interface," *International Journal of Thermophysics*, vol. 34, no. 1, pp. 64–77, 2013.

[269] K. Sääskilahti, J. Oksanen, J. Tulkki, and S. Volz, "Spectral mapping of heat transfer mechanisms at liquid-solid interfaces," *Physical Review E*, vol. 93, no. 5, pp. 1–8, 2016.

[270] S. Alosious, S. K. Kannam, S. P. Sathian, and B. D. Todd, "Nanoconfinement Effects on the Kapitza Resistance at Water-CNT Interfaces," *Langmuir*, vol. 37, no. 7, pp. 2355–2361, 2021.

[271] A. Pham, M. Barisik, and B. Kim, "Pressure dependence of Kapitza resistance at gold/water and silicon/water interfaces," *Journal of Chemical Physics*, vol. 139, no. 24, p. 244702, 2013.

[272] B. Y. Cao, J. H. Zou, G. J. Hu, and G. X. Cao, "Enhanced thermal transport across multilayer graphene and water by interlayer functionalization," *Applied Physics Letters*, vol. 112, no. 4, pp. 1–5, 2018.

[273] C. U. Gonzalez-Valle, L. E. Paniagua-Guerra, and B. Ramos-Alvarado, "Implications of the Interface Modeling Approach on the Heat Transfer across Graphite-Water Interfaces," *Journal of Physical Chemistry C*, vol. 123, no. 36, pp. 22311–22323, 2019.

[274] D. Alexeev, J. Chen, J. H. Walther, K. P. Giapis, P. Angelikopoulos, and P. Koumoutsakos, "Kapitza Resistance between Few-Layer Graphene and Water: Liquid Layering Effects," *Nano Letters*, vol. 15, no. 9, pp. 5744–5749, 2015.

[275] S. Alosious, S. K. Kannam, S. P. Sathian, and B. D. Todd, "Kapitza resistance at water-graphene interfaces," *The Journal of chemical physics*, vol. 152, no. 22, p. 224703, 2020.

[276] A. T. Pham, M. Barisik, and B. H. Kim, "Interfacial thermal resistance between the graphene-coated copper and liquid water," *International Journal of Heat and Mass Transfer*, vol. 97, pp. 422–431, 2016.

[277] G. Chen, J. Chen, and Z. Wang, "Thermal Transport at Interface Between Single-Layer Graphene and Water Film," *International Journal of Thermophysics*, vol. 41, no. 4, pp. 1–19, 2020.

[278] A. Lafuma and D. Quéré, "Superhydrophobic states," *Nature Materials*, vol. 2, no. 7, pp. 457–460, 2003.

[279] D. Quéré, "Wetting and roughness," *Annual Review of Materials Research*, vol. 38, pp. 71–99, 2008.

[280] P. Kapitza, "The study of heat transfer in helium ii," *J. Phys.(Moscow)*, vol. 4, p. 181, 1941.

[281] H. Heinz, R. A. Vaia, B. L. Farmer, and R. R. Naik, "Accurate simulation of surfaces and interfaces of face-centered cubic metals using 12-6 and 9-6 lennard-jones potentials," *Journal of Physical Chemistry C*, vol. 112, no. 44, pp. 17281–17290, 2008.

[282] S. Merabia, S. Shenogin, L. Joly, P. Keblinski, and J.-L. Barrat, "Heat transfer from nanoparticles: a corresponding state analysis.," *Proceedings of the National Academy of Sciences of the United States of America*, vol. 106, no. 36, pp. 15113–15118, 2009.

[283] H. Los and A. Fasolino, "Intrinsic long-range bond-order potential for carbon: Performance in Monte Carlo simulations of graphitization," *Physical Review B - Condensed Matter and Materials Physics*, vol. 68, no. 2, p. 24107, 2003.

[284] M. Neek-Amal, R. Asgari, and M. R. Rahimi Tabar, "The formation of atomic nanoclusters on graphene sheets," *Nanotechnology*, vol. 20, no. 13, p. 135602, 2009.

[285] F. Römer, A. Lervik, and F. Bresme, "Nonequilibrium molecular dynamics simulations of the thermal conductivity of water: a systematic investigation of the SPC/E and TIP4P/2005 models.," *The Journal of Chemical Physics*, vol. 137, no. 7, p. 74503, 2012.

[286] M. L. Ramires, C. A. Nieto Castro, Y. Nagasaka, A. Nagashima, M. J. Assael, and W. A. Wakeham, "Standard Reference Data for the Thermal Conductivity of Water," *Journal of Physical and Chemical Reference Data*, vol. 24, no. 3, pp. 1377–1381, 1995.

[287] P. J. In 'T Veld, A. E. Ismail, and G. S. Grest, "Application of Ewald summations to long-range dispersion forces," *Journal of Chemical Physics*, vol. 127, no. 14, p. 144711, 2007.

[288] F. H. Stillinger, "Water revisited," *Science*, vol. 209, no. 4455, 1980.

[289] M. J. Gillan, D. Alfè, and A. Michaelides, "Perspective: How good is DFT for water?," *Journal of Chemical Physics*, vol. 144, no. 13, 2016.

[290] T. D. Kühne, M. Krack, and M. Parrinello, "Static and dynamical properties of liquid water from first principles by a novel car-parrinello-like approach http://pubs.acs.org," *Journal of Chemical Theory and Computation*, vol. 5, no. 2, pp. 235–241, 2009.

[291] H. S. Lee and M. E. Tuckerman, "Dynamical properties of liquid water from ab initio molecular dynamics performed in the complete basis set limit," *Journal of Chemical Physics*, vol. 126, no. 16, 2007.

[292] I. de Almeida Ribeiro and M. de Koning, "Non-Newtonian flow effects in supercooled water," *Physical Review Research*, vol. 2, no. 2, pp. 1–5, 2020.

[293] A. Kayal and A. Chandra, "Orientational order and dynamics of interfacial water near a hexagonal boron-nitride sheet: An ab initio molecular dynamics study," *Journal of Chemical Physics*, vol. 147, no. 16, 2017.

[294] N. Mauger, T. Plé, L. Lagardère, S. Bonella, E. Mangaud, J.-P. Piquemal, and S. Huppert, "Nuclear Quantum Effects in liquid water at near classical computational cost using the adaptive Quantum Thermal Bath," *arxiv*, 2021.

[295] M. Rossi, V. Kapil, and M. Ceriotti, "Fine tuning classical and quantum molecular dynamics using a generalized Langevin equation," *Journal of Chemical Physics*, vol. 148, no. 10, 2018.

[296] M. Ceriotti, G. Bussi, and M. Parrinello, "Nuclear quantum effects in solids using a colored-noise thermostat," *Physical Review Letters*, vol. 103, no. 3, pp. 1–4, 2009.

[297] M. D. Ben, J. Hutter, and J. VandeVondele, "Probing the structural and dynamical properties of liquid water with models including non-local electron correlation," *The Journal of Chemical Physics*, vol. 143, no. 5, p. 54506, 2015.

[298] M. H. Cohen and D. Turnbull, "Molecular transport in liquids and glasses," *The Journal of Chemical Physics*, vol. 31, no. 5, pp. 1164–1169, 1959.

[299] D. Turnbull and M. H. Cohen, "Free-volume model of the amorphous phase: Glass transition," *The Journal of Chemical Physics*, vol. 34, no. 1, pp. 120–125, 1961.

[300] M. I. Ojovan and D. V. Louzguine-Luzgin, "Revealing Structural Changes at Glass Transition via Radial Distribution Functions," *Journal of Physical Chemistry B*, vol. 124, no. 15, pp. 3186–3194, 2020.

[301] H. Tong and H. Tanaka, "Structural order as a genuine control parameter of dynamics in simple glass formers," *Nature Communications*, vol. 10, no. 1, pp. 4–6, 2019.

[302] M. Dzugutov, "A universal scaling law for atomic diffusion in condensed matter," *Nature*, vol. 381, no. 6578, pp. 137–139, 1996.

[303] I. Yokoyama, "A relationship between excess entropy and diffusion coefficient for liquid metals near the melting point," *Physica B: Condensed Matter*, vol. 254, no. 3-4, pp. 172–177, 1998.

[304] A. Baranyai and D. J. Evans, "Direct entropy calculation from computer simulation of liquids," *Journal of Non-Crystalline Solids*, vol. 117-118, no. PART 2, pp. 593–596, 1990.

[305] Y. D. Fomin, V. N. Ryzhov, B. A. Klumov, and E. N. Tsiok, "How to quantify structural anomalies in fluids?," *The Journal of Chemical Physics*, vol. 141, no. 3, p. 34508, 2014.

[306] M. K. Nandi, A. Banerjee, S. Sengupta, S. Sastry, and S. M. Bhattacharyya, "Unraveling the success and failure of mode coupling theory from consideration of entropy," *The Journal of Chemical Physics*, vol. 143, no. 17, p. 174504, 2015.

[307] J. Mittal, J. R. Errington, and T. M. Truskett, "Quantitative Link between Single-Particle Dynamics and Static Structure of Supercooled Liquids," *The Journal of Physical Chemistry B*, vol. 110, no. 37, pp. 18147–18150, 2006.

[308] J. Mittal, J. R. Errington, and T. M. Truskett, "Relationships between Self-Diffusivity, Packing Fraction, and Excess Entropy in Simple Bulk and Confined Fluids," *The Journal of Physical Chemistry B*, vol. 111, no. 34, pp. 10054–10063, 2007.

[309] R. Chopra, T. M. Truskett, and J. R. Errington, "On the use of excess entropy scaling to describe single-molecule and collective dynamic properties of hydrocarbon isomer fluids," *Journal of Physical Chemistry B*, vol. 114, no. 49, pp. 16487–16493, 2010.

[310] I. H. Bell, J. C. Dyre, and T. S. Ingebrigtsen, "Excess-entropy scaling in supercooled binary mixtures," *Nature Communications*, vol. 11, no. 1, p. 4300, 2020.

[311] B. Rotenberg, "Use the force! Reduced variance estimators for densities, radial distribution functions, and local mobilities in molecular simulations," *The Journal of Chemical Physics*, vol. 153, no. 15, p. 150902, 2020.

[312] C. Desgranges and J. Delhommelle, *Introduction to Quantum Mechanics*. Cambridge University Press, 2020.

[313] D. Marx and J. Hutter, *Ab initio molecular dynamics: Basic theory and advanced methods*. Cambridge University Press, 2009.

[314] D. Marx and M. Parrinello, "Ab initio path integral molecular dynamics: Basic ideas," *Journal of Chemical Physics*, vol. 104, no. 11, pp. 4077–4082, 1996.

[315] R. Iftimie, P. Minary, and M. E. Tuckerman, "Ab initio molecular dynamics: Concepts, recent developments, and future trends," *Proceedings of the National Academy of Sciences of the United States of America*, vol. 102, no. 19, pp. 6654–6659, 2005.

[316] R. Nityananda, P. Hohenberg, and W. Kohn, "Inhomogeneous electron gas," *Resonance*, vol. 22, no. 8, pp. 809–811, 2017.

[317] D. S. Sholl and J. A. Steckel, *Density Functional Theory: A Practical Introduction*. John Wiley & Sons, 2009.

[318] H. Eschrig, *The Fundamentals of Density Functional Theory*, vol. 642. Springer, 2003.

[319] M. Probert, *Electronic structure: basic theory and practical methods, 2nd edition*. Cambridge university press, 2021.

[320] J. P. Perdew, A. Ruzsinszky, J. Tao, V. N. Staroverov, G. E. Scuseria, and G. I. Csonka, "Prescription for the design and selection of density functional approximations: More constraint satisfaction with fewer fits," *Journal of Chemical Physics*, vol. 123, no. 6, p. 62201, 2005.

[321] C. J. Cramer, *Essentials of Computational Chemistry Theories and Models Second Edition*. John Wiley & Sons, 2004.

[322] J. VandeVondele, M. Krack, F. Mohamed, M. Parrinello, T. Chassaing, and J. Hutter, "Quickstep: Fast and accurate density functional calculations using a mixed Gaussian and plane waves approach," *Computer Physics Communications*, vol. 167, no. 2, pp. 103–128, 2005.

[323] J. P. Perdew, K. Burke, and M. Ernzerhof, "Generalized gradient approximation made simple," *Physical Review Letters*, vol. 77, no. 18, pp. 3865–3868, 1996.

[324] S. Grimme, "Accurate description of van der Waals complexes by density functional theory including empirical corrections," *Journal of Computational Chemistry*, vol. 25, no. 12, pp. 1463–1473, 2004.

[325] S. Grimme, "Semiempirical GGA-type density functional constructed with a long-range dispersion correction," *Journal of Computational Chemistry*, vol. 27, no. 15, pp. 1787–1799, 2006.

[326] J. Klimeš, D. R. Bowler, and A. Michaelides, "Chemical accuracy for the van der Waals density functional," *Journal of Physics Condensed Matter*, vol. 22, no. 2, p. 22201, 2010.

[327] J. Klimeš, D. R. Bowler, and A. Michaelides, "Van der Waals density functionals applied to solids," *Physical Review B - Condensed Matter and Materials Physics*, vol. 83, no. 19, p. 195131, 2011.

[328] J. Sun, A. Ruzsinszky, and J. Perdew, "Strongly Constrained and Appropriately Normed Semilocal Density Functional," *Physical Review Letters*, vol. 115, no. 3, p. 36402, 2015.

[329] J. VandeVondele and J. Hutter, "Gaussian basis sets for accurate calculations on molecular systems in gas and condensed phases," *The Journal of Chemical Physics*, vol. 127, no. 11, p. 114105, 2007.

[330] I.-C. Yeh and G. Hummer, "System-Size Dependence of Diffusion Coefficients and Viscosities from Molecular Dynamics Simulations with Periodic Boundary Conditions," *The Journal of Physical Chemistry B*, vol. 108, no. 40, pp. 15873–15879, 2004.

[331] S. Tazi, A. Boţan, M. Salanne, V. Marry, P. Turq, and B. Rotenberg, "Diffusion coefficient and shear viscosity of rigid water models," *Journal of Physics: Condensed Matter*, vol. 24, no. 28, p. 284117, 2012.

[332] D. C. Wallace, "On the role of density fluctuations in the entropy of a fluid," *The Journal of Chemical Physics*, vol. 87, no. 4, pp. 2282–2284, 1987.

[333] Y. Jung, J. P. Garrahan, and D. Chandler, "Excitation lines and the breakdown of Stokes-Einstein relations in supercooled liquids," *Physical Review E*, vol. 69, no. 6, p. 61205, 2004.

[334] G. Camisasca, H. Pathak, K. T. Wikfeldt, and L. G. M. Pettersson, "Radial distribution functions of water: Models vs experiments," *The Journal of Chemical Physics*, vol. 151, no. 4, p. 044502, 2019.

[335] K. R. Kristiansen, V. M. Barragán, and S. Kjelstrup, "Thermoelectric Power of Ion Exchange Membrane Cells Relevant to Reverse Electrodialysis Plants," *Physical Review Applied*, vol. 11, no. 4, 2019.

[336] A. P. Straub and M. Elimelech, "Energy Efficiency and Performance Limiting Effects in Thermo-Osmotic Energy Conversion from Low-Grade Heat," *Environmental Science and Technology*, vol. 51, no. 21, pp. 12925–12937, 2017.

[337] E. Oyarzua, J. H. Walther, C. M. Megaridis, P. Koumoutsakos, and H. A. Zambrano, "Carbon Nanotubes as Thermally Induced Water Pumps," *ACS Nano*, vol. 11, no. 10, pp. 9997–10002, 2017.

[338] B. Derjaguin and G. Sidorenkov, "Thermoosmosis at ordinary temperatures and its analogy with the thermomechanical effect in helium II," *CR Acad. Sci*, vol. 32, pp. 622–626, 1941.

[339] M. S. Dariel and O. Kedem, "Thermoosmosis in semipermeable membranes," *Journal of Physical Chemistry*, vol. 79, no. 4, pp. 336–342, 1975.

[340] J. I. Mengual, J. Aguilar, and C. Fernandez-Pineda, "Thermoosmosis of water through cellulose acetate membranes," *Journal of Membrane Science*, vol. 4, no. C, pp. 209–219, 1978.

[341] R. Piazza, "'Thermal forces': Colloids in temperature gradients," *Journal of Physics Condensed Matter*, vol. 16, no. 38, 2004.

[342] V. M. Barragán and S. Kjelstrup, "Thermo-osmosis in Membrane Systems: A Review," *Journal of Non-Equilibrium Thermodynamics*, vol. 42, no. 3, pp. 217–236, 2017.

[343] R. Ganti, Y. Liu, and D. Frenkel, "Molecular Simulation of Thermo-osmotic Slip," *Physical Review Letters*, vol. 119, no. 3, pp. 1–5, 2017.

[344] L. Fu, S. Merabia, and L. Joly, "What Controls Thermo-osmosis? Molecular Simulations Show the Critical Role of Interfacial Hydrodynamics," *Physical Review Letters*, vol. 119, no. 21, p. 214501, 2017.

[345] R. Rajegowda and S. P. Sathian, "Analysing thermophoretic transport of water for designing nanoscale-pumps," *Physical Chemistry Chemical Physics*, vol. 20, no. 48, pp. 30321–30330, 2018.

[346] K. Prakash, D. K. V. S, S. K. Kannam, and S. P. Sathian, "Non-isothermal flow of an electrolyte in a charged nanochannel," *Nanotechnology*, vol. 31, no. 42, 2020.

[347] B. V. Derjaguin, "Structural And Thermodynamic Peculiarities Of The Boundary Layers Of Liquids," *Pure and Applied Chemistry*, vol. 52, no. 5, 1980.

[348] R. Rusconi, L. Isa, and R. Piazza, "Thermal-lensing measurement of particle thermophoresis in aqueous dispersions," *Journal of the Optical Society of America B*, vol. 21, no. 3, 2004.

[349] S. Nedev, S. Carretero-Palacios, P. Kühler, T. Lohmüller, A. S. Urban, L. J. Anderson, and J. Feldmann, "An optically controlled microscale elevator using plasmonic janus particles," *ACS Photonics*, vol. 2, no. 4, 2015.

[350] A. P. Bregulla, A. Würger, K. Günther, M. Mertig, and F. Cichos, "Thermo-Osmotic Flow in Thin Films," *Physical Review Letters*, vol. 116, no. 18, pp. 1–5, 2016.

[351] J. Anderson, "Colloid Transport By Interfacial Forces," *Annual Review of Fluid Mechanics*, vol. 21, no. 1, pp. 61–99, 1989.

[352] B. V. Derjaguin, N. V. Churaev, and V. M. Muller, *Surface Forces*. Springer, 1987.

[353] E. Ruckenstein, "Can phoretic motions be treated as interfacial tension gradient driven phenomena?," *Journal of Colloid and Interface Science*, vol. 83, no. 1, pp. 77–81, 1981.

[354] R. S. Maheedhara, H. Jing, H. S. Sachar, and S. Das, "Highly enhanced liquid flows via thermoosmotic effects in soft and charged nanochannels," *Physical Chemistry Chemical Physics*, vol. 20, no. 37, pp. 24300–24316, 2018.

[355] X. Wang, M. Liu, D. Jing, A. Mohamad, and O. Prezhdo, "Net Unidirectional Fluid Transport in Locally Heated Nanochannel by Thermo-osmosis," *Nano Letters*, vol. 20, no. 12, pp. 8965–8971, 2020.

[356] S. Kjelstrup and D. Bedeaux, *Non-equilibrium thermodynamics of heterogeneous systems, second edition*, vol. 20. World Scientific, 2020.

[357] L. Onsager, "Reciprocal relations in irreversible processes. I.," *Physical Review*, vol. 37, no. 4, pp. 405–426, 1931.

[358] L. Onsager, "Reciprocal relations in irreversible Processes. II.," *Physical Review*, vol. 38, no. 12, pp. 2265–2279, 1931.

[359] J. Israelachvili, *Intermolecular and Surface Forces*. Academic Press, 2011.

[360] M. Gouy, "Sur la constitution de la charge électrique à la surface d'un électrolyte," *Journal de Physique Théorique et Appliquée*, vol. 9, no. 1, pp. 457–468, 1910.

[361] D. L. Chapman, " LI. A contribution to the theory of electrocapillarity ," *The London, Edinburgh, and Dublin Philosophical Magazine and Journal of Science*, vol. 25, no. 148, pp. 475–481, 1913.

[362] A. S. Dukhin and P. J. Goetz, *Fundamentals of interface and colloid science*, vol. 24. Academic press, 2010.

[363] M. H. Blees, *Foundations of Colloid Science*, vol. 210. Oxford University Press, 2002.

[364] D. Andelman, "Electrostatic properties of membranes: The poisson-boltzmann theory," in *Handbook of Biological Physics*, vol. 1, pp. 603–642, Elsevier, 1995.

[365] T. Markovich, D. Andelman, and R. Podgornik, "Charged Membranes: Poisson-Boltzmann theory, DLVO paradigm and beyond," *arXiv preprint arXiv:1603.09451*, 2016.

[366] A. V. Delgado, F. González-Caballero, R. J. Hunter, L. K. Koopal, and J. Lyklema, "Measurement and interpretation of electrokinetic phenomena," *Journal of Colloid and Interface Science*, vol. 309, no. 2, pp. 194–224, 2007.

[367] R. Hartkamp, A. L. Biance, L. Fu, J. F. Dufrêche, O. Bonhomme, and L. Joly, "Measuring surface charge: Why experimental characterization and molecular modeling should be coupled," *Current Opinion in Colloid and Interface Science*, vol. 37, pp. 101–114, 2018.

[368] N. Kavokine, R. R. Netz, and L. Bocquet, "Fluids at the Nanoscale: From Continuum to Subcontinuum Transport," *Annual Review of Fluid Mechanics*, vol. 53, no. 1, pp. 377–410, 2021.

[369] Y. Levin, "Electrostatic correlations: From plasma to biology," *Reports on Progress in Physics*, vol. 65, no. 11, pp. 1577–1632, 2002.

[370] Y. Levin, E. Trizac, and L. Bocquet, "On the fluid-fluid phase separation in charged-stabilized colloidal suspensions," *Journal of Physics Condensed Matter*, vol. 15, no. 48 SPEC. ISS., pp. S3523–S3536, 2003.

[371] L. Joly, C. Ybert, E. Trizac, and L. Bocquet, "Liquid friction on charged surfaces: From hydrodynamic slippage to electrokinetics," *Journal of Chemical Physics*, vol. 125, no. 20, p. 204716, 2006.

[372] D. J. Bonthuis and R. R. Netz, "Beyond the continuum: How molecular solvent structure affects electrostatics and hydrodynamics at solid-electrolyte interfaces," *Journal of Physical Chemistry B*, vol. 117, no. 39, pp. 11397–11413, 2013.

[373] D. M. Huang, C. Cottin-Bizonne, C. Ybert, and L. Bocquet, "Ion-specific anomalous electrokinetic effects in hydrophobic nanochannels," *Physical Review Letters*, vol. 98, no. 17, pp. 1–4, 2007.

[374] S. Koneshan, J. C. Rasaiah, R. M. Lynden-Bell, and S. H. Lee, "Solvent structure, dynamics, and ion mobility in aqueous solutions at 25 °C," *Journal of Physical Chemistry B*, vol. 102, no. 21, pp. 4193–4204, 1998.

[375] K. E. Bett and J. B. Cappi, "Effect of pressure on the viscosity of water [1]," 1965.

[376] K. R. Harris and L. A. Woolf, "Temperature and volume dependence of the viscosity of water and heavy water at low temperatures," *Journal of Chemical and Engineering Data*, vol. 49, no. 4, 2004.

[377] T. Werder, J. H. Walther, R. L. Jaffe, T. Halicioglu, and P. Koumoutsakos, "Erratum: On the water-carbon interaction for use in molecular dynamics simulations of graphite and carbon nanotubes (Journal of Physical Chemistry B (2003) 107B (1349))," *Journal of Physical Chemistry B*, vol. 112, no. 44, p. 14090, 2008.

[378] B. Hafskjold and T. Ikeshoji, "Microscopic pressure tensor for hard-sphere fluids," *Physical Review E - Statistical Physics, Plasmas, Fluids, and Related Interdisciplinary Topics*, vol. 66, no. 1, p. 11203, 2002.

[379] I. Kusaka, "Statistical Mechanics of Inhomogeneous Fluids," *Statistical Mechanics for Engineers*, vol. 379, no. 1776, pp. 259–308, 2015.

[380] R. Ganti, Y. Liu, and D. Frenkel, "Hamiltonian Transformation to Compute Thermo-osmotic Forces," *Physical Review Letters*, vol. 121, no. 6, p. 68002, 2018.

[381] F. S. Gaeta, G. Perna, G. Scala, and F. Bellucci, "Nonisothermal matter transport in sodium chloride and potassium chloride aqueous solutions. 1. Homogeneous system (thermal diffusion)," *Journal of Physical Chemistry*, vol. 86, no. 15, pp. 2967–2974, 1982.

[382] S. A. Putnam and D. G. Cahill, "Transport of nanoscale latex spheres in a temperature gradient," *Langmuir*, vol. 21, no. 12, 2005.

[383] A. Würger, "Transport in Charged Colloids Driven by Thermoelectricity," *Physical Review Letters*, vol. 101, no. 10, p. 108302, 2008.

[384] A. Würger, "Thermal non-equilibrium transport in colloids," *Reports on Progress in Physics*, vol. 73, no. 12, 2010.

[385] D. Boda, K. Y. Chan, and D. Henderson, "Monte Carlo simulation of an ion-dipole mixture as a model of an electrical double layer," *Journal of Chemical Physics*, vol. 109, no. 17, 1998.

[386] E. Díaz-Herrera and F. Forstmann, "The density and polarization of an ion-dipole-electrolyte near a charged wall," *The Journal of Chemical Physics*, vol. 102, no. 22, 1995.

[387] V. Warshavsky and M. Marucho, "Polar-solvation classical density-functional theory for electrolyte aqueous solutions near a wall," *Physical Review E*, vol. 93, no. 4, 2016.

[388] A. Härtel, M. Janssen, D. Weingarth, V. Presser, and R. V. Roij, "Heat-to-current conversion of low-grade heat from a thermocapacitive cycle by supercapacitors," *Energy and Environmental Science*, vol. 8, no. 8, pp. 2396–2401, 2015.

[389] M. Dietzel and S. Hardt, "Thermoelectricity in Confined Liquid Electrolytes," *Physical Review Letters*, vol. 116, no. 22, p. 225901, 2016.

[390] Y. Jin, R. Tao, S. Luo, and Z. Li, "Size-Sensitive Thermoelectric Properties of Electrolyte-Based Nanofluidic Systems," *Journal of Physical Chemistry Letters*, vol. 12, no. 4, pp. 1144–1149, 2021.

[391] S. D. Lecce, T. Albrecht, and F. Bresme, "Taming the thermodiffusion of alkali halide solutions in silica nanopores," *Nanoscale*, vol. 12, no. 46, 2020.

[392] M. Dietzel and S. Hardt, "Flow and streaming potential of an electrolyte in a channel with an axial temperature gradient," *Journal of Fluid Mechanics*, vol. 813, pp. 1060–1111, 2017.

[393] W. Q. Chen, M. Sedighi, and A. P. Jivkov, "Thermo-osmosis in hydrophilic nanochannels: mechanism and size effect," *Nanoscale*, pp. 1696–1716, 2021.

[394] J. R. Errington, T. M. Truskett, and J. Mittal, "Excess-entropy-based anomalies for a waterlike fluid," *The Journal of chemical physics*, vol. 125, no. 24, p. 244502, 2006.

[395] M. Agarwal, M. P. Alam, and C. Chakravarty, "Thermodynamic, diffusional, and structural anomalies in rigid-body water models," *The Journal of Physical Chemistry B*, vol. 115, no. 21, pp. 6935–6945, 2011.

[396] G. Weisbuch and M. Gueron, "Scaling Length for Charged Interfaces.," *Journal de physique Paris*, vol. 44, no. 2, pp. 251–256, 1983.

[397] R. E. Rice and F. H. Horne, "Analytical solutions to the linearized poisson—boltzmann equation in cylindrical coordinates for different ionic—strength distributions," *Journal of Colloid and Interface Science*, vol. 105, pp. 172–182, 5 1985.

[398] P. Berg and K. Ladipo, "Exact solution of an electro-osmotic flow problem in a cylindrical channel of polymer electrolyte membranes," *Proceedings of the Royal Society A: Mathematical, Physical and Engineering Sciences*, vol. 465, pp. 2663–2679, 9 2009.

[399] P. Berg and J. Findlay, "Analytical solution of the Poisson–Nernst–Planck–Stokes equations in a cylindrical channel," *Proceedings of the Royal Society A: Mathematical, Physical and Engineering Sciences*, vol. 467, pp. 3157–3169, 11 2011.

[400] S. Faucher, N. Aluru, M. Z. Bazant, D. Blankschtein, A. H. Brozena, J. Cumings, J. Pedro de Souza, M. Elimelech, R. Epsztein, J. T. Fourkas, A. G. Rajan, H. J. Kulik, A. Levy, A. Majumdar, C. Martin, M. McEldrew, R. P. Misra, A. Noy, T. A. Pham, M. Reed, E. Schwegler, Z. Siwy, Y. Wang, and M. Strano, "Critical Knowledge Gaps in Mass Transport through Single-Digit Nanopores: A Review and Perspective," *The Journal of Physical Chemistry C*, vol. 123, pp. 21309–21326, 9 2019.